

STRUCTURAL DYNAMICS OF
PHOTOEXCITED NANOLAYERED
PEROVSKITES STUDIED BY ULTRAFAST
X-RAY DIFFRACTION

PUBLIKATIONSBASIERTE DISSERTATION

Zur Erlangung des akademischen Grades
“doctor rerum naturalium”
(Dr. rer. nat.)
in der Wissenschaftsdisziplin: “Experimentalphysik”

eingereicht an der
Mathematisch-Naturwissenschaftlichen Fakultät
der Universität Potsdam

von
Marc Herzog
geboren am 01.05.1981 in Eisenhüttenstadt

Published online at the
Institutional Repository of the University of Potsdam:
URL <http://opus.kobv.de/ubp/volltexte/2012/6263/>
URN [urn:nbn:de:kobv:517-opus-62632](http://nbn-resolving.org/urn:nbn:de:kobv:517-opus-62632)
<http://nbn-resolving.de/urn:nbn:de:kobv:517-opus-62632>

To Peggy

ABSTRACT

This publication-based thesis represents a contribution to the active research field of ultrafast structural dynamics in laser-excited nanostructures. The investigation of such dynamics is mandatory for the understanding of the various physical processes on microscopic scales in complex materials which have great potentials for advances in many technological applications. I theoretically and experimentally examine the coherent, incoherent and anharmonic lattice dynamics of epitaxial metal-insulator heterostructures on timescales ranging from femtoseconds up to nanoseconds. To infer information on the transient dynamics in the photoexcited crystal lattices experimental techniques using ultrashort optical and x-ray pulses are employed. The experimental setups include table-top sources as well as large-scale facilities such as synchrotron sources.

At the core of my work lies the development of a linear-chain model to simulate and analyze the photoexcited atomic-scale dynamics. The calculated strain fields are then used to simulate the optical and x-ray response of the considered thin films and multilayers in order to relate the experimental signatures to particular structural processes. This way one obtains insight into the rich lattice dynamics exhibiting coherent transport of vibrational energy from local excitations via delocalized phonon modes of the samples. The complex deformations in tailored multilayers are identified to give rise to highly nonlinear x-ray diffraction responses due to transient interference effects. The understanding of such effects and the ability to precisely calculate those are exploited for the design of novel ultrafast x-ray optics. In particular, I present several Phonon Bragg Switch concepts to efficiently generate ultrashort x-ray pulses for time-resolved structural investigations.

By extension of the numerical models to include incoherent phonon propagation and anharmonic lattice potentials I present a new view on the fundamental research topics of nanoscale thermal transport and anharmonic phonon-phonon interactions such as nonlinear sound propagation and phonon damping. The former issue is exemplified by the time-resolved heat conduction from thin SrRuO₃ films into a SrTiO₃ substrate which exhibits an unexpectedly slow heat conductivity. Furthermore, I discuss various experiments which can be well reproduced by the versatile numerical models and thus evidence strong lattice anharmonicities in the perovskite oxide SrTiO₃.

The thesis also presents several advances of experimental techniques such as time-resolved phonon spectroscopy with optical and x-ray photons as well as concepts for the implementation of x-ray diffraction setups at standard synchrotron beamlines with largely improved time-resolution for investigations of ultrafast structural processes.

This work forms the basis for ongoing research topics in complex oxide materials including electronic correlations and phase transitions related to the elastic, magnetic and polarization degrees of freedom.

KURZDARSTELLUNG

Diese publikationsbasierte Dissertation ist ein Beitrag zu dem aktuellen Forschungsgebiet der ultraschnellen Struktur­dynamik in laserangeregten Nanostrukturen. Die Erforschung solcher Vorgänge ist unabdingbar für ein Verständnis der vielseitigen physikalischen Prozesse auf mikroskopischen Längenskalen in komplexen Materialien, welche enorme Weiterentwicklungen für technologische Anwendungen versprechen. Meine theoretischen und experimentellen Untersuchungen betrachten kohärente, inkohärente und anharmonische Gitterdynamiken in epitaktischen Metal-Isolator-Heterostrukturen auf Zeitskalen von Femtosekunden bis Nanosekunden. Um Einsichten in solche transienten Prozesse in laserangeregten Kristallen zu erhalten, werden experimentelle Techniken herangezogen, die ultrakurze Pulse von sichtbarem Licht und Röntgenstrahlung verwenden.

Ein zentraler Bestandteil meiner Arbeit ist die Entwicklung eines Linearkettenmodells zur Simulation und Analyse der laserinitiierten Atombewegungen. Die damit errechneten Verzerrungsfelder werden anschließend verwendet, um die Änderung der optischen und Röntgeneigenschaften der betrachteten Dünnschicht- und Vielschichtsysteme zu simulieren. Diese Rechnungen werden dann mit den experimentellen Daten verglichen, um die experimentellen Signaturen mit errechneten strukturellen Prozessen zu identifizieren. Dadurch erhält man Einsicht in die vielseitige Gitterdynamiken, was z.B. einen kohärenten Transport der Vibrationsenergie von lokal angeregten Bereichen durch delokalisierte Phononmoden offenbart. Es wird gezeigt, dass die komplexen Deformationen in maßgeschneiderten Vielschichtsystemen hochgradig nichtlineare Röntgenbeugungseffekte auf Grund von transienten Interferenzerscheinungen verursachen. Das Verständnis dieser Prozesse und die Möglichkeit, diese präzise zu simulieren, werden dazu verwendet, neuartige ultraschnelle Röntgenoptiken zu entwerfen. Insbesondere erläutere ich mehrere Phonon-Bragg-Schalter-Konzepte für die effiziente Erzeugung ultrakurzer Röntgenpulse, die in zeitaufgelösten Strukturanalysen Anwendung finden.

Auf Grund der Erweiterung der numerischen Modelle zur Beschreibung von inkohärenter Phononenausbreitung und anharmonischer Gitterpotentiale decken diese ebenfalls die aktuellen Themengebiete von Wärmetransport auf Nanoskalen und anharmonischer Phonon-Phonon-Wechselwirkung (z.B. nichtlineare Schallausbreitung und Phonondämpfung) ab. Die erstere Thematik wird am Beispiel der zeitaufgelösten Wärmeleitung von einem dünnen SrRuO₃-Film in ein SrTiO₃-Substrat behandelt, wobei ein unerwartet langsamer Wärmetransport zu Tage tritt. Außerdem diskutiere ich mehrere Experimente, die auf Grund der sehr guten Reproduzierbarkeit durch die numerischen Modelle starke Gitteranharmonizitäten in dem oxidischen Perowskit SrTiO₃ bezeugen.

Diese Dissertation erarbeitet zusätzlich verschiedene Weiterentwicklungen von experimentellen Methoden, wie z.B. die zeitaufgelöste Phononenspektroskopie mittels optischer Photonen und Röntgenphotonen, sowie Konzepte für die Umsetzung von Röntgenbeugungsexperimenten an Standard-Synchrotronquellen mit stark verbesserter Zeitauf­lösung

für weitere Studien von ultraschnellen Strukturvorgängen.

CONTENTS

List of Papers	xi
Comments on Papers	xiii
List of Figures	xvii
Abbreviations	xix
1 Introduction	1
1.1 Topical introduction	2
1.2 The scope and structure of this work	3
2 Simulation of photoexcited linear lattice dynamics observed by UXR	5
2.1 Linear-chain model (LCM) of coherent photoexcited lattice dynamics	5
2.1.1 From photoexcitation to thermal expansion	5
2.1.2 The linear-chain model (LCM)	9
2.1.3 Photoexcited lattice dynamics of thin films	10
2.1.4 Photoexcited lattice dynamics of superlattices	14
2.2 Calculation and interpretation of UXR response of photoexcited lattice dynamics using the LCM	17
2.2.1 Dynamical x-ray diffraction in combination with the LCM	17
2.2.2 Transient splitting of Bragg peaks	18
2.2.3 UXR response of superlattices	22
2.2.4 Limitations of the instantaneous stress assumption	24
3 The role of incoherent lattice dynamics	27
3.1 Incorporation of heat diffusion into the LCM	28
3.2 Coherent and incoherent lattice dynamics in thin films	29
3.3 Heat diffusion in superlattices	31
4 Nonlinear lattice dynamics	33
4.1 Light scattering from coherent phonons	34
4.2 The anharmonic linear-chain model	35
4.3 Nonlinear strain propagation in SrTiO ₃	37
4.4 Attenuation of quasi-monochromatic phonons	39
4.4.1 Generation and detection of quasi-monochromatic phonon wavepackets	39
4.4.2 Anharmonic decay of coherent phonons – UXR	41
4.4.3 Anharmonic decay of coherent phonons – All-optical experiments	47
5 The Phonon Bragg Switch	53
5.1 X-ray pulse shaping by forbidden SL reflections	55
5.2 X-ray pulse shaping by photoexcited thin films	57
5.2.1 Truncation of x-rays by impulsive thermal expansion	57
5.2.2 Slicing of x-rays by coherent thin-film dynamics	58
6 Summary and Outlook	61
Bibliography	65
Acknowledgments	75

Papers

I	Analysis of ultrafast x-ray diffraction data in a linear-chain model of the lattice dynamics	81
II	Tailoring interference and nonlinear manipulation of femtosecond x-rays	95
III	Ultrafast manipulation of hard x-rays by efficient Bragg switches	107
IV	Transient x-ray reflectivity of epitaxial oxide superlattices investigated by femtosecond x-ray diffraction	113
V	Comparing the oscillation phase in optical pump-probe spectra to ultrafast x-ray diffraction in the metal-dielectric SrRuO ₃ /SrTiO ₃ superlattice	119
VI	Nanoscale heat transport studied by high-resolution time-resolved x-ray diffraction	127
VII	Calibrated real time detection of nonlinearly propagating giant strain waves	141
VIII	Detecting optically synthesized quasi-monochromatic sub-terahertz phonon wavepackets by ultrafast x-ray diffraction	149
IX	Shortening x-ray pulses for pump-probe experiments at synchrotrons	155
X	Ultrafast switching of hard x-rays	161
XI	Normalization schemes for ultrafast x-ray diffraction using a table-top laser-driven plasma source	177
XII	Subpicosecond hard x-ray streak camera using single-photon counting	187

LIST OF PAPERS

This thesis is based on the following papers which can be found at the end of this document and are referred to in the text by their roman numerals. A short summary of the papers as well as the description of my respective contributions can be found in the subsequent section.

I Analysis of ultrafast x-ray diffraction data in a linear-chain model of the lattice dynamics

M. Herzog, D. Schick, P. Gaal, R. Shayduk, C. von Korff Schmising and M. Bargheer.

Appl. Phys. A **106**, 489 (2012).

II Tailoring interference and nonlinear manipulation of femtosecond x-rays

M. Herzog, D. Schick, W. Leitenberger, R. Shayduk, R. M. van der Veen, C. J. Milne, S. L. Johnson, I. Vrejoiu and M. Bargheer.

New J. Phys. **14**, 013004 (2012).

III Ultrafast manipulation of hard x-rays by efficient Bragg switches

M. Herzog, W. Leitenberger, R. Shayduk, R. M. van der Veen, C. J. Milne, S. L. Johnson, I. Vrejoiu, M. Alexe, D. Hesse and M. Bargheer.

Appl. Phys. Lett. **96**, 161906 (2010).

IV Transient x-ray reflectivity of epitaxial oxide superlattices investigated by femtosecond x-ray diffraction

M. Herzog, W. Leitenberger, R. Shayduk, R. M. van der Veen, C. J. Milne, S. L. Johnson, I. Vrejoiu, M. Alexe, D. Hesse and M. Bargheer.

Ultrafast Phenomena XVII - Proceedings of the 17th International Conference, 290 (2011).

V Comparing the oscillation phase in optical pump-probe spectra to ultrafast x-ray diffraction in the metal-dielectric SrRuO₃/SrTiO₃ superlattice

A. Bojahr, D. Schick, L. Maerten, M. Herzog, I. Vrejoiu, C. von Korff Schmising, C. J. Milne, S. L. Johnson and M. Bargheer.

Phys. Rev. B **85**, 224302 (2012).

VI Nanoscale heat transport studied by high-resolution time-resolved x-ray diffraction

R. Shayduk, H. Navirian, W. Leitenberger, J. Goldshteyn, I. Vrejoiu, M. Weinelt, P. Gaal, M. Herzog, C. von Korff Schmising and M. Bargheer.
New J. Phys. **13**, 093032 (2011).

VII Calibrated real time detection of nonlinearly propagating giant strain waves

A. Bojahr, M. Herzog, D. Schick, I. Vrejoiu and M. Bargheer.
submitted.

VIII Detecting optically synthesized quasi-monochromatic sub-terahertz phonon wavepackets by ultrafast x-ray diffraction

M. Herzog, A. Bojahr, J. Goldshteyn, W. Leitenberger, I. Vrejoiu, D. Khakhulin, M. Wulff, R. Shayduk, P. Gaal and M. Bargheer.
Appl. Phys. Lett. **100**, 094101 (2012).

IX Shortening x-ray pulses for pump-probe experiments at synchrotrons

H. A. Navirian, M. Herzog, J. Goldshteyn, W. Leitenberger, I. Vrejoiu, D. Khakhulin, M. Wulff, R. Shayduk, P. Gaal and M. Bargheer.
J. Appl. Phys. **109**, 126104 (2011).

X Ultrafast switching of hard x-rays

P. Gaal, D. Schick, M. Herzog, A. Bojahr, R. Shayduk, J. Goldshteyn, H. A. Navirian, W. Leitenberger, I. Vrejoiu, D. Khakhulin, M. Wulff and M. Bargheer.
submitted.

XI Normalization schemes for ultrafast x-ray diffraction using a table-top laser-driven plasma source

D. Schick, A. Bojahr, M. Herzog, C. von Korff Schmising, R. Shayduk, W. Leitenberger, P. Gaal and M. Bargheer.
Rev. Sci. Instrum. **83**, 025104 (2012).

XII Subpicosecond hard x-ray streak camera using single-photon counting

H. Enquist, H. Navirian, R. Nüske, C. von Korff Schmising, A. Jurgilaitis, M. Herzog, M. Bargheer, P. Sondhaus and J. Larsson.
Opt. Lett. **35**, 3219 (2010).

COMMENTS ON PAPERS

Here, I give a brief summary of the papers listed in the previous section by presenting the respective key statement(s) and outline my contributions to each of the papers.

I Analysis of ultrafast x-ray diffraction data in a linear-chain model of the lattice dynamics

The paper presents the concept and implications of a one-dimensional linear-chain model (LCM) for the simulation and analysis of coherent lattice dynamics in nanolayered crystalline heterostructures after photoexcitation by ultrafast laser pulses. In addition to theoretical discussion, we compare the LCM results to previous and new UXRd studies on a metal-insulator superlattice (SL) and found the apparent damping of the characteristic SL eigenmode to arise from the mechanical coupling to the substrate. Moreover, we discovered a Bragg peak splitting instead of continuous shifting for strongly excited SLs.

This publication forms the basis of the numerical simulations employed in this thesis. After adaption of the LCM from Ref. 1 and further developments (especially combining the LCM with dynamical x-ray diffraction (XRD) calculations) I performed most of the analysis and calculations presented in this paper. Furthermore, the presented UXRd experiments were partly conducted by myself.

II Tailoring interference and nonlinear manipulation of femtosecond x-rays

In this paper we present the modulations of SL Bragg peaks after photoexcitation with ultrashort laser pulses. The dynamical XRD simulations using the lattice dynamics calculated by the LCM reproduce the various UXRd measurements very accurately. The mechanisms responsible for the observed linear and nonlinear x-ray responses including constructive and destructive x-ray interference effects are explained by a simple envelope model.

All the UXRd measurements (Swiss Light Source) and simulations presented in this paper were performed by myself. Moreover, I executed almost the entire analysis and developed the presented interpretations.

III Ultrafast manipulation of hard x-rays by efficient Bragg switches

In this letter we re-investigated the x-ray response of a optically excited SrRuO₃/SrTiO₃ SL and discovered a SL peak exhibiting a strong nonlinear response to the photoexcited SL phonon mode. By presenting simulations of a properly tailored SL, we stress the great potential of the observed x-ray response as a Phonon Bragg Switch for the shortening of synchrotron x-ray pulses.

For this publication I carried out the shown UXRD measurements at the Swiss Light Source and performed the data analysis as well as the simulations.

IV Transient x-ray reflectivity of epitaxial oxide superlattices investigated by femtosecond x-ray diffraction

This proceeding summarizes the contents of Paper **III** which were presented at the international conference ‘Ultrafast Phenomena XVII’.

V Comparing the oscillation phase in optical pump-probe spectra to ultrafast x-ray diffraction in the metal-dielectric SrRuO₃/SrTiO₃ superlattice

This paper is dedicated to the phase of the photoexcited SL oscillations which encodes the mechanism of the ultrafast stress generation in a SrRuO₃/SrTiO₃ SL. After deducing time delay zero very carefully, we observe a fluence-dependent oscillation phase. In addition to the regular electron-phonon coupling, the results indicate an increasing influence of alternative stress generation mechanisms such as electronic pressure, impulsive stimulated Raman scattering or temperature and/or mode-dependent Grüneisen coefficients.

For this publication I performed the measurements, the analysis and the simulations regarding the UXRD data. Moreover, I actively participated in the interpretation of all the experimental results.

VI Nanoscale heat transport studied by high-resolution time-resolved x-ray diffraction

Here, we investigate the thermal relaxation of a SL by heat conduction from the SL into the substrate. We perform synchrotron-based high-precision UXRD measurements and record the transient shifts of the SL and substrate peaks over a large time range. The results are accurately reproduced by the regular heat equation assuming the bulk thermal properties of the constituting materials.

I prepared detailed simulations of the thermal transport and dynamical XRD and participated in the data analysis.

VII Calibrated real time detection of nonlinearly propagating giant strain waves

We present a UXRd-calibrated fluence-dependent study of the transient broadband optical reflectivity of a $\text{La}_{0.7}\text{Sr}_{0.3}\text{MnO}_3$ thin film on SrTiO_3 . At high fluence we observe a splitting of the sound velocity of the wavepackets propagating through the STO substrate. The results of lattice-dynamics calculations using an anharmonic lattice potential accurately explain the experimental results.

After performing the all-optical pump-probe measurements I actively participated in the data analysis. Moreover, I assisted in the development of the anharmonic LCM and the resulting simulations.

VIII Detecting optically synthesized quasi-monochromatic sub-terahertz phonon wavepackets by ultrafast x-ray diffraction

By optical multiple pulse excitation of a SrRuO_3 thin film transducer we tailor quasi-monochromatic coherent phonon wavepackets whose generation and propagation into the SrTiO_3 substrate is monitored by UXRd. We observe a very fast attenuation of these sound pulses which can be approximated by standard theoretical models. The results evidence that the phonon damping rate is mainly due to anharmonic phonon-phonon scattering.

Among other colleagues of the Potsdam group, I participated in the data acquisition during a 5-days synchrotron beamtime at the ESRF. I exclusively performed the data analysis as well as the required UXRd simulations and the comparison to the theoretical models.

IX Shortening x-ray pulses for pump-probe experiments at synchrotrons

In this paper we present the concept of a x-ray pulse sorting Phonon Bragg Switch for UXRd setups at synchrotrons. We exploit the peak shift of a photoexcited SL to truncate the synchrotron x-ray pulse and evidence this process by the increased time-resolution of a subsequent UXRd experiment on similar dynamics in a second SL.

Among other colleagues of the Potsdam group, I participated in the data acquisition during a 5-days synchrotron beamtime at the ESRF. I participated in the data analysis and interpretation to a great extent and supported the conclusions by simulations of the lattice dynamics and the recorded UXRd signals.

X Ultrafast switching of hard x-rays

This manuscript discussed a novel concept of a Phonon Bragg Switch exploiting the coherent lattice dynamics of a photoexcited SrRuO₃ thin film and the corresponding transient Bragg peak shift to slice synchrotron x-ray pulses down to a few picoseconds. Using these short x-ray pulses, we present a proof-of-principle experiment demonstrating the potential of this technique which can be optimized to have a performance similar to femto-slicing techniques.

Among other colleagues of the Potsdam group, I participated in the data acquisition during a 5-days synchrotron beamtime at the ESRF. I assisted in the data analysis and provided detailed UXRD simulations which improved the understanding of the working principle of the Phonon Bragg Switch and allowed the optimization of this device.

XI Normalization schemes for ultrafast x-ray diffraction using a table-top laser-driven plasma source

This paper presents the laser-driven plasma x-ray source (PXS) used in our group for UXRD experiments. In particular, we explain various normalization schemes which compensate for the intensity fluctuations of the x-ray source. The different approaches are discussed in detail and experimental results exhibiting signal-to-noise reductions are shown.

I generally supported the long-term development of our PXS and always provided detailed UXRD simulations prior to and/or after the numerous experiments performed with this source on various materials and sample structures. In particular, I performed the simulations shown and discussed in this publication.

XII Subpicosecond hard x-ray streak camera using single-photon counting

This letter presents a hard x-ray streak camera with sub-picosecond time-resolution exploiting single-photon counting. After discussing the device and its working principles, several experimental results are shown which evidence the good time-resolution. One of the experiments uses the transient x-ray response of a photoexcited SL.

Together with some colleagues of the Larsson group in Lund, Sweden, I performed the UXRD experiments on our well-characterized SrRuO₃/SrTiO₃ SL. I also assisted in the analysis and interpretation of the UXRD data.

LIST OF FIGURES

2.1	Optical excitation of electrons and the subsequent relaxation processes in a metal.	7
2.2	Schematic of a linear chain of masses and springs and the photogenerated stress symbolized by spacer sticks.	9
2.3	Results of the LCM for a 94.8 nm thick SRO layer on a STO substrate assuming different optical penetration depths.	11
2.4	Transient average strain of the SRO and STO layers of the SL after photoexcitation.	16
2.5	Stationary and transient rocking curves of a 94.8 nm thick SRO thin film on a STO substrate.	19
2.6	Transient strain from LCM calculations assuming $\xi_{\text{SRO}} = 44$ nm and comparison of the PXS data with LCDX results.	20
2.7	Comparison of UXRD data with LCDX results for different optical penetration depths.	21
3.1	Transient PXS rocking curves of 15.4 nm SRO on a STO substrate and a comparison of the inferred transient SRO peak position with the corresponding LCDX calculations including heat diffusion.	30
4.1	Anharmonic interatomic potential of STO deduced from the all-optical pump-probe experiments presented in Paper VII by the anharmonic (diatomic) LCM.	39
4.2	Experimental and simulated transient rocking curves of an STO substrate through which a quasi-monochromatic phonon wavepacket is propagating. Pulse-to-pulse build-up of the squared amplitude spectrum of the LA phonon modes predicted by the harmonic LCM.	40
4.3	Transient rocking curves and normalized change of x-ray intensity of the phonon-induced first-order sideband of a STO substrate Bragg peak.	43
4.4	Decay times derived from phonon-induced UXRD transients and comparison to theoretical models.	44
4.5	Transient rocking curves and Q -dependent decay times of the phonon-induced first-order STO substrate sideband calculated by aLCDX. Simulated intensity transient of the integrated sideband intensity and the dependence of its decay time on phonon amplitude.	46
4.6	Second-order optical cross-correlation of a pump pulse train with $\tau_p = 15.5$ ps. Broadband differential optical reflectivity of a 36 nm LSMO film on STO after excitation with the characterized pump pulse train.	48
4.7	Background-subtracted phonon oscillations extracted from the optical data shown in Fig. 4.6 and the deduced phonon spectrum.	49

4.8	Decay of the optical reflectivity oscillation amplitude around the fundamental phonon frequency revealing the phonon amplitude lifetime which exhibits a strong dependence on integrated pump fluence.	50
4.9	Comparison of the phonon amplitude lifetimes obtained from UXRD and all-optical experiments with the theoretical models described in Section 4.4.2. . .	50
5.1	Schematic experimental setup for the implementation of a Phonon Bragg Switch (PBS) for UXRD experiments at synchrotrons. Comparison of x-ray pulse shapes diffracted from different PBS devices.	55

ABBREVIATIONS

aLCDX	Anharmonic linear-chain model and dynamical x-ray diffraction
BSP	Bipolar strain pulse
DECP	Displacive excitation of coherent phonons
ISRS	Impulsive stimulated Raman scattering
LA	Longitudinal acoustic
LCDX	Linear-chain model (harmonic) and dynamical x-ray diffraction
LCM	Linear-chain model
LSMO	$\text{La}_{1-x}\text{Sr}_x\text{MnO}_3$, Lanthanum Strontium Manganite
PXS	Plasma X-ray Source
RD	Relaxation damping
SRO	SrRuO_3 , Strontium Ruthenate
STO	SrTiO_3 , Strontium Titanate
TE	Thermoelastic
UXRD	Ultrafast x-ray diffraction
XRD	X-ray diffraction
ZFLAP	Zone-folded longitudinal acoustic phonon

INTRODUCTION

This work presents the most important theoretical and experimental results of my graduate studies in the ultrafast dynamics group of Prof. Matias Bargheer at the University of Potsdam in form of a cumulative dissertation. That is, this thesis is based on twelve published and unpublished manuscripts containing the major results of my work. These manuscripts and papers are appended to the end of the thesis and are referred to in the text by their roman numerals as given in the List of Papers.

The thesis addresses the rapidly growing topic of structural dynamics in nanostructured condensed matter triggered by optical excitation with ultrashort laser pulses. The employed experimental methods to investigate these photoinduced structural dynamics use ultrashort optical and x-ray pulses. The experimental results are analyzed by comparison to numerical models which are developed in this thesis in order to investigate the rich laser-induced coherent, incoherent and anharmonic lattice dynamics. The results discovered during my graduate studies (in collaboration with the Potsdam group as well as international research groups) reveal very interesting and important physical effects in photoexcited nanostructures, e.g.,

- decay of localized vibrational states due to coherent energy transport via delocalized eigenmodes (Paper **I**)
- transient nonlinear x-ray interference effects in tailored epitaxial multilayers (Paper **II**)
- optical synthesis and x-ray detection of quasi-monochromatic phonon wavepackets (Paper **VIII**)
- nonlinear propagation and attenuation of acoustic phonons due to the anharmonic lattice potential in SrTiO₃ (Papers **VII** and **VIII**)
- several realizations of efficient Phonon Bragg Switches for the generation of ultrashort x-ray pulses (Papers **III,IV,IX** and **X**)

Since the space in publications is usually limited the appended papers focus on the main experimental and numerical results. Also the theory is usually discussed in a very compact form. Therefore, this thesis does not only summarize but also extends the content of the papers. In addition, I partly present recent unpublished experimental results, further theoretical calculations and a more in-depth analysis of recently published results in the field of linear and nonlinear structural dynamics in photoexcited nanostructures.

1.1 Topical introduction

In general, the atomistic nature of matter implies that all macroscopic dynamics are governed by microscopic processes and interactions. If we consider matter—in particular solids—to be built up from atoms which are connected by covalent and/or ionic bonds the fundamental microscopic processes are the motion of electrons and atoms. The electrons can either be bound to the atoms/ions (dielectrics) or they are allowed to more or less freely move around within the solid (metals) by ballistic or diffusive propagation and, moreover, the spin state of the electronic system determines the magnetic properties of the material. The atoms, however, are elastically bound around their equilibrium positions within the framework of the solid. Here, the fundamental lengthscale is on the order of $1 \text{ \AA} = 10^{-10} \text{ m}$. The fundamental timescale of microscopic processes is two-fold. Electronic motion usually takes place on a sub-femtosecond (fs) to 10 fs timescale whereas the atomic motion has a lower bound on the order of 10 fs. The motions of atoms within a solid can in principle be divided into coherent and incoherent (statistical) motion, i.e., wave-like phonon propagation and heat transport, respectively.

In addition to the fundamental interest in such microscopic physical processes, the understanding of those is essential for various technological advances in the fields of signal processing, data storage and sensors exploiting the materials' elastic, magnetic and/or electric degrees of freedom [2, 3]. The couplings and correlations between these subsystems in so-called multiferroics which are often mediated by the crystal lattice promise novel high-performance devices [4, 5]. The demand for the ever increasing speed of such technologies triggered attempts to control and switch the state of matter exploiting optical pulses [2, 4, 6–8]. Moreover, the miniaturization of electronic devices in the past inevitably brought up the issue of nanoscale thermal transport [9]. The full control not only of the macroscopic but also the microscopic quantum state of many-body systems by, e.g., light-matter interactions, may open the gate to novel and efficient quantum information processing devices [10].

If one desires to understand and experimentally investigate such processes, the fundamental length and timescales call for sophisticated experimental techniques. Possible methods to resolve the small lengthscales are scattering techniques using neutrons, electrons or x-rays [11–14]. For structural dynamics on larger lengthscales scattering of optical photons may also be employed. If one additionally wants to follow the dynamics in time, one standard technique is the pump-probe method [15, 16]. The sample of interest is excited by an external stimulus (such as a laser pulse or an electric/magnetic pulse) and subsequently probed by a suitably chosen ultrashort probe pulse (e.g. optical light, x-rays, neutrons, electrons or an electric current) which is influenced by the triggered dynamics of the sample. The controlled variation of the time delay t between the pump and the probe pulse yields snapshots of the sample dynamics which are encoded in the change of the measured probe signal $S(t)$. The time-resolution of the pump-probe method crucially depends on the pulse durations of the pump and probe pulses which therefore select the dynamics that can be accessed by the particular experiment. For instance, neutron pulses are only available at pulse durations down to milliseconds [17, 18] which currently rules out such particles as a good probe for atomic/lattice dynamics in the time domain. The kind of dynamics accessible by a particular experiment is also selected by the nature of the probe pulse. For instance, the limited penetration depth of electrons ($\approx 10 - 100 \text{ nm}$) gives a more surface-sensitive probe [19] whereas (non-resonant) x-ray diffraction (XRD) yields structural information up to a probe depth of $1 - 100 \text{ }\mu\text{m}$ [20]. Both techniques experienced a rapid development in recent years [13, 14, 21, 22].

1.2 The scope and structure of this work

As indicated above, one promising perspective for controlling the state of matter is its manipulation by light, in particular, by ultrashort optical laser pulses. In this work I consider numerical models and experiments based on pump-probe techniques for the investigation of photoinduced structural dynamics of crystalline solids. The materials are typically excited by ultrashort laser pulses of 800 nm wavelength and probed by either visible laser or x-ray pulses. The main focus in this thesis, however, is put on ultrafast x-ray diffraction (UXRD). Over the past two decades UXRD has proven to be a versatile experimental method to unambiguously infer structural dynamics of laser-excited materials [14, 23–31].

My investigations are focussed on materials with perovskite crystal structure. These oxides are of cubic or pseudocubic ABO_3 -type structure where A and B are different cations [32]. Since lots of combinations of A and B cations can be practically realized, perovskites offer a broad spectrum of physical properties interesting for fundamental research as well as technological applications. For instance, perovskites exhibit different phases including insulating dielectrics, metals, ferro-/antiferroelectrics, ferro-/antiferromagnets, multiferroics, superconductors or thermoelectrics [32–34] and phase transitions can often be triggered by optical excitation [15, 35, 36]. The samples discussed in this work are restricted to a few representatives of perovskites, namely, the insulator $SrTiO_3$ and the ferroelectric metals $SrRuO_3$ and $La_{0.7}Sr_{0.3}MnO_3$. Moreover, I focus on epitaxial nanolayers grown on a supporting substrate by pulsed laser deposition at the Max-Planck-Institute for Microstructure Physics in Halle, Germany [37]. The sample geometries range from thin films, bilayers and multilayers to superlattices.

At the core of the current work lies the development and improvement of computational models for the photoinduced lattice dynamics of the nanolayered heterostructures. The first part of Chapter 2 presents a one-dimensional linear-chain model (LCM) of masses and (harmonic) springs representing the relevant sample dimension perpendicular to the layer interface(s). This LCM is used to simulate the coherent structural dynamics of metallic thin films and metal-insulator superlattices after a quasi-instantaneous optical excitation. I then discuss general features of these dynamics. This part of the thesis is based on and extends the considerations in Paper **I**. The second part of Chapter 2 is dedicated to the calculation and interpretation of UXRD signals from the lattice motions obtained from the LCM. These combined calculations are compared to experimental UXRD results for the chosen sample structures. The excellent agreement demonstrates that the LCM correctly captures the essential photoinduced lattice dynamics in metal-insulator nanolayered systems. Moreover, it is possible to relate the general UXRD features to the corresponding structural changes as discussed in Paper **II**. Very recent experimental results (Paper **V**) suggest fluence-dependent changes of the excitation mechanism possibly related to impulsive stimulated Raman scattering (ISRS), electronic pressure or mode-dependent Grüneisen coefficients. These effects require modifications of the LCM (such as non-instantaneous stress generation) in order to reproduce the experiments. This issue is addressed in the final section of Chapter 2.

Considering the photoexcited lattice dynamics on larger timescales or in smaller sample structures one can no longer neglect the effect of thermal transport. This issue is addressed in Paper **VI** with very high experimental accuracy. Chapter 3 summarizes and continues these investigations by including heat conduction in the LCM. The model is then tested by comparison to UXRD experiments on a very thin laser-excited metal film. The calculations reveal very good agreement thereby identifying thermal properties of the metal film which deviate from the static bulk literature values.

In Chapter 4 I discuss and further analyze time-resolved optical and XRD measurements presented in Papers **VIII** and **VII**. These experimental results strongly indicate the effect of lattice anharmonicities by significant deviation of the acoustic phonon propagation and lifetime from the established theoretical models. Moreover, these quantities are found to depend on the phonon amplitude. The LCM is extended to allow for an arbitrary interatomic potential of the considered crystal lattice. Although the model is restricted to merely include a cubic term in the potential (in addition to the harmonic quadratic term) its calculated results exhibit very good agreement to the experimental data in terms of lifetime, nonlinear propagation and modifications of the spectra of the photogenerated coherent phonons.

The presented LCM and its variations which include physical effects of heat conduction and lattice anharmonicities prove to be valid by its very precise predictions of the experimental signals. Slight deviations of the calculations from the experimental results, however, carry the potential of indicating new physical aspects of the considered systems as pointed out in this thesis. In addition to this great potential of the discussed models, Chapter 5 presents other application-oriented benefits of the ability to precisely predict the UXRD response of photoexcited nanolayered heterostructures. Our discovery of an efficient Phonon Bragg Switch [38, 39] (discussed in detail in Papers **III** and **IV**) and the understanding of the physical processes behind this behaviour by means of the LCM (Paper **II**) exemplify the use of these calculations for the design of novel x-ray optics in the field of time-resolved XRD. Since this first superlattice-based Phonon Bragg Switch we developed and tested several strategies for the efficient generation of ultrashort x-ray pulses. Chapter 5 summarizes and unifies the related discussions presented in Papers **II-IV**, **IX** and **X**.

Finally, Chapter 6 summarizes this thesis and gives an outlook to physical problems which may be elucidated in the near future with the help of the models and the knowledge presented in this thesis.

SIMULATION OF PHOTOEXCITED LINEAR LATTICE DYNAMICS OBSERVED BY UXRD

This chapter is divided into two main parts. Section 2.1 addresses the crystal lattice response of metal-insulator heterostructures after the excitation by ultrashort laser pulses and how such lattice dynamics can be modeled. After a brief summary of the complex relaxation dynamics of the optically excited electrons in metals in Section 2.1.1, I present a simple linear-chain model (LCM) in Section 2.1.2 which summarizes the essential details of the model reported in Paper I. The application of the LCM to two particular sample geometries in Sections 2.1.3 and 2.1.4 demonstrates that this simple model is capable of predicting the coherent lattice dynamics of an arbitrary nanolayered heterostructure assuming an instantaneous onset of a photoinduced thermal stress and neglecting heat diffusion.

Section 2.2 is dedicated to the numerical simulation of time-resolved dynamical x-ray diffraction from the photoinduced lattice dynamics calculated by the LCM. The brief introduction of dynamical x-ray diffraction and its extension by the integration of the LCM results (Section 2.2.1) is followed by a comparison of the simulations to previously published (Papers I-V) and unpublished UXRD experiments conducted by our research group on epitaxial thin metallic films and metal-insulator superlattices (Sections 2.2.2 and 2.2.3). An excellent agreement of simulation and experiment is revealed and the observed UXRD features can be uniquely related to the structure-dynamical features of the respective samples obtained from the LCM. The validity of the assumptions entering the LCM for the considered cases is thus verified. However, Section 2.2.4 presents UXRD data which also indicate limitations of these basic assumptions and suggest more complex mechanisms behind the laser-induced stress generation.

2.1 Linear-chain model (LCM) of coherent photoexcited lattice dynamics

2.1.1 From photoexcitation to thermal expansion

In general, when irradiating condensed matter with intense and ultrashort laser pulses, the light pulses directly interact with the charges present in the material. Depending

on the wavelength of the used laser light and the material under consideration, this can trigger structural dynamics either directly via infrared absorption or indirectly via Raman excitation and/or electron-phonon coupling processes. The indirect processes occur via excitation of real or virtual electronic states. Raman excitation of coherent optical phonons—which is a two-photon process involving virtual (non-resonant) or real (resonant) electronic levels—is considered to be the dominant process in transparent media. In opaque materials either conduction band electrons (metals) or electron-hole pairs (semiconductors) are excited or generated which subsequently couple their energy to the lattice whereby coherent and incoherent phonons may be excited.

Within the course of this thesis I restrict my considerations to the excitation of metallic solids by optical laser pulses with a wavelength of 800 nm, in particular I focus on the perovskite oxides SrRuO₃ (SRO) and La_{0.7}Sr_{0.3}MnO₃ (LSMO). Moreover, this work is exclusively dedicated to the photoexcitation of nanolayered sample structures, i.e., the samples are supposed to consist of one or more (metal) slabs having a typical thickness on the nanometer lengthscale which are epitaxially deposited on a single-crystal substrate. Since the beam profile of the exciting laser on the sample typically has dimensions of several 100 μm I can further restrict my considerations of the photoinduced structural dynamics to the direction along the surface normal throughout this thesis [40]. I define this direction as the z -axis.

During the photoexcitation the photons are predominantly absorbed by the conduction band electrons of the metal which is represented by a large optical conductivity $\tilde{\sigma}(\omega)$ around visible photon energies [41]. According to the Lambert-Beer law the intensity of the optical light after passing through an absorbing material of length z is given by

$$I(z) = I_0 e^{-\alpha z} \quad (2.1)$$

where I_0 is the initial intensity of the light and the absorption coefficient $\alpha(\omega) = \text{Re} \tilde{\sigma}(\omega) [n(\omega) \varepsilon_0 c_0]^{-1}$ is directly related to the real part of the optical conductivity [41]. The constants ε_0 and c_0 are the vacuum permittivity and speed of light, respectively, and $n(\omega)$ is the frequency-dependent refractive index of the absorbing material. The optical penetration depth into this material is given by $\xi = \alpha^{-1}$. Equation (2.1) directly implies the density of deposited optical energy by its derivative $\rho_E(z) = dI(z)/dz$ which also has an exponential spatial dependence.

At this stage, the electronic subsystem is in a state far from equilibrium as is depicted in Fig. 2.1(a) by the non-Fermi-Dirac distribution of the electron energies just after laser excitation. After an initial coherent (ballistic) electron transport the strong electron-electron interaction rapidly restores an incoherent thermal equilibrium [42]. In the case of SRO, Kostic and co-workers deduced a low-frequency electron scattering rate $\Gamma_{e-e} \approx 2.3 \times 10^{14} \text{ s}^{-1}$ corresponding to a mean scattering time $\tau_{e-e} = \Gamma_{e-e}^{-1} \approx 4.2 \text{ fs}$ at 145 K [44]. Invoking typical Fermi velocities in SRO of $v_F \sim 10^7 \text{ cm/s}$ [45–47] one obtains a mean free path of about 0.5 nm which in fact poses an upper limit due to the increasing scattering rate as one approaches room temperature. Therefore, the spatial energy density profile in SRO is effectively not altered by ballistic electron propagation¹.

The established thermal equilibrium of the electron gas now allows the definition of temperature. First of all, the final temperature $T_e(z)$ of the electrons depends on the

¹The velocity of the conduction band electrons gained by the absorption of photons is up to one order of magnitude larger than v_F . However, within Landau's Fermi liquid theory, the scattering rate is proportional to T^2 which suggests that the estimated free mean path also holds for the excited electrons [48–50].

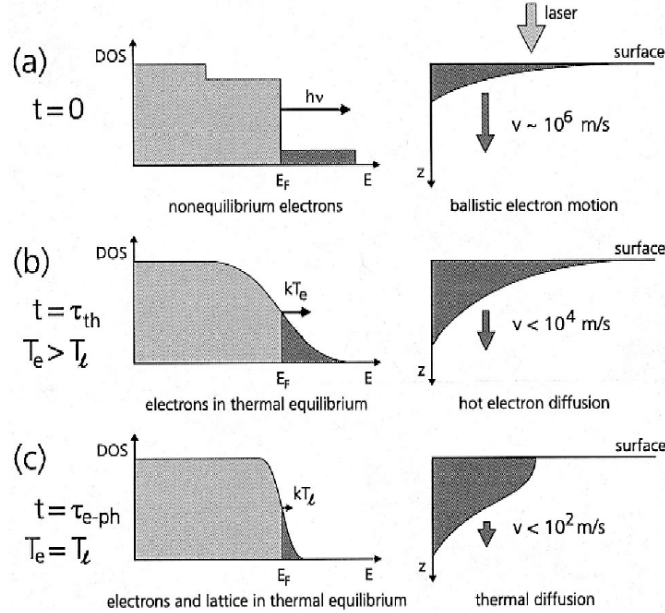


Figure 2.1: Schematic of the optical excitation of electrons and the subsequent relaxation processes in a metal from Ref. 42. (a) The absorbed photon energy promotes conduction band electrons into states of higher energy giving rise to a non-equilibrium state. The increased kinetic energy of the excited electrons results in ballistic electron motion into deeper parts of the metal. (b) Incoherent electron-electron scattering restores a thermal equilibrium (Fermi-Dirac distribution) at an elevated temperature of the electronic system after the thermalization time τ_{th} . Now the energy transport is of diffusive nature within the electron gas. (c) Finally, an equilibrium between the electrons and the lattice is established on a timescale given by the electron-phonon relaxation time $\tau_{\text{e-ph}}$. Energy transport now proceeds by lattice thermal diffusion according to the Fourier law [43].

amount of deposited energy, i.e. on $\rho_E(z)$. For laser fluences² on the order of 1-100 mJ/cm² typically used in our experiments the electron temperature easily increases up to thousands of Kelvin as the electronic heat capacity is small compared to the phononic heat capacity of the solid [43]. Moreover, the heat capacity of a free-electron gas is not independent of its temperature but is given by

$$C_e(T_e) = A_S T_e \quad (2.2)$$

where A_S is the constant Sommerfeld parameter [43]. In many metals (at least elemental metals) this approximation holds up to several thousand Kelvin [51]. In materials exhibiting strong electron correlations (e.g. SRO and LSMO) this approximation might not hold up to such high temperatures. Altogether, this means that the spatial temperature profile $T_e(z)$ may not be simply proportional to the energy density $\rho_E(z)$.

The subsequent process of electron diffusion which is furthermore capable of redistributing the heat within the sample is typically orders of magnitudes slower compared to the ballistic transport as is indicated in Fig. 2.1(b) [42]. Depending on the material under investigation the heated electronic system more or less rapidly ($\tau_{\text{e-ph}} \approx 100$ fs to 10 ps) couples to the lattice degrees of freedom (electron-phonon coupling) leading to equilibration of these two subsystems (Fig. 2.1(c))³. The metals considered in the current work (SRO and

²The physical quantity fluence is the energy flux through a given area integrated over a certain time interval. In the particular context of laser pulse irradiation, it is given by the ratio of the pulse energy and the irradiated area usually defined by the full width at half maximum (FWHM) of the laser beam profile on the sample surface.

³A more general and rigorous treatment of the electron-phonon equilibration leads to the so-called

LSMO) have a very efficient electron-phonon coupling resulting in very fast equilibration times on the order of a few hundred femtoseconds [53]. In Paper **V** we were able to narrow this time scale down to $\lesssim 200$ fs in case of SRO. Continuing the above discussion, this implies that after thermalization the hot electrons have virtually no time to diffuse across the metal layer before the electronic and phononic subsystems are equilibrated and the spatial energy density profile $\rho_E(z)$ thus retains its shape. The final lattice temperature profile $T_l(z)$ then essentially depends only on the lattice heat capacity C_l since the electron heat capacity is negligible after equilibration. The lattice heat capacity C_l is only constant if the solid is initially above its Debye temperature Θ_D [43]. Similar to the electron gas, the temperature dependence of the lattice heat capacity may result in a modified spatial lattice temperature profile deviating from the initial energy density $\rho_E(z)$.

Due to the generally anharmonic nature of interatomic potentials the lattice temperature increase $\Delta T_l(z)$ gives rise to the thermal stress

$$\sigma(z) = -3B\alpha(T_l)\Delta T_l(z) \quad (2.3)$$

where B and $\alpha(T_l)$ are the bulk modulus and the linear thermal expansion coefficient of the solid, respectively. As already discussed by Thomsen *et al.* this expression is valid for isotropic media [40] which is a good approximation for SRO and LSMO. Due to the fast electron-phonon coupling time of these materials, the photoinduced thermal stress $\sigma(z)$ builds up within a few hundred femtoseconds which launches coherent longitudinal acoustic (LA) phonons in form of sharp strain wave fronts [40]. Since the timescale of the build-up of $\sigma(z)$ is much shorter than any structural dynamics of interest in this thesis it can be effectively considered as instantaneous.

As a first approximation, one may assume the lattice heat capacity C_l to be constant which holds for a sufficiently small temperature rise $\Delta T(z)$. Then (2.3) becomes

$$\sigma(z) = -\frac{3B\alpha(T_l)}{\rho C_l}\rho_E(z) = -\gamma\rho_E(z) \quad (2.4)$$

where I introduced the mass density ρ and the averaged Grüneisen parameter γ . In fact, γ is only weakly changing over a wide temperature range for nearly any material since α and C_l have a very similar temperature-dependence [54, 55]. That is, relation (2.4) also holds to a good approximation for an arbitrary photoinduced temperature rise $\Delta T(z)$. After the coherent strain waves have left the excited layer, a quasi-static expansion field $\varepsilon(z) \propto \sigma(z)$ due to the incoherently excited phonon population remains. The proportionality reflects Hooke's law of elasticity. In this context quasi-static means that the timescale of the subsequent heat diffusion dynamics is orders of magnitude larger. The influence of heat diffusion is discussed in Chapter 3.

In conclusion, as a first approximation the photoinduced thermal expansion of metallic layers by sufficiently short laser pulses can be considered to be the result of an instantaneous force or stress $\sigma(z)$ being proportional to the deposited energy density $\rho_E(z)$. Thus, $\sigma(z)$ has a depth profile that is defined by the exponential penetration depth ξ of the optical pump light. The impulsive heating of the absorbing layers in the heterostructures triggers longitudinal sound waves which start to propagate across the sample, eventually travel into the substrate and leave behind thermally expanded layers. The details of these processes are discussed in the following.

two-temperature model [42, 52]

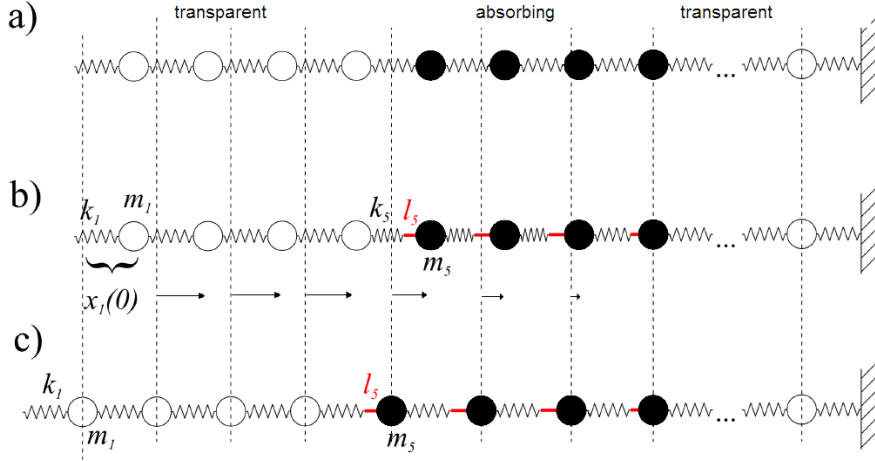


Figure 2.2: This figure is adapted from Paper I. (a) Schematic of the linear chain where the empty and solid balls represent one unit cell of different materials, respectively, and the zigzag lines represent the springs (interatomic forces). (b) The instantaneous insertion of incompressible spacer sticks at $t = 0$ according to the photoinduced stress profile $\sigma(z)$. The stress generation shifts the equilibration positions of the masses (dashed lines). (c) After the coherent strain waves have entirely propagated into the substrate all masses have reached their equilibrium positions, i.e., the expansion field $\varepsilon(z) \propto \sigma(z)$ remains.

2.1.2 The linear-chain model (LCM)

The current section gives a brief summary of Paper I where all the technical details of the model are presented and its implications in particular for SLs are extensively discussed.

In order to simulate the lattice dynamics of photoexcited epitaxial metal films, we set up a linear-chain model (LCM) of masses and springs [1, 56, 57] which is schematically shown in Fig. 2.2(a). Since we generally intend to describe arbitrarily nanolayered systems and the photoexcited area of the samples is usually orders of magnitudes larger we are faced with a one-dimensional (1D) physical problem. Thus, a 1D-LCM is sufficient to capture the relevant physical processes. The masses of the linear chain represent a general sub-volume of the crystal and the springs represent the forces acting between these sub-volumes which microscopically originate from the interatomic forces of the lattice. In fact, we focus on LA phonons and thus choose each unit cell of the lattice to be represented by one mass unit. We assume the classic harmonic interaction which only acts between nearest neighbours. This interaction is represented by the springs of the LCM. The spring constant K quantifying the force amplitude between the neighbouring masses is defined such that it gives rise to the literature value of the LA sound velocity of the respective material(s), i.e., $K = mv_{\text{LA}}^2/c^2$ where m and c are the mass and lattice parameter (the size) of one unit cell along the surface normal and v_{LA} is the velocity of LA phonons. The spring constant has to be defined for each constituting material. In Chapter 4 I relax the assumption of a harmonic interaction between the atoms of the crystal lattice and discuss the influence of anharmonic interaction potentials.

Section 2.1.1 and Paper I motivate that as a first approximation the photoexcited stress builds up quasi-instantaneously which shifts the equilibrium positions of the masses on the linear chain without any motion of the masses and thus forces are exerted on the masses (deformation potential). This process can be thought of as inserting incompressible spacer sticks between masses and springs at $t = 0$ [28] which is depicted in Fig. 2.2(b). The length l_i of each stick is proportional to the exponential stress profile $\sigma(z)$ evaluated at the

position z_i of the i th unit cell. The dashed lines in Fig. 2.2 indicate the shifted equilibrium positions. Mathematically, the instantaneous insertion of spacer sticks into the linear chain can be done most conveniently in form of modified initial conditions at $t = 0$ of the coupled harmonic oscillator differential equations. In Paper I, these equations are then solved analytically by solving the related eigenvalue problem. The solution contains the entire structural dynamics by giving the position and velocity of each mass at any time. This method has the advantage to enable a normal-mode analysis of the lattice dynamics, i.e., the solution directly yields the spectral amplitude and phase of each normal mode defined on the linear chain (also known as phonon mode). As shown in Chapter 4, this feature is particularly valuable if the UXRd diffraction curves resulting from such structural dynamics need to be calculated.

After the build-up of the laser-induced stress and the launch of the coherent sound waves the heat deposited in the metal layers starts to diffuse into colder regions of the sample. The heat diffusion is a much slower process as indicated in Fig. 2.1. In fact, the timescale of heat conduction in perovskite SLs has been previously studied and the findings suggested that heat diffusion can be neglected on the timescale of the coherent lattice dynamics [58–60]. This implies that the spatial stress profile $\sigma(z)$ (and hence the stick lengths) is time-independent which will thus be the applied approximation throughout this chapter. It is nevertheless straightforward to extend the presented LCM to additionally account for heat diffusion. In combination with new experimental results, this will be discussed in Chapter 3.

The presented LCM can be applied to any nanolayered sample structure in which photoexcitation leads to a quasi-instantaneous local stress generation. In the following sections I discuss the results for two special cases, namely, epitaxial thin films and epitaxial superlattices on a single-crystalline substrate.

2.1.3 Photoexcited lattice dynamics of thin films

The present section discusses the application of the LCM to the simplest heterostructure possible, that is, a thin metallic film which is deposited epitaxially on a transparent single-crystalline substrate and is excited by an ultrashort laser pulse. Since this is a prototypical scenario which is in this form not included in any of the attached papers, I will discuss this case in more detail. The thin-film geometry nicely exemplifies the structure-dynamical features occurring in impulsively photoexcited nanolayered systems and thus in particular forms the basis for the related dynamics of SLs. The latter is addressed in Section 2.1.4.

As an example, I focus on a SRO thin film of thickness $d_{\text{SRO}} = 94.8$ nm with an out-of-plane lattice parameter $c_{\text{SRO}} = 3.949$ Å epitaxially grown on a STO substrate by pulsed laser deposition [37] which will be revisited in Section 2.2.2 concerning its theoretical and experimental UXRd response. The structural parameters are derived by fitting static high-resolution XRD curves presented in Section 2.2.2. The literature value of the penetration depth of the 800 nm pump light into SRO is $\xi_{\text{SRO}}^0 \approx 52$ nm [44, 61]. As explained in Section 2.1.1, I apply the reasonable assumption that the spatial stress profile within the SRO layer is proportional to the energy density profile ρ_E defined by the Lambert-Beer law in (2.1).

For such a sample structure the LCM yields a transient strain field presented in Fig. 2.3(a). A more detailed view is given by lineouts at selected time delays in Fig. 2.3(b). Generally, the instantaneously photoexcited stress in SRO launches strain waves (or coherent LA phonon wavepackets) wherever the stress for an atom (or atomic layer) is unbalanced, i.e., where the spatial stress pattern has non-zero gradients [1, 62]. For thin films

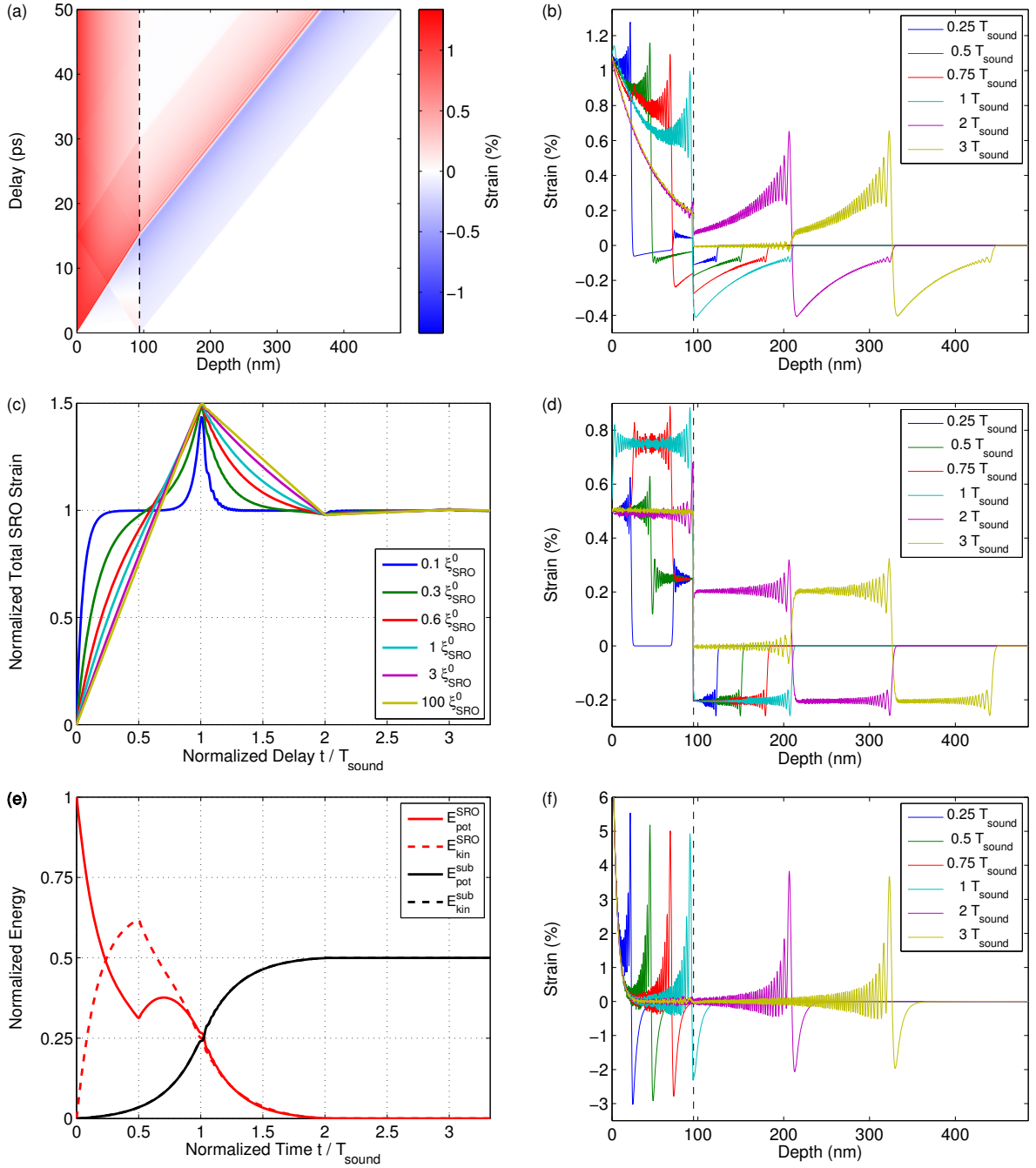


Figure 2.3: (a) Result of the LCM for a 94.8 nm thick SRO layer on a STO substrate. The surface plot shows the spatiotemporal strain pattern after photoexcitation assuming $\xi_{\text{SRO}}^0 = 52$ nm. The dashed line indicates the layer-substrate interface. (b),(d),(f) Transient strain patterns at selected time delays for $\xi_{\text{SRO}} = \xi_{\text{SRO}}^0$, $\xi_{\text{SRO}} = 100\xi_{\text{SRO}}^0$ and $\xi_{\text{SRO}} = 0.1\xi_{\text{SRO}}^0$, respectively. The dashed lines indicate the layer-substrate interface. (c) Comparison of the normalized total SRO strain vs. time delay for different ξ_{SRO} . (e) Normalized potential and kinetic energies of the SRO layer and substrate, respectively. Note that $E_{\text{pot}}^{\text{sub}}$ and $E_{\text{kin}}^{\text{sub}}$ are identical and thus the curves are overlaid.

with thickness d smaller than the optical penetration depth ξ this essentially means that sharp strain waves are launched from the sample surface and the layer-substrate interface, respectively, since at these points the largest gradients are present. The blue curve in Fig. 2.3(b) clearly reveals the coherent expansion wave originating from the sample surface and although the considered SRO layer is rather thick compared to its penetration depth the strain waves launched at the interface are still visible. Altogether, the impulsive heating of the SRO layer triggers coherent expansion waves starting from the surface and interface, respectively, propagating into the SRO layer and a compression wave starting from the interface propagating into the substrate. The interface strain waves are not existent if $d \gg \xi$.

A closer look at the transient strain fields in Fig. 2.3(b) reveals that the strain waves are superimposed by a peculiar fine structure which is most pronounced on the tensile component launched at the sample surface. Since we solve the differential equations of the linear chain analytically these features are no numerical artifacts. In fact, these oscillations are a characteristic feature of a discretized linear chain and do not occur in elastic continuum models [40]. The high-frequency oscillations on top of the strain waves are a result of the fact that the motion on the linear chain is essentially initiated at the surface and interface due to the large gradients of the thermal stress $\sigma(z)$ at these points⁴. A more detailed analysis (not shown) reveals that these very early motions of the surface and interface atoms show an oscillatory behaviour and in addition to the total expansion of the layer thus represent an acoustic oscillation of the entire surface. This coherent acoustic surface/interface mode is responsible for the observed high-frequency oscillations. Note, that the frequency of these oscillations actually depends on the particular discretization of the linear chain. If one defines one linear-chain mass per atom which means twice as many masses as in the current consideration the frequency is twice as high. Moreover, the coherent surface/interface oscillations only occur if the assumption of a quasi-instantaneous stress generation holds. If, e.g., the pump pulse duration or the electron-phonon relaxation time would be too large these features could not be excited. Nevertheless, it would be very interesting—albeit challenging—to observe such features in experiments and to investigate a possible coupling to optical phonons and the amplitude and lifetime of the high-frequency acoustic phonons (which would be closely related to Chapter 4). In the following, however, I focus on the main features of the photoinduced lattice dynamics and do not further discuss the high-frequency oscillations.

The strain waves launched at the surface and interface travel through the materials at their respective LA sound velocity v_{LA} . The literature value $v_{\text{LA}}^{\text{SRO}} = 6.3 \text{ nm/ps}$ [63] implies a transit time of the sound through the SRO layer of $T_{\text{sound}} = d_{\text{SRO}}/v_{\text{LA}}^{\text{SRO}} \approx 15 \text{ ps}$ which is directly verified by the LCM results (see Fig. 2.3(a) and cyan curve in Fig. 2.3(b)). At $t = T_{\text{sound}}$ the total strain of the SRO layer reaches its maximum (cyan curve in Fig. 2.3(c)) since both expansion wave fronts have traversed the layer and add up coherently. The expansion wave from the surface then continues to propagate into the substrate and together with the compression wave originating from the interface it forms a so-called bipolar strain pulse (BSP) which continues to travel deeper into the substrate [40]. In the present case, the reflection of the sound waves at the interface quantified by

$$R = \left(\frac{\rho_2 v_{\text{LA}}^{(2)} - \rho_1 v_{\text{LA}}^{(1)}}{\rho_2 v_{\text{LA}}^{(2)} + \rho_1 v_{\text{LA}}^{(1)}} \right)^2 \quad (2.5)$$

⁴Since the largest gradient is present at the surface the high-frequency oscillations are most pronounced on the expansion wave originating from there.

is negligible since the acoustic impedance mismatch $\rho_2 v_{\text{LA}}^{(2)} - \rho_1 v_{\text{LA}}^{(1)}$ is very small for the combination of SRO and STO (ρ_i and $v_{\text{LA}}^{(i)}$ are the mass density and the LA sound velocity of the neighboring materials, respectively) [57, 64]. The expansion wave originating from the interface is reflected from the surface at $t = T_{\text{sound}}$ and thereby converted into a compression wave effectively truncating the expansion wave initially launched at the surface. In total, the exit of the expansion part of the BSP from the SRO layer leads to a decrease of the total SRO strain between T_{sound} and $2T_{\text{sound}}$ as can be inferred from Fig. 2.3(c). For $t > 2T_{\text{sound}}$ a static expansion or dilation of the SRO layer remains which can be thought of as the sum of all spacer sticks in SRO initiating the stress in the first place. This static expansion of the layer represents the incoherently excited thermal phonon population, i.e., thermal expansion. As we will see below, this behaviour for $t > 2T_{\text{sound}}$ only holds due to the negligible acoustic impedance mismatch of SRO and STO.

Apart from nonlinear effects at very high laser intensities [65], the penetration depth $\xi = \alpha^{-1}$ of light with a given wavelength into a particular medium is a constant quantity and given by the material's dielectric function (see Section 2.1.1). In the LCM one can, however, easily vary ξ in order to further investigate the photoexcited lattice dynamics of thin films. Figures 2.3(d) and (f) present plots similar to Fig. 2.3(b), however, for the limiting cases of $\xi_{\text{SRO}} \gg d_{\text{SRO}}$ and $\xi_{\text{SRO}} \ll d_{\text{SRO}}$. All three simulations are chosen to have an identical mean SRO expansion of 0.5% for $t \rightarrow \infty$ which is a realistic strain level in pump-probe experiments⁵. At a first glance, the structural layer and substrate dynamics seem to be rather different in the three cases. However, the general features of propagating sharp coherent strain fronts are similar and for $t \rightarrow \infty$ one also observes a statically expanded layer and a propagating wavepacket (the BSP) in the substrate in all cases. The normalized transient strain of the entire SRO layer—which is related to the position of Bragg peaks in UXR experiments (see Section 2.2)—is shown in Fig. 2.3(c) for different values of ξ_{SRO} and reveals even more similarities. Although the exact evolution of the total SRO strain varies for different ξ_{SRO} (due to differing shapes of the wavepackets), the maximum SRO strain is always reached at $t = T_{\text{sound}}$ and, moreover, is in all cases 50% larger than the stationary value for $t > 2T_{\text{sound}}$. The latter is merely given by the photoinduced thermal (incoherent) expansion of SRO defined by the initial condition entering the LCM (see Section 2.1.2). Note, that this stationary expansion is here already reached after $2T_{\text{sound}}$ due to the almost perfect acoustic impedance matching of SRO and STO. If there existed a significant acoustic mismatch a decreasing portion of the acoustic phonon wavepackets would coherently bounce back and forth several times within the layer until all their energy would eventually be successively transmitted into the substrate as can be seen, e.g., in UXR experiments of Nicoul and co-workers on Gold layers on Mica substrates [66]. Moreover, the data shown by Nicoul *et al.* also roughly exhibit the apparently general feature of the 50% increased strain maximum at T_{sound} relative to the final incoherent strain.

The reason for this universal *50% increased coherent strain maximum* can be explained by the following energy considerations. As explained above, for $t > 2T_{\text{sound}}$ the layer has reached its stationary incoherent expansion and a coherent BSP is propagating through the substrate (see Figs. 2.3(b), (d) and (f)). The latter has a net strain of zero since no photoexcitation of the substrate is present. Therefore, the two parts of the strain pulse (compressive and tensile) carry the same amount of integrated strain albeit with different sign. The final potential energy stored in the BSP, $E_{\text{pot}}^{\text{sub}}$ (black solid line in Fig. 2.3(e)),

⁵In the case of $\xi_{\text{SRO}} \ll d_{\text{SRO}}$ this results in huge strains at the layer surface which would most likely yield irreversible damage in real experiments.

thus originates in equal parts from the compressive and the tensile component, respectively, which is also visualized by the fact that $E_{\text{pot}}^{\text{sub}}$ reaches half of its final value at $t = T_{\text{sound}}$ where one of the two BSP components has entered the substrate. The potential energy of the SRO layer, $E_{\text{pot}}^{\text{SRO}}$, is maximal at $t = 0$ due to the photoexcited thermal stress and the related shift of equilibrium positions of the masses in the linear chain. One can think of the layer as being compressed with respect to its stationary incoherent expansion at late times. Eventually, $E_{\text{pot}}^{\text{SRO}}$ vanishes for $t > 2T_{\text{sound}}$ since all springs in the layer have relaxed, i.e., the layer has reached its stationary expansion and no coherent dynamics are left⁶. The vibrational energy is carried away by the coherent BSP in form of potential and kinetic energy. At $t = T_{\text{sound}}$ one finds that $E_{\text{pot}}^{\text{SRO}}$ is 1/4 of its initial value. Due to the squared dependence of potential energy on the strain amplitude this implies that relative to the stationarily expanded state for $t > 2T_{\text{sound}}$ the tensile strain amplitude at $t = T_{\text{sound}}$ is 1/2 of the compressive strain amplitude at $t = 0$. In other words, relative to the final state the maximum relative layer expansion amounts to 50% of the initial relative compression. The preceding arguments hold independent of ξ_{SRO} , i.e., the values of the potential and kinetic energy at $t = T_{\text{sound}}$ and $t = 2T_{\text{sound}}$ in Fig. 2.3(e) are invariant similar to Fig. 2.3(c) (not shown). Hence, the 50% increased coherent strain maximum found in Fig. 2.3(c) is indeed a general feature of a photoexcited thin film on an unexcited substrate.

As a side remark, if the film was free-standing, i.e., detached from the substrate, no BSP could leave the layer which would result in a 100% increased coherent strain maximum as was theoretically discussed and experimentally observed by femtosecond electron diffraction on a photoexcited Gold film in the work of Li *et al.* [67].

2.1.4 Photoexcited lattice dynamics of superlattices

In the following I consider the photoinduced structural dynamics of a more complex class of heterostructures known as superlattice (SL) [57]. Since the essential details of the LCM results on SLs are already explained in Paper I the current section represents a short summary.

A SL is an epitaxial heterostructure realized by periodically stacking layers of different materials. The simplest type of SL is formed by N_{SL} -fold repetition of an epitaxial bilayer (basis) of thickness $d_{\text{SL}} = d_1 + d_2$ where d_1 and d_2 is the thickness of layer 1 and 2, respectively. Within the current work I restrict my considerations on SLs which are composed of a metallic and an insulating material with perovskite crystal structure. While the metallic layers are impulsively heated by the absorption of the pump pulse which results in the discussed coherent and incoherent expansion dynamics, the insulating layers remain unexcited. Hence, such a SL can be considered as a repetitive arrangement of several thin films generating lattice dynamics as discussed in Section 2.1.3. Due to the additional SL periodicity d_{SL} the photogenerated stress pattern as well as the lattice distortions also attain this periodicity which is reflected in, e.g., the backfolding of the phonon dispersion relation into the mini-Brillouin zone [56, 57].

The details of the photoinduced structural dynamics of SLs are extensively discussed in Papers I and III as well as in Refs. 1, 28, 30, 56, 57, 59, 60, 68. In particular, there exist two distinct timescales which are discussed in the following.

⁶Note again that this only holds for negligible acoustic impedance mismatch. For a significant acoustic mismatch the total strain of the layer will oscillate around the stationary value which will be reached at later times.

Fast timescale in SLs – Folded Phonons

The fast lattice dynamics are governed by the so-called fundamental SL phonon mode (or zone-folded longitudinal acoustic phonon (ZFLAP), see e.g. Refs. 28, 56). In a nutshell, the spatial periodicity of a SL, d_{SL} , gives rise to the decrease of the Brillouin zone by backfolding the phonon dispersion relation into the mini-Brillouin zone ($-\pi/d_{\text{SL}} \leq Q \leq \pi/d_{\text{SL}}$) [57]. In particular, the backfolding maps LA phonons with a specific non-zero wavevector Q onto the Brillouin zone center⁷ ($Q = 0$) which can then be considered as optical (SL) phonons since they represent a deformation within one super unit cell and they become Raman or infrared-active [69, 70]. In Section 2.1.3 I explain the basic lattice dynamics triggered by the photoexcitation of a single metal film. As the SLs considered here are a periodic repetition of metal films, coherent strain waves are launched from each metal film into both directions. Due to the spatial SL period d_{SL} , the superposition of all waves in the SL then forms a standing strain wave of spatial period d_{SL} which represents a temporally periodic expansion and compression of the SRO and STO layers, respectively⁸. For acoustically matched materials, these structural oscillations have a fundamental frequency $\omega_{\text{SL}} = 2\pi/T_{\text{SL}}$ where the oscillation period is defined by the transit time of the sound waves through one bilayer (basis) of the SL⁹, i.e.,

$$T_{\text{SL}} = T_1 + T_2 = \frac{d_1}{v_{\text{LA}}^1} + \frac{d_2}{v_{\text{LA}}^2} \quad (2.6)$$

The result of the LCM for a particular SRO/STO SL is presented and discussed in detail in Paper I (Fig. 5(a)). To emphasize and visualize the structural SL dynamics a little more, Fig. 2.4 shows the individual transient strain averaged over all SRO and STO layers of the SL. One clearly observes the periodic expansion and compression of the SRO and STO layers, respectively, which is due to the standing strain wave (SL phonon mode) triggered by the impulsive heating of the metallic SRO layers. One of the major conclusions in Paper I is that the mechanical coupling of the SL to the substrate leads to the apparent damping of the SL oscillations, however, the vibrational energy is in fact coherently transported into the substrate. From the viewpoint of the employed normal-mode picture this coherent energy transport is merely due to the superposition of the oscillating eigenmodes (phonon modes) which extend throughout the SL and the substrate, i.e., the entire linear chain. The decay of the SL oscillations in Fig. 2.4 which is also observed in UXR studies [1, 28, 53, 59, 60, 68, 71] is thus due to the fact that only the SL is monitored. Paper I also explains that the coherent strain waves entering the substrate can be observed by investigation of the substrate Bragg peak. This topic is also discussed in great detail in Chapter 4.

In case of the considered particular SRO/STO SL, the SL oscillation period is $T_{\text{SL}} = 3.2$ ps. On one hand, T_{SL} can be calculated by (2.6) given the layer thicknesses and sound velocities are known. On the other hand, T_{SL} can be inferred from experiments

⁷In general, SLs having an arbitrary acoustic impedance mismatch exhibit acoustic bandgaps in their phonon dispersion relation which is in analogy to the nearly-free electron model giving rise to electronic band structures [43]. The band edge states are symmetric and antisymmetric, respectively, with respect to the atomic displacement.

⁸This corresponds to a mode which is symmetric with respect to strain but is antisymmetric with respect to the atomic displacement since the former is related to the latter by a spatial derivative.

⁹Equation (2.6) (and thus (2.7)) is only strictly valid in the limiting case of negligible acoustic impedance mismatch. In that case there is no acoustic bandgap, the symmetric and antisymmetric modes are degenerate and the sound velocity of acoustic waves through the SL is given by eq. (2.7). In the general case of arbitrary acoustic impedance mismatch the bandgaps lead to modified frequencies ω_{SL} which are determined by the SL phonon dispersion relation derived in Ref. 57.

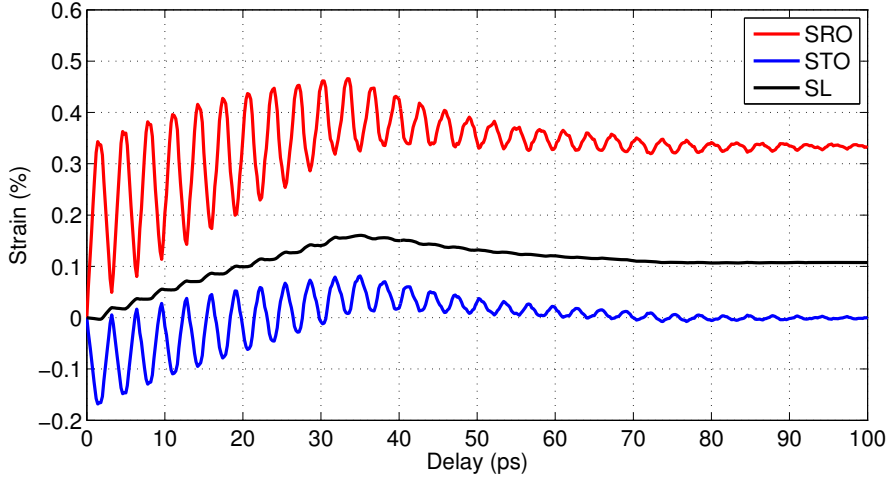


Figure 2.4: Transient average strain of the SRO (red line) and STO (blue line) layers of the SL after photoexcitation. The black line shows the strain of the entire SL.

which in turn allows for the determination of layer thicknesses or sound velocities (of course three of the four independent quantities have to be known). As Section 2.2 points out, the most direct way to obtain detailed information on the structural dynamics is UXRD. In fact, UXRD was successfully employed to reveal the SL oscillation of this particular SRO/STO SL sample including its period and phase (see Papers **II-V**, **XI**, **XII** and Refs. 53, 59, 60, 71, 72). If one is merely interested in the frequency of the SL oscillation, it is usually sufficient to exploit the lattice-dynamics-induced modulation of optical constants by experimentally simpler all-optical scattering or pump-probe techniques [56, 69, 73]. In Paper **V**, we carefully compare the transient optical and UXRD response of this SL both of which exhibit oscillations with 3.2 ps period.

Slow timescale in SLs – Expansion

The second, slower timescale of the structural SL dynamics is comparable to the discussions in Section 2.1.3 as it represents an overall expansion of the SL. The black line in Fig. 2.4 shows how the SL strain evolves after the pump pulse has arrived. This behavior is essentially identical to the one observed in thin films (Fig. 2.3(c)) and all conclusions drawn for thin films hold. In particular, the 50% increased coherent strain maximum can also be found in the SL as is partly discussed in Paper **I**. A closer look into Fig. 2.4 reveals a multiple step-like expansion of the SL. This is caused by the successive reflections of the compression waves at the surface whereby they are converted into expansion waves effectively increasing the expansion of the SL. The maximum expansion of the SL is reached after $T_{\text{SL}}^{\text{exp}} = N_{\text{SL}} d_{\text{SL}} / v_{\text{SL}}$ which is the ratio of the total SL thickness and the average LA sound velocity in the SL (in analogy to the thin film considerations). Note, that v_{SL} is not simply given by the arithmetic mean of the sound velocities of the constituting materials but instead reads

$$v_{\text{SL}} = \frac{d_{\text{SL}}}{T_{\text{SL}}} = \frac{v_{\text{LA}}^1 v_{\text{LA}}^2 d_{\text{SL}}}{d_1 v_{\text{LA}}^2 + d_2 v_{\text{LA}}^1} \quad (2.7)$$

which is based on the transit time of the sound waves through one bilayer given by eq. (2.6).

In Figure 2.4 one can also see that STO indeed plays a passive role in the sense that it merely guides the acoustic waves but it is not optically excited. Only SRO remains expanded after the coherent sound waves have left the SL into the substrate. Again, within

the LCM, the absolute expansion of the SRO layers and hence the SL is given by the sum of all inserted spacer sticks which represent the incoherently excited phonons giving rise to the thermal expansion. As will be discussed in Chapter 3, the passive behavior of STO will no longer hold if one allows for heat diffusion between the individual layers.

2.2 Calculation and interpretation of UXR response of photoexcited lattice dynamics using the LCM

While the previous sections introduced the LCM to model the structural dynamics of nanolayered metal-insulator heterostructures after optical excitation, the aim of the current section is to employ the LCM output in order to simulate the resulting transient signals recorded in UXR experiments. First, I introduce dynamical XRD and its calculation using the results of the LCM. Second, I discuss the implications of the particular sample structures considered in the previous sections and how the various features of the complex UXR signals can be related to the general features of the structure dynamics. This emphasizes the great potential of UXR experiments and their analysis by the presented numerical models in order to infer the laser-induced lattice dynamics of nanolayered heterostructures. Finally, I mention the limitations of the assumption of instantaneous stress generation which have very recently been elucidated in a fluence-dependent UXR study on a SRO/STO SL.

2.2.1 Dynamical x-ray diffraction in combination with the LCM

The key aspect and the heart of XRD is the fact that the x-ray waves partially diffracted by atomic planes have a specific phase relation due to the periodic repetition of these planes in a crystal lattice and that therefore x-rays are essentially only diffracted by a crystal as very distinct reflections. This is encoded in Laue's famous diffraction condition

$$\mathbf{q} = \mathbf{k}_{\text{out}} - \mathbf{k}_{\text{in}} = \mathbf{G} \quad (2.8)$$

where the wavevector transfer \mathbf{q} given by the vectorial difference of the diffracted and incident x-ray wavevector \mathbf{k}_{out} and \mathbf{k}_{in} , respectively, has to be equal to a reciprocal lattice vector \mathbf{G} [20]. As the vector \mathbf{G} is the normal to a set of lattice planes and its magnitude is inversely proportional to the distance between the lattice planes, XRD is one of the best methods to uniquely determine the structure of a given crystal.

Throughout the current work I restrict the considerations to the case of symmetric XRD (also known as Θ - 2Θ scans), i.e., the wavevector transfer \mathbf{q} is orthogonal to the sample surface which allows for the extraction of structural information only along the surface normal. As motivated in Section 2.1.2, the structural dynamics of interest here are confined to this dimension which implies that symmetric XRD contains the entire structural information and antisymmetric XRD is redundant. Therefore, also the probe process of XRD is reduced to only one dimension.

XRD can often be considered in the context of kinematical diffraction theory which assumes the scattering effects to be comparatively weak [20]. If one, however, considers XRD from highly perfect and quasi-infinite crystals where scattering effects are no longer small and multiple scattering events play an important role, one has to employ the more complex theory of dynamical XRD. Although the samples considered here usually have

dimensions around ten to a few hundred nanometers where kinematical theory would suffice, our partial interest in structural dynamics near or at the substrate Bragg peaks (e.g. in Papers **I**, **VI** and **VIII**) demands the use of the dynamical theory. The mathematical description of dynamical diffraction initially developed for symmetric XRD¹⁰ by Darwin in 1914 [75] has been discussed in detail, e.g., in Refs. 1, 20, 74, 76. In particular, I adopt the method described in Ref. 1. Here, the reflection and transmission of the x-ray waves at each lattice plane due to the a given electron density and the phase obtained by propagation between the atomic layers are represented by respective matrices within a transfer matrix approach. The phase between the waves reflected from adjacent lattice planes depends explicitly on the distance between them. That is where the spatiotemporal strain field from the LCM calculations which defines the deformation of each unit cell enters the XRD calculations. The XRD response of the sample of interest is thus evaluated at each time step of the LCM calculation which yields the transient signals usually recorded in UXRDX experiments.

In the following I summarize the predictions of the calculations combining the LCM and dynamical XRD (also referred to as LCDX in Paper **II** and below) for the previously discussed cases of photoexcited thin films and superlattices.

2.2.2 Transient splitting of Bragg peaks

In this section I reconsider the simplest sample structure of a thin epitaxial metallic film on a bulk substrate. I again focus on the special case of a 94.8 nm SRO thin film on a STO substrate which was already used in Section 2.1.3 to exemplify the theoretical lattice dynamics of photoexcited thin films. I present unpublished UXRDX data and compare these to LCDX simulations. Similar to Section 2.1.3, the present section is therefore discussed in more detail.

The static rocking curve of the SRO thin film on STO measured at the EDR beamline at BESSY II is shown by the symbols in panel (a) of Figure 2.5. The dynamical XRD calculation (red line) which includes the instrumental function of the experiment allows for the precise determination of the thickness ($d_{\text{SRO}} = 94.8$ nm) and the out-of-plane lattice parameter ($c_{\text{SRO}} = 3.949$ Å) of the SRO layer by matching the position and the width (and also the period of the Laue oscillations) of the SRO Bragg peak, respectively. The UXRDX response of the (002) SRO Bragg reflection upon optical pumping was measured in a pump-probe scheme at the laser-based Plasma X-ray Source (PXS) at the University of Potsdam which is described in detail in Paper **XI**. The results are presented in Figure 2.5(b). The incident excitation fluence of the 800 nm pump pulses, i.e., the optical energy per unit area impinging on the sample surface, was ≈ 30 mJ/cm². The transit time $T_{\text{sound}} \approx 15$ ps of LA sound waves through the SRO layer was already introduced in Section 2.1.3. At that time delay the stationary SRO Bragg peak (initially around $\Theta_0 = 23.0^\circ$) is shifted by $\approx 0.2^\circ$ towards lower angles indicating an expansion by $\approx 0.8\%$. Recall, that this does not correspond to the final incoherent thermal expansion since the coherent lattice dynamics result in the 50% increased coherent strain maximum at T_{sound} . The Bragg peak will thus shift back by 1/3 within another 15 ps.

The transient average SRO strain extracted from LCM calculations presented in Fig. 2.3 revealed a continuous rise of the SRO strain for $0 < t < T_{\text{sound}}$. In contrast, the SRO Bragg peak in Fig. 2.5(b) does not simply shift continuously. Instead, the initial SRO

¹⁰For an arbitrary XRD geometry, e.g., asymmetric Bragg reflections, the very general Takagi-Taupin equation has to be solved [74].

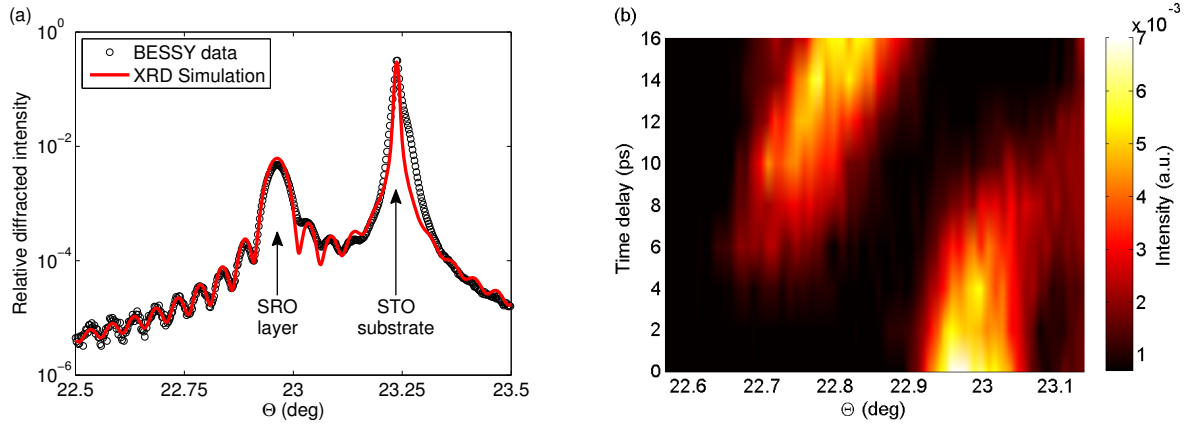


Figure 2.5: (a) Stationary (002) rocking curve of a 94.8 nm thick SRO thin film on a STO substrate measured at BESSY II. The solid line is the result of a dynamical XRD simulation from which the structural parameters of the layer given in the text are deduced. The simulation accounts for the finite instrumental resolution. (b) Transient rocking curves after excitation by 800 nm pump pulses with an incident fluence of ≈ 30 mJ/cm² measured with a PXS at the University of Potsdam. The SRO peak does not shift continuously but instead a new peak appears at lower angles. Note, that the stationary rocking curve in panel (a) was actually measured at a photon energy of $E_{\text{exp}} = 8.662$ keV. In order to compare the data to the transient rocking curves in panel (b) the experimental Θ -axis is converted to an artificial photon energy of $E_{\text{plot}} = 8.048$ keV corresponding to the Cu $K_{\alpha 1}$ radiation generated by the PXS.

peak disappears while a strongly shifted new peak arises at lower angles. Moreover, as time goes on, one observes that the initial peak as well as the new peak shift to higher angles and both follow a bent “trajectory”.

Figure 2.6(a) shows a close-up view for the relevant timescale of the LCM results similar to Fig. 2.3(a). As explained above, this spatiotemporal strain field now serves as an input for the dynamical XRD simulation which then yields the solid lines in Fig. 2.6(b)¹¹. Comparing the LCDX simulations to the UXR data, we find perfect agreement. In particular, the transient splitting of the Bragg peak as well as the individual Bragg angle changes are accurately reproduced.

The physical origin of the particular features in the UXR response (Fig. 2.6(b)) is directly related to the lattice dynamics (Fig. 2.6(a)). The instantaneous stress generation assumed in the LCM (see Section 2.1.3) launches a sharp tensile strain wave starting at the surface which is represented in Fig. 2.6(a) by the red color code. In particular, at $t = T_{\text{sound}}/2$ this creates a state where half of the layer is expanded (red) and the other half remains mainly unstrained (white) which then gives rise to two distinct Bragg peaks (cf. green line in Fig. 2.3(b)). In other words, the transient splitting of the SRO Bragg peak is due to and in turn proves the quasi-instantaneous build-up of the photogenerated stress. In the picture of two differently strained portions of SRO, Fig. 2.6(a) implies an expanded layer which is growing in thickness and a more or less unstrained layer whose thickness gradually reduces as time goes on. In reciprocal space, this translates into Bragg peaks of decreasing and increasing width, respectively, which can indeed be inferred from the UXR data in Fig. 2.6(b). Similar splittings of Bragg peaks have been observed before in bulk LuMnO₃ by Lee *et al.* on much longer timescales although the particular lattice dynamics are not explained in detail [77]. The authors claim that the anisotropic nature of the thermal expansion of LuMnO₃ (hexagonal lattice) had to be accounted for in order to

¹¹The XRD simulations include the instrumental function of the PXS (angular resolution, Cu $K_{\alpha 1}$ and $K_{\alpha 2}$ radiation) to obtain perfect agreement with the data.

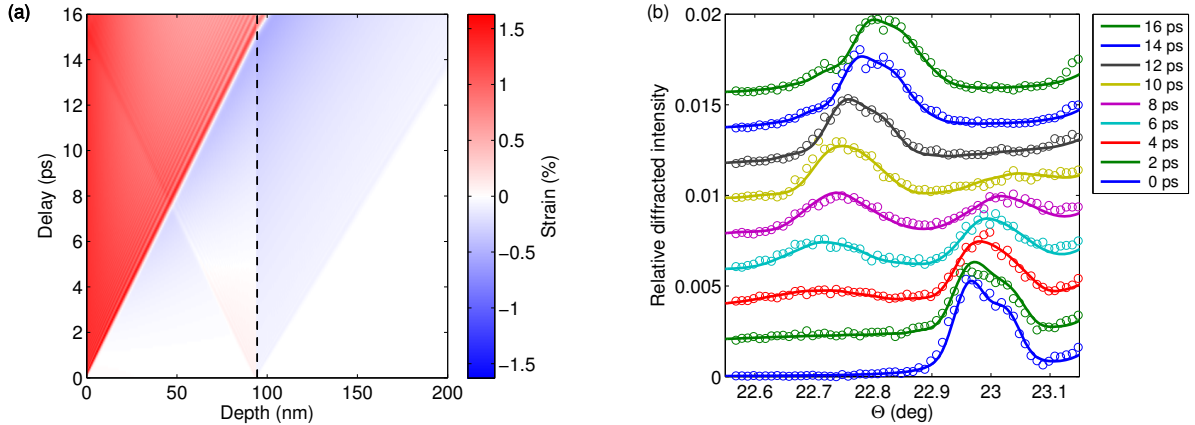


Figure 2.6: (a) Transient strain from LCM calculations assuming $\xi_{\text{SRO}} = 44$ nm. The white dashed line marks the interface between the SRO layer and the STO substrate. (b) Comparison of the PXS data with dynamical XRD simulations using the LCM results from panel (a). The curves are displaced for the sake of visibility.

reproduce the data. Since SRO has an isotropic thermal expansion (pseudocubic lattice) such effects do not play a role here¹².

In addition to the quasi-instantaneous build-up, the second major assumption used in the LCM is that the stress profile has an exponential shape given by the optical penetration depth ξ_{SRO} of the 800 nm pump light into SRO, i.e., $\sigma(z) \propto \exp(-z/\xi_{\text{SRO}})$. The perfect agreement presented in Fig. 2.6(b) could be achieved by the use of $\xi_{\text{SRO}} = 44$ nm which significantly deviates from the literature value of 52 nm [44, 61]. This deviation is addressed further below. In Fig. 2.7(a) I compare the measured rocking curve at $t = 6$ ps with the LCDX simulations assuming different values of the optical penetration depth. The different exponential stress patterns $\sigma(z)$ imply different near-surface strains (at 6 ps) compared to the final average SRO strain (at 15 ps). This results in slightly different positions of the shifted peak around 22.7° . The best overall agreement is obtained for $\xi_{\text{SRO}} \approx 44$ nm. To depict the effect of optical penetration depth in more detail, Figures 2.7(b) and (c) present surface plots of the calculated transient rocking curves for 36 and 52 nm, respectively. Clearly, a smaller penetration depth results in a larger initial splitting and more bent-like trajectories of the peaks. This is due to the more rapidly decreasing average strain of the expanded portion of the layer caused by a larger gradient of the photoexcited stress profile. If one looks into the “unstrained” portion of the layer in more detail, one finds that it is actually not completely unstrained. Instead, with decreasing penetration depth (hence increasing gradients) an increasingly relevant compression wave is launched by these gradients eventually giving rise to a total compression. This is the reason why the original SRO peak not only vanishes but also shifts to higher angles. As can be seen from Figures 2.7(b) and (c), this effect becomes more pronounced for lower ξ_{SRO} . Another manifestation of the exponential expansion profile is the asymmetry of the shifted Bragg peak towards lower angles for late time delays in Fig. 2.6(b).

Altogether, the assumption of a quasi-instantaneous exponential stress profile is valid which is evidenced by the perfect agreement of the LCDX simulations with the UXRD data in Fig. 2.6(b). The question remains why the exponential stress and hence the expansion profile derived from the UXRD data reveals a decay constant of 44 nm which is significantly

¹²Precisely, SRO has an orthorhombically distorted perovskite structure, however, since the distortion is fairly small it can be considered as being pseudocubic [1, 63]. The same holds for LSMO.

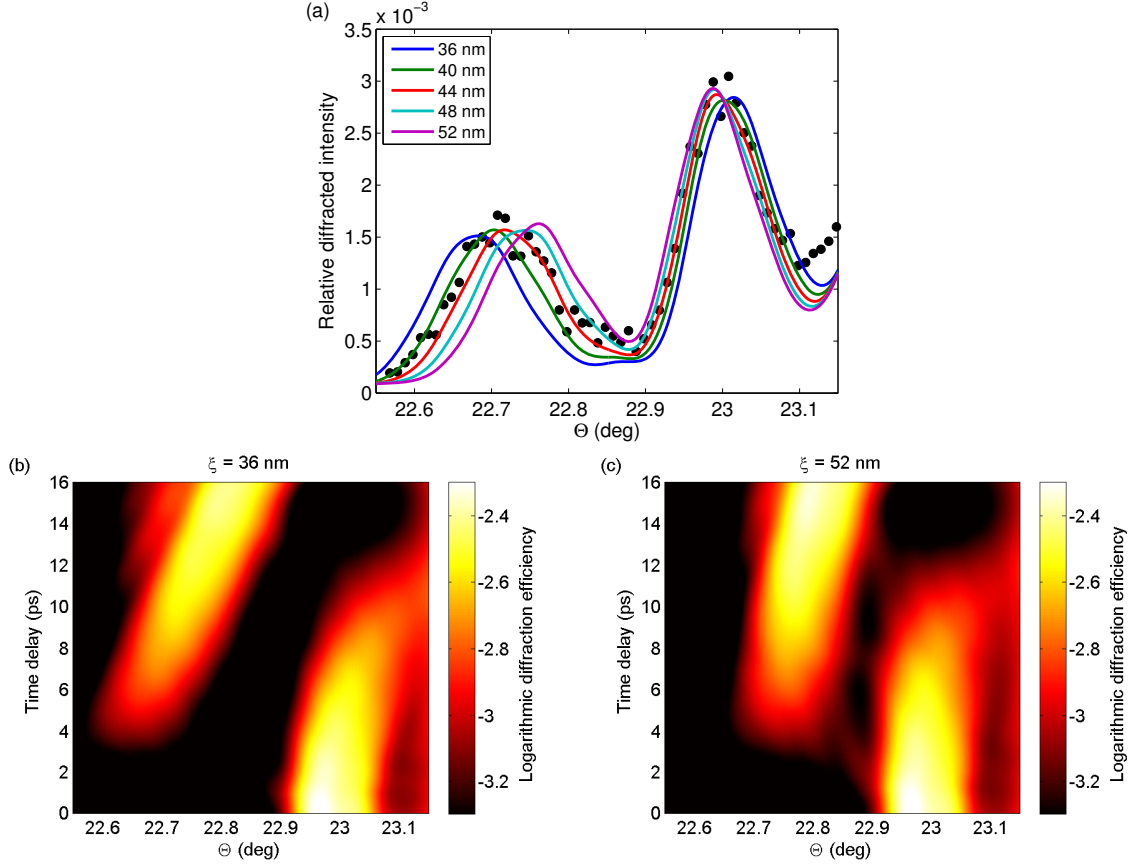


Figure 2.7: (a) Comparison of the SRO thin-film UXR data at $t = 6$ ps with LCDX results for different optical penetration depths. (b)-(c) Surface plot of transient rocking curves for (b) $\xi_{\text{SRO}} = 36$ nm and (c) $\xi_{\text{SRO}} = 52$ nm.

shorter than the optical penetration depth of 52 nm in bulk SRO [44, 61]. In principle, there are two possible reasons for the suppressed length scale. First, the optical properties of thin films may differ from the bulk properties due to the stationary strains induced by epitaxy [78, 79]. In order to check this possibility Dr. Andreas Hertwig from the Bundesanstalt für Materialforschung und -prüfung (BAM) in Berlin, Germany, performed spectroscopic ellipsometry measurements on the very same SRO thin film. The preliminary analysis of the data indeed shows a slightly increased imaginary part of the refractive index at 800 nm compared to the bulk value which implies an optical penetration depth $\xi_{\text{SRO}}^{\text{BAM}} \approx 49 \pm 1$ nm [80]. This value is only weakly dependent on surface and interface roughnesses assumed in the fitting models of the data analysis. That is, the considered SRO sample has a slightly reduced optical penetration depth which, however, is still larger than the 44 nm deduced from the UXR experiments.

The second mechanism which could cause an apparent decrease of the observed length scale of the thermal expansion profile is a temperature-dependent lattice Grüneisen parameter $\gamma = \gamma(T)$ of SRO which could in principle be responsible for an overproportional stress near the sample surface where the temperature rise is much larger than near the substrate. A slight increase of γ with increasing temperature below the Debye temperature Θ_D is in fact known for many materials [55]. This effect is due to the fact that the mode-dependent Grüneisen coefficients which are in general independently defined for each phonon mode are not equal as opposed to the assumptions in a simple Einstein or Debye model. For example, Ishidate *et al.* found very large differences between the mode-

dependent Grüneisen parameters in STO [81]. Moreover, the UXR D experiments on the SRO thin film discussed in the current section were conducted at 300 K which is well below the Debye temperature of 448 K of SRO [63]. Altogether, it is not very unlikely that a temperature-dependent Grüneisen parameter is responsible for the reduced decay length of the photogenerated strain in the SRO layer. Nevertheless, it is not completely clear whether steady state properties hold on ultrafast timescales where the material may be far away from equilibrium. For instance, the non-thermal population of the phonons at early times and possibly differing mode-specific Grüneisen parameters could generate stress profiles not explained by simple thermal expansion and an average Grüneisen coefficient. All these mechanisms could be investigated, e.g., by a precise fluence-dependent UXR D study of the transient SRO peak shifts and is out of the scope of this work.

In conclusion, the example of UXR D on a thin film of SRO shows that the LCDX calculations (i.e. LCM in combination with dynamical XRD simulations) precisely captures the qualitative and quantitative lattice dynamics in thin films triggered by ultrafast laser pulses. Moreover, quantitative deviations from the bulk properties of SRO could be identified by the help of the LCDX simulations which emphasizes the capabilities and the potential of these numerical models.

2.2.3 UXR D response of superlattices

After we have found perfect agreement of the LCDX predictions and the results of UXR D experiments in case of thin metal films, the present section addresses the transient signals obtained in UXR D experiments on metal-insulator SLs. In analogy to the previous section, I relate the general experimental findings to the knowledge gained in Section 2.1.4 on the photoinduced lattice dynamics of such SLs. As discussed before, there exist two intrinsic timescales for the SLs, namely, the oscillation period T_{SL} of the fundamental (folded) SL phonon mode and the timescale of SL expansion, $T_{\text{SL}}^{\text{exp}} = N_{\text{SL}}T_{\text{SL}}$ (cf. Section 2.1.4). Both of these related but different structural dynamics within a SL manifest in distinct features in the UXR D response.

Fast timescale – SL oscillations

As briefly mentioned in Section 2.1.4, the lattice dynamics triggered by optically pumping a metal-insulator SL resembles an oscillating standing wave ($Q = 0$) by expansion of the metal layers and a concomitant compression of the insulating layers. In bulk crystals, homogeneous optical phonons ($Q = 0$) are periodic coherent motions of the atoms within each unit cell with respect to each other [43]. The phase relations of the x-ray waves scattered from these atoms are thus altered periodically causing a modulation of the x-ray structure factor and giving rise to oscillations of the Bragg peak intensity [20, 30]. Several UXR D experiments could identify the optical excitation of coherent optical phonons [27, 82, 83]. Since the size of the unit cell is not changed by optical phonon modes no changes of the Bragg angles are observed. Mathematically, this is identical to the described dynamics of the super unit cell and its implications for UXR D. Here, we also have deformations within one super unit cell without changing its size due to the SL phonon mode ($Q = 0$). This results in intensity modulations of the SL Bragg peaks which have been previously measured in UXR D experiments [1, 28, 53, 59, 60, 68].

The main focus of Paper **II** is to explain the nature of SL x-ray diffraction curves and how these change due to the photoinduced coherent lattice dynamics on the timescale of the SL phonon mode. Both can be described in a simple envelope model (EM) which

relates the modulations of the various SL Bragg peaks to the change of the x-ray structure factor of the super unit cell. The latter can be depicted by an effective envelope function resulting from the complex interference of the XRD curves of each individual layer within the super unit cell. The EM assumes simplified structural deformations (homogeneous layer compression and expansion) which alter the single layer diffraction curves (shifts to higher and lower Bragg angles, respectively) and consequently modify the envelope function. Since the envelope function essentially dictates the intensity of the SL Bragg peaks they will also be subject to transient changes.

The proposed EM allows to qualitatively explain the observed features in UXR experiments and in many cases even gives good quantitative estimates. However, some of the observations presented in Paper **II** cannot be captured by this simplified model and require the detailed LCDX calculations. Similar to Section 2.2.2, we found a very high degree of agreement between the LCDX and experimental results. We could successfully reproduce and therefore explain various responses of the SL Bragg peaks to the photoinduced lattice dynamics. These included linear and highly non-linear dependencies on the SL phonon mode amplitude as well as constructive and destructive x-ray interference effects. All these phenomena and the fact that we understand the underlying processes almost perfectly give rise to the ability to specifically design nanolayered x-ray optics which are mandatory for high-precision and time-resolved UXR experiments. A particular application of this knowledge is discussed in Chapter 5 where the generation of ultrashort x-rays by a so-called Phonon Bragg Switch is proposed and first successful experiments are presented.

Slow timescale – SL expansion

In Section 2.1.4 I have also investigated in detail the dynamics on a slower timescale corresponding to the expansion of the entire SL. There, I found that the dynamics are essentially identical to the expansion dynamics of photoexcited thin metal films. This immediately suggests that also the transient signatures in UXR should be similar to the case of thin films discussed in Section 2.2.2.

We investigated and analyzed the structural SL dynamics on the timescale of expansion T_{SL}^{exp} in great detail in Paper **I**. The study indeed revealed that the effects of SL Bragg peak splitting as well as the 50% increased coherent strain maximum discovered in thin films (Section 2.1.3 and 2.2.2) also hold for SLs (see Fig. 2 in Paper **I**). Moreover, the study discusses the coherent transport of energy into the underlying substrate by the unfolding of the SL phonon mode due to the mechanical coupling of the SL to the substrate [84]. A signature of the coherent propagation of the sound waves into the substrate is the reported rise of shoulders of the substrate Bragg peak (see Fig. 3 in Paper **I**). Note that such simulations inevitably require the dynamical XRD calculations employed throughout this thesis. The topic of coherent phonon propagation into and inside the substrate is addressed in more detail, however, under slightly different aspects in Chapter 4.

Again, one of the major conclusions to be drawn from the excellent agreement of experiment and simulation presented in Papers **I** and **II** is that the photogenerated lattice dynamics are very well captured by the LCM and that its implied approximations (e.g. exponential shape and quasi instantaneous build-up of the stress) for the chosen materials SRO, LSMO and STO are justified.

2.2.4 Limitations of the instantaneous stress assumption

One of the crucial assumptions on which the entire framework of the LCM and its implications for UXRD are based until now is the instantaneous generation of a displacive force or stress initiated by the laser pulse excitation. One numerical advantage of this approximation is that one can incorporate the stress into the system of coupled harmonic oscillator differential equations by imposing a non-vanishing initial condition at $t = 0$ which gives rise to the possibility of solving the equations by solving the related eigenvalue problem. A time-dependent driving force $\sigma(z, t)$ increases the complexity of the mathematical problem and must then be solved either numerically (cf. Section 4.2) or by successively adapting the initial condition between time steps (cf. Section 3.1). The dynamics considered so far did not require the assumption of a time-dependent force or, more precisely, the force driving the dynamics in real experiments is much faster than all phonon frequencies involved in the photoexcited lattice dynamics. For instance, the intrinsic timescale of the SRO/STO SL oscillations considered above, T_{SL} , was determined to be about one order of magnitude slower than the estimated rise time of the photogenerated stress [53]. The modulation amplitude of the UXRD signals does then not allow for the deduction of an accurate value of the rise time as it practically makes no difference whether it is faster by one or many orders of magnitudes. Hence the instantaneous LCM could perfectly reproduce the experimental signatures.

There is, however, one aspect in the UXRD data on SLs which crucially reflects how fast the photoinduced stress has built up and what its physical origin is, namely, the phase of the SL oscillation [28, 53, 72, 73, 85, 86]. Unfortunately, this is probably the most difficult task in optical pump – x-ray probe experiments since there is practically no direct and accurate measure of the *time-delay zero* where the pump and probe pulses arrive at the sample simultaneously. One approach to estimate time zero is to investigate a reference sample having a response as fast as possible such as non-thermal melting [29, 87–89] or photoinduced structural dynamics in solids as discussed in this thesis. In any case the question remains whether the assumption of an instantaneous response of the reference sample is absolutely correct. Alternative approaches use x-ray-induced changes of the electronic system which is subsequently probed by optical means [90, 91].

Although time zero could not be precisely determined, the fluence-dependent study of the SRO/STO SL oscillations recorded at the MicroXAS-FEMTO beamline of the Swiss Light Source reported in Paper **II** could be reproduced fairly accurately by the LCDX calculations. Here, the time zero was adjusted until experiment and calculation coincided. A very careful analysis of the oscillation phase in Paper **V** revealed a relative fluence-dependent phase shift of about 150 ± 50 fs which could be verified by all-optical pump-probe experiments (Figs. 1 and 2 in Paper **V**). Additionally, a lot of effort has been made to independently determine time zero with the help of the PXS at the University of Potsdam whereby the absolute oscillation phase of the very same SRO/STO SL could be deduced with an accuracy of ± 100 fs (for all the technical details see Paper **V**). In particular, in the low-excitation regime we observed a delay of the oscillation phase of ≈ 150 fs whereas the phase delay vanishes at high fluence. As explained in Paper **V**, several mechanisms could potentially cause the fluence-dependent phase shift such as electronic pressure [66, 67, 92–95], time and temperature-dependent electron-phonon interactions (e.g. time-dependent and/or mode-specific Grüneisen coefficients) [81, 96, 97] or a change of the relative contributions from displacive excitation (DECP) and impulsive stimulated Raman scattering (ISRS) [28, 73, 86]. The former two mechanisms would imply an effective decrease of the rise time of the driving force while the latter gives rise to the mixing of the

intrinsically different oscillation phases of DECP and ISRS.

In order to capture the changing rise time of the photogenerated stress the LCM has to be extended to include non-instantaneous driving forces. This extension is presented in Chapter 3. Nevertheless, to gain more insight into the underlying microscopic nature of the stress generation in the studied metals by ultrafast laser pulses additional experiments have to be performed and different sample structures may have to be considered. For instance, changing the wavelength of the pump pulses (UV, infrared or Terahertz radiation) and/or varying the temperature of the materials will further elucidate the physics of ultrafast photoexcited solids.

THE ROLE OF INCOHERENT LATTICE DYNAMICS

The previous chapter dealt with the question how the crystal lattice of epitaxial nanolayered heterostructures responds to impulsive heating of the metal layers by ultrafast laser pulses. By proposing a linear-chain model and comparing its numerical results to UXRD experiments, it could be verified that coherent sound waves are launched if the heating of the layers is much faster than the timescale set by sound propagation through the layers. One central assumption was that the laser-induced thermal stress in the metal layers is time-independent which proved to be valid in the considered cases. However, the heat exclusively deposited in the metallic layers has to eventually diffuse into the neighbouring layers and into the substrate due to finite temperature gradients as dictated by the Fourier law [64]

$$\mathbf{Q} = -k\nabla T \quad (3.1)$$

where \mathbf{Q} is the local heat flux, k is the thermal conductivity and ∇T is the local temperature gradient. This will render the local stress time-dependent since it is a function of the local temperature. In one dimension (1D), denoted by z , without heat sources, the Fourier law implies the 1D heat equation [64]

$$\frac{\partial T}{\partial t} = \frac{k}{C_p \rho} \frac{\partial^2 T}{\partial z^2} \quad (3.2)$$

where C_p is the specific heat capacity and ρ is the mass density of the solid. The prefactor on the right side of (3.2) is also known as the thermal diffusivity $D_{\text{th}} = k/C_p \rho$. The fundamental solution¹ of this partial differential equation assuming no boundaries is given by [64, 98]

$$\Phi(z, t) = \frac{1}{\sqrt{4\pi D_{\text{th}} t}} \exp\left(-\frac{z^2}{4D_{\text{th}} t}\right) \quad (3.3)$$

The standard deviation of this Gaussian-like solution is $\sigma(t) = \sqrt{2D_{\text{th}} t}$ and represents a measure of the width and thereby of how far the heat has propagated². This relation

¹The fundamental solution represents the solution of a differential equation with a point source as the initial condition (delta function). In case of the heat equation this means the heat can be thought of as deposited at a single point at $t = 0$ which results in a divergent temperature at this point. The evolution of the temperature field for $t > 0$ is governed by the heat equation. The knowledge of the fundamental solution allows to obtain the solution for any initial condition by simple convolution [98].

²The relation $\sigma \propto \sqrt{t}$ is due to the fact that heat propagation is a diffusion process and is thus related to the concepts of Brownian motion and random walks [64].

Table 3.1: Comparison of heat propagation distance σ and time t for a point source of heat in STO according to the fundamental solution (3.3) of the heat equation (3.2). The effective heat velocity $v = \sigma/t$ is also shown. Note that the LA sound velocity of STO is $v_{\text{LA}}^{\text{STO}} \approx 7900$ m/s [81, 99, 100].

Distance σ (nm)	Time t (ps)	Avg. heat velocity $v = \sigma/t$ (m/s)
1	0.17	5800
5	4.3	1200
10	17	580
25	110	230
50	430	120
100	1700	60

implies an increasingly fast heat transport if the spatial distances become smaller. Some representative values are shown in Table 3.1. For instance, for sample structures on the order of 100 nm such as the SRO thin film discussed in Section 2.1.3 and Section 2.2.2 the timescale of heat diffusion is on the order of nanoseconds. This verifies the previously drawn conclusion that heat diffusion can be neglected on the timescale of the coherent lattice dynamics for the considered SRO thin film (< 100 ps). To follow the incoherent lattice dynamics at later times one may then solve the heat diffusion equation (3.2) separately with the appropriate initial and boundary conditions and combine the results with the LCM calculations. If the sample structure dimensions reach down to ≈ 10 nm, which is a typical size of the SLs considered in this thesis, the heat equation suggests that thermal diffusion may not be neglected any more. The results of the LCM as presented in Chapter 2 may then differ from reality in some aspects. In the following, I will present some cases which require a modification of the LCM to include the effect of heat diffusion.

Note, that for sub-nm structures the heat equation implies heat propagation velocities larger than the speed of sound (Table 3.1). Since heat transport is a result of anharmonic phonon scattering the heat can actually not propagate faster than the energy carrying phonons themselves. This illustrates the break-down of the Fourier heat equation when the characteristic length scales become comparable to the sample dimensions [101–106]. Not only because of a high technological relevance, e.g., for circuits, thermoelectrics and photovoltaics [106], the issue of nanoscale thermal transport is a very active research topic which is, however, still not fully understood as summarized in Ref. 9 and references therein. The investigation of heat transport in nanolayered structures such as thin films and SLs may hence be beneficial for developing a complete physical picture of such processes.

3.1 Incorporation of heat diffusion into the LCM

In Section 2.1.2 I explained that the photoinduced displacive stress can be thought of as spacer sticks which are inserted between the masses and the springs of the linear chain at $t = 0$ thereby compressing the springs and generating potential energy (cf. Fig. 2.3(e)). Since this insertion is assumed to happen instantaneously it generates the coherent sound waves described in Section 2.1. In order to include the process of heat diffusion, one can first solve the heat equation (3.2) for the given initial and boundary conditions on a defined time grid t_j maintaining the assumption of an instantaneous build-up of the lattice temperature. This way one obtains a matrix, $T_{i,j} = T(x_i, t_j)$ which specifies the spatiotemporal temperature field for each unit cell at the spatial and temporal coordinates x_i and t_j , respectively (cf. Paper I). This matrix can be converted into a matrix containing

the length of each stick at all predefined time steps by assuming linear thermal expansion, i.e. $S_{i,j} = c_i \alpha_i (T_{i,j} - T_0)$, where c_i and α_i are the size and linear thermal expansion coefficient of the i th unit cell, respectively, and T_0 is the initial temperature. In a nutshell, one can now solve the system of differential equations of the linear chain successively by adapting the initial conditions after each time step according to the stick length matrix $S_{i,j}$ which encodes the heat diffusion.

In the above formalism the matrix $S_{i,j}$ plays the role of a general force which does not have to be governed by the heat equation but can in fact resemble any kind of time-dependent force. As an alternative to a Heaviside-like displacive excitation which is employed throughout this thesis, one may also use the matrix $S_{i,j}$ to simulate different excitation mechanisms such as, e.g., a delta-like Raman excitation of coherent phonons³ or more complex scenarios where the stress is generated simultaneously by electronic and phononic pressure components [67] which are related by the two-temperature model [42, 52]. Note, that for time-dependent forces one may also consider solving the system of differential equations numerically as briefly discussed in Section 4.2.

3.2 Coherent and incoherent lattice dynamics in thin films

In the following I apply the heat-diffusion LCM to the case of a rather thin SRO layer⁴ ($d_{\text{SRO}} = 15.4 \text{ nm}$) on a STO substrate in order to demonstrate the capabilities of the model and to discuss the influence of heat diffusion in nanometer-scale thin films. According to Table 3.1, the small thickness of the SRO layer leads to an accelerated heat diffusion from the layer to the substrate. Note, however, that the estimations in Table 3.1 only hold for a two-sided thermal contact of a point source whereas the present case treats a one-sided thermal contact of a finite source region which implies a slower heat conduction. In comparison to the thicker SRO layer investigated in Chapter 2, the thinner layer is not only expected to show a faster heat transfer but also the transit time of the coherent sound waves through the layer is decreased. The calculation yields $T_{\text{sound}} = 2.45 \text{ ps}$. The comparison of the timescales for the coherent and incoherent lattice dynamics shows a rather large difference and one could in principle treat these dynamics separately. Nevertheless, I choose this sample in order to compare the simulation to available UXR data and, more importantly, if layers of this size are used to build up a SL the timescale separation is no longer possible.

We conducted UXR experiments on this thin SRO layer using the PXS at the University of Potsdam. Figure 3.1(a) shows the recorded rocking curves at selected time delays after pumping the sample with $\approx 30 \text{ mJ/cm}^2$ at 800 nm wavelength. Since the SRO layer is fairly thin and the diffraction efficiency of a thin film in the kinematical limit has a squared dependence on the layer thickness [107] the signal-to-noise ratio of the PXS data is not as good as for the thicker SRO layer discussed in Section 2.2.2. Another consequence of a much thinner film is that the Bragg peak is significantly broadened. As the peak width is now comparable to the maximum change of the Bragg angle the peak splitting identi-

³Raman scattering excites optical phonons which are not described within the LCM presented here. One could refine the linear chain by simply defining two masses per unit cell. For the perovskite crystal structure this would already represent the lower limit in a 1D linear chain as the unit cell only contains 2 atomic layers along the c -axis. However, in order to describe all optical phonon modes of the perovskite unit cell a 1D LCM is not sufficient.

⁴This SRO thin-film sample will be reconsidered in Chapter 4.

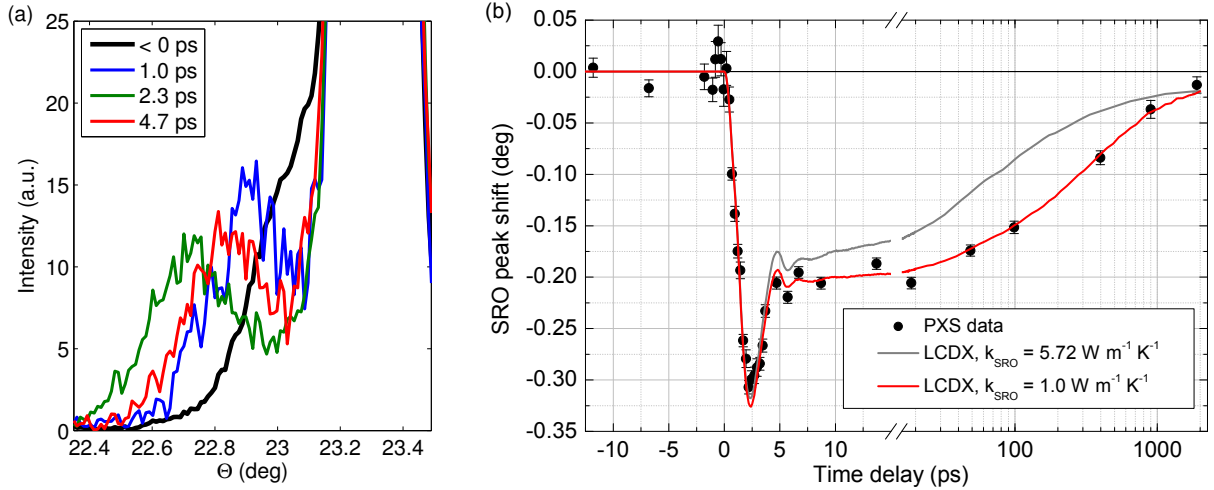


Figure 3.1: (a) Transient PXS rocking curves of 15.4 nm SRO on a STO substrate at selected time delays after laser excitation with $\approx 30 \text{ mJ/cm}^2$ at 800 nm wavelength. (b) Transient change of the SRO Bragg peak angle deduced from the PXS data (black bullets) and from LCDX calculations including heat diffusion. The grey solid line assumes the bulk SRO heat conductivity $k_{\text{SRO}} = 5.72 \text{ W m}^{-1} \text{ K}^{-1}$ [63] and the red solid line assumes $k_{\text{SRO}} = 1.0 \text{ W m}^{-1} \text{ K}^{-1}$.

fied in Section 2.2.2 is not observed in the present case⁵. The broadened Bragg peak in combination with the rather limited angular resolution of the PXS also somewhat merges the unexcited SRO peak with the substrate peak.

Nevertheless, it is possible to extract the transient position of the SRO peak due to the photoinduced expansion by fitting the rocking curves with a Gaussian after an appropriate subtraction of the substrate peak. The extracted transient change of the SRO peak position is depicted by the symbols in Fig. 3.1(b) and the error bars represent the 68% confidence interval of the fitting parameter. The maximum peak shift is reached after 2.5 ps which perfectly matches the estimation of T_{sound} . Furthermore, the data nicely verify the universal feature of the 50% increased coherent strain maximum discussed in Chapter 2.

After $t \approx 5 \text{ ps}$ the coherent LA phonons have essentially left the SRO layer which is then expanded due to the incoherently excited phonons, i.e., heat. As predicted, the heat subsequently diffuses out of the SRO layer into the STO substrate comparatively slowly giving rise to a backshift of the SRO Bragg peak on a few-nanoseconds timescale. The solid lines in Fig. 3.1(b) represent the change of the SRO peak position obtained from LCDX calculations including heat diffusion which have been analyzed in the same way as the PXS data. Employing the literature value for the heat conductivity of bulk SRO, $k_{\text{SRO}} = 5.72 \text{ W m}^{-1} \text{ K}^{-1}$ [63], the analysis yields the solid grey line in Fig. 3.1(b). Clearly, the simulation deviates quite strongly from the PXS data and exhibits a much faster relaxation of the SRO layer. However, an excellent agreement of calculation and measurement can be achieved by setting $k_{\text{SRO}} = 1.0 \text{ W m}^{-1} \text{ K}^{-1}$. This indicates that the 1D heat equation (3.2) is a valid model on the lengthscales of the considered SRO thin film ($\sim 10 \text{ nm}$) albeit with a strongly reduced heat conductivity. Possible reasons for the suppressed conductivity may be, e.g., thermal interface resistance or the lack of the contribution of certain heat-carrying phonon modes due to the nanostructure of the sample

⁵In fact, the conclusions drawn in Section 2.2.2 regarding the Bragg peak splitting do not apply here. Due to a layer thickness (15.4 nm) much smaller than the optical penetration depth ($\approx 50 \text{ nm}$) the tensile strain waves launched at the surface and the layer-substrate interface are comparable in amplitude. Accordingly, the SRO layer is not half-expanded and half-unstrained at $t = T_{\text{sound}}/2$ as deduced for the thicker sample considered in Section 2.2.2 and does therefore not exhibit the discussed Bragg peak splitting.

(see Paper **VI** and references therein as well as Ref. 108). However, one would actually expect that both effects produce only small deviations from the bulk thermal conductivity at the given structural size. Therefore, further investigations are required to clarify the nature of the strongly reduced thermal conductivity.

3.3 Heat diffusion in superlattices

Similar to the heat diffusion from a photoexcited thin film into its supporting substrate the heat deposited optically in the metal layers of the previously considered metal-insulator SLs will diffuse into the adjacent unexcited insulator layers. The SRO/STO SL I have examined in the preceding chapter has layer dimensions very similar to the SRO thin film discussed in Section 3.2. However, as indicated before, for a two-sided thermal contact one expects a significant acceleration of the temperature equilibration among the individual layers according to the 1D heat equation (3.2).

Numerous experimental and theoretical approaches to the topic of static thermal transport in SLs have been discussed in the literature. Many experiments on different types of SLs evidence a significant reduction of the cross-plane thermal conductivity as the SL period is decreased [108–112]. This effect is mainly attributed to an increased scattering of acoustic phonons by the layer interfaces. Theoretical models have also predicted an increase for very thin semiconductor SLs [113]. Previous UXRD experiments on a SRO/STO SL suggested a surprisingly strong suppression of heat conduction from the SRO into the STO layers up to 200 ps [60].

In Paper **VI** we re-addressed the topic of time-resolved heat conduction in SLs with much higher precision by optical pump–x-ray probe experiments at the EDR beamline at the synchrotron source BESSY II⁶. We considered a SL made from metallic LSMO and STO which is considered to be similar to the SRO/STO SL investigated in Ref. 60 in terms of its optical, mechanical and structural properties. Due to the limited time-resolution of the synchrotron pulses of ≈ 100 ps we were not able to observe the coherent SL dynamics. In analogy to the previous section, we monitored the heat flowing out of the SL into the STO substrate by recording the transient shift of the respective Bragg peaks over a wide range of time delays up to 4 μ s. If the heat conduction between the individual layers of the SL was permanently suppressed as reported in Ref. 60 the net heat flux into the substrate would also be hindered and one would thus observe a delayed relaxation of the SL expansion and an accordingly delayed onset of the substrate expansion. However, the results of the very sensitive experiments presented in Fig. 4 of Paper **VI** could be almost perfectly simulated by the predictions of the 1D heat equation (3.2) using bulk thermal properties reported in the literature for LSMO and STO. In conclusion, in case of the LSMO/STO SL we found no evidence of a deviation from the heat conduction laws on timescales from several 100 ps up to a few μ s and on length scales of ≈ 10 nm (defined by the layer thickness of the SL). This result is supported by the simple argument that the mean free path of thermal phonons at room temperature in the considered SL, $\bar{L} \approx 1$ nm, is much smaller than the SL period d_{SL} which suggests that heat diffusion should be bulk-like [9]. Also thermal interface resistance could be excluded by the analysis.

The above conclusion seems to somewhat contradict the findings of Section 3.2 where a significantly suppressed heat conductivity of a thin SRO film on a STO substrate was identified. This may indicate that the LSMO and SRO nanolayers are not as similar as expected regarding their thermal transport properties. However, it is not clear whether

⁶Details on the experimental setup and methods at BESSY II can be found in Ref. [114]

the observed differences are intrinsic for the nanolayered materials or whether they arise from the interface to the STO layers or substrate. A comparison of static rocking curves of the SRO/STO SL (Fig. 1(a) in Paper **III**) and the LSMO/STO SL (Fig. 2(a) in Paper **II** and Fig. 3(a) in Paper **VI**) measured at BESSY II reveal that the structural quality of both SLs is comparable and almost perfect. That is, phonon scattering from the interfaces should be small in both cases. Note that the low heat conductivity from the thin SRO film into the STO substrate found in Section 3.2 qualitatively supports the reduced heat conductivity of the SRO/STO SL reported in Ref. 60 but does not suffice to quantitatively reproduce the authors conclusions.

Finally, the topic of thermal transport on small length and timescales in SRO and LSMO is still not entirely understood and thus additional investigations have to be performed. The LCM including the effect of lattice heat diffusion and its combination with dynamical XRD calculations has nevertheless proven to be a powerful tool for the precise analysis of UXRD measurements on photoexcited nanolayered crystal structures. It therefore represents a suitable toolkit to investigate the physical mechanisms of coherent and incoherent structural dynamics in such systems.

NONLINEAR LATTICE DYNAMICS

The previous chapters discussed the lattice dynamics of photoexcited nanolayered structures and their supporting substrate assuming a harmonic interaction of the neighbouring atoms forming the lattice. That is, the forces exerted on the atoms are proportional to the nearest-neighbour distances which can be described by quadratic interatomic potentials. Of course, this approximation cannot hold for arbitrarily large mutual displacements of the atoms. The physical nature of the effective interatomic potential is manifold and includes repulsive forces (electrostatic repulsion, Pauli exclusion principle) and attractive forces (Van-der-Waals, Ionic, Covalent bonding) depending on atoms involved in a particular crystal [43]. All of these interactions are intrinsically nonlinear which renders the effective interatomic potential anharmonic in general. For very small deformations a harmonic approximation may be applied as was done in the previous chapters. However, some particular physical aspects which rely on anharmonic phonon-phonon interactions (e.g. thermal expansion, thermal conduction, sound attenuation, etc.) already indicate that even for small strain amplitudes nonlinearities cannot be completely neglected [43, 115]. In particular, the thermal expansion of the metallic layers which is responsible for the generation of the coherent phonons considered in this thesis is only possible due to the anharmonic nature of the crystal lattice. Having said that, a thorough description of the excitation mechanism in the metal layers is out of the scope of this thesis. The concept of incorporating the photogenerated stress in form of (possibly time-dependent) initial conditions is continued in the following sections. Nevertheless, the above considerations suggest that nonlinear interactions have to be included into the lattice dynamics calculation as they will strongly affect the propagation and population of phonons in anharmonic lattices.

As mentioned above and realized fairly early [116], lattice anharmonicity gives rise to and thus influences very basic physical effects such as thermal expansion and conduction [43] which are highly relevant from a technological standpoint [117]. Moreover, it creates a temperature and pressure-dependence of the material's elastic constants [81, 99, 118] and allows for interaction of different vibrational modes which gives rise to phonon damping [119–121] and nonlinear phononics [122, 123]. The importance of higher-order contributions to the interatomic potentials has also been directly measured on dynamical effects in the frequency and time-domain [27, 124–129].

In the current chapter, I do not exclusively focus on UXRD experiments but also invoke results from all-optical pump-probe reflectivity measurements. Specific features of the latter experimental method also reflect the triggered structural dynamics and unambiguously indicate the importance of lattice anharmonicity. Therefore, Section 4.1 presents a brief introduction to light scattering from phonons and how optical pump-probe tech-

niques in addition to UXRD can be used to study structural dynamics in solids. In the subsequent sections, which are closely related to Papers **VIII** and **VII**, I introduce the anharmonic LCM (Section 4.2) and compare its predictions to all-optical pump-probe and UXRD experiments on photoexcited nanolayered oxides (Sections 4.3 and 4.4). In particular, the anharmonic propagation and attenuation of high-amplitude longitudinal acoustic (LA) phonons in STO will be considered in detail.

4.1 Light scattering from coherent phonons

Not only since the discoveries by Raman [130, 131] it is known that in addition to reflection and refraction light can be scattered by static or dynamic fluctuations of matter having a characteristic size smaller than or comparable to the wavelength of the light. Such scattering effects can be due to elastic scattering from particles and thermal fluctuations (Mie and Rayleigh scattering [41, 132]) or inelastic scattering from quasi-particles such as optical phonons (Raman scattering) or acoustic phonons (Brillouin scattering) [133]. The information one can obtain from the scattered light can thus be used to gain insight into these fundamental and material specific processes. Since the main focus of this thesis is on photoexcited longitudinal acoustic phonons Brillouin scattering will be of primary interest.

As I have discussed in detail, the absorption of an ultrashort light pulse (pump) can lead to an impulsive excitation of coherent phonons by which a second ultrashort light pulse (probe) can be scattered. By varying the time delay t between the pump and the probe pulse one can extract the time evolution of the coherent phonons. This class of experiments is known as pump-probe technique [16]. The typical experiment considered throughout this thesis is the photoexcitation of a thin metal film which thereby acts as a transducer launching longitudinal sound waves inside the film and into the supporting substrate [40]. These phonon wavepackets possess a certain spectrum of phonon modes each of which is then capable of scattering the photons of the probe pulses given the energy and momentum conservation regarding the participating photons and phonons is fulfilled. The conservation laws generally imply a modified Laue (diffraction) condition (see Paper **VIII** and references therein)

$$\mathbf{q} = \mathbf{k}_{\text{out}} - \mathbf{k}_{\text{in}} = \mathbf{G} \pm \mathbf{Q} \quad (4.1)$$

where \mathbf{Q} is a particular phonon wavevector. Equation (4.1) is similar to (2.8) but in addition to the diffraction of (x-ray) photons from a reciprocal lattice vector \mathbf{G} it includes the diffraction from a phonon of wavevector \mathbf{Q} . Interestingly, (4.1) holds in principle for any photon energy. For hard x-rays which typically have wavevectors comparable to or larger than $G = |\mathbf{G}|$ this implies that a monochromatic phonon appears in XRD as sidebands to the bulk Bragg reflections at $G \pm Q$ where we again assume symmetric XRD along the z -direction¹. These sidebands represent an additional Fourier component due to the spatial periodicity $\Lambda = 2\pi/Q$ imprinted in the crystal by the phonon. In contrast, the wavevector of optical photons is at least three orders of magnitude smaller than that of hard x-ray photons in which case (4.1) can only be fulfilled if $\mathbf{G} = 0$. In other words, the wavelength of optical light is too large to be sensitive to the crystal structure itself. However, optical photons can still be diffracted from phonons present in the bulk material. Classically, this can be viewed as the diffraction of waves from a Bragg grating due to the periodic modulation of the optical constants by the phonon. As explained in Paper **VII**

¹For a three-dimensional treatment see, e.g., Ref. 134

as well as in Refs. 73, 100, 133, 135, 136, for optical experiments (mostly in reflection geometry) (4.1) can be recast as

$$q = \frac{4\pi}{\lambda} n(\lambda) \cos \beta = \pm Q \quad (4.2)$$

where $n(\lambda)$ is the refractive index of the scattering material at the optical probe wavelength λ and β is the internal angle of propagation towards the surface normal². Equation (4.2) reveals that either the scattering angle or the probe wavelength can be tuned to access different phonon wavevectors Q . Depending on the phase of the oscillating phonon, the diffracted (Brillouin scattered) wave interferes constructively or destructively with a reference wave which gives rise to oscillations of frequency $\Omega(Q)$ in the transient diffraction/reflection signals [24, 73, 100, 134–137]. In optical reflectivity measurements this reference wave is the wave reflected at the sample surface and interfaces. The generally nonlinear phonon dispersion³ relates the phonon frequency Ω to the phonon wavevector Q . Since the LA phonons discussed throughout this thesis have wavevectors near the Brillouin-zone center the dispersion relation reduces to the linear equation

$$\Omega = v_{\text{LA}} Q \quad \left(Q \ll \frac{\pi}{c} \right) \quad (4.3)$$

where c is the lattice parameter. That is, the ratio of the experimental quantities Ω and q reveals the longitudinal sound velocity v_{LA} of the scattering material.

To simulate the transient optical reflectivity from coherent phonons in nanolayered solids one can employ a transfer matrix approach similar to the dynamical XRD calculation mentioned in Section 2.2 where the Fresnel-like reflection and transmission amplitudes of each unit cell are given by the strain-dependent (and thus time-dependent) optical constants. This approach can be applied to an arbitrarily layered structure and it includes the multiple reflections from the various interfaces. When restricted to phonons inside a homogeneous layer, e.g., the substrate, this dynamical approach is equivalent to the kinematic approach presented in Ref. 40 since the strain-induced gradients of the optical constants are typically very small.

The all-optical pump-probe experiments I discuss in the following employ ultrashort pump pulses of 800 nm wavelength. As probe pulses we utilize an ultrashort white-light supercontinuum which is produced by self-phase modulation in a sapphire disc [138]. The reflected broadband optical pulses are recorded with a multichannel spectrometer (AvaSpec, AVANTES) at different pump-probe time delays similar to setups used by other groups [135, 139].

4.2 The anharmonic linear-chain model

Before addressing specific experiments revealing the anharmonic nature of the interatomic forces in a crystal lattice I briefly introduce a generalized LCM which accounts for such anharmonicities. The model is also discussed in Paper **VII**.

²For x-rays the refractive index n is practically unity and the scattering angle Θ is usually measured with respect to the surface, i.e., $\cos \beta \mapsto \sin \Theta$.

³As opposed to simple elastic continuum models [40, 57], the LCM introduced in Section 2.1 already implies the basic nonlinear LA phonon dispersion relation of 1D crystal lattices. The extension to two masses per unit cell would also yield the dispersion relation for optical phonons of a diatomic linear chain. The derivation of these relations is presented in nearly any textbook on solid state physics, e.g., in Refs. 43, 55

The LCM exploited in the previous chapters and its technical details were presented in Paper **I**. The model treated the unit cells as symbolic masses and only the nearest-neighbour harmonic interaction was accounted for which can be thought of as springs connecting adjacent masses. In the following we extend this model in order to include more general interatomic forces. As opposed to the harmonic LCM, we evaluate the anharmonic LCM by using two different masses per unit cell connected by identical springs (also known as diatomic or alternating linear chain) [57]. This refined model resembles the two different lattice planes of the perovskite unit cell, e.g., SrO and TiO₂ in case of STO. The reason for doing so is that for such a complex and nonlinear dynamical system proposed below there may not exist a unique or general transformation between the two descriptions “one mass per unit cell” and “one mass per lattice plane”. In order to be as close to reality as possible we thus choose the latter. In the following I focus exclusively on acoustic deformations of the diatomic linear chain by considering the strain of an entire unit cell. Furthermore, we maintain the assumption of nearest-neighbour interactions which implies that the independent variable for the force acting between the i th and the $(i + 1)$ th mass in the linear chain is their distance⁴ $\Delta_i = x_{i+1} - x_i$. The total force on one mass is of course given by the difference of the forces exerted by the two neighbouring masses. The anharmonic LCM carrying N masses (2 per unit cell) can thus be described by the following set of N nonlinear differential equations⁵

$$m_i \ddot{x}_i = \frac{\partial U_i(\Delta_i)}{\partial \Delta_i} - \frac{\partial U_{i-1}(\Delta_{i-1})}{\partial \Delta_{i-1}} + m_i \gamma_i (\dot{\Delta}_i - \dot{\Delta}_{i-1}) + F_i(t) \quad (4.4)$$

Here, m_i is the mass of the i th unit cell, U_i is an arbitrary potential between two masses, γ_i is a material specific damping constant and $F_i(t)$ is a time-dependent force acting on the i th mass which is proportional to the photoinduced stress $\sigma(x_i)$. The damping term in (4.4) is a phenomenological term that accounts for internal irreversible processes due to anharmonic coupling to the bath of incoherent thermal phonons which lead to an inevitable decay of coherent phonons in real crystals [140, 141]. These kind of effects will be discussed in more detail in Section 4.4.2.

As a first approximation, we restrict our considerations to the second and third-order term of the Taylor series of U . The former yields the harmonic interaction and the latter introduces a slight anharmonicity of odd symmetry. The set of nonlinear differential equations which then have to be solved read

$$m_i \ddot{x}_i = (K_i \Delta_i - K_{i-1} \Delta_{i-1}) - (A_i \Delta_i^2 - A_{i-1} \Delta_{i-1}^2) + (m_i \gamma_i \dot{\Delta}_i - m_{i-1} \gamma_{i-1} \dot{\Delta}_{i-1}) + F_i(t) \quad (4.5)$$

where $K_i > 0$ is the formerly introduced force constant of the springs connecting the i th and the $(i + 1)$ th mass and $A_i > 0$ is the anharmonicity parameter. As we intend to simulate the anharmonic lattice dynamics of nanolayered heterostructures, we separated the terms belonging to either side of the i th mass in order to account for any interfaces between different materials.

The system of nonlinear ordinary differential equations (ODE) (4.5) is much more complicated than the linear system discussed in Chapter 2 and Paper **I**. We therefore do not attempt to solve this system analytically but employ built-in ODE solver routines of the numerical computing software MATLAB. As opposed to the analytical approach for

⁴Although I previously defined the relevant spatial dimension as the z -axis, I use x_i in this section in accordance with Paper **VII**.

⁵In fact, the differential equations describing the end masses include the terms indexed either by i or $i + 1$, respectively, as these only experience a force from one side.

the harmonic LCM where the photoinduced stress σ is incorporated as modified initial condition, σ enters the equations via the source term $F_i(t)$ in (4.5). The numerical results can then be analyzed directly or serve as an input for the dynamical XRD calculations.

The issue of nonlinear sound propagation has been previously discussed in the literature. Theoretical models use either a linear-chain approach similar to the model proposed above [140, 141] or solve the Korteweg-de Vries-Burgers equation which represents a continuum-model approach [142–144]. One of the major implications of nonlinear sound propagation which is, however, out of the scope of this thesis is the formation and propagation of acoustic solitons. Such solitons are extensively studied in the context of lattice anharmonicities and have been experimentally observed by optical means and successfully simulated by the previously mentioned models [140–144].

The following sections present time-resolved optical and XRD experiments which directly evidence the influence of anharmonic effects on sound propagation. The experimental findings are carefully analyzed and related to the general features of the results from the anharmonic LCM.

4.3 Nonlinear strain propagation in SrTiO₃

The first indications that the inclusion of higher-order terms in the crystal lattice potential is required were found in all-optical pump-probe experiments which I performed on strongly photoexcited thin metallic films on STO substrates. The current section summarizes the experimental and numerical results presented in detail in Paper VII.

Paper VII presents the results of all-optical broadband pump-probe experiments on a thin film of metallic LSMO ($d_{\text{LSMO}} = 36$ nm) grown on top of a STO substrate. The LSMO layer is optically excited by 800 nm pump pulses at different fluences. As extensively discussed in Section 2.1.3, the impulsively expanding metal layer launches a coherent bipolar strain pulse (BSP) into the STO substrate propagating at the speed of sound $v_{\text{LA}}^{\text{STO}}$ (see also Fig. 2.3). Within a harmonic LCM considered so far this phonon wavepacket is subject only to normal dispersion but not to any kind of damping or other nonlinear effects. Of course, this is a valid approximation only on sufficiently small time and strain scales. As motivated in Section 4.1, such a phonon wavepacket can be observed by time-resolved optical reflectivity measurements resulting in characteristic oscillations in the recorded signals which is shown in Fig. 2 of Paper VII. Given the optical constants of the STO substrate and the chosen experimental geometry, each optical probe wavelength λ is uniquely related to a phonon wavevector Q by eq. (4.2). The transient reflectivity data are then analyzed for each λ (and thus Q) by a Fast Fourier Transform (FFT) which yields the observed Q -dependent oscillation frequency $\Omega(Q)$. By making use of eq. (4.3) one can precisely deduce $v_{\text{LA}}^{\text{STO}}$.

The experimental data presented in Fig. 2 of Paper VII exhibit a fluence and probe wavelength-dependent beating of the oscillations. The more sophisticated analysis performed to obtain Fig. 3 of Paper VII revealed a sound velocity independent of Q at low pump fluence matching the literature values which is in accordance with the linear LA phonon dispersion relation (4.3) and the harmonic LCM⁶. At higher pump fluences, Fig. 3 in Paper VII evidences the occurrence of two separated sound velocities the difference of which increases with increasing pump fluence. These features cannot be explained by a simple harmonic LCM and thus suggest additional interactions. Similar experiments with

⁶The harmonic LCM discussed in this thesis does not include damping and would thus not reproduce the decay of the measured oscillations.

an amorphous Al layer on STO have been performed by Brivio *et al.* [136]. In contrast to our results, the authors find a Q -dependent STO sound velocity which deviates from the expected linear LA phonon dispersion relation. The authors, however, do not attempt to physically interpret the results and since no pump fluence or excitation density is given one cannot speculate about lattice anharmonicity as a reason for their findings.

In order to interpret our experimental data we employed the anharmonic LCM presented in Section 4.2. The finite third-order term in the interatomic potential produces an asymmetry of the interatomic forces. As reported in Paper **VII**, this asymmetry gives rise to different propagation velocities of the tensile and expansive parts of the BSP. Since the influence of the third-order term in the potential becomes increasingly important at larger strain amplitudes (and pump fluences), the velocity splitting is fluence-dependent. This qualitatively explains the results shown in Fig. 3 of Paper **VII**.

By using the well-understood lattice dynamics of photoexcited thin films (Section 2.1.2) and its manifestation in UXR D experiments (Section 2.2), it is possible to calibrate the amplitude of the BSP in the STO substrate by evaluation of the transient shift of the Bragg peak corresponding to the photoexcited LSMO layer. The recorded LSMO peak shift shown in Fig. 1 of Paper **VII** reflects the LSMO strain amplitude and thereby also the strain amplitude in the BSP. We thus adjust the average LSMO strain amplitude calculated by the anharmonic LCM to match the peak shift in the UXR D data as described in Section 2.2. The spatiotemporal strain pattern obtained from the anharmonic LCM then serves as an input for the simulation of the transient optical reflectivity due to the phonon-induced modulation of the optical constants⁷ [40]. Finally, the comparison of these simulations to the experimental optical data allows us to deduce the quantitative contribution of the third-order term in the interatomic potential and the empirical damping coefficient γ of STO. The very good agreement of the simulations with the experimental data as presented in Paper **VII** could be achieved assuming the interatomic potential of STO plotted in Fig. 4.1 which has the analytical expression

$$U(x) = \frac{K}{2}x^2 - \frac{A}{3}x^3, \quad K = 255.1 \frac{\text{kg}}{\text{s}^2}, \quad A = 1.79 \cdot 10^{13} \frac{\text{kg}}{\text{m s}^2} \quad (4.6)$$

where K and A are the spring constant and anharmonicity parameter of the diatomic linear chain, respectively, in SI units. Note, that the value of K reproduces the longitudinal sound velocity of STO measured in the experiment (7990 m/s). Furthermore, we assumed a damping coefficient $\gamma = 1.0 \cdot 10^{13} \text{ s}^{-1}$ although the damping cannot be determined very accurately from the available data sets. The presented experiment thus verifies that the lattice anharmonicity is an important ingredient for coherent sound propagation at large but accessible strain amplitudes in STO. A similar conclusion was recently drawn for optical phonons in STO [128].

After matching the transient reflectivity data we further investigated the properties of the simulated phonon wavepacket as it propagates through the STO substrate. The evolution of the spatial shape of the wavepacket and its transient amplitude spectra are plotted in Fig. 4 of Paper **VII**. As opposed to the case of harmonic interactions where the phonon spectrum remains unchanged for all times, we observe a shift of spectral weight towards lower phonon wavevectors Q . The minima in the phonon spectrum thereby pass through the Q -range to which the optical photons are sensitive giving rise to the beatings observed in the optical reflectivity data. The occurrence of acoustic solitons is suppressed

⁷The simulations were briefly mentioned at the end of Section 4.1. The calculations require the knowledge of the photoelastic constants which were partly taken from the literature [145].

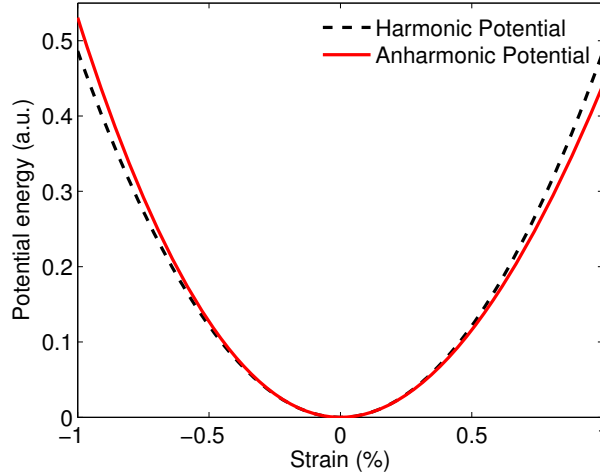


Figure 4.1: Anharmonic interatomic potential of STO (red solid line) deduced from the all-optical pump-probe experiments presented in Paper **VII** by the anharmonic (diatomic) LCM. The harmonic potential (black dashed line) to which the harmonic LCM is restricted is also shown for comparison.

in our experiments and simulations due to the high temperature of 300 K giving rise to a relatively large damping coefficient γ in eq. (4.5). As a next step we intend to cool the sample with a cryostat in order to decrease the phonon damping and to verify the formation of acoustic solitons. It would also be very interesting—albeit challenging—to observe acoustic solitons with structural probes such as UXR in the future.

4.4 Attenuation of quasi-monochromatic phonons

In addition to the previously discussed experiment, we found strong evidences for anharmonic lattice effects in STO in various other experiments. In the following I present synchrotron-based UXR experiments (Sections 4.4.1 and 4.4.2) which exhibit the decay of a phonon-induced sideband Bragg peak indicating a considerably reduced lifetime of the phonons due to anharmonicity. This interpretation is supported by all-optical pump-probe experiments discussed in Section 4.4.3.

4.4.1 Generation and detection of quasi-monochromatic phonon wavepackets

In the preceding section I concluded that lattice anharmonicities modify the phonon spectrum via damping and spectral weight transfer which we deduced from all-optical pump-probe experiments. It would thus be favourable to generate phonon wavepackets of narrow bandwidth (ideally quasi-monochromatic in the sense of the Fourier limit of short pulses) in order to unambiguously study the transient anharmonicity-induced modification of such phonon pulses.

In Paper **VIII**, we present the successful generation of quasi-monochromatic LA phonon wavepackets in a STO substrate by the excitation of a 15.4 nm thin SRO layer with a train of 8 ultrashort optical pulses mutually separated by $\tau_p = 7.2$ ps ($\nu_p = 1/\tau_p = 140$ GHz). The efficient generation of such wavepackets by optical means is evidenced by UXR experiments conducted at the ID09B beamline of the European Synchrotron Radiation Facility (ESRF) in Grenoble, France. As explained in Section 4.1, the additional transient

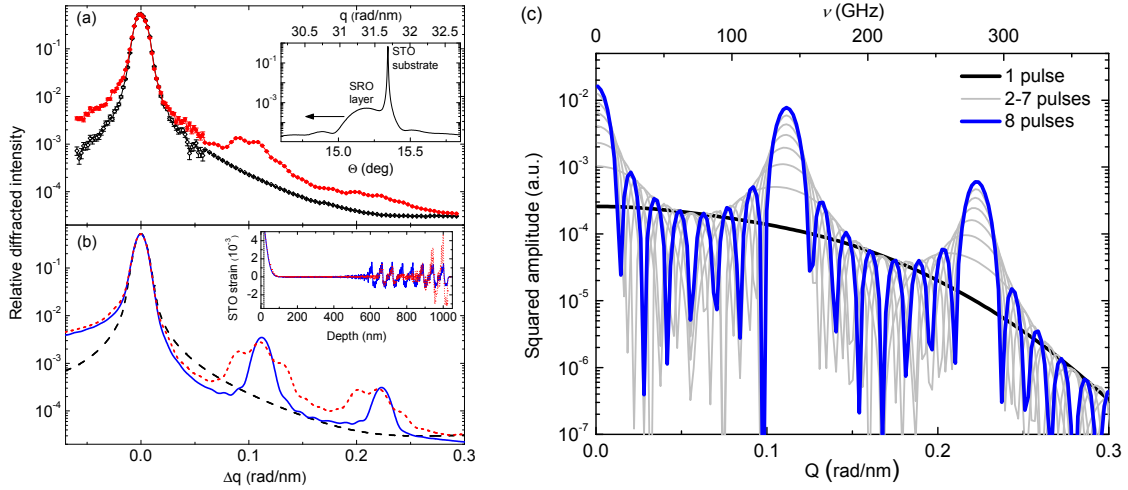


Figure 4.2: Left panel: The experimental (a) and simulated (b) transient rocking curves around the (002) STO substrate peak exhibiting the sidebands which reveal the quasi-monochromatic phonon spectrum 130 ps after pulse-train excitation of a 15.4 nm thin SRO film transducer on a STO substrate. The figure is adapted from Paper **VIII**. See the paper for more details. Right panel: Squared amplitude spectrum of the LA phonon modes (LCM) of the thin SRO film on STO after each pulse for a uniform excitation pulse train of 8 pulses with separation of $\tau_p = 7.2$ ps ($\nu_p = 1/\tau_p = 140$ GHz). In contrast to the initially broad phonon spectrum of a single-pulse excitation, only phonons around $Q_p = 2\pi\nu_p/v_{\text{LA}}^{\text{STO}}$ and its higher harmonics interfere constructively. The final spectrum (blue line) yields the blue rocking curve in panel (b). The increase of phonon amplitude around $Q = 0$ (and thus $\Omega = 0$) is due to the long-lived expansion of the SRO film.

spatial periodicity $\Lambda = 2\pi/Q$ imprinted in the crystal by a LA phonon with a wavevector Q gives rise to discrete sidebands to the STO substrate Bragg reflection at positions $G \pm Q$. Consequently, the entire phonon spectrum is mapped by UXRD onto the vicinity of the substrate peak⁸. In fact, the intensity of an XRD sideband corresponding to a phonon mode Q with amplitude A is proportional to the squared phonon amplitude, i.e., $I(Q) \propto A^2$, as can be verified with dynamical XRD calculations. UXRD therefore measures the transient squared amplitude phonon spectrum. Depending on the time-resolution of the experiment one may also obtain the frequency and phase of the phonon from the intensity oscillations discussed in Section 4.1. For much smaller phonon frequencies this could be shown in, e.g., Refs. 25, 134, 137, 146.

The upper panel of Fig. 4.2(a) is adapted from Paper **VIII** and shows the measured rocking curves around the STO substrate at a time delay of 130 ps (red bullets) and before the laser-pulse excitation (black diamonds). The data after excitation reveal separate sidebands of the STO substrate peak around $Q_p \approx 0.11$ rad/nm and integer multiples thereof which evidences an accordingly shaped phonon spectrum. In essence, each of the employed 8 pulses generates a coherent broadband BSP which in total forms a phonon wavepacket of narrow spectral bandwidth. This is depicted in Fig. 4.2(c) which shows the coherent pulse-to-pulse build-up of the narrow bandwidth phonon spectrum as calculated by the LCM. Only phonons around the pulse repetition rate $\nu_p = 140$ GHz and its higher harmonics—albeit at much weaker intensities—interfere constructively which explains the

⁸In case of the considered symmetric XRD which is structurally sensitive only to the direction perpendicular to the layer surface eq. (4.1) becomes a scalar relation. In principle, the mapping of the phonon spectrum then holds for all possible diffraction orders of the substrate given a sufficiently large photon wavevector. If not stated differently, we exclusively consider the (002) reflections (in reciprocal lattice units) since for the perovskite crystal structure the x-ray structure factor of this diffraction order is maximized.

appearance of the observed sidebands. The calculated XRD rocking curve of the final phonon spectrum (blue line in Fig. 4.2(c)) is presented by the blue solid line in Fig. 4.2(b). The position of the sidebands predicted by the simulation is confirmed by the experimental data. This verifies the longitudinal sound velocity in STO determined by the linear LA phonon dispersion relation $\Omega_p = 2\pi\nu_p = v_{\text{LA}}^{\text{STO}}Q_p$ even without having the time-resolution required to directly observe the phonon oscillations. Consequently, one thus has the opportunity to tune the central wavevector Q_p of the phonon wavepacket by the pulse train repetition rate ν_p for Q -dependent investigations.

The fairly broad sidebands found in the experiments indicate an imperfect phonon spectrum generated by the pump pulse train. By varying the individual pump pulse energies in the simulation (non-uniform energy distribution) we could verify that this spectral broadening is due to the fact that the portion of the sample probed by the x-rays (diameter $\approx 50 \mu\text{m}$) was not equally excited by the individual pump pulses (diameter $\approx 500 \mu\text{m}$). The corresponding XRD and LCM simulations are shown as red dashed lines in Fig. 4.2(b) and its inset, respectively.

The higher harmonics at integer multiples of $Q_p = 0.11 \text{ rad/nm}$ observed in both simulation and experiment are due to the rectangular-like shape of the individual BSPs. In general, an optimized phonon spectrum is obtained if the time separation between the pump pulses τ_p is equal to twice the transit time of the sound waves through the metallic layer of thickness d , i.e., $\tau_p^{\text{opt}} = 2T_{\text{sound}} = 2d/v_{\text{LA}}$. Since the temporal pulse duration of each BSP is also given by $2T_{\text{sound}}$, the above relation implies that there is no time gap between the individual BSPs and the phonon wavepacket thus has no zero-strain gaps between the BSPs⁹. For symmetry reasons, the spectrum of such a square-wave-like wavepacket does not exhibit even harmonics and, for instance, the second harmonic in all panels of Fig. 4.2 would be suppressed.

4.4.2 Anharmonic decay of coherent phonons – UXRD

After the successful generation of coherent quasi-monochromatic LA phonon wavepackets described above we focused on the dynamics of such wavepackets. The variation of the pump-probe time delay allowed us to follow these dynamics by monitoring transient rocking curves of the STO substrate peak vicinity. In Paper **VIII**, we identified a strongly reduced decay time of the intensity of the first-order sideband ($\approx 130 \text{ ps}$) as compared to the harmonic LCDX predictions ($\approx 600 \text{ ps}$). In fact, the phonons described by the harmonic LCM have infinite lifetime. Nevertheless, the harmonic LCDX calculations do predict a decay of intensity which is essentially due to the fact that the phonon wavepacket travels deeper into the substrate and thus gradually vanishes beyond the extinction depth of the x-rays. The experimental observation therefore clearly suggests that decay processes of anharmonic nature not included in the harmonic LCM are responsible for relatively short lifetimes of the photoexcited phonons.

It is long-known that the coupling of coherent acoustic phonons to thermally excited incoherent phonons via lattice anharmonicities leads to damping of the coherent phonon. The theories of sound attenuation can be divided into two distinct regimes depending on the ratio of the considered phonon frequency Ω and the mean scattering time $\bar{\tau}$ of thermal phonons [147, 148]. If $\Omega\bar{\tau} \gg 1$, referred to as the collisionless regime [149], one has to consider individual phonon scattering events by a quantum mechanical description

⁹Compare the schematic wavepacket in Fig. 1(b) and the calculated one in the inset of Fig. 2(b) of Paper **VIII**. The latter exhibits small zero-strain gaps between the individual BSPs since the laser pulse separation τ_p was slightly larger than the optimum value τ_p^{opt} for the employed SRO layer.

as pioneered by Landau and Rumer in 1937 [150] and further developed by other authors [151]. This regime is not further discussed in the following analysis. For $\Omega\bar{\tau} \ll 1$, also referred to as the hydrodynamic regime [149], the sound attenuation can be described within the classical framework of thermodynamics by the anharmonic interaction of the coherent phonon with a bath of thermal phonons. This approach was first developed by Akhiezer in 1939 [152] and later refined by Woodruff and Ehrenreich [153]. In addition to these references, Akhiezer’s mechanism of relaxation damping (RD) has been explained in various publications [147, 148, 154]. In a nutshell, it describes the damping of sound via the modulation of the solid’s elastic constants in the compressed and rarefied regions of the acoustic wave, respectively, which is due to lattice anharmonicities. The associated changes in frequencies of the thermal phonons result in a non-thermal distribution thereof which is relaxed towards local thermal equilibrium via anharmonic phonon-phonon scattering. This process, however, is entropy-increasing and thus irreversibly removes energy from the driving sound wave which results in damping. Some later works develop theories which are valid for both the collisionless and the hydrodynamic regime [147, 154]. For quantitative comparisons I use the expression for the phonon amplitude decay rate Γ_{RD} presented by Koreeda *et al.* [149]

$$\tau_{\text{RD}}^{-1} = \Gamma_{\text{RD}} = \frac{3\alpha^2 BT\bar{\tau}}{\rho C_l} \Omega^2 \quad (4.7)$$

where α is the linear thermal expansion coefficient, B is the bulk modulus, T is the temperature, ρ is the mass density and C_l is the heat capacity per unit mass.

A second decay mechanism of acoustic phonons which is related to Akhiezer’s relaxation damping is the so-called thermoelastic damping (TED) [154–156]. As explained above, the driving sound wave gives rise to small temperature variations and thus to temperature gradients. Consequently, heat diffusion between these regions occurs which represents another channel of energy loss for the driving sound wave. This contribution can be quantified by [155, 156]

$$\tau_{\text{TED}}^{-1} = \Gamma_{\text{TED}} = \left(\frac{C_{11} + 2C_{12}}{C_{11}} \right)^2 \frac{k\alpha^2 T}{2\rho v_{\text{LA}} C_l^2} \Omega^2 \quad (4.8)$$

where C_{11} and C_{12} are the elastic constants and k is the heat conductivity.

The above theories predict that the decay rate of acoustic phonons in the hydrodynamical regime is proportional to Ω^2 . The phonon wavepackets excited in single crystal STO by trains of ultrashort laser pulses considered in Paper **VIII** have a central angular frequency of $\Omega_p = 2\pi\nu_p \approx 870$ GHz and a comparison to the mean scattering time of thermal phonons¹⁰ ($\bar{\tau}^{-1} \approx 2.8$ THz) justifies the validity of the hydrodynamical regime. Note, however, that the values are not far from the cross-over to the collisionless regime. Although these theories are based on lattice anharmonicities (strain-dependence of elastic constants, heat conduction) they do not involve the actual amplitude of the coherent sound wave under investigation. As concluded in Section 4.3, however, the strain amplitude plays an important role for the sound propagation when considering lattice anharmonicities.

In the following I present an extended analysis of the decay of quasi-monochromatic phonon wavepackets investigated at the ESRF and partly published in Paper **VIII**. The

¹⁰The mean scattering time of thermal phonons can be estimated from the thermal diffusivity by the relation $D_{\text{th}} = \bar{\tau}\bar{v}^2/3$ where \bar{v} is the mean velocity of thermal phonons [43, 55]. For the estimations I used the experimental thermal diffusivity of STO from Wang *et al.* [157], Debye’s mean thermal velocity $\bar{v}^3 = 3(v_{\text{LA}}^{-3} + 2v_{\text{TA}}^{-3})^{-1}$ [149, 157] and the longitudinal (LA) and transverse (TA) sound velocities from Ref. 99.

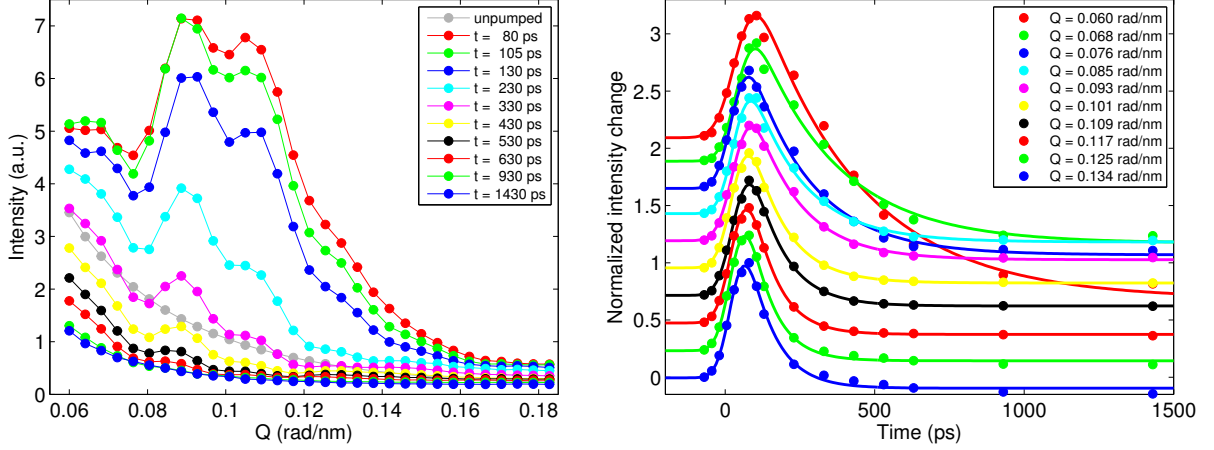


Figure 4.3: (a) Transient rocking curves of the phonon-induced first-order sideband of the (002) STO substrate Bragg peak at selected time delays plotted vs. phonon wavevector Q . (b) Normalized change of x-ray intensity obtained from (a) for selected Q . The solid lines are fits according to eq. (4.12). The curves are displaced for clarity.

transient rocking curves of the first-order sideband measured at selected pump-probe time delays are plotted in Fig. 4.3(a). The topmost curve represents the maximum intensity of the phonon-induced sideband. We observe a complete decay of the coherent phonon spectrum within 1 ns. The plot shown in Fig. 4.3(b) alternatively presents the normalized change of x-ray intensity at selected phonon wavevectors across the sideband. After the generation of the phonon wavepacket sideband around time zero the transients exhibit an exponential decay with a decay constant depending on the phonon wavevector Q . Note, that the time-resolution of the transients is limited by the length of the probing x-ray pulses from the ESRF (≈ 100 ps). Hence, the data can be analyzed by a fitting function $F(t, Q)$ which is obtained by convoluting a Gaussian function $G(t)$ with an exponential decay function $I(t, Q)$ set to zero for $t < 0$, i.e.,

$$G(t) = \frac{2}{\sqrt{2\pi}\sigma^2} \exp\left(-\frac{t^2}{2\sigma^2}\right), \quad I(t, Q) = \Theta(t) \left[I_0(Q) \exp\left(-\frac{t}{\tau_{\text{int}}(Q)}\right) + I_\infty(Q) \right] \quad (4.9)$$

where σ is the width of the Gaussian¹¹ and $I_0(Q)$, $\tau_{\text{int}}(Q)$ and $I_\infty(Q)$ are the Q -dependent amplitude, decay time and the offset of the exponential decay, respectively. Here, $G(t)$ essentially represents the time-resolution of the experiment and $I(t, Q)$ models the transient x-ray intensity due to the photoexcited phonon spectrum. Of course, the phonons are not excited instantaneously as suggested by the Heaviside function $\Theta(t)$, however, due to the limited time-resolution the rise of the phonon sideband cannot be resolved and is thus effectively included in σ . The offset I_∞ is included since the substrate shoulder on which the sideband resides shifts to lower Bragg angles due to the heat conduction from the excited SRO layer into the STO substrate. The local x-ray intensity in the Q -range plotted in Fig. 4.3(a) after ≈ 1 ns is thus smaller as before the excitation. The analytical

¹¹The width σ is identical to the standard deviation of the Gaussian and is related to the full width at half maximum (FWHM) by $\text{FWHM} = 2\sqrt{2\ln 2}\sigma$. The fit parameter σ is chosen to be independent of Q since the x-ray pulse duration is fixed in the experiment.

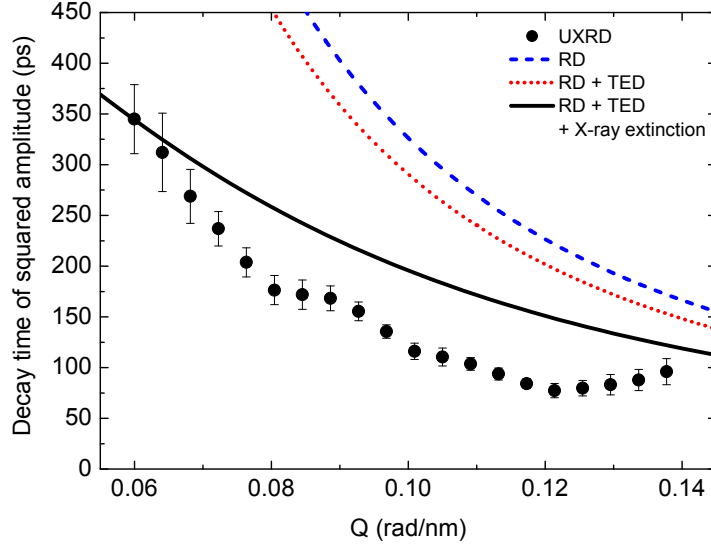


Figure 4.4: Decay times (symbols) from best fits of the phonon-induced intensity transients partly shown in Fig. 4.3(b). The error bars represent the 68% confidence intervals of the fitted parameter. The lines show the theoretical decay times which are obtained by Akhiezer’s relaxation damping (RD) (blue dashed line), RD and thermoelastic damping (TED) (red dotted line) and additionally including the 600 ps decay predicted by the harmonic LCDX calculation due to the finite x-ray extinction depth (black solid line). The different contributions are combined by summation of the corresponding decay rates Γ .

expression for $F(t, Q)$ then reads

$$F(t, Q) = (G * I)(t, Q) \quad (4.10)$$

$$= \int_{-\infty}^{\infty} G(\zeta) I(t - \zeta, Q) d\zeta \quad (4.11)$$

$$= I_0(Q) e^{\frac{\sigma^2}{2\tau_{\text{int}}(Q)^2}} \left[1 + \text{erf} \left(\frac{t}{\sqrt{2}\sigma} - \frac{\sigma}{\sqrt{2}\tau_{\text{int}}(Q)} \right) \right] e^{-\frac{t}{\tau_{\text{int}}(Q)}} + I_{\infty}(Q) \left[1 + \text{erf} \left(\frac{t}{\sqrt{2}\sigma} \right) \right] \quad (4.12)$$

where erf is the error function defined as

$$\text{erf}(x) = \frac{2}{\sqrt{\pi}} \int_0^x e^{-y^2} dy \quad (4.13)$$

The measured intensity transients shown in Fig. 4.3(b) can now be analyzed by means of (4.12) and the best fits are plotted as solid lines. The intensity decay times $\tau_{\text{int}}(Q)$ extracted from the best fits are shown as symbols in Fig. 4.4. Recall that if x-ray extinction is negligible (e.g. near the sample surface) the recorded phonon-induced x-ray intensity measures the squared phonon amplitude. As the phonon wavepacket travels deeper into the substrate the x-ray extinction yields an additional decay contribution. In total, the actual phonon amplitude thus has a decay time

$$\tau_{\text{ph}} = \Gamma_{\text{ph}}^{-1} = 2(\Gamma_{\text{int}} - \Gamma_{\text{ext}})^{-1} = 2 \left(\frac{1}{\tau_{\text{int}}} - \frac{1}{\tau_{\text{ext}}} \right)^{-1} \quad (4.14)$$

where $\tau_{\text{ext}} = \Gamma_{\text{ext}}^{-1} = 600$ ps. This formula converts the phonon amplitude decay time into the x-ray intensity decay time and vice versa. The experimental results of the Q -dependent

x-ray intensity decay times presented in Fig. 4.4 are compared to the theoretical predictions by Akhiezer’s RD τ_{RD} (blue dashed line) and additionally including TED τ_{TED} (red dotted line) as well as the decay predicted by the harmonic LCDX calculations due to the finite x-ray extinction depth τ_{ext} (black solid line). The different contributions are combined by summation of the corresponding decay rates Γ_i similar to (4.14). Although there is a rather good qualitative agreement of the Q -dependence, the experimental intensity decays faster than predicted by the theoretical models. The deviation from the combined models appears to be large where the x-ray intensity of the sideband just after generation $I_{\text{max}}(Q)$ is large (cf. Fig. 4.3(a)). As discussed in Section 4.4.1, a larger intensity $I_{\text{max}}(Q)$ implies a larger amplitude of the phonon with wavevector Q . Since the influence of lattice anharmonicity increases for larger phonon amplitudes Fig. 4.4 suggests that the deviations could indeed be due to higher order terms in the interatomic potentials.

In order to test this conjecture, I use the anharmonic LCM in combination with dynamical XRD calculations (aLCDX) to simulate the experimental results. For the simulations I assume the non-uniform pulse energy distribution within the pulse train which was suggested in Paper **VIII**. Similar to the explanations in Section 4.3, the strain amplitude of the photoexcited LSMO layer (and hence the phonon wavepacket in the substrate) employed in the simulation is calibrated by the measured shift of the corresponding Bragg peak (not shown). Using the nonlinear lattice potential deduced in Section 4.3 (see eq. (4.6)) I readily obtained quite satisfactory results roughly matching the experimental data. However, to further improve the agreement—especially the particular decay behaviour of the phonon sideband—I adjusted the damping coefficient γ and anharmonicity coefficient A to be about 90% of the values given in Section 4.3, respectively¹². This way the intensity decay of the sideband agrees with the theoretical predictions for low strain amplitudes (black line in Fig. 4.4) where explicit anharmonicity is negligible and merely the phenomenological damping coefficient γ causes the decay. Moreover, A was adjusted to give rise to the approx. 130 ps decay time of the transient sideband intensity integrated over $0.08 \text{ rad/nm} \leq Q \leq 0.14 \text{ rad/nm}$ which was revealed in Paper **VIII**. Figure 4.5(c) presents the change of integrated intensity obtained from the aLCDX calculations including the fit according to (4.12). A possible reason for the slight deviation from the values for γ and A obtained in Section 4.3 could be terms in the interatomic potential of yet higher order. Since the strain amplitude in the single BSP excited in the experiments described in Section 4.3 is much higher than in the individual BSPs investigated in the current section, terms of order higher than three have different contributions. This may therefore lead to different effective third-order potentials to which I restrict the considerations here.

The transient rocking curves of the first-order sideband obtained by the adjusted aLCDX calculations including the experimental angular and time-resolution are plotted in Fig. 4.5(a) for the same time delays as in Fig. 4.3(a). For computational reasons the presented calculations neglect the effect of heat conduction which would generate a slowly decaying component due to the shifting wings of the STO substrate peak. Given the complexity of the model we find very good agreement of the calculated and measured rocking curves in terms of position, width and shape as well as the timing of the decay. In principle, one could further improve the shape agreement of the rocking curves by tweaking the pump pulse energy distribution within the pulse train, however, for the sake of comparability with Paper **VIII** I keep the pump pulse energy distribution derived there. In order to quantify the intensity decay and thus yield a measure of the Q -dependent phonon lifetime I performed the same analysis presented for the experimental data, i.e., fitting the

¹²Precisely, I used $A = 1.59 \cdot 10^{13} \text{ kg}/(\text{m s}^2)$, $\gamma = 8.7 \cdot 10^{12} \text{ s}^{-1}$ and the same spring constant K .

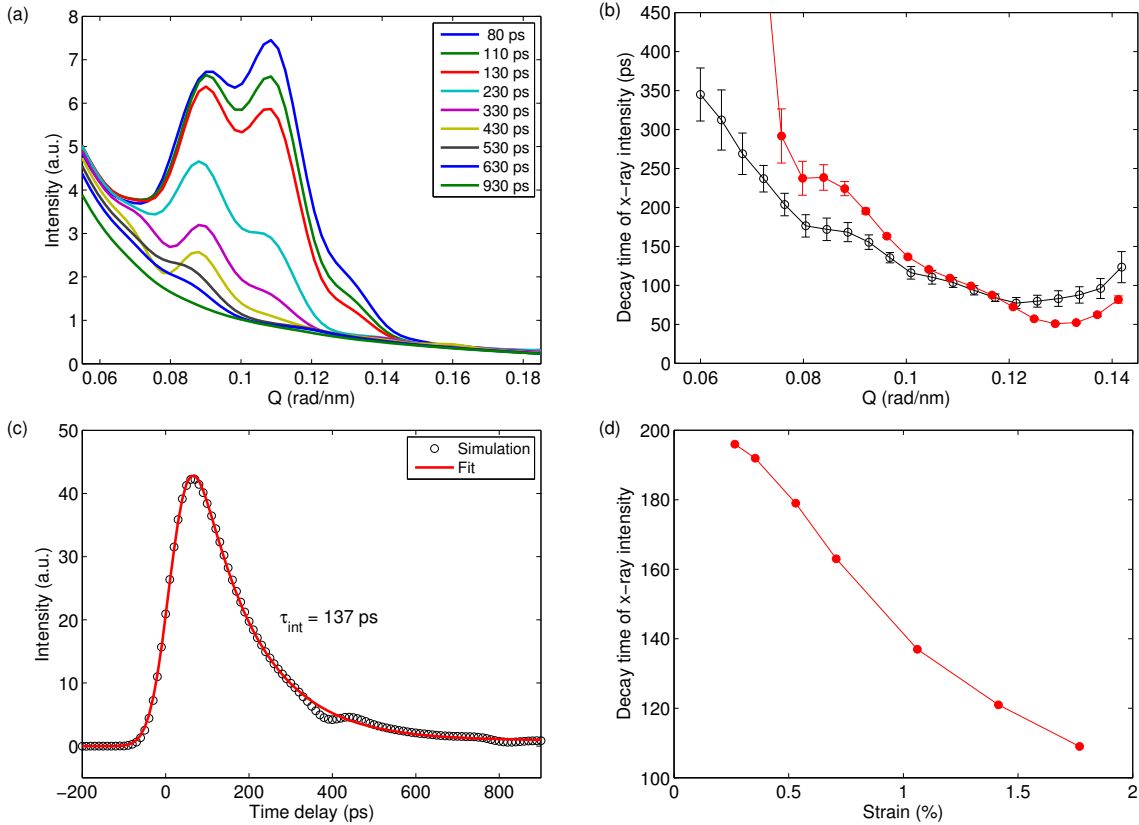


Figure 4.5: (a) Rocking curves of the first-order phonon sideband calculated by aLCDX for the same time delays as in Fig. 4.3. (b) Q -dependent intensity decay times derived from the aLCDX calculation (red bullets) and the experimental decay times (black circles). (c) Transient intensity of the phonon sideband integrated over $0.08 \text{ rad/nm} \leq Q \leq 0.14 \text{ rad/nm}$. (d) Strain-dependence of the decay time of the integrated intensity shown in panel (c) due to the lattice anharmonicity. The strain values represent the average strain of the SRO layer due to the pulse train excitation.

intensity transients for each Q by (4.12). The resulting decay constants $\tau_{\text{int}}(Q)$ are shown in Fig. 4.3(b) (red bullets) and exhibit a very satisfying agreement with the experimental values (black circles). The diverging deviation of the calculated and experimental values below $Q \approx 0.08 \text{ rad/nm}$ is due to the neglected heat conduction. As indicated above, the heat-induced shift of the STO substrate shoulder to lower Q results in a decreasing component of the intensity transient which has a timescale of several 100 ps as Section 3.2 revealed. The contribution of this slow background dynamics is largest for $Q \approx 0.08$ since there the shoulder intensity is high and the phonon amplitude is fairly low.

I mentioned earlier that the influence of the anharmonicity becomes increasingly important if the strain amplitude of the phonon wavepacket increases. We do not have fluence-dependent UXR measurements on the nonlinear propagation of quasi-monochromatic phonon wavepackets. However, this aspect can of course be easily checked in simulations. The decay time of the transient integrated intensity shown in Fig. 4.5(c) is calculated for different strain amplitudes of the coherent sound wave. The results are plotted in Fig. 4.5(d) versus the photoinduced thermal expansion of the SRO layer. As discussed in Section 2.1.3 the integrated strain of each of the BSPs generated by the individual pump pulses of the pulse train is proportional to the layer strain after the coherent strain pulses have left the layer. The aLCDX calculations indeed predict a drastic decrease of the decay time which thus implies a significantly shortened phonon lifetime. The decay time appears to converge to ≈ 200 ps towards zero strain which shows that the higher order term in

the interatomic potential U becomes negligible at low strain amplitudes¹³. Moreover, this matches the value given by the theoretical models (black line in Fig. 4.4).

In conclusion, after the successful generation and detection of narrow-bandwidth LA phonon wavepackets as presented in Paper **VIII** I analyzed the Q -dependence of the characteristic sideband intensity decay. In addition to the previously identified nonlinear propagation of sound in STO, the deviation from standard theoretical models for phonon lifetimes in the discussed frequency and temperature regimes suggests that the anharmonicity of the interatomic potentials have to be taken into account when considering the propagation of coherent phonons generated by strong laser-pulse excitation. The very good agreement obtained by calculations employing an anharmonic linear-chain and dynamical XRD verify this assumption and, in particular, reveal that the experimental data can be reproduced with high accuracy merely including a third-order term in the interatomic potential.

The following section presents complementary all-optical pump-probe measurements which evidence the fluence-dependence of the phonon lifetimes and thus support the conclusions drawn so far.

4.4.3 Anharmonic decay of coherent phonons – All-optical experiments

The important UXRD results discussed in the previous section and in Paper **VIII** where collected during 5 days of beamtime at the ID09B of the ESRF. Since time is usually rather limited during synchrotron beamtimes we did not measure the fluence or temperature-dependence of the anharmonic phonon decay which would give much more insight in the quantitative role of lattice anharmonicities. However, as mentioned above one can also employ all-optical pump-probe techniques to obtain information of similar kind.

The Brillouin scattering condition (4.2) implies that the wavevector of visible light is not large enough to probe the fundamental wavevector of the phonon wavepackets generated in the UXRD experiments ($Q_p \approx 0.11$ rad/nm). The phonon wavevectors that are accessible by photons in the visible range (400 . . . 800 nm) in a backscattering geometry ($\beta = 0$) are a factor of 2 smaller than Q_p [136]. However, the fundamental wavevector of the photoexcited phonon wavepacket can be tuned by the pulse repetition rate ν_p within the pump pulse train as discussed in Section 4.4.1. One has to bear in mind that this may change the particular phonon dynamics (such as decay rate) since these are in general Q -dependent (see Section 4.4.2). As also discussed in Section 4.4.1, an optimized phonon spectrum is obtained by matching the metal layer thickness to a given pump pulse separation $\tau_p = 1/\nu_p$. For this reason, we used a 36 nm LSMO layer as the transducer in the following all-optical experiments.

Prior to the experiment the pump pulse train is characterized by second-order optical cross-correlation using a nonlinear β -Barium Borate (BBO) crystal [65]. If one pulse of the pulse train and a single reference pulse—both with sufficiently high intensity—are temporally overlapped in the BBO crystal the second harmonic of the fundamental laser wavelength (800 nm) is generated by sum-frequency generation. The resulting transient intensity of the second harmonic is shown as a thin black line in Fig. 4.6(a). The extracted mean pulse separation is $\tau_p = 15.5$ ps which corresponds to a pulse repetition rate $\nu_p = 65$ GHz and an estimated phonon wavevector in STO of $Q_p = 0.051$ rad/nm.

¹³At very low strain amplitudes the presented fitting procedure of the integrated x-ray intensity becomes less meaningful due to the very low intensity of the phonon sideband in combination with the considered angular and time-resolution of the actual experiment.

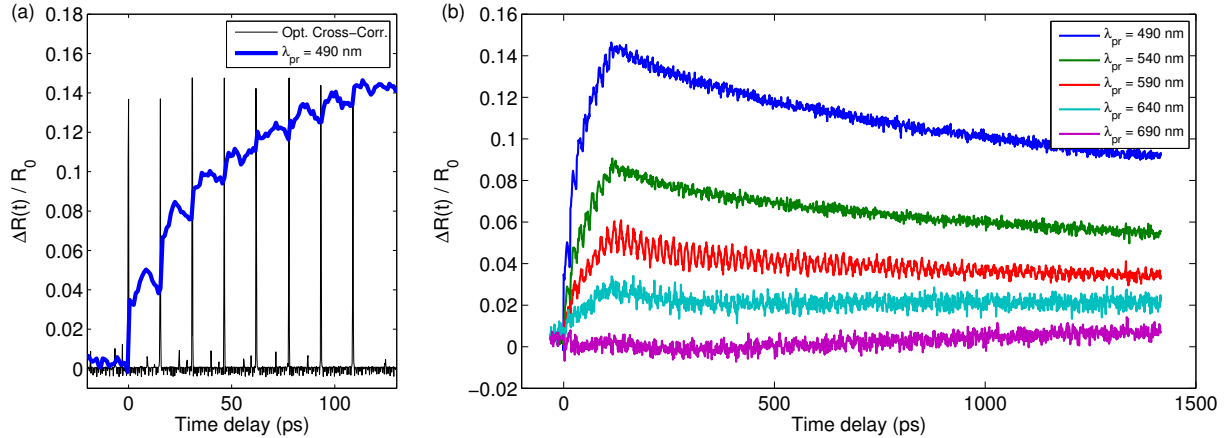


Figure 4.6: (a) Second-order optical cross-correlation (black thin line) of the pump pulse train and a single pulse both at 800 nm wavelength. The mean pulse separation is $\tau_p = 15.5 \pm 0.2$ ps. The small peaks are due to reflections inside the nonlinear BBO crystal. Note, that the pulse intensities are not necessarily proportional to the real pulse energies due to possible mismatches of the individual spatial overlaps. The equidistant quasi-instantaneous reflectivity rises at a probe wavelength of 490 nm (also shown in panel (b)) due to the heating of the electronic system in LSMO by the individual pump pulses verify the timing of the pump pulse train. (b) Raw transient differential optical reflectivity of 36 nm LSMO on STO at selected probe wavelengths measured at quasi-normal incidence after excitation with a pump pulse train having an integral fluence of 55 mJ/cm².

Figure 4.6(b) presents the relative change in reflectivity $\Delta R(t)/R_0$ of a 36 nm thick LSMO layer on STO for selected probe wavelengths after excitation with the pulse train (first pulse at $t = 0$). Clearly, the particular dynamics of the transient reflectivity strongly depend on the probe wavelength λ_{pr} . As discussed in Section 2.1.1, each of the pump pulses impulsively heats the conduction band electrons and subsequently the lattice of the metallic LSMO layer. This process gives rise to the equidistant quasi-instantaneous rises of the reflectivity at $\lambda_{pr} = 490$ nm as shown in Fig. 4.6(a) which verifies the time separation τ_p of the pump pulses. Static measurements on LSMO reveal a pronounced increase of the optical conductivity (and thus reflectivity [41]) with temperature for $\lambda_{pr} \lesssim 600$ nm which is related to the ferromagnetic phase transition of LSMO around $T_c = 360$ K [158]. The strongly increased reflectivity towards the blue end of the visible spectrum is verified by the pump-probe data in Fig. 4.6(b). The heat diffusion from LSMO into the STO substrate slowly recovers the initial reflectivity on a nanosecond to microsecond timescale.

The crucial features of the optical reflectivity transients, however, are the pronounced oscillations in an intermediate wavelength range. In order to investigate the oscillations in more detail, the slowly varying incoherent background is subtracted and the remaining signal is shown in the surface plot in Fig. 4.7 (right panel). The excitation of the LSMO layer by the pulse train and hence the generation of the quasi-monochromatic phonon wavepacket in the STO substrate take place for $0 < t < 120$ ps. As explained in Section 4.1, the strong oscillations for $t > 120$ ps evidence the propagation of the coherent wavepacket into deeper parts of the STO substrate. The wavelength-dependent amplitude of the oscillations¹⁴ is shown in the left panel of Fig. 4.7. The scattering condition (4.2) uniquely relates the probe wavelength to the phonon wavevector that this wavelength is sensitive to. In addition, the well-accepted formalism of Thomsen *et al.* [40] reveals that the oscillation

¹⁴The amplitude spectrum is obtained by calculating the modulus of the Fast Fourier Transform (FFT) of the reflectivity transients for each probe wavelength and averaging across the peak corresponding to the oscillation.

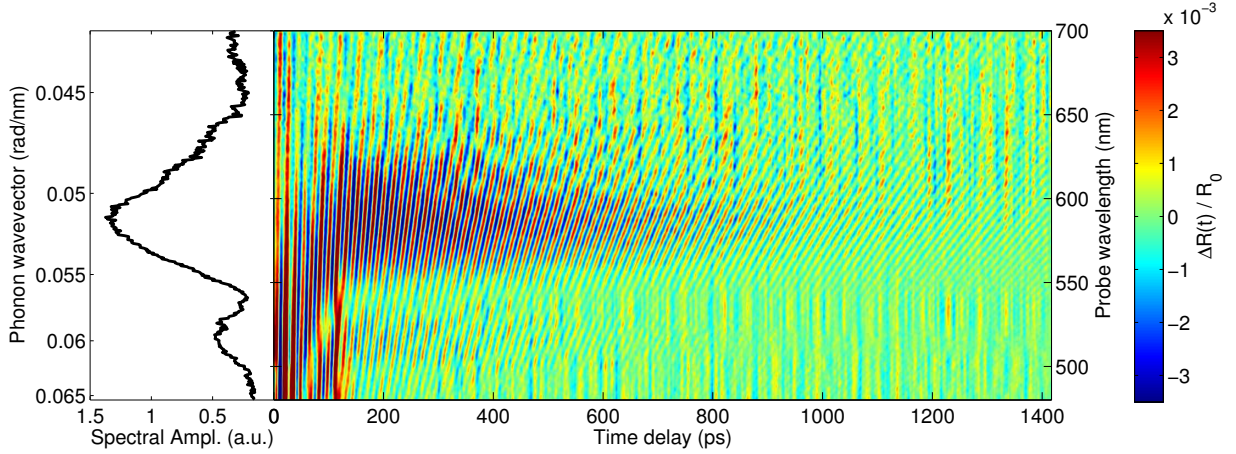


Figure 4.7: Right panel: Transient reflectivity signal vs. probe wavelength after subtraction of the slow dynamics from the transients shown in Fig. 4.6(b). The data surface plot has been slightly smoothed along both directions to show the oscillations clearer. The slanted structures due to the wavelength-dependent oscillation frequency evidence the propagating phonon wavepacket inside the STO substrate. The upright structures ($t > 200$ ps) are due to measurement noise. Left panel: Phonon amplitude spectrum deduced from the probe wavelength-dependent oscillation amplitudes.

amplitude of the reflectivity is proportional to the phonon amplitude. Thus, the left panel of Fig. 4.7 directly visualizes the photoexcited phonon (amplitude) spectrum which evidences a narrow bandwidth of the phonon wavepacket¹⁵. Moreover, even the first-order side maxima predicted by the LCM (cf. Fig. 4.2(c)) are clearly observed.

In analogy to the UXR D experiments where we monitored the intensity decay of the sideband representing the attenuation of the squared amplitude of the phonon wavepacket, one can now investigate the transient oscillation amplitudes in Fig. 4.7 to obtain information on the dynamics of the wavepacket. Note, however, that the oscillation amplitude in the optical experiments is directly proportional to the phonon amplitude [40]. One way to extract the decay time of the oscillation amplitude for each $Q(\lambda_{\text{pr}})$ is to divide the time range of the reflectivity transients into N_{win} equal parts and compute the Fast Fourier Transform (FFT) of each window. The oscillation amplitude obtained from the FFT for each $Q(\lambda_{\text{pr}})$ and each of the N_{win} time windows is then fitted with an exponential decay function to determine the decay time constant of the phonon oscillation $\tau_{\text{osc}}(\lambda_{\text{pr}})$. As an example, Figure 4.8(a) shows the extracted transient oscillation amplitude (black bullets) for the reflectivity transient at $\lambda_{\text{pr}} = 590$ nm after excitation with an integrated fluence of 55 mJ/cm^2 (red line in Fig. 4.6(b)). The red solid line in Fig. 4.8(a) represents the best exponential fit which yields a decay time constant of ≈ 810 ps. Since the first FFT window covers the time range where the pump pulse train is still generating the phonon amplitude we omit this data point in the fitting process.

After performing the analysis for all measured fluences and probe wavelengths λ_{pr} I determine a representative decay time of the phonon wavepacket by averaging the derived values $\tau_{\text{osc}}(\lambda_{\text{pr}})$ around the maximum of the phonon spectrum, i.e., from 570 nm to 600 nm. The dependence of this average phonon lifetime on integrated pump fluence is plotted in Fig. 4.8(b). The all-optical data exhibit a decreasing lifetime of the phonon wavepacket around the fundamental wavevector for increasing pump fluence and accordingly increasing

¹⁵Due to an improved multi-reflection mirror which produces the pump pulse train (cf. Paper VIII) the relative bandwidth of the phonon wavepacket in the optical experiments is much smaller than the one observed in the UXR D experiments discussed in Section 4.4.2 and Paper VIII.

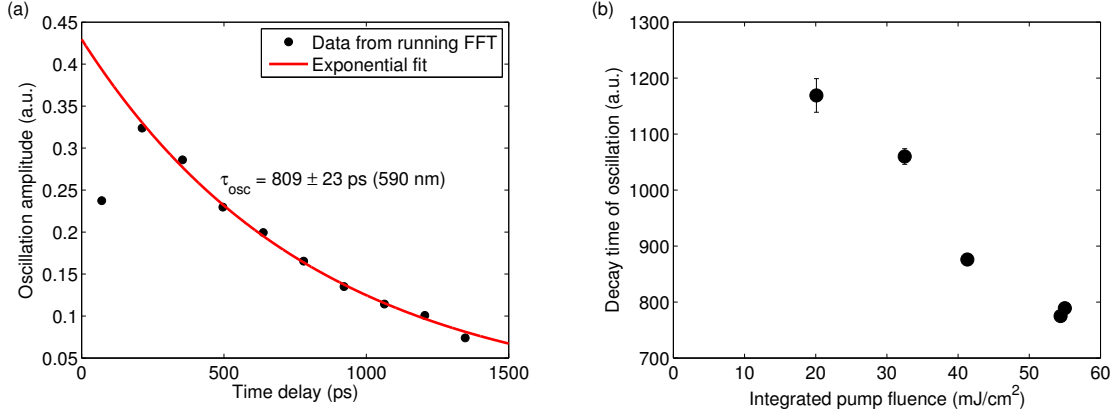


Figure 4.8: (a) Decay of the optical oscillation amplitude (black bullets) determined by a moving FFT from the reflectivity transient at $\lambda_{\text{pr}} = 590$ nm. The red solid line represents the best exponential fit revealing a phonon amplitude lifetime of ≈ 810 ps. (b) Lifetime of the phonon amplitude versus integrated pump fluence.

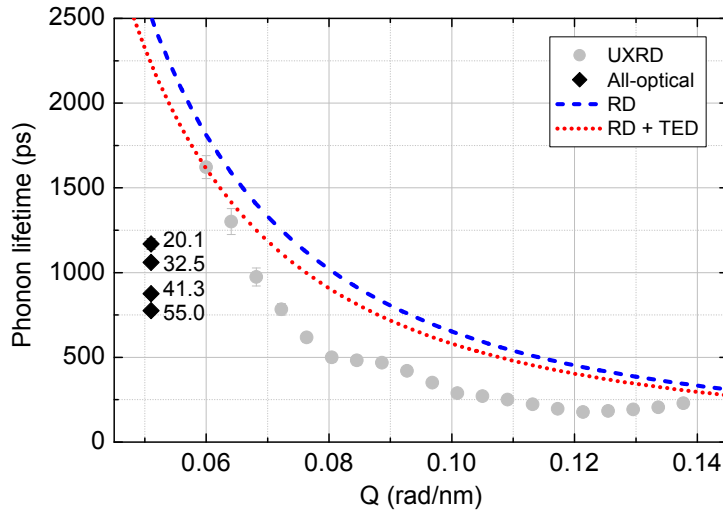


Figure 4.9: Comparison of the phonon amplitude lifetimes obtained from UXR and all-optical experiments with the theoretical models described in Section 4.4.2.

strain amplitudes. This result qualitatively follows the prediction by the aLCDX calculations presented in Fig. 4.5(d) which gives additional support of the important role of lattice anharmonicities in the conducted experiments.

Figure 4.9 compares the phonon lifetimes derived from the all-optical experiments to the ones obtained from the previously discussed UXR experiments. Note that, in contrast to Section 4.4.2 where I discussed and plotted the x-ray intensity decay time, Fig. 4.9 presents the actual phonon lifetime, i.e., the exponential decay constant of the phonon amplitude. As pointed out in Section 4.4.2 the x-ray intensity decay time and the phonon amplitude decay time are related by eq. (4.14) whereas the decay time of the optical reflectivity oscillations directly yields the phonon lifetime. Although the number of data points in Fig. 4.8(b) is little a qualitative comparison to Fig. 4.5(d) suggests a low-fluence lifetime of ≈ 1300 ps at the photogenerated central phonon wavevector $Q_p = 0.051$ rad/nm. In contrast, the theoretical estimation by combining RD and TED (eqs. (4.7) and (4.8)) at this phonon wavevector yield a much larger value of $\tau_{\text{ph}} \approx 2250$ ps as depicted in Fig. 4.9 by the red dotted line. Interestingly, the phonon-induced reflectivity oscillations from a single

BSP analyzed in Paper **VII** exhibit a similar decay time of ≈ 1200 ps at low pump fluence. A cross-check with the anharmonic LCM using the parameters calibrated to reproduce the UXRD phonon sideband decay discussed in Section 4.4.2 yields the very same theoretical phonon decay of ≈ 2250 ps at $Q_p = 0.051$ rad/nm. This suggests that there may be a probe-related artificial decay in our optical reflectivity data similar to the x-ray extinction in UXRD experiments. In optical reflectivity experiments this could be caused by a limited coherence length of the ultrashort pulses reflected at the sample surface and the phonon wavepacket leading to a faster decay of the interference effect that gives rise to the oscillations in the experimental signals. Further investigations are thus required to conclusively elucidate the mechanism of the additional real or artificial phonon decay observed in the presented all-optical pump-probe experiments. Nevertheless, the data clearly support the conclusions drawn from the time-resolved optical and x-ray experiments on STO discussed in Sections 4.3 and 4.4, respectively: the propagation of coherent phonons in STO launched by the impulsive heating of metallic thin film transducers is no longer well-described by a harmonic LCM (or continuum model) if the strain amplitude exceeds 0.1% which in case of SRO or LSMO transducers is equivalent to a pump fluence $F \gg 1$ mJ/cm².

THE PHONON BRAGG SWITCH

The experimental method which is extensively used in this work to obtain information about the ultrafast dynamics of photoexcited solid is the pump-probe technique [15, 16]. The time-resolution of this method crucially depends on the pulse durations of the pump and probe pulses (see Section 1.1). Nowadays, laser systems providing intense sub-100-fs laser pulses are widely available. Generating ultrashort x-ray pulses, however, usually requires much more engineering and financial efforts. Established techniques are laser-based plasma x-ray sources (PXS) (see Paper **XI** and references therein), low-alpha modes and femto-slicing of electron bunches at synchrotrons [159–162] and (x-ray) free-electron lasers (FEL) [163, 164]. The rather limited capacities of all sources worldwide and other disadvantages such as short/long-term stability (PXS, FEL) or low flux (PXS, femto-slicing) on one hand call for improvements and extensions of these existing techniques and sources and on the other hand suggest the need for alternative techniques.

In the following, I summarize an alternative concept of ultrashort x-ray pulse generation which exploits the structural dynamics of photoexcited solids and the concomitant modulation of the solid’s x-ray response. I then discuss particular approaches which utilize the photoexcited structural dynamics of thin films and SLs previously considered in this thesis.

The concept for the generation of ultrashort x-ray pulses by means of a so-called Phonon Bragg Switch (PBS) was proposed by Bucksbaum and co-workers in 1999 [38]. The authors suggested to photoexcite coherent optical phonons with non-vanishing wavevector Q in a bulk material by ISRS. As discussed in Section 4.1, this would give rise to transient sidebands of the bulk Bragg reflection whose intensity would oscillate at the frequency of the optical phonon. In principle, this realizes an increased x-ray diffraction efficiency within one oscillation period of the optical phonon which is usually on the order of $10 \dots 1000$ fs. Due to the possibility of coherently controlling the optical phonon mode one could switch off the phonon oscillation with a second properly delayed laser pulse and thereby effectively realize a single ultrashort x-ray gate. If one shines long x-ray pulses (or even cw x-rays) on the crystal fulfilling the Bragg condition of the transient sideband the photoexcited bulk crystal would essentially reflect only a single sub-ps x-ray pulse. This ultrashort pulse of hard x-rays could then be exploited as a probe pulse for UXRD experiments with high time-resolution. In analogy to the technique of femto-slicing of electron bunches in a few storage rings around the world one could also consider this x-ray gating as femto-x-ray slicing. The main difference is that one directly slices a small portion of x-rays out of a long x-ray pulse without disturbing the electron bunches inside the storage ring. Similar to the slicing of electron bunches the laser and sliced x-ray pulse are inherently synchronized.

A few years later, however, the authors estimated that for a GaAs crystal the efficiency of this technique is unlikely to provide a sufficiently high switching contrast since the required phonon amplitudes would be too large [39].

Throughout this chapter we adapt the basic idea of modulating the x-ray diffraction efficiency of a PBS by photoinduced structural dynamics. A primary x-ray pulse with rather long pulse duration (e.g. as generated by synchrotron sources) is then modified by the PBS's transient x-ray response to form a potentially ultrashort secondary x-ray pulse which may then serve as a probe pulse in subsequent UXR experiments. Mathematically, one can formulate the process in the following way. The first laser pump pulse $L_1(t)$ with fluence F_1 gives rise to a time-dependent x-ray diffraction efficiency (x-ray response) $R_1(t, \Theta_1, F_1)$ which generally depends on the chosen Bragg angle Θ_1 and the pump fluence F_1 ¹. Given a certain time delay τ_1 between $L_1(t)$ and the primary x-ray pulse $X_1(t)$, the secondary x-ray pulse diffracted from the PBS is given by

$$X_2(t, \Theta_1, F_1) = R_1(t + \tau_1, \Theta_1, F_1)X_1(t) \quad (5.1)$$

Here, $\tau_1 = 0$ is defined to be the time delay at which the center-of-masses of L_1 and X_1 arrive at the PBS simultaneously and $\tau_1 > 0$ implies that the laser hits the PBS before the x-ray pulse. Equation (5.1) directly implies that the shape of the secondary x-ray pulse X_2 can be controlled by varying Θ_1 and F_1 . The schematic setup for the described diffraction process is depicted in Fig. 5.1(a)-(b). The secondary x-ray pulse X_2 can then be guided to the sample of interest to probe the unknown x-ray response $R_2(t, \Theta_2, F_2)$ at various time delays τ_2 after the excitation of the sample by a second laser pump pulse L_2 . Using a slow (integrating) detector, the measured signal $S(\tau_2, \Theta_1, F_1, \Theta_2, F_2)$ of this latter UXR experiment is then given by a convolution of X_2 with R_2 , i.e.,

$$S(\tau_2, \Theta_1, F_1, \Theta_2, F_2) = \int_{-\infty}^{\infty} R_2(t + \tau_2, \Theta_2, F_2)X_2(t, \Theta_1, F_1) dt \quad (5.2)$$

If one has an independent measure of $X_2(t)$ the unknown sample response $R_2(t)$ can be extracted from the measured signal $S(\tau_2, \Theta_1, F_1, \Theta_2, F_2)$ by a simple deconvolution. Although this inverse transformation is mathematically always feasible, limited signal-to-noise ratios in real experiments do not allow to obtain R_2 with an arbitrary probe function X_2 . In order to retrieve information on the sample dynamics with high time-resolution it is mandatory to have a probe pulse X_2 that is shorter than the characteristic timescales contained in the sample response R_2 . Ideally, X_2 is a single Gaussian with a sufficiently short temporal width. Accordingly, one has to choose an appropriate response R_1 of the PBS to generate an such optimized x-ray probe pulse X_2 .

An important part of my work was to find and optimize a PBS response R_1 in order to realize optical-pump x-ray-probe measurements at regular synchrotron beamlines with sub-ps time-resolution. Achieving this goal would vastly increase the number of potentially available sources of sub-ps x-rays which would circumvent the restriction to expensive and rare setups such as femto-slicing, FELs or PXSs. Of course, these established sources partly have other indispensable advantages, e.g., sub-100-fs pulse duration or table-top setups (PXS).

The following sections describe the different sample geometries and related dynamics which we used to considerably decrease the pulse durations of synchrotron x-ray pulses.

¹In general, R_1 is constant before the laser pulse excitation and shows an arbitrary behaviour after the excitation.

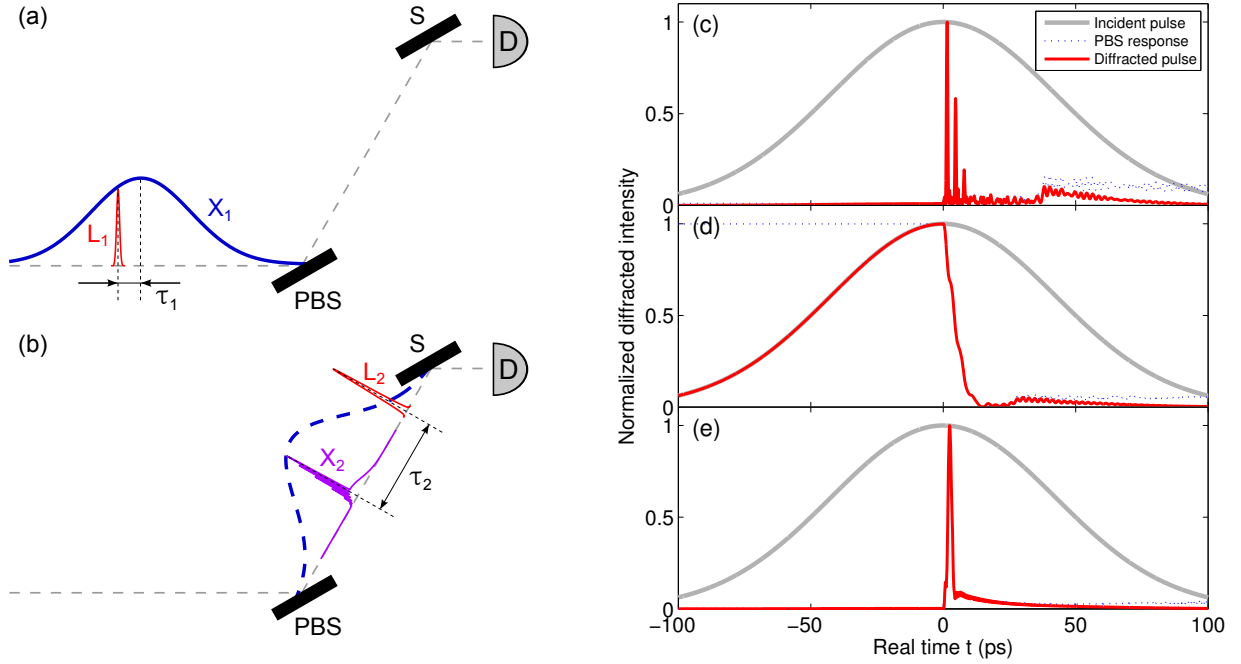


Figure 5.1: Left panel: Schematic of the experimental setup to implement a Phonon Bragg Switch (PBS) for UXRD experiments using a double-crystal XRD layout. The x-ray pulse originating from the synchrotron and the laser pump pulse enter the figure from the left propagating along the dashed grey line towards the integrating x-ray detector D. (a) The laser pump pulse L_1 and the x-ray probe pulse X_1 arrive at the PBS with a respective time delay τ_1 . (b) The x-ray response of the PBS R_1 has modified the initial x-ray pulse shape into X_2 according to eq. (5.1). The secondary x-ray pulse X_2 subsequently probes the structural dynamics of an unknown sample S at varying time delays τ_2 with respect to the second laser pump pulse L_2 . The signal measured at the detector D is given by eq. (5.2). Right panel: LCDX calculations (including heat diffusion) of the x-ray pulse shapes diffracted from different PBS devices exploiting the transient XRD efficiency of (c) the forbidden SL peak of the SRO/STO SL (Papers **II-IV**), (d) the SRO layer peak shifting away from its initial position (Section 2.2.2) and (e) the 50% increased coherent strain maximum of a thinner SRO layer (see e.g. Section 3.2). For further descriptions of the individual devices see Sections 5.1 and 5.2. In all three cases the first time delay is set to $\tau_1 = 0$.

Several experiments are presented which evidence the successful shortening of x-ray pulses and the subsequent utilization of these in UXRD experiments. The technical potential of this work also gave rise to a long-term project at the EDR beamline of the synchrotron source BESSY II in Berlin Adlershof which is in parts dedicated to the implementation and optimization of an experimental setup exploiting the discussed concepts of x-ray pulse shortening for ultrafast x-ray science.

5.1 X-ray pulse shaping by forbidden SL reflections

In Section 2.2.3 as well as in Papers **II** and **III** I theoretically and experimentally considered the intensity modulations of the SL Bragg reflections from a metal-insulator SL due to the photoexcited structural dynamics. In addition to the very accurate LCDX calculations, I also presented a simple envelope model (EM) which is able to semi-quantitatively explain the measured signals on different SL reflections. In particular, I discussed the highly nonlinear response of a SRO/STO SL peak which is nearly forbidden in the unexcited state and attains strongly increased diffraction efficiency in a threshold-like manner after excitation with an ultrashort laser pulse. The nature of this behaviour which we

measured in great detail at the Swiss Light Source (Fig. 3(b) in Paper **II** and Fig. 2 in Paper **III**) could be uniquely identified in Paper **II** by the help of the EM. For the unexcited SL, the considered SL peak has a position very close to the minima of both individual single-layer envelope functions which results in the very weak static diffraction efficiency. As explained in Section 2.1.4 the laser excitation triggers the SL phonon mode which essentially compresses and expands the metal and insulator layers, respectively. This shifts the respective single-layer envelopes and thus strongly increases the diffraction efficiency of the quasi-forbidden SL peak. The modulation of the SL peak intensity is in analogy to the intensity modulations of the optical phonon sidebands described by Bucksbaum *et al.* and Sheppard *et al.* who initially proposed the concept of a PBS [38, 39]. An optical phonon near the Brillouin-zone center modulates the x-ray structure factor of the lattice unit cell and similarly the SL phonon mode which also lies at the Brillouin-zone center in a backfolded scheme modulates the x-ray structure factor of the superlattice unit cell (bilayer).

The fact that this particular SL peak is statically nearly forbidden in combination with the strong nonlinear increase of the reflected x-ray intensity with phonon amplitude immediately gave rise to the potential use of this response as a PBS. Following the idea presented above, the SL-PBS could be illuminated by a long synchrotron pulse and simultaneously excited by an ultrashort laser pulse. Since the SL peak is nearly forbidden before and after the coherent dynamics and the x-ray flux of the long x-ray pulse is quasi-constant during this time, eq. (5.1) implies that the reflected x-rays will be shaped into a few isolated pulses of ≈ 1 ps duration as indicated by Fig. 2 in Paper **III**. To verify this behaviour the LCDX predictions² of the particular x-ray response are presented in Fig. 5.1(c). Here, I assume an incident x-ray pulse X_1 of gaussian shape centered at $t = 0$ with a FWHM of 100 ps (solid grey line) which is typical for standard synchrotrons. The laser pump pulse excites the SL dynamics at $t = 0$ (i.e. at time delay $\tau_1 = 0$) and thus triggers the transient x-ray response R_1 of the PBS (dotted blue line). In the present case of a forbidden SL peak, the diffracted x-ray pulse X_2 (solid red line) determined by eq. (5.1) indeed exhibits separated pulses in form of a pulse train and has almost no preceding or subsequent intensity. However, there is a weak and rather long post-pulse around $t = 50$ ps. A closer analysis of this contribution shows that these diffracted x-rays are due to the unfolding of the SL phonon mode into the substrate (Paper **I** and Ref. 84). This produces a propagating phonon wavepacket which exhibits a characteristic phonon spectrum defined by the SL geometry and which gives rise to corresponding sidebands of the substrate Bragg peak similar to the discussions in Section 4.4.

As shown in Paper **III**, the advantage of using SLs as a PBS is the tunability of pulse duration, pulse repetition rate and switching contrast by variation of the SL geometry. By properly tailoring the SL one can also avoid the weak post-pulse around $t = 50$ ps in Fig. 5.1(c). The disadvantage is that the SL mode automatically generates the pulse train, however, usually one would like to have a single ultrashort pulse in order to avoid the deconvolution process which may become impossible due to the inevitable experimental fluctuations. In principle, one might think about coherent control of the photoexcited SL phonons, however, this task is not as straightforward as for the ISRS-excited optical phonons. Due to the displacive excitation it is not possible to cancel the first excitation by a second pump pulse. Alternatively, one could combine appropriate responses of different

²The LCDX calculations include the heat diffusion inside the SL since Section 3.3 revealed that this process cannot be neglected for such thin SLs if one considers the intensity of the SL reflections. Fortunately, the equilibration of heat leads to a faster decay of the SL oscillations in the UXRD signal which is preferable for the function of a SL-PBS.

SLs to eventually select only a single pulse but due to the rather weak diffraction efficiency of each reflection the flux of the resulting x-ray pulse would probably be too low to use it in real experiments.

In order to overcome the disadvantages of the SL-PBS, we also looked at different approaches using thin films instead of SLs.

5.2 X-ray pulse shaping by photoexcited thin films

In addition to the previously discussed manipulation of hard x-rays by photoexcited SLs, we tried different approaches to improve the efficiency and the diffracted pulse shape of the PBS. A simpler geometry which was also extensively discussed in previous chapters of this thesis is a thin film on a substrate. In Sections 2.1.3 and 2.2.2 I presented the laser-induced structural dynamics of metallic thin films and their manifestation in particular UXR features, respectively. First of all, the impulsive heating of the metal layer leads to a thermal expansion which results in a change of the Bragg angle in XRD. Second, I theoretically and experimentally verified that the coherent dynamics of the thin film lead to a splitting of the Bragg peak and, moreover, to a 50% increased coherent strain maximum. In the following, I discuss how both UXR signatures can be exploited to modify the shape of hard x-ray pulses.

5.2.1 Truncation of x-rays by impulsive thermal expansion

As indicated above, the thermal expansion of the metal film results in a change in the Bragg condition for the x-rays. In particular, for sufficiently high pump fluence the diffracted x-ray intensity at the original layer peak position decreases and remains low as depicted in Figs. 2.5 and 2.6. Fixing the experimental Bragg angle to the initial position of the layer peak, a properly delayed long x-ray pulse would thus be truncated by a sufficiently fast decay of the diffracted x-ray intensity. Of course, the latter can be tuned due to its proportionality to the layer thickness, albeit at the cost of maximum diffraction intensity and hence switching efficiency. In any case, the fluence has to be high enough to induce a thermal Bragg peak shift which is larger than the width of the peak. Only under such circumstances one obtains a good switching contrast.

As an example, consider the UXR response of the SRO thin film which has been extensively discussed in Section 2.2.2. Since the LCDX calculations exhibit almost perfect agreement with the experimental PXS data, I use the simulation with an adapted instrumental function for typical synchrotron beamline experiments in order to calculate the shape of the diffracted synchrotron x-ray pulse. Assuming the same 100 ps x-ray pulse as before incident at the Bragg angle of the undisturbed SRO layer Bragg peak, the diffracted x-ray pulse shape is shown in Fig. 5.1(d). Indeed, the synchrotron pulse gets truncated and thus shortened by the reflectivity drop of the thin-film PBS at the fixed initial Bragg angle³. By changing the relative timing τ_1 of the x-ray pulse and pump laser one can vary the pulse duration of the diffracted x-ray pulse. This shortened pulse can then be exploited to perform UXR experiments with improved time-resolution as compared to the unmodified synchrotron pulse.

³The very little contribution after ≈ 25 ps is due to the return of the high-angle wing of the layer Bragg peak to the initial Bragg angle. This can be circumvented by applying a slightly higher pump fluence which would cause the peak shift to be larger and would thus avoid the revival of the diffraction efficiency within the incident x-ray pulse duration.

In Paper **IX** we report on the successful implementation of the above concept in a real UXR experiment conducted at the ID09B beamline at the synchrotron source ESRF in Grenoble, France. In this paper we present the feasibility of the proposed experimental setup and, moreover, prove the shortening of the ESRF x-ray pulse by truncating it with the described thin-film dynamics. In fact, in the described experiment we exploited the transient change of XRD efficiency from a LSMO/STO SL peak, however, as discussed in Section 2.2.3, the slow-timescale UXR features of SLs are essentially identical to those of a thin film (change of Bragg angle by impulsive thermal expansion via splitting of the Bragg peak). Since we chose a time delay $\tau_1 \approx 0$, i.e. the center-of-mass of the laser and x-ray pulses arrive simultaneously at the PBS, the ESRF pulse duration is effectively reduced by a factor of 2.

5.2.2 Slicing of x-rays by coherent thin-film dynamics

In the previous section I explained how a long synchrotron x-ray pulse can be shortened by truncation due to a drop in the XRD efficiency of an impulsively expanding thin film (and/or SL). This drop is due to the fact that the Bragg condition is no longer fulfilled at the initial Bragg angle Θ_i for the expanded layer. Instead, the Bragg peak has shifted to a lower angle $\Theta_f < \Theta_i$ which is determined by the stationary thermal expansion. Furthermore, the analysis in Section 2.2.2 revealed that the thin-film Bragg peak temporarily even shifts to much lower angles compared to the “final” Bragg angle Θ_f of the thermally expanded layer (50% increased coherent strain maximum). This implies that in a certain angular range $\Theta < \Theta_f$ the diffraction efficiency of the thin-film is significantly increased only within a short time window which is on the order of T_{sound} .

Since the SRO thin film considered in Section 2.2.2 does not have the appropriate dimensions ($d_{\text{SRO}} = 94.8$ nm) to function as an efficient thin-film PBS, Fig. 5.1(e) shows the switching effect from a much thinner SRO thin film ($d_{\text{SRO}} = 15.4$ nm) which was already introduced in Chapter 3 and Section 4.4. The LCDX calculation shows that fixing the Bragg angle at an appropriate value $\Theta < \Theta_f$ and inducing the right strain amplitude in the SRO layer indeed gives rise to the diffraction of a single short pulse from the thin-film PBS. The fact that the considered SRO layer is rather thin results in very short-lived coherent dynamics within this layer⁴ which thus yields a very short x-ray pulse of ≈ 1.5 ps. The drawback of a thin film is of course that the maximum diffraction efficiency (and hence the switching contrast) is limited. The choice of the particular design of a PBS thus depends on the requirements of the subsequent UXR experiments in terms of switching contrast and/or time-resolution.

During a follow-up beamtime at the ESRF we revisited the above experiment (Fig. 5.1(a) and (b)) using the thinner SRO film ($d_{\text{SRO}} = 15.4$ nm) as the PBS. Although the on and off contrasts of the switching could not be completely optimized during the time-limited beamtime, we were able to demonstrate the much higher time-resolution of the concept of slicing synchrotron x-ray pulses by exploiting the coherent structural dynamics of thin films. The details of the experiment and the obtained results are discussed in Paper **X**.

⁴The trailing and slowly decaying intensity is again due to the low-angle wing of the layer peak which remains at the set Bragg angle. However, it actively decays within the x-ray pulse duration due to the heat diffusion from the thin SRO layer into the substrate. As this process is accelerated in very thin films (cf. Table 3.1) the LCDX calculation shown in Fig. 5.1(e) includes the effect of heat diffusion.

In conclusion, the most promising approach so far is the concept of x-ray-slicing by exploiting the coherent lattice dynamics of a substrate-supported thin metal film. Estimations show that such a thin-film PBS may be optimized to realize switching contrasts and diffraction efficiencies similar to the rather complex and elaborate techniques of electron-bunch femto-slicing and plasma x-ray sources (PXS). As opposed to these techniques, the PBS may be operated not only at kHz repetition rates but even up to MHz rates which approaches the x-ray repetition rates at synchrotrons and would thus drastically increase the x-ray flux available for UXRD experiments. The proposed concept, however, is not capable of efficiently generating x-ray pulses with pulse durations on the order of 100 fs. Nevertheless, a variety of physical, chemical and biological research areas could profit from a 1-ps time-resolution [14] which can in principle be available at any beamline being equipped with a standard ultrafast laser system and our proposed concept of a thin-film PBS. In analogy to the discussion in Paper **XII**, ultrashort x-ray pulses such as generated by the thin-film PBS may be utilized in order to characterize ultrafast streak cameras operating in the hard x-ray regime.

SUMMARY AND OUTLOOK

This thesis presents various theoretical and experimental advances in the research field of ultrafast structural dynamics in solids. In particular, the lattice dynamics of nanolayered heterostructures such as substrate-supported thin films and superlattices (SLs) after the absorption of intense and ultrashort laser pulses are considered. At the core of the theoretical treatments lies the development and improvement of a numerical linear-chain model (LCM) in order to describe and understand the photoinduced coherent and incoherent lattice dynamics. The key ingredients to the LCM are

- instantaneous generation of thermal stress with arbitrary spatial profile
→ coherent lattice dynamics = strain waves
- time-dependence of the thermal stress profile
→ incoherent lattice dynamics = heat diffusion
- anharmonic interatomic potentials of the crystal lattice
→ nonlinear lattice dynamics = anharmonic phonon-phonon interaction

The LCM is partly solved analytically which enables the analysis of local structural dynamics in terms of the superposition of delocalized normal modes (phonon modes). The numerical results of the LCM are subsequently used in dynamical x-ray diffraction calculations (LCDX) to obtain simulations of the concomitant transient x-ray response. The various time-resolved optical and x-ray diffraction (XRD) experiments conducted throughout my studies which are presented in this thesis and in the papers successively necessitated the inclusion of the different physical aspects stated above in order to account for the observed coherent, incoherent and anharmonic lattice dynamics, respectively.

In a next step, the development of this versatile model for photoexcited structural dynamics and the related ultrafast x-ray diffraction (UXRD) response allowed for the detailed analysis the recorded experimental results on different sample structures and materials. These studies gave rise to advances in the understanding of physical processes related to photoexcited structural dynamics and their manifestation in optical and UXRD signals as well as the progression of experimental means to study such processes. The key points presented in this thesis include

- nonlinear transient interference effects of x-rays in photoexcited superlattices (Section 2.2.3 and Paper **II**)
- time-resolved phonon spectroscopy by Brillouin scattering using optical and x-ray photons (Section 4.1 and Papers **I, VII-VIII**)

-
- nonlinear phonon dynamics in SrTiO₃ such as nonlinear propagation and attenuation of sound due to anharmonic lattice potentials (Chapter 4 and Papers **VII-VIII**)
 - thermal transport in nanolayered heterostructures on ultrafast timescales (Chapter 3 and Paper **VI**)
 - generation of acoustic phonon wavepackets with tunable pulse shape and spectrum by optical means (Section 4.4.1 and Paper **VIII**)
 - realization of several efficient Phonon Bragg Switch concepts (Chapter 5 and Papers **III-IV,IX-X**)

In all cases, the experimental results are accurately reproduced by the numerical models which conclusively reveals the respective lattice dynamics in the photoexcited thin films, superlattices and their substrates. The investigations presented in this thesis thus show that the LCDX calculations in combination with UXRD experiments offer a powerful and extendable toolbox to study ultrafast laser-induced lattice dynamics in great detail. In addition, I point out the potential of the numerical models for the design of novel ultrafast multilayer optics.

Future Prospects

Despite the very good agreement between simulations and experiments displaying the effects of coherent, incoherent and anharmonic phonon propagation the presented studies partly exhibit slight deviations. This suggests that there are still effects which are not clearly understood and/or not taken into account correctly by the LCM. In the following I list a few topics which are ready to be addressed having the toolbox presented in this thesis or which require further extensions of the numerical models.

A very active research topic is the issue of nanoscale heat transport. As motivated in this thesis, UXRD on photoexcited nanostructures is a promising technique to gain more insight into this topic on very small length and timescales. Although I found in Chapter 3 that the standard heat equation was able to reproduce the relaxation dynamics of a photoexcited thin SRO film, I deduced a strongly reduced heat conductivity of SRO. The reason for this reduction is not yet clear and will have to be investigated by systematic experiments varying the pump fluence, temperature and thickness of the SRO layer. In addition, the effect of heat conduction in SRO especially in its ferromagnetic phase is an interesting topic since magnons significantly influence the thermal properties and thermal transport out of the SRO layers [165]. In order to understand the underlying general physical laws of nanoscale heat conduction systematic studies with different thin-film and superlattice geometries are desirable.

In general, the exact nature of the mechanism of stress generation in the considered metal layers is still unclear. It would be very interesting to perform investigations which shed some light on the issue of which phonon modes (or which phonon cascades) mainly contribute to the stress and strain generation. Possible experiments could include the resonant excitation of particular phonon modes by THz radiation and subsequent probing of the layer or SLs by optical and x-ray techniques. As presented in this thesis and in Paper **V** the excitation mechanism appears to change from low to high-excitation regimes. Possible contributions may stem from electronic and phononic pressure as well as displacive and Raman excitation processes. Also temperature and mode-dependent Grüneisen coefficients

are likely to play an important role at sufficiently large excitation densities. Again, a systematic temperature and fluence dependent study is necessary to unravel the variations of the excitation mechanisms. Very closely related is the issue of magnetostriction which was shown to play an important role for the build-up of the photoinduced stress in SRO on ultrafast timescales [53]. Similar investigations could be performed for the ferromagnetic metal LSMO.

When investigating the lattice dynamics of photoexcited thin films in this thesis the solutions of the discretized LCM (which reflects the atomistic nature of matter) exhibited high-frequency oscillations superimposed with the tensile and compressive strain waves. Given a sufficiently fast stress generation, these high-frequency phonons would be interesting to observe in properly chosen experiments. Possible detection schemes could be interferometric optical techniques or scattering/diffraction techniques using electrons or x-rays which are sensitive to the relatively high wavevector Q . In any case, the potential samples will have to be cooled to cryogenic temperatures due to a very high anharmonic phonon damping as discussed in this thesis.

Finally, the anharmonic lattice interactions in STO and similar materials represent another wide research topic which can be addressed by ultrafast reflection/scattering techniques and analyzed by the help of the anharmonic LCM presented in this thesis. Here, changing the temperature and the pump fluence will give a more detailed picture of the interatomic potentials and the related phonon-phonon scattering and decay mechanisms. As mentioned earlier in this work, an important implication of nonlinear sound propagation is the formation of acoustic solitons which are expected appear fairly early (hundreds of picoseconds) in STO due to the relatively large lattice anharmonicity and the large photo-generated strain amplitudes. Another task in the near future could thus be the observation of such acoustic solitons in STO by the various detection methods discussed in this thesis.

BIBLIOGRAPHY

1. C. von Korff Schmising. “Femtosecond X-Ray Scattering in Condensed Matter”. Ph.D. thesis, Humboldt-Universität zu Berlin (2008).
2. A. Kirilyuk, A. V. Kimel and T. Rasing. “Ultrafast optical manipulation of magnetic order”. *Rev. Mod. Phys.* **82**, 2731 (2010).
3. M. Dawber, K. M. Rabe and J. F. Scott. “Physics of thin-film ferroelectric oxides”. *Rev. Mod. Phys.* **77**, 1083 (2005).
4. W. Eerenstein, N. D. Mathur and J. F. Scott. “Multiferroic and magnetoelectric materials”. *Nature* **442**, 759 (2006).
5. R. Ramesh and N. A. Spaldin. “Multiferroics: progress and prospects in thin films”. *Nat. Mater.* **6**, 21 (2007).
6. A. V. Kimel, A. Kirilyuk, A. Tsvetkov, R. V. Pisarev and T. Rasing. “Laser-induced ultrafast spin reorientation in the antiferromagnet TmFeO₃”. *Nature* **429**, 850 (2004).
7. T. Kampfrath, A. Sell, G. Klatt, A. Pashkin, S. Mahrlein, T. Dekorsy, M. Wolf, M. Fiebig, A. Leitenstorfer and R. Huber. “Coherent terahertz control of antiferromagnetic spin waves”. *Nat. Photonics* **5**, 31 (2011).
8. D. Daranciang, M. J. Highland, H. Wen, S. M. Young, N. C. Brandt, H. Y. Hwang, M. Vattilana, M. Nicoul, F. Quirin, J. Goodfellow, T. Qi, I. Grinberg, D. M. Fritz, M. Cammarata, D. Zhu, H. T. Lemke, D. A. Walko, E. M. Dufresne, Y. Li, J. Larsson, D. A. Reis, K. Sokolowski-Tinten, K. A. Nelson, A. M. Rappe, P. H. Fuoss, G. B. Stephenson and A. M. Lindenberg. “Ultrafast Photovoltaic Response in Ferroelectric Nanolayers”. *Phys. Rev. Lett.* **108**, 087601 (2012).
9. D. G. Cahill, W. K. Ford, K. E. Goodson, G. D. Mahan, A. Majumdar, H. J. Maris, R. Merlin and S. R. Phillpot. “Nanoscale thermal transport”. *J. Appl. Phys.* **93**, 793 (2003).
10. K. C. Lee, M. R. Sprague, B. J. Sussman, J. Nunn, N. K. Langford, X. M. Jin, T. Champion, P. Michelberger, K. F. Reim, D. England, D. Jaksch and I. A. Walmsley. “Entangling Macroscopic Diamonds at Room Temperature”. *Science* **334**, 1253 (2011).
11. H. E. Fischer, A. C. Barnes and P. S. Salmon. “Neutron and x-ray diffraction studies of liquids and glasses”. *Rep. Prog. Phys.* **69**, 233 (2006).
12. J. H. Lakey. “Neutrons for biologists: a beginner’s guide, or why you should consider using neutrons”. *J. R. Soc. Interface* **6**, S567 (2009).
13. A. H. Zewail. “4D Ultrafast Electron Diffraction, Crystallography, and Microscopy”. *Ann. Rev. Phys. Chem.* **57**, 65 (2006).
14. M. Chergui and A. H. Zewail. “Electron and X-Ray Methods of Ultrafast Structural Dynamics: Advances and Applications”. *ChemPhysChem* **10**, 28 (2009).
15. R. D. Averitt and A. J. Taylor. “Ultrafast optical and far-infrared quasiparticle dynamics in correlated electron materials”. *J. Phys. Condens. Matter* **14**, R1357 (2002).

16. M. Cardona. *Light Scattering in Solids VIII - Fullerenes, Semiconductor Surfaces, and Coherent Phonons* (Springer, 2000), 1st edn..
17. O. Isnard. “A review of in situ and/or time resolved neutron scattering”. *C. R. Phys.* **8**, 789 (2007).
18. S. Mühlbauer, C. Pfleiderer, P. Böni, E. M. Forgan, E. H. Brandt, A. Wiedenmann, U. Keiderling and G. Behr. “Time-resolved stroboscopic neutron scattering of vortex lattice dynamics in superconducting niobium”. *Phys. Rev. B* **83**, 184502 (2011).
19. N. Gedik, D.-S. Yang, G. Logvenov, I. Bozovic and A. H. Zewail. “Nonequilibrium Phase Transitions in Cuprates Observed by Ultrafast Electron Crystallography”. *Science* **316**, 425 (2007).
20. J. Als-Nielsen and D. McMorrow. *Elements of Modern X-Ray Physics* (John Wiley & Sons, Ltd., 2001).
21. B. J. Siwick, J. R. Dwyer, R. E. Jordan and R. J. D. Miller. “An Atomic-Level View of Melting Using Femtosecond Electron Diffraction”. *Science* **302**, 1382 (2003).
22. M. Eichberger, H. Schafer, M. Krumova, M. Beyer, J. Demsar, H. Berger, G. Moriena, G. Sciaini and R. J. D. Miller. “Snapshots of cooperative atomic motions in the optical suppression of charge density waves”. *Nature* **468**, 799 (2010).
23. C. Rischel, A. Rousse, I. Uschmann, P.-A. Albouy, J.-P. Geindre, P. Audebert, J.-C. Gauthier, E. Froster, J.-L. Martin and A. Antonetti. “Femtosecond time-resolved X-ray diffraction from laser-heated organic films”. *Nature* **390**, 490 (1997).
24. C. Rose-Petruck, R. Jimenez, T. Guo, A. Cavalleri, C. W. Siders, F. Rksi, J. A. Squier, B. C. Walker, K. R. Wilson and C. P. J. Barty. “Picosecond-milliangstrom lattice dynamics measured by ultrafast X-ray diffraction”. *Nature* **398**, 310 (1999).
25. A. M. Lindenberg, I. Kang, S. L. Johnson, T. Missalla, P. A. Heimann, Z. Chang, J. Larsson, P. H. Bucksbaum, H. C. Kapteyn, H. A. Padmore, R. W. Lee, J. S. Wark and R. W. Falcone. “Time-Resolved X-Ray Diffraction from Coherent Phonons during a Laser-Induced Phase Transition”. *Phys. Rev. Lett.* **84**, 111 (2000).
26. A. Rousse, C. Rischel and J.-C. Gauthier. “Femtosecond x-ray crystallography”. *Rev. Mod. Phys.* **73**, 17 (2001).
27. K. Sokolowski-Tinten, C. Blome, J. Blums, A. Cavalleri, C. Dietrich, A. Tarasevitch, I. Uschmann, E. Forster, M. Kammler, M. Horn-von Hoegen and D. von der Linde. “Femtosecond X-ray measurement of coherent lattice vibrations near the Lindemann stability limit”. *Nature* **422**, 287 (2003).
28. M. Bargheer, N. Zhavoronkov, Y. Gritsai, J. C. Woo, D. S. Kim, M. Woerner and T. Elsaesser. “Coherent Atomic Motions in a Nanostructure Studied by Femtosecond X-ray Diffraction”. *Science* **306**, 1771 (2004).
29. A. M. Lindenberg, J. Larsson, K. Sokolowski-Tinten, K. J. Gaffney, C. Blome, O. Synnergren, J. Sheppard, C. Caleman, A. G. MacPhee, D. Weinstein, D. P. Lowney, T. K. Allison, T. Matthews, R. W. Falcone, A. L. Cavalieri, D. M. Fritz, S. H. Lee, P. H. Bucksbaum, D. A. Reis, J. Rudati, P. H. Fuoss, C. C. Kao, D. P. Siddons, R. Pahl, J. Als-Nielsen, S. Duesterer, R. Ischebeck, H. Schlarb, H. Schulte-Schrepping, T. Tschentscher, J. Schneider, D. von der Linde, O. Hignette, F. Sette, H. N. Chapman, R. W. Lee, T. N. Hansen, S. Techert, J. S. Wark, M. Bergh, G. Huldtt, D. van der Spoel, N. Timneanu, J. Hajdu, R. A. Akre, E. Bong, P. Krejci, J. Arthur, S. Brennan, K. Luening and J. B. Hastings. “Atomic-Scale Visualization of Inertial Dynamics”. *Science* **308**, 392 (2005).
30. M. Bargheer, N. Zhavoronkov, M. Woerner and T. Elsaesser. “Recent Progress in Ultrafast X-ray Diffraction”. *ChemPhysChem* **7**, 783 (2006).
31. A. Cavalleri, S. Wall, C. Simpson, E. Statz, D. W. Ward, K. A. Nelson, M. Rini and R. W. Schoenlein. “Tracking the motion of charges in a terahertz light field by femtosecond X-ray diffraction”. *Nature* **442**, 664 (2006).

32. I. Vrejoiu, M. Alexe, D. Hesse and U. Gösele. “Functional Perovskites – From Epitaxial Films to Nanostructured Arrays”. *Adv. Funct. Mater.* **18**, 3892 (2008).
33. J. B. Goodenough. “Electronic and ionic transport properties and other physical aspects of perovskites”. *Rep. Prog. Phys.* **67**, 1915 (2004).
34. C. Israel, M. J. Calderon and N. D. Mathur. “The current spin on manganites”. *Mater. Today* **10**, 24 (2007).
35. D. Fausti, R. I. Tobey, N. Dean, S. Kaiser, A. Dienst, M. C. Hoffmann, S. Pyon, T. Takayama, H. Takagi and A. Cavalleri. “Light-Induced Superconductivity in a Stripe-Ordered Cuprate”. *Science* **331**, 189 (2011).
36. F. Quirin, M. Vattilana, U. Shymanovich, A.-E. El-Kamhawy, A. Tarasevitch, J. Hohlfeld, D. von der Linde and K. Sokolowski-Tinten. “Structural dynamics in FeRh during a laser-induced metamagnetic phase transition”. *Phys. Rev. B* **85**, 020103 (2012).
37. I. Vrejoiu, G. Le Rhun, L. Pintilie, D. Hesse, M. Alexe and U. Gösele. “Intrinsic Ferroelectric Properties of Strained Tetragonal PbZr_{0.2}Ti_{0.8}O₃ Obtained on Layer-by-Layer Grown, Defect-Free Single-Crystalline Films”. *Adv. Mater.* **18**, 1657 (2006).
38. P. H. Bucksbaum and R. Merlin. “The phonon Bragg switch: a proposal to generate sub-picosecond X-ray pulses”. *Solid State Commun.* **111**, 535 (1999).
39. J. M. H. Sheppard, P. Sondhaus, R. Merlin, P. H. Bucksbaum, R. W. Lee and J. S. Wark. “Simulations of the phonon Bragg switch in GaAs”. *Solid State Commun.* **136**, 181 (2005).
40. C. Thomsen, H. T. Grahn, H. J. Maris and J. Tauc. “Surface generation and detection of phonons by picosecond light pulses”. *Phys. Rev. B* **34**, 4129 (1986).
41. H. Kuzmany. *Solid-state spectroscopy - an introduction* (Springer Verlag, Berlin, 2009), 2nd. edn..
42. J. Hohlfeld, S. S. Wellershoff, J. Güdde, U. Conrad, V. Jähnke and E. Matthias. “Electron and lattice dynamics following optical excitation of metals”. *Chem. Phys.* **251**, 237 (2000).
43. C. Kittel. *Introduction to solid state physics* (Wiley, New York [u.a.], 1996), 7th edn..
44. P. Kostic, Y. Okada, N. C. Collins, Z. Schlesinger, J. W. Reiner, L. Klein, A. Kapitulnik, T. H. Geballe and M. R. Beasley. “Non-Fermi-Liquid Behavior of SrRuO₃: Evidence from Infrared Conductivity”. *Phys. Rev. Lett.* **81**, 2498 (1998).
45. P. B. Allen, H. Berger, O. Chauvet, L. Forro, T. Jarlborg, A. Junod, B. Revaz and G. Santi. “Transport properties, thermodynamic properties, and electronic structure of SrRuO₃”. *Phys. Rev. B* **53**, 4393 (1996).
46. D. J. Singh. “Electronic and magnetic properties of the 4d itinerant ferromagnet SrRuO₃”. *J. Appl. Phys.* **79**, 4818 (1996).
47. B. Nadgorny, M. S. Osofsky, D. J. Singh, G. T. Woods, J. R. J. Soulen, M. K. Lee, S. D. Bu and C. B. Eom. “Measurements of spin polarization of epitaxial SrRuO₃ thin films”. *Appl. Phys. Lett.* **82**, 427 (2003).
48. E. Abrahams. “Electron-Electron Scattering in Alkali Metals”. *Phys. Rev.* **95**, 839 (1954).
49. A. J. Schofield. “Non-Fermi liquids”. *Contemp. Phys.* **40**, 95 (1999).
50. M. Dressel and M. Scheffler. “Verifying the Drude response”. *Ann. Phys. (Leipzig)* **15**, 535 (2006).
51. Z. Lin, L. V. Zhigilei and V. Celli. “Electron-phonon coupling and electron heat capacity of metals under conditions of strong electron-phonon nonequilibrium”. *Phys. Rev. B* **77**, 075133 (2008).
52. S. I. Anisimov, B. L. Kapeliovich and T. L. Perel'man. “Electron emission from metal surfaces exposed to ultrashort laser pulses”. *Sov. Phys. JETP* **39**, 375 (1974).

53. C. von Korff Schmising, A. Harpoeth, N. Zhavoronkov, Z. Ansari, C. Aku-Leh, M. Woerner, T. Elsaesser, M. Bargheer, M. Schmidbauer, I. Vrejoiu, D. Hesse and M. Alexe. "Ultrafast magnetostriction and phonon-mediated stress in a photoexcited ferromagnet". *Phys. Rev. B* **78**, 060404 (2008).
54. E. Grüneisen. "Theorie des festen Zustandes einatomiger Elemente". *Ann. Phys.* **344**, 257 (1912).
55. N. W. Ashcroft and N. D. Mermin. *Solid state physics* (Saunders College, Fort Worth, 1976), 1st edn..
56. C. Colvard, T. A. Gant, M. V. Klein, R. Merlin, R. Fischer, H. Morkoc and A. C. Gossard. "Folded acoustic and quantized optic phonons in (GaAl)As superlattices". *Phys. Rev. B* **31**, 2080 (1985).
57. M. Cardona. *Light Scattering in Solids V - Superlattices and Other Microstructures* (Springer, 1989), 1st edn..
58. C. von Korff Schmising, M. Bargheer, M. Kiel, N. Zhavoronkov, M. Woerner, T. Elsaesser, I. Vrejoiu, D. Hesse and M. Alexe. "Ultrafast structure and polarization dynamics in nanolayered perovskites studied by femtosecond X-ray diffraction". *J. Phys. Conf. Ser.* **92**, 012177 (2007).
59. M. Woerner, C. von Korff Schmising, M. Bargheer, N. Zhavoronkov, I. Vrejoiu, D. Hesse, M. Alexe and T. Elsaesser. "Ultrafast structural dynamics of perovskite superlattices". *Appl. Phys. A* **96**, 83 (2009).
60. C. von Korff Schmising, A. Harpoeth, N. Zhavoronkov, M. Woerner, T. Elsaesser, M. Bargheer, M. Schmidbauer, I. Vrejoiu, D. Hesse and M. Alexe. "Femtosecond X-ray diffraction from nanolayered oxides". *Physics Procedia* **3**, 333 (2010).
61. H. S. Choi, J. Bak, J. S. Ahn, N. J. Hur, T. W. Noh and J. H. Cho. "Determination of the Optical Constants of (Ca,Sr)RuO₃ Films". *J. Korean Phys. Soc.* **33**, 184 (1998).
62. C. von Korff Schmising, M. Bargheer, M. Kiel, N. Zhavoronkov, M. Woerner, T. Elsaesser, I. Vrejoiu, D. Hesse and M. Alexe. "Strain propagation in nanolayered perovskites probed by ultrafast x-ray diffraction". *Phys. Rev. B* **73**, 212202 (2006).
63. S. Yamanaka, T. Maekawa, H. Muta, T. Matsuda, S. Kobayashi and K. Kurosaki. "Thermophysical properties of SrHfO₃ and SrRuO₃". *J. Solid State Chem.* **177**, 3484 (2004).
64. L. D. Landau and E. M. Lifshitz. *Course of Theoretical Physics Vol. 6 - Fluid mechanics* (Pergamon Pr., Oxford, 1987), 2nd edn..
65. C. Rullière (Ed.). *Femtosecond laser pulses : principles and experiments* (Springer, New York, 2005), 2nd edn..
66. M. Nicoul, U. Shymanovich, A. Tarasevitch, D. von der Linde and K. Sokolowski-Tinten. "Picosecond acoustic response of a laser-heated gold-film studied with time-resolved x-ray diffraction". *Appl. Phys. Lett.* **98**, 191902 (2011).
67. J. Li, R. Clinite, X. Wang and J. Cao. "Simulation of ultrafast heating induced structural dynamics using a one-dimensional spring model". *Phys. Rev. B* **80**, 014304 (2009).
68. C. von Korff Schmising, M. Bargheer, M. Kiel, N. Zhavoronkov, M. Woerner, T. Elsaesser, I. Vrejoiu, D. Hesse and M. Alexe. "Coupled Ultrafast Lattice and Polarization Dynamics in Ferroelectric Nanolayers". *Phys. Rev. Lett.* **98**, 257601 (2007).
69. C. Colvard, R. Merlin, M. V. Klein and A. C. Gossard. "Observation of Folded Acoustic Phonons in a Semiconductor Superlattice". *Phys. Rev. Lett.* **45**, 298 (1980).
70. D. A. Tenne, A. Bruchhausen, N. D. Lanzillotti-Kimura, A. Fainstein, R. S. Katiyar, A. Cantarero, A. Soukiassian, V. Vaithyanathan, J. H. Haeni, W. Tian, D. G. Schlom, K. J. Choi, D. M. Kim, C. B. Eom, H. P. Sun, X. Q. Pan, Y. L. Li, L. Q. Chen, Q. X. Jia, S. M. Nakhmanson, K. M. Rabe and X. X. Xi. "Probing Nanoscale Ferroelectricity by Ultraviolet Raman Spectroscopy". *Science* **313**, 1614 (2006).

71. F. Zamponi, Z. Ansari, C. von Korff Schmising, P. Rothhardt, N. Zhavoronkov, M. Woerner, T. Elsaesser, M. Bargheer, T. Trobitzsch-Ryll and M. Haschke. “Femtosecond hard X-ray plasma sources with a kilohertz repetition rate”. *Appl. Phys. A* **96**, 51 (2009).
72. C. von Korff Schmising, M. Bargheer, M. Kiel, N. Zhavoronkov, M. Woerner, T. Elsaesser, I. Vrejoiu, D. Hesse and M. Alexe. “Accurate time delay determination for femtosecond X-ray diffraction experiments”. *Appl. Phys. B* **88**, 1 (2007).
73. A. Bartels, T. Dekorsy, H. Kurz and K. Köhler. “Coherent Zone-Folded Longitudinal Acoustic Phonons in Semiconductor Superlattices: Excitation and Detection”. *Phys. Rev. Lett.* **82**, 1044 (1999).
74. A. Authier. *Dynamical Theory of X-Ray Diffraction* (Oxford University Press, 2003).
75. C. G. Darwin. “The Theory of X-ray Reflection. Part II.” *Phil. Mag.* **27**, 675 (1914).
76. S. A. Stepanov, E. A. Kondrashkina, R. Köhler, D. V. Novikov, G. Materlik and S. M. Durbin. “Dynamical x-ray diffraction of multilayers and superlattices: Recursion matrix extension to grazing angles”. *Phys. Rev. B* **57**, 4829 (1998).
77. H. J. Lee, J. Workman, J. S. Wark, R. D. Averitt, A. J. Taylor, J. Roberts, Q. McCulloch, D. E. Hof, N. Hur, S.-W. Cheong and D. J. Funk. “Optically induced lattice dynamics probed with ultrafast x-ray diffraction”. *Phys. Rev. B* **77**, 132301 (2008).
78. H. L. Liu, K. S. Lu, M. X. Kuo, L. Uba, S. Uba, L. M. Wang and H. T. Jeng. “Magneto-optical properties of $\text{La}_{0.7}\text{Sr}_{0.3}\text{MnO}_3$ thin films with perpendicular magnetic anisotropy”. *J. Appl. Phys.* **99**, 043908 (2006).
79. M. Veis, Š. Višňovský, P. Lecoeur, A.-M. Haghiri-Gosnet, J.-P. Renard, P. Beauvillain, W. Prellier, B. Mercey, J. Mistrík and T. Yamaguchi. “Magneto-optic spectroscopy of $\text{La}_{2/3}\text{Sr}_{1/3}\text{MnO}_3$ films on SrTiO_3 (1 0 0) and (1 1 0) substrates”. *J. Phys. D: Appl. Phys.* **42**, 195002 (2009).
80. A. Hertwig. (private communication) (2012).
81. T. Ishidate, S. Sasaki and K. Inoue. “Brillouin scattering of SrTiO_3 under high pressure”. *High Pressure Res.* **1**, 53 (1988).
82. D. M. Fritz, D. A. Reis, B. Adams, R. A. Akre, J. Arthur, C. Blome, P. H. Bucksbaum, A. L. Cavalieri, S. Engemann, S. Fahy, R. W. Falcone, P. H. Fuoss, K. J. Gaffney, M. J. George, J. Hajdu, M. P. Hertlein, P. B. Hillyard, M. Horn-von Hoegen, M. Kammler, J. Kaspar, R. Kienberger, P. Krejcik, S. H. Lee, A. M. Lindenberg, B. McFarland, D. Meyer, T. Montagne, A. D. Murray, A. J. Nelson, M. Nicoul, R. Pahl, J. Rudati, H. Schlarb, D. P. Siddons, K. Sokolowski-Tinten, T. Tschentscher, D. von der Linde and J. B. Hastings. “Ultrafast Bond Softening in Bismuth: Mapping a Solid’s Interatomic Potential with X-rays”. *Science* **315**, 633 (2007).
83. S. L. Johnson, E. Vorobeva, P. Beaud, C. J. Milne and G. Ingold. “Full Reconstruction of a Crystal Unit Cell Structure during Coherent Femtosecond Motion”. *Phys. Rev. Lett.* **103**, 205501 (2009).
84. M. Trigo, Y. M. Sheu, D. A. Arms, J. Chen, S. Ghimire, R. S. Goldman, E. Landahl, R. Merlin, E. Peterson, M. Reason and D. A. Reis. “Probing Unfolded Acoustic Phonons with X Rays”. *Phys. Rev. Lett.* **101**, 025505 (2008).
85. C.-K. Sun, J.-C. Liang and X.-Y. Yu. “Coherent Acoustic Phonon Oscillations in Semiconductor Multiple Quantum Wells with Piezoelectric Fields”. *Phys. Rev. Lett.* **84**, 179 (2000).
86. K. J. Yee, Y. S. Lim, T. Dekorsy and D. S. Kim. “Mechanisms for the Generation of Coherent Longitudinal-Optical Phonons in $\text{GaAs}/\text{AlGaAs}$ Multiple Quantum Wells”. *Phys. Rev. Lett.* **86**, 1630 (2001).
87. C. W. Siders, A. Cavalleri, K. Sokolowski-Tinten, C. Tóth, T. Guo, M. Kammler, M. H. v. Hoegen, K. R. Wilson, D. v. d. Linde and C. P. J. Barty. “Detection of Nonthermal Melting by Ultrafast X-ray Diffraction”. *Science* **286**, 1340 (1999).

88. K. Sokolowski-Tinten, C. Blome, C. Dietrich, A. Tarasevitch, M. Horn von Hoegen, D. von der Linde, A. Cavalleri, J. Squier and M. Kammler. "Femtosecond X-Ray Measurement of Ultrafast Melting and Large Acoustic Transients". *Phys. Rev. Lett.* **87**, 225701 (2001).
89. H. A. Navirian, H. Enquist, T. N. Hansen, A. Mikkelsen, P. Sondhaus, A. Srivastava, A. A. Zakharov and J. Larsson. "Repetitive ultrafast melting of InSb as an x-ray timing diagnostic". *J. Appl. Phys.* **103**, 103510 (2008).
90. C. Gahl, A. Azima, M. Beye, M. Deppe, K. Dobrich, U. Hasslinger, F. Hennies, A. Melnikov, M. Nagasono, A. Pietzsch, M. Wolf, W. Wurth and A. Fohlisch. "A femtosecond X-ray//optical cross-correlator". *Nat. Photonics* **2**, 165 (2008).
91. S. M. Durbin, T. Clevenger, T. Graber and R. Henning. "X-ray pump optical probe cross-correlation study of GaAs". *Nat. Photonics* **6**, 111 (2012).
92. M. Perner, S. Grésillon, J. März, G. von Plessen, J. Feldmann, J. Porstendorfer, K. J. Berg and G. Berg. "Observation of Hot-Electron Pressure in the Vibration Dynamics of Metal Nanoparticles". *Phys. Rev. Lett.* **85**, 792 (2000).
93. J. Wang and C. Guo. "Effect of electron heating on femtosecond laser-induced coherent acoustic phonons in noble metals". *Phys. Rev. B* **75**, 184304 (2007).
94. J. Tang. "Coherent phonon excitation and linear thermal expansion in structural dynamics and ultrafast electron diffraction of laser-heated metals". *J. Chem. Phys.* **128**, 164702 (2008).
95. P.-T. Tai, P. Yu and J. Tang. "Laser-Fluence Dependence of Acoustic Phonon Excitation in Metallic Thin Films and Determination of the Grüneisen Parameter". *J. Phys. Chem. C* **113**, 15014 (2009).
96. K. T. Tsen, J. G. Kiang, D. K. Ferry and H. Morkoc. "Subpicosecond time-resolved Raman studies of LO phonons in GaN: Dependence on photoexcited carrier density". *Appl. Phys. Lett.* **89** (2006).
97. F. S. Krasniqi, S. L. Johnson, P. Beaud, M. Kaiser, D. Grolimund and G. Ingold. "Influence of lattice heating time on femtosecond laser-induced strain waves in InSb". *Phys. Rev. B* **78**, 174302 (2008).
98. L. C. Evans. *Partial differential equations*, vol. 19 of *Graduate studies in mathematics* (American Mathematical Society, Providence, RI, 1998).
99. R. O. Bell and G. Rupprecht. "Elastic Constants of Strontium Titanate". *Phys. Rev.* **129**, 90 (1963).
100. Y. H. Ren, M. Trigo, R. Merlin, V. Adyam and Q. Li. "Generation and detection of coherent longitudinal acoustic phonons in the $\text{La}_{0.67}\text{Sr}_{0.33}\text{MnO}_3$ thin films by femtosecond light pulses". *Appl. Phys. Lett.* **90**, 251918 (2007).
101. C. L. Tien and G. Chen. "Challenges in Microscale Conductive and Radiative Heat Transfer". *J. of Heat Transfer* **116**, 799 (1994).
102. G. Chen. "Thermal conductivity and ballistic-phonon transport in the cross-plane direction of superlattices". *Phys. Rev. B* **57**, 14958 (1998).
103. W. S. Capinski, H. J. Maris, T. Ruf, M. Cardona, K. Ploog and D. S. Katzer. "Thermal-conductivity measurements of GaAs/AlAs superlattices using a picosecond optical pump-and-probe technique". *Phys. Rev. B* **59**, 8105 (1999).
104. B. Yang and G. Chen. "Partially coherent phonon heat conduction in superlattices". *Phys. Rev. B* **67**, 195311 (2003).
105. G. Chen. "Ballistic-Diffusive Heat-Conduction Equations". *Phys. Rev. Lett.* **86**, 2297 (2001).
106. M. E. Siemens, Q. Li, R. Yang, K. A. Nelson, E. H. Anderson, M. M. Murnane and H. C. Kapteyn. "Quasi-ballistic thermal transport from nanoscale interfaces observed using ultrafast coherent soft X-ray beams". *Nat. Mater.* **9**, 26 (2010).

107. V. Holy, U. Pietsch and T. Baumbach. *High-resolution X-ray Scattering from Thin Films and Multilayers*. Springer Tracts in Modern Physics (Springer, 1999), 1st edn..
108. R. Venkatasubramanian. “Lattice thermal conductivity reduction and phonon localizationlike behavior in superlattice structures”. *Phys. Rev. B* **61**, 3091 (2000).
109. R. Venkatasubramanian, E. Siivola, T. Colpitts and B. O’Quinn. “Thin-film thermoelectric devices with high room-temperature figures of merit”. *Nature* **413**, 597 (2001).
110. Y. Shen, D. R. Clarke and P. A. Fuierer. “Anisotropic thermal conductivity of the Aurivillius phase, bismuth titanate ($\text{Bi}_4\text{Ti}_3\text{O}_{12}$): A natural nanostructured superlattice”. *Appl. Phys. Lett.* **93**, 102907 (2008).
111. M. Hase and J. Tominaga. “Thermal conductivity of GeTe/Sb₂Te₃ superlattices measured by coherent phonon spectroscopy”. *Appl. Phys. Lett.* **99**, 031902 (2011).
112. J.-W. Jiang, J.-S. Wang and B.-S. Wang. “Minimum thermal conductance in graphene and boron nitride superlattice”. *Appl. Phys. Lett.* **99**, 043109 (2011).
113. J. Garg, N. Bonini and N. Marzari. “High Thermal Conductivity in Short-Period Superlattices”. *Nano Lett.* **11**, 5135 (2011).
114. H. Navirian, R. Shayduk, W. Leitenberger, J. Goldshteyn, P. Gaal and M. Bargheer. “Synchrotron-based ultrafast x-ray diffraction at high repetition rates”. *Rev. Sci. Instrum.* **83**, 063303 (2012).
115. L. Colombo and S. Giordano. “Nonlinear elasticity in nanostructured materials”. *Rep. Prog. Phys.* **74**, 116501 (2011).
116. K. S. Krishnan. “Anharmonicity of the Lattice Oscillations in the Alkali Halide Crystals”. *Nature* **166**, 114 (1950).
117. O. Delaire, J. Ma, K. Marty, A. F. May, M. A. McGuire, M.-H. Du, D. J. Singh, A. Podlesnyak, G. Ehlers, M. D. Lumsden and B. C. Sales. “Giant anharmonic phonon scattering in PbTe”. *Nat. Mater.* **10**, 614 (2011).
118. A. G. Beattie and G. A. Samara. “Pressure Dependence of the Elastic Constants of SrTiO₃”. *J. Appl. Phys.* **42**, 2376 (1971).
119. B. Berre, K. Fossheim and K. A. Müller. “Critical Attenuation of Sound by Soft Modes in SrTiO₃”. *Phys. Rev. Lett.* **23**, 589 (1969).
120. R. Nava, R. Callarotti, H. Ceva and A. Martinet. “Hypersonic Attenuation by Low-Frequency Optical Phonons in SrTiO₃ Crystals”. *Phys. Rev.* **188**, 1456 (1969).
121. T.-M. Liu, S.-Z. Sun, C.-F. Chang, C.-C. Pan, G.-T. Chen, J.-I. Chyi, V. Gusev and C.-K. Sun. “Anharmonic decay of subterahertz coherent acoustic phonons in GaN”. *Appl. Phys. Lett.* **90**, 041902 (2007).
122. N. S. Shiren. “Nonlinear Acoustic Interaction in MgO at 9 Gc/sec”. *Phys. Rev. Lett.* **11**, 3 (1963).
123. M. Forst, C. Manzoni, S. Kaiser, Y. Tomioka, Y. Tokura, R. Merlin and A. Cavalleri. “Nonlinear phononics as an ultrafast route to lattice control”. *Nat. Phys.* **7**, 854 (2011).
124. A. Cavalleri, C. W. Siders, F. L. H. Brown, D. M. Leitner, C. Tóth, J. A. Squier, C. P. J. Barty, K. R. Wilson, K. Sokolowski-Tinten, M. Horn von Hoegen, D. von der Linde and M. Kammler. “Anharmonic Lattice Dynamics in Germanium Measured with Ultrafast X-Ray Diffraction”. *Phys. Rev. Lett.* **85**, 586 (2000).
125. M. Hase, M. Kitajima, S.-i. Nakashima and K. Mizoguchi. “Dynamics of Coherent Anharmonic Phonons in Bismuth Using High Density Photoexcitation”. *Phys. Rev. Lett.* **88**, 067401 (2002).
126. M. Scheuch, T. Kampfrath, M. Wolf, K. von Volkman, C. Frischkorn and L. Perfetti. “Temperature dependence of ultrafast phonon dynamics in graphite”. *Appl. Phys. Lett.* **99**, 211908 (2011).

127. T. Lan, X. Tang and B. Fultz. “Phonon anharmonicity of rutile TiO_2 studied by Raman spectrometry and molecular dynamics simulations”. *Phys. Rev. B* **85**, 094305 (2012).
128. I. Katayama, H. Aoki, J. Takeda, H. Shimosato, M. Ashida, R. Kinjo, I. Kawayama, M. Tonouchi, M. Nagai and K. Tanaka. “Ferroelectric Soft Mode in a SrTiO_3 Thin Film Impulsively Driven to the Anharmonic Regime Using Intense Picosecond Terahertz Pulses”. *Phys. Rev. Lett.* **108**, 097401 (2012).
129. O. Delaire, M. B. Stone, J. Ma, A. Huq, D. Gout, C. Brown, K. F. Wang and Z. F. Ren. “Anharmonic phonons and magnons in BiFeO_3 ”. *Phys. Rev. B* **85**, 064405 (2012).
130. C. V. Raman. “A new radiation”. *Indian J. Phys.* **2**, 387 (1928).
131. C. V. Raman and K. S. Krishnan. “A New Type of Secondary Radiation”. *Nature* **121** (1928).
132. M. Quinten. *Optical Properties of Nanoparticle Systems* (Wiley - VCH, 2011), 1st edn..
133. M. Cardona. *Light Scattering in Solids I - Introductory Concepts* (Springer, 1983), 2nd edn..
134. J. Larsson, A. Allen, P. H. Bucksbaum, R. W. Falcone, A. Lindenberg, G. Naylor, T. Missalla, D. A. Reis, K. Scheidt, A. Sjögren, P. Sondhauss, M. Wulff and J. S. Wark. “Picosecond X-ray diffraction studies of laser-excited acoustic phonons in InSb ”. *Appl. Phys. A* **75**, 467 (2002).
135. E. Pontecorvo, M. Ortolani, D. Polli, M. Ferretti, G. Ruocco, G. Cerullo and T. Scopigno. “Visualizing coherent phonon propagation in the 100 GHz range: A broadband picosecond acoustics approach”. *Appl. Phys. Lett.* **98**, 011901 (2011).
136. S. Brivio, D. Polli, A. Crespi, R. Osellame, G. Cerullo and R. Bertacco. “Observation of anomalous acoustic phonon dispersion in SrTiO_3 by broadband stimulated Brillouin scattering”. *Appl. Phys. Lett.* **98**, 211907 (2011).
137. D. A. Reis, M. F. DeCamp, P. H. Bucksbaum, R. Clarke, E. Dufresne, M. Hertlein, R. Merlin, R. Falcone, H. Kapteyn, M. M. Murnane, J. Larsson, T. Missalla and J. S. Wark. “Probing Impulsive Strain Propagation with X-Ray Pulses”. *Phys. Rev. Lett.* **86**, 3072 (2001).
138. R. R. Alfano (Ed.). *The Supercontinuum Laser Source* (Springer, 2006), 2nd edn..
139. D. Polli, L. Lüer and G. Cerullo. “High-time-resolution pump-probe system with broadband detection for the study of time-domain vibrational dynamics”. *Rev. Sci. Instrum.* **78**, 103108 (2007).
140. E. Arévalo, Y. Gaididei and F. G. Mertens. “Soliton dynamics in damped and forced Boussinesq equations”. *Eur. Phys. J. B* **27**, 63 (2002).
141. E. Arévalo, F. G. Mertens, Y. Gaididei and A. R. Bishop. “Thermal diffusion of supersonic solitons in an anharmonic chain of atoms”. *Phys. Rev. E* **67**, 016610 (2003).
142. H. Y. Hao and H. J. Maris. “Experiments with acoustic solitons in crystalline solids”. *Phys. Rev. B* **64**, 064302 (2001).
143. O. L. Muskens and J. I. Dijkhuis. “High Amplitude, Ultrashort, Longitudinal Strain Solitons in Sapphire”. *Phys. Rev. Lett.* **89**, 285504 (2002).
144. P. J. S. van Capel and J. I. Dijkhuis. “Time-resolved interferometric detection of ultrashort strain solitons in sapphire”. *Phys. Rev. B* **81**, 144106 (2010).
145. A. A. Giardini. “Stress-Optical Study of Strontium Titanate”. *J. Opt. Soc. Am.* **47**, 726 (1957).
146. O. Synnergren, T. N. Hansen, S. Canton, H. Enquist, P. Sondhauss, A. Srivastava and J. Larsson. “Coherent phonon control”. *Appl. Phys. Lett.* **90**, 171929 (2007).
147. H. J. Maris. “The absorption of sound waves in perfect dielectric crystals”. *Phil. Mag.* (1965).

148. V. V. Lemanov and G. A. Smolenskii. "Hypersonic waves in crystals". *Sov. Phys. Usp.* **15**, 708 (1973).
149. A. Koreeda, T. Nagano, S. Ohno and S. Saikan. "Quasielastic light scattering in rutile, ZnSe, silicon, and SrTiO₃". *Phys. Rev. B* **73**, 024303 (2006).
150. L. D. Landau and G. Rumer. "On the absorption of sound in solids". *Phys. Z. Sowjetunion* **11**, 18 (1937).
151. I. Pomeranchuk. "On the thermal conductivity of dielectrics at the temperatures higher than the Debye temperature". *J. Phys. (USSR)* **4**, 259 (1941).
152. A. Akhieser. "On the absorption of sound in solids". *J. Phys. (USSR)* **1**, 277 (1939).
153. T. O. Woodruff and H. Ehrenreich. "Absorption of Sound in Insulators". *Phys. Rev.* **123**, 1553 (1961).
154. B. C. Daly, K. Kang, Y. Wang and D. G. Cahill. "Picosecond ultrasonic measurements of attenuation of longitudinal acoustic phonons in silicon". *Phys. Rev. B* **80**, 174112 (2009).
155. H. E. Bömmel and K. Dransfeld. "Excitation and Attenuation of Hypersonic Waves in Quartz". *Phys. Rev.* **117**, 1245 (1960).
156. J. Y. Duquesne and B. Perrin. "Ultrasonic attenuation in a quasicrystal studied by picosecond acoustics as a function of temperature and frequency". *Phys. Rev. B* **68**, 134205 (2003).
157. Y. Wang, K. Fujinami, R. Zhang, C. Wan, N. Wang, Y. Ba and K. Koumoto. "Interfacial Thermal Resistance and Thermal Conductivity in Nanograined SrTiO₃". *Appl. Phys. Express* **3**, 031101 (2010).
158. M. Quijada, J. Černe, J. R. Simpson, H. D. Drew, K. H. Ahn, A. J. Millis, R. Shreekala, R. Ramesh, M. Rajeswari and T. Venkatesan. "Optical conductivity of manganites: Crossover from Jahn-Teller small polaron to coherent transport in the ferromagnetic state". *Phys. Rev. B* **58**, 16093 (1998).
159. M. Abo-Bakr, J. Feikes, K. Holldack, P. Kuske, W. B. Peatman, U. Schade, G. Wüstefeld and H. W. Hübers. "Brilliant, Coherent Far-Infrared (THz) Synchrotron Radiation". *Phys. Rev. Lett.* **90**, 094801 (2003).
160. R. W. Schoenlein, S. Chattopadhyay, H. H. W. Chong, T. E. Glover, P. A. Heimann, C. V. Shank, A. A. Zholents and M. S. Zolotarev. "Generation of Femtosecond Pulses of Synchrotron Radiation". *Science* **287**, 2237 (2000).
161. S. Kahn, K. Holldack, T. Kachel, R. Mitzner and T. Quast. "Femtosecond Undulator Radiation from Sliced Electron Bunches". *Phys. Rev. Lett.* **97**, 074801 (2006).
162. P. Beaud, S. L. Johnson, A. Streun, R. Abela, D. Abramssohn, D. Grolimund, F. S. Krasniqi, T. Schmidt, V. Schlott and G. Ingold. "Spatiotemporal Stability of a Femtosecond HardX-Ray Undulator Source Studied by Control of Coherent Optical Phonons". *Phys. Rev. Lett.* **99**, 174801 (2007).
163. K. Tiedtke, A. Azima, N. von Bargen, L. Bittner, S. Bonfigt, S. Düsterer, B. Faatz, U. Frühling, M. Gensch, C. Gerth, N. Guerassimova, U. Hahn, T. Hans, M. Hesse, K. Honkavaar, U. Jastrow, P. Juranic, S. Kapitzki, B. Keitel, T. Kracht, M. Kuhlmann, W. B. Li, M. Martins, T. Núñez, E. Plönjes, H. Redlin, E. L. Saldin, E. A. Schneidmiller, J. R. Schneider, S. Schreiber, N. Stojanovic, F. Tavella, S. Toleikis, R. Treusch, H. Weigelt, M. Wellhöfer, H. Wabnitz, M. V. Yurkov and J. Feldhaus. "The soft x-ray free-electron laser FLASH at DESY: beamlines, diagnostics and end-stations". *New J. Phys.* **11**, 023029 (2009).
164. P. Emma, R. Akre, J. Arthur, R. Bionta, C. Bostedt, J. Bozek, A. Brachmann, P. Bucksbaum, R. Coffee, F.-J. Decker, Y. Ding, D. Dowell, S. Edstrom, A. Fisher, J. Frisch, S. Gilevich, J. Hastings, G. Hays, P. Hering, Z. Huang, R. Iverson, H. Loos, M. Messerschmidt, A. Miahnahri, S. Moeller, H.-D. Nuhn, G. Pile, D. Ratner, J. Rzepiela, D. Schultz, T. Smith, P. Stefan, H. Tompkins, J. Turner, J. Welch, W. White, J. Wu, G. Yocky and J. Galayda. "First lasing and operation of an angstrom-wavelength free-electron laser". *Nat. Photonics* **4**, 641 (2010).

165. M. C. Langner, C. L. S. Kantner, Y. H. Chu, L. M. Martin, P. Yu, R. Ramesh and J. Orenstein. “Effective thermal boundary resistance from thermal decoupling of magnons and phonons in SrRuO₃ thin films”. *Phys. Rev. B* **82**, 054425 (2010).

ACKNOWLEDGMENTS

First of all, special thanks to my supervisor Prof. Matias Bargheer who provided an environment which allowed to conduct blooming research and having fun at the same time. He was also always willing to give technical, physics-related and mental support.

Many thanks also to all of my colleagues of the Ultrafast Dynamics group at the University of Potsdam and BESSY who supported me wherever I needed help with the experiments, theories or data analysis and who also gave me good times whenever we engaged in non-physics-related activities. As always, the secretaries Katharina Wallroth, Susanne Rolle and Marlies Path deserve special thanks for keeping the administrative things off my back.

I am very grateful for all the support I received during the numerous experiments at the SLS, especially by Chris Milne and Steve Johnson, and at the ESRF by Dmitry Khakhulin and Michael Wulff. Valuable insight is also due to the measurements of Dr. Andreas Hertwig from the Bundesanstalt für Materialforschung und -prüfung (BAM) in Berlin.

I also owe special thanks to Dr. Ionela Vrejoiu from the Max-Planck-Institute for Microstructure Physics in Halle, Germany. Ionela always provided us with high quality samples and was always willing to further improve those for our demanding experiments.

Last but not least, I want to thank my family and especially Peggy and Juri for grounding me from time to time when physics seemed to absorb myself too much.

SELBSTÄNDIGKEITSERKLÄRUNG

Hiermit erkläre ich, dass ich die vorliegende Dissertation „Structural Dynamics of Photoexcited Nanolayered Perovskites Studied by Ultrafast X-ray Diffraction“ selbstständig erarbeitet und verfasst habe und alle Hilfsmittel und Hilfen angegeben habe.

Ich erkläre, dass ich mich nicht für einen Doktorgrad anderwärts beworben habe und auch einen dementsprechenden Doktorgrad nicht besitze.

Des weiteren erkläre ich, dass ich von der zugrunde liegenden Promotionsordnung Kenntnis genommen habe.

Marc Herzog, Potsdam, den 13. November 2012

Analysis of ultrafast x-ray diffraction data in a linear-chain model of the lattice dynamics

M. Herzog, D. Schick, P. Gaal, R. Shayduk,
C. von Korff Schmising and M. Bargheer.

Appl. Phys. A **106**, 489 (2012).

Analysis of ultrafast X-ray diffraction data in a linear-chain model of the lattice dynamics

M. Herzog · D. Schick · P. Gaal · R. Shayduk ·
C. v. Korff Schmising · M. Bargheer

Received: 15 August 2011 / Accepted: 30 November 2011 / Published online: 15 December 2011
© Springer-Verlag 2011

Abstract We present ultrafast X-ray diffraction (UXRD) experiments which sensitively probe impulsively excited acoustic phonons propagating in a SrRuO₃/SrTiO₃ superlattice and further into the substrate. These findings are discussed together with previous UXRD results (Herzog et al. in Appl. Phys. Lett. 96, 161906, 2010; Woerner et al. in Appl. Phys. A 96, 83, 2009; v. Korff Schmising in Phys. Rev. B 78, 060404(R), 2008 and in Appl. Phys. B 88, 1, 2007) using a normal-mode analysis of a linear-chain model of masses and springs, thus identifying them as linear-response phenomena. We point out the direct correspondence of calculated observables with X-ray signals. In this framework the complex lattice motion turns out to result from an interference of vibrational eigenmodes of the coupled system of nanolayers and substrate. UXRD in principle selectively measures the lattice motion occurring with a specific wavevector, however, each Bragg reflection only measures the amplitude of a delocalized phonon mode in a spatially localized region, determined by the nanocomposition of the sample or the extinction depth of X-rays. This leads to a decay of experimental signals although the excited modes survive.

1 Introduction

Ultrafast X-ray diffraction (UXRD) is capable of monitoring atomic motion in solids on the atomic length and timescale. It has been applied to the study of optical and acoustic phonons and in particular to zone-folded longitudinal acoustic phonons (ZFLAPs) in superlattices (SLs), which can be viewed as acoustic or optical phonons, from the perspective of the bulk or the SL-mini-Brillouin zone, respectively [5, 6]. In theory, the mini-Brillouin zone is defined for an infinite SL. Experimentally, this is approximated by periodically stacking a large number P of epitaxial double layers of two different crystal lattices (e.g. GaAs/AlGaAs) on top of each other. Such a SL with $P = 2000$ and a double layer period d_{SL} was recently investigated after homogeneous excitation with femtosecond laser pulses [7]. The resulting standing strain wave was essentially an optical phonon with wavevector $Q = 0$, as it corresponded to the motion of atoms within the super unit cell (one double layer GaAs/AlGaAs) and to a good approximation the substrate could be neglected. No lineshift of the Bragg reflection was observed, evidencing that the size of the super unit cell remained constant on the timescale of the experiment. When the number P of double layers is smaller, e.g. $P = 11$, as was the case in a previously studied oxide SL of SrRuO₃/SrTiO₃ (SRO/STO), the coupling to the substrate leads to a decay of the SL motion [1–4, 8]. The timescale of this decay is set by the SL expansion time, corresponding to the time $T = D/v_{SL} \approx 35$ ps it takes an acoustic phonon to traverse the SL thickness $D = P \cdot d_{SL} \approx 250$ nm at the average sound velocity v_{SL} [9, 10].

A key advantage of UXRD is the direct correspondence of the real-space periods with the wavevector transfer $\mathbf{q} = \mathbf{k} - \mathbf{k}' = \mathbf{G} \pm \mathbf{Q}$ encoded in a generalized Laue condition, where $G = |\mathbf{G}| = 2\pi/c$ is a reciprocal lattice vector corresponding to the real-space lattice spacing c and \mathbf{Q} is the

M. Herzog · D. Schick · P. Gaal · M. Bargheer (✉)
Institute of Physics and Astronomy, University Potsdam,
Karl-Liebknecht-Strasse 24-25, 14476 Potsdam, Germany
e-mail: bargheer@uni-potsdam.de

R. Shayduk · M. Bargheer
Helmholtz-Zentrum Berlin für Materialien und Energie GmbH,
Hahn-Meitner-Platz 1, 14109 Berlin, Germany

C. v. Korff Schmising
Atomic Physics Division, Department of Physics, Lund
University, P.O. Box 118 22100 Lund, Sweden

wavevector of a specific phonon mode. In SLs $G = n \cdot g$ ($n \in \mathbb{N}$) is an integer multiple of the reciprocal SL vector $g = 2\pi/d_{\text{SL}}$ [11]. The first achievement of UXRD was to show that coherent acoustic phonons in bulk lattices lead to a temporal modulation of the X-ray diffraction signal at $G \pm Q$ according to the phonon dispersion relation $\omega(Q)$ [12–14]. The SL phonon modes exhibit a time dependence according to their frequency $\omega_{\text{SL}} = \omega(Q = 0)$ as an intensity modulation of the SL Bragg peak, as they are optical modes at the mini-Brillouin zone center ($Q = 0$). Exciting a thin Ge film resulted in sidebands to the bulk reflection of a Si substrate at G_{Si} and a continuous shift and broadening of the Ge reflection at G_{Ge} [15]. Experiments on InGaAs/InAlAs SLs also reported shifts of the SL Bragg peaks, and in addition the “unfolding” of the SL phonon with wavevector Q_{SL} into the InP substrate leading to new reflections at $G_{\text{sub}} \pm Q_{\text{SL}}^*$ [16]. In all these cases, the excitation of a broad acoustic phonon spectrum leads to a continuous shift of peaks or the development of a sideband to an existing peak.

In this paper we present UXRD measurements on a photoexcited SRO/STO SL that shows the disappearance of a Bragg reflection at a particular $G = n \cdot g$ and its reappearance at a different $G' = n \cdot g'$ corresponding to an expanded SL without exhibiting a continuous shifting of the rocking curve. In addition, very clear sidebands to the bulk substrate reflection show up. Continuous shifts as well as sidebands of thin film and substrate Bragg peaks have been previously discussed in the context of acoustic sound propagation [12–18]. Here, we focus on analysing such features, including recently published UXRD data on the same SRO/STO SL, within a simple linear-chain model which describes the longitudinal phonon spectrum of the SL on a substrate. We discuss in detail which modes are optically excited and how this gives rise to both propagating and standing waves in the structure. We analyze how the different features of the lattice dynamics can be directly measured and calibrated by UXRD and calculate rocking curves using dynamical X-ray diffraction theory. It turns out that the disappearance and reappearance or rather splitting of the Bragg peak reflects the short-timescale dynamics of the coherent acoustic phonon spectrum within the SL for strong excitation. The sidebands of the substrate peak measure the appearance of this coherent wavepacket distortion in the substrate, whereas the appearance of the $G_{\text{sub}} \pm Q_{\text{SL}}^*$ peaks [16] show the spatial period of the SL phonon after it has propagated (unfolded) into the substrate. All these phenomena are quantitatively predicted by the presented model and therefore identified as a linear response of the sample.

2 Experiments

2.1 Results

Figure 1 shows the TEM cross section of the SRO/STO SL together with a schematic of the experiment. An optical pump pulse is absorbed by the metallic SRO layers of the sample leading to a quasi-instantaneous spatial stress profile $\Delta(z)$ indicated by the red line. A time-delayed X-ray probe pulse measures the excited sample by diffraction of monochromatic X-ray photons impinging on the sample at different Bragg angles.

We used the laser-based femtosecond X-ray diffractometer at University of Potsdam, which is very similar to the one described recently [19], for measuring a particular SL reflection, whereas transients of the STO substrate peak were recorded at the Femto-slicing beamline of the Swiss Light Source (SLS) [20]. The inset of Fig. 2 shows an overview of the sample’s diffraction profile around the bulk (0 0 2) reflection of the substrate. The time dependence of the strongest SL peak with the SL-Miller index (0 0 116) has been characterized previously according to its so-called shift within 30 ps and its intensity modulation which shows a period of 3.2 ps due to the SL phonon [1–4]. This modulation decays with a similar time constant of approx. 30 ps.

A new and more detailed set of experimental results on this (0 0 116) reflection is presented in Fig. 2. We measured the time-dependent diffracted X-ray intensity $I(q, t)$ for different wavevector transfers $q = \sin(\theta)4\pi/\lambda$. The Bragg reflectivity is defined by $R(q, t) = I(q, t)/I_0(q)$, where $I_0(q)$ is the X-ray intensity incident on the sample. Figure 2(c) shows the difference spectra $R(q, t) - R_0(q)$, i.e.,

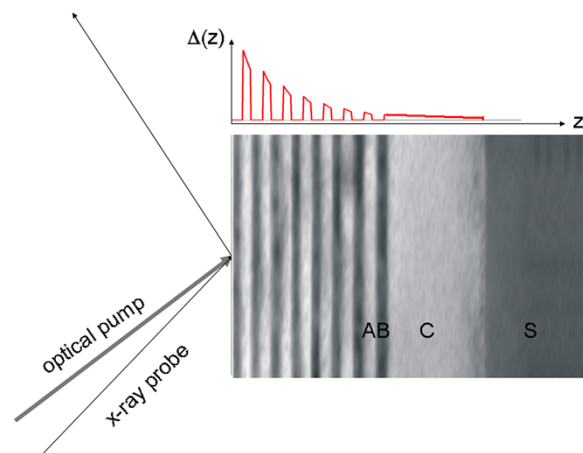


Fig. 1 Schematic of the experiment. An optical laser pulse excites a SL sample with the stacking sequence $(B_n/A_m)_pCS$ (shown here as a TEM image), generating a stress profile $\Delta(z, t = 0)$ (upper panel). In the particular sample shown $A = \text{SRO} = \text{SrRuO}_3$, $B = \text{STO} = \text{SrTiO}_3$, contact layer $C = A$ and substrate $S = B$

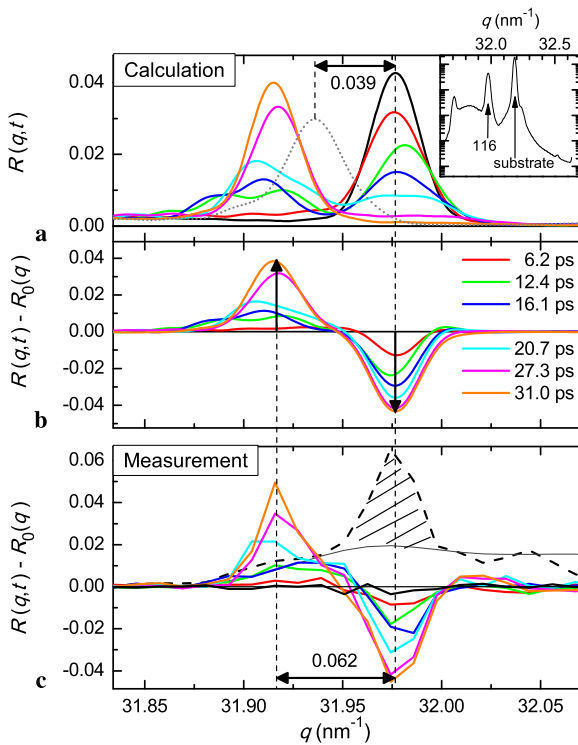


Fig. 2 (a) Calculated rocking curves in the vicinity of the (0 0 116) SL reflection as a function of pump-probe time delay. The short dashed line shows the peak after the strain waves have left the SL ($t \gtrsim 70$ ps). *Inset*: Extended rocking curve including the (0 0 2) STO substrate peak [1]. (b) Derived difference rocking curves with same color code for $t > 0$. (c) Measured unpumped rocking curve (dashed line) including background contribution (thin black line). The thick black line shows the difference curve for $t = 0$. Other lines show the measured difference rocking curves with the same color code as in panel (a)

the changes of the Bragg-reflectivity curve of the sample for a specific time delay t with respect to the spectra averaged over time delays before the excitation pulse $R_0(q) = R(q, t \leq 0)$ (dashed line). This procedure removes a background contribution to the signal (thin black line) which originates from the focusing of X-rays by a multilayer mirror and leads to signals on the X-ray CCD detector at all angles. For comparison, panel (b) shows the good agreement to the corresponding difference spectra from the simulation (see theory section) and panel (a) shows the calculated spectra directly, clearly representing the disappearance of the right peak and its reappearance to the left. Note that the appearing peak has strongly shifted components around 31.9 nm^{-1} for early times ($0 < t < 20$ ps) and it slightly moves back toward larger angles at later times ($t > 20$ ps). The details such as height, position and shape of the peaks in the experimental and calculated difference spectra show excellent agreement. The spectrum for $t = 0$ (thick black line in Fig. 2(c)) demonstrates that the difference spectra ac-

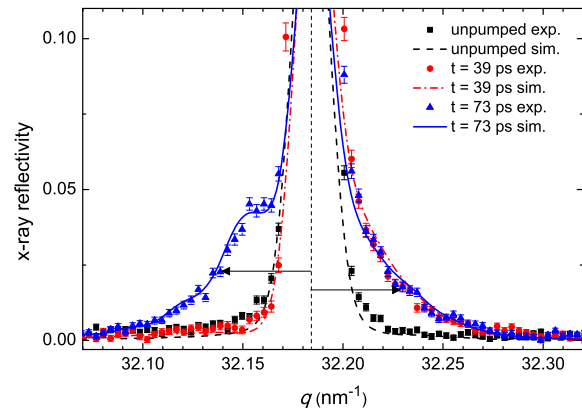


Fig. 3 X-ray diffraction curves in the vicinity of the (0 0 2) STO substrate reflection. *Symbols* report the measured data, *lines* correspond to simulations (see text). At 39 ps (73 ps) after the laser-pulse excitation a compression (expansion) wave has entered the substrate, giving rise to the shoulder on the high-angle (low-angle) side. The asymmetry originates from complex interferences of the X-rays from the distorted and undistorted parts of the substrate

tually lead to a correct subtraction of the unwanted background as the experimentally measured difference signal is approximately zero.

Without detailed simulation, the splitting of the SL-Bragg peak for intermediate times can be attributed to two regions of the SL, one having the static spatial SL-period d_{SL} (right peak) and one exhibiting an expanded lattice. The maximum strain of the entire SL occurs at a time delay of approx. 35 ps and is calculated by

$$\epsilon_{\max} = \frac{D_{\max} - D(0)}{D(0)} = \frac{q_{\max}^{-1} - q(0)^{-1}}{q(0)^{-1}} \quad (1)$$

From Fig. 2 we read $\epsilon_{\max} \approx 0.062/31.975 = 1.9 \cdot 10^{-3}$. This experiment was performed at the femtosecond X-ray diffractometer in Potsdam with laser pulses (≈ 100 fs, 800 nm) at a fluence of approx. 10 mJ/cm^2 .

In addition, we monitored the shoulders of the STO substrate reflection with a higher angular resolution by performing diffraction experiments with the highly collimated X-rays at the FEMTO-slicing beamline at the SLS. The resulting rocking curves recorded under somewhat increased fluence and at 400 nm pump wavelength are presented in Fig. 3. Cross-checks with 800 nm pump pulses show similar results. From the angular separation of the shoulder from the substrate peak we can estimate the amplitude of the strain wave in the substrate to be $\epsilon_{\text{STO}} = \Delta c/c = 0.04/32.2 \approx 1.24 \cdot 10^{-3}$, which is slightly smaller than the expansion of the SL observed above.

2.2 Discussion of results

In the following we discuss how the total optical excitation energy is deposited in the lattice. Using the absorption depth $\zeta_{\text{SRO}} = 52$ nm and the absorbed pump fluence $F \approx 10$ mJ/cm², the energy density absorbed by the conduction band electrons of SRO in each layer exponentially decays from $\rho_E^{\text{SRO}} \approx 1.8 \cdot 10^9$ J/m³ in the first to $\rho_E^{\text{SRO}} \approx 4.3 \cdot 10^8$ J/m³ in the tenth layer [1]. This energy is then coupled to phonons of SRO on a 100 fs timescale which essentially leads to the expansion of the SRO layers [1–4]. We assume that the expansion of the SL is induced exclusively by an expansion of SRO layers with a linear thermal expansion coefficient $\alpha_{\text{SRO}} = 1 \cdot 10^{-5}$ K⁻¹ and a volumetric heat capacity $C_{\text{SRO}}^{\text{heat}} = 3 \cdot 10^6$ J/(K m³) of SRO [9]. The average deposited energy density $\rho_{\text{av}}^{\text{SRO}} \approx 1.04 \cdot 10^9$ J/m³ in the SRO layers then corresponds to a temperature rise of $\Delta T = \rho_{\text{av}}^{\text{SRO}}/C_{\text{SRO}}^{\text{heat}} \approx 347$ K. The relative expansion of the entire SL due to the exclusive expansion of SRO is $\epsilon(\Delta T) = d_{\text{SRO}}\alpha\Delta T/d_{\text{SL}} \approx 1.2 \cdot 10^{-3}$ which is similar to ϵ_{max} .

In a next step, we calculate the energy density transferred to coherent acoustic strain in the SL and later on in the substrate from the measured UXR D data. First, we estimate the amount of energy in the coherent acoustic modes that lead to the observed maximum shift of the SL reflection (Fig. 2). The elastic modulus $E = v_{\text{SL}}^2 \cdot \rho$ is calculated from the averaged longitudinal sound velocity v_{SL} and the mass density ρ of STO and SRO. From the observed maximum strain ϵ_{max} in the SL with a thickness of $D = 250$ nm we infer the deformation energy density of the SL, i.e. the integrated energy in the longitudinal acoustic modes, to be $\rho_{\text{LA}}^{\text{SL}} = 1/2 E \epsilon_{\text{max}}^2 = 5.3 \cdot 10^5$ J/m³, corresponding to a fraction of approx. $5.2 \cdot 10^{-4}$ of the optically deposited energy density. We will see in the discussion of the theory section that this overestimates the coherent sound energy. In fact, not the maximally shifted curve in Fig. 2(a) but rather the gray dotted curve shows the peak shift corresponding to the heat expansion $\epsilon_{\text{heat}} = 1.2 \cdot 10^{-3}$ of the sample which—as we will show—also corresponds to the amplitude of the coherent strain wave.

Second, we alternatively consider the observed shoulders of the substrate peak in Fig. 3. As no heat is deposited in the substrate, the lattice deformation indicated by these shoulders must originate from the coherent sound waves propagating into the substrate. In the theory section we will show that in fact both the splitting of the SL peak and the substrate peak shoulders probe the same superposition of eigenmodes, however, the SL peak probes these delocalized phonons locally within the 250 nm thick SL, whereas the substrate shoulders probe the same modes locally in the first few microns of the substrate. During the propagation into the substrate the ratio of the sound velocities $s = v_{\text{STO}}/v_{\text{SL}} \approx 1.3$

leads to a traveling wave with total length of $l_W = 2sD = 650$ nm (compressive + tensile part). The average compressive and tensile strain ϵ_{STO} inferred from the substrate peak shoulders on the high- q and low- q side, respectively, yields an energy density $\rho_{\text{LA}}^{\text{STO}} = 3.5 \cdot 10^5$ J/m³. Comparing this to $\rho_{\text{LA}}^{\text{SL}}$ one finds that the energy density of the coherent sound is smaller in the substrate, however, the acoustic energy fluence $F_{\text{LA}} = \rho_{\text{LA}}^{\text{STO}} \cdot l_W \approx \rho_{\text{LA}}^{\text{SL}} \cdot D$, i.e., the coherent acoustic energy per excited sample area, is conserved (cf. Fig. 7).

This implies that at the used pump fluence, only a fraction of $F_{\text{LA}}/F = 5 \cdot 10^{-4}$ of the deposited energy is converted into coherent acoustic waves, whereas the rest remains as incoherent phonons, i.e. lattice heat. Note that the energy density ρ_{LA} of the coherent wave is proportional to the square of the strain ϵ^2 , whereas the deposited heat energy $\rho_{\text{av}}^{\text{SRO}}$ is proportional to ϵ according to linear heat expansion. For lower fluences an even smaller fraction of light energy is converted to the coherent sound wave.

3 Theory

In order to analyze the experimental results quantitatively, to visualize the dynamics and to verify that even under such strong excitation the response of the sample is still linear, we set up a linear-chain model of masses and springs. A similar linear-chain model was presented in Ref. [21] for the discussion of ultrafast electron diffraction data on a thin metal film. In the following we describe the extension to superlattices. More importantly, we present a normal-mode analysis of this linear-chain model and discuss how this is relevant to the interpretation of diffraction data.

3.1 Linear-chain model

We consider a multilayer with the stacking sequence $(B_n/A_m)_P CS$ composed of m unit cells of an opaque material A and n unit cells of a transparent material B epitaxially grown as a SL with P periods on a virtually infinitely thick and transparent substrate S with a thin contact (electrode) layer C (cf. Fig. 1). The SL is excited with an ultrashort optical light pulse. This heats up the opaque layers A and induces expansive thermal stress $\Delta(z)$ on a timescale τ_Δ short compared to all atomic motions that are of interest in this paper ($\tau_\Delta \ll 1/\omega_{\text{SL}}$). The excitation stress $\Delta(z_A) \sim e^{z_A/\zeta_A}$ varies as a function of penetration depth z_A through opaque layers A and is basically determined by the bulk optical absorption length ζ_A . As a first approximation, we assume that on the timescale of interest, the thermal stress remains constant after the excitation, i.e. $\Delta(z, t) = \Delta(z)H(t)$, where $H(t)$ is a Heaviside step function in time t . In other words, we disregard slow cooling by heat conduction. This assumption is justified independent of the photon energy [3]. We

disregard the distinction of electron and phonon contributions to the stress [21] as this should only marginally affect the timing in our experiments.

For the simulation of acoustic waves in the structure we construct a one-dimensional model of N masses and springs along the z -direction (c -axis), where each unit cell is represented by a mass m_A , m_B , m_C and m_S , respectively, which are connected by springs having a force constant $k_i = m_i v_i^2 / c_i^2$. Here v_i is the longitudinal sound velocity, m_i is the mass and c_i is the out-of-plane lattice constant of the i th unit cell ($i = 1, 2, \dots, N$).¹ This model allows for the simulation of all longitudinal acoustic modes propagating perpendicular to the surface of the sample. It neglects longitudinal optical modes of the bulk crystals A , B , C and S and all transverse motions. Alternatively, one could follow a continuum-model approach [6], however, here we want to focus on a normal-mode analysis.

To calculate the displacements $x_i(t) = z_i(t) - z_i^0$ from the equilibrium positions z_i^0 in a linear chain of N masses m_i that are connected by springs with force constants k_i and are subject to an additional force $F_i(t)$ (optically induced stress), we have to solve a system of N linear inhomogeneous differential equations

$$m_i \ddot{x}_i = -k_i(x_i - x_{i-1}) - k_{i+1}(x_i - x_{i+1}) + F_i(t) \quad (2)$$

where $i = 1, \dots, N$.

Unlike Ref. [21] we do not solve this set of equations by numerical integration (such as Runge–Kutta methods) but rather find the general solution

$$\mathbf{X}(t) = \sum_{j=1}^N \mathcal{E}_j \cdot A_j e^{i\omega_j t} \quad (3)$$

by diagonalization of the force matrix (see Appendix) in terms of eigenvectors \mathcal{E}_j to the eigenvalues (eigenfrequencies) ω_j of the system, which in fact represent the acoustic phonon modes of this nanostructure. $\mathbf{X}(t)$ is a vector containing the time-dependent coordinates $x_i(t)$ of all masses. The appropriate boundary condition is depicted in Fig. 4 which shows that at $t = 0$ the springs are quasi-instantaneously compressed (laser induced stress $\Delta(z)$ in SRO) and subsequently evolve toward the configuration for $t \rightarrow \infty$ where all springs attain their original length.

We use the physical insight that the additional time-independent forces proportional to $\Delta(z)$ trigger a “displacive excitation of coherent phonons” (DECP) by displacing the equilibrium position of the masses. Since the essential effect of heating material A is its expansion while keeping the compressibility constant, we can visualize this

¹This corresponds to an elastic modulus $E = \rho v^2$ in a continuum-model approach.

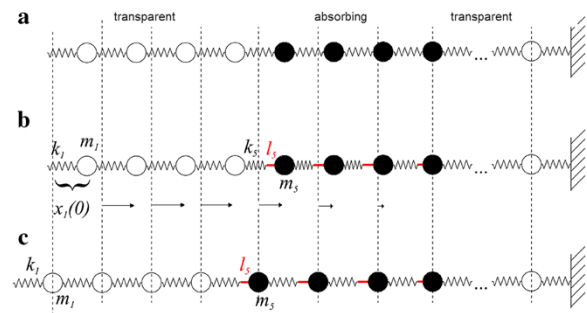


Fig. 4 Schematic of the linear-chain model. (a) For $t < 0$ all masses are at rest. (b) At $t = 0$ an excitation stress Δ is induced, which is subsequently constant. In the linear-chain schematic it is represented by incompressible sticks, which lead to an instantaneous compression of the springs in the opaque material A . The force constant of the springs remains unchanged. For $t > 0$ masses move according to the new forces. (c) Rest positions of masses x^∞ for $t \rightarrow \infty$

process by instantaneously inserting incompressible spacer sticks between the springs and the atoms, which have a length proportional to $\Delta(z)$ (see Fig. 4(b)). After very long times ($t \rightarrow \infty$), the linear chain would relax into configuration (Fig. 4(c)) where all springs are at their equilibrium length, which they had before excitation (Fig. 4(a)). After solving the equations for all coordinates $x_i(t)$, one can now analytically calculate the relative displacement of the masses $\Delta x_i = x_i - x_{i-1}$ and the corresponding strain $\epsilon_i = [\Delta x_i(t) - \Delta x_i(0)] / \Delta x_i(0)$ for any time t and any given initial stress profile $\Delta(z)$.

This model contains no anharmonic interaction potential and we expect a linear response of the lattice dynamics proportional to the excitation stress $\Delta(z)$. The amplitude of $\Delta(z)$ is the only fitting parameter in this simulation. The lattice parameters, elastic constants, heat capacity etc. are taken from the literature, as well as the absorption length ζ_A . The calibration of the stress amplitude is simply achieved by matching the experimentally observed change of SL-Bragg angle to the average lattice expansion. Figure 5 shows the result of such a calculation for an SRO/STO SL including the ≈ 42 nm SRO contact layer [1] with an absorption length of the optical excitation light of $\zeta_{\text{SRO}} = 52$ nm [22]. Both standing strain wave contributions with the spatial period of the SL and propagating strain waves can be seen in this contour plot. The slopes of the diagonal stripes directly visualize the local average sound velocity $v_{\text{SL}} = \Delta z / \Delta t$, which is slightly different in the SL, contact layer and substrate.

In order to discuss the significance of eigenmodes in SLs we compare the situation of a few-period SL with $P = 11$ to an infinite SL by imposing periodic boundary conditions. Such an infinite SL was well approximated in the experiments on a GaAs/AlGaAs SL with $P = 2000$ [7, 23]. For better comparison, the present calculation is performed for the SRO/STO SL discussed above using periodic boundary

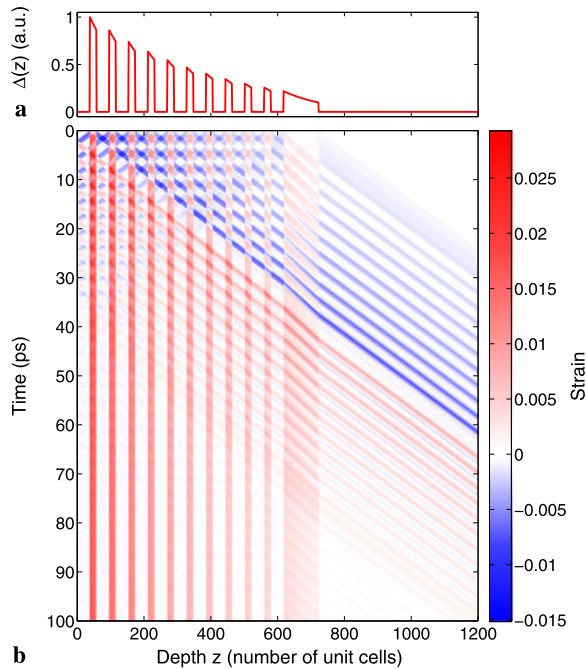


Fig. 5 (a) Stress profile $\Delta(z, t = 0)$. (b) Contour plot showing the calculated strain in the sample as a function of space and time for the SRO/STO SL investigated experimentally [1–4]

conditions. Plotting the eigenfrequencies ω_j as a function of the normal-mode wavevector Q_j visualizes the phonon dispersion relation $\omega(Q)$ (cf. Fig. 6(b)). For a SL it is useful to recall that the dispersion relation can be represented in a smaller mini-Brillouin zone, where the zone boundary is given by π/d_{SL} instead of π/c if d_{SL} is the thickness of one SRO/STO double layer. Figure 6(a) compares the squared modulus $|A_j|^2$ of the complex amplitudes for the eigenmodes with frequency ω_j (cf. (3)) in an infinite SL with homogeneous excitation ($\zeta \rightarrow \infty$, red dots), in the $P = 11$ SL with homogeneous excitation (thin green line) and in the $P = 11$ SL with the experimental absorption length of $\zeta_{\text{SRO}} = 52$ nm (black) [22]. As the spatial symmetry of the excitation pattern $\Delta(z)$ intrinsically mimics the symmetry of the SL, only eigenmodes with a wavevector equal to integer multiples of the reciprocal SL wavevector $Q_{\text{SL}} = g = 2\pi/d_{\text{SL}}$ are selected. For an infinite SL such modes are optical phonons at the zone center of the mini-Brillouin zone scheme (zone-folded dispersion relation plotted in green in Fig. 6(b)). In this case only few modes are excited. One of them has almost unit probability and we refer to it as the symmetric SL mode with period $T_{\text{SL}} = 2\pi/\omega_{\text{SL}}$, as it corresponds to an expansion of the SRO layers symmetric with respect to the center of the SRO layer [5]. The related asymmetric mode and all higher harmonics have at least two orders of magnitude less weight. Note that the splitting of the symmetric and asymmetric mode is very

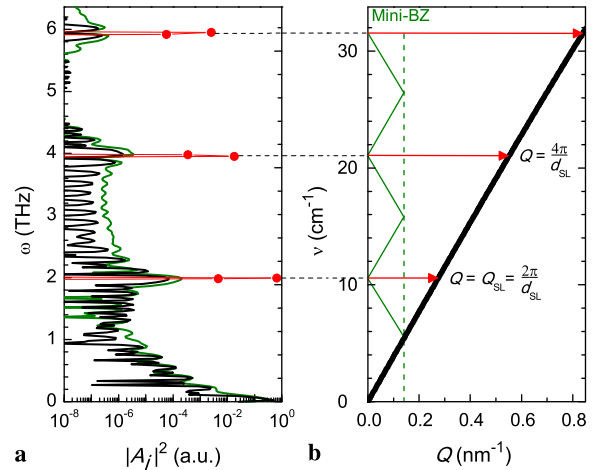


Fig. 6 (a) Phonon population spectrum of strain evolution decomposed into amplitudes $|A_j|^2$ of eigenmodes to eigenfrequency ω_j for the infinite SRO/STO SL (periodic boundary condition) with homogeneous excitation ($\zeta_{\text{SRO}} \rightarrow \infty$, red dots) and for the finite SL ($P = 11$) with homogeneous excitation (thin green line) and the experimental optical penetration depth of $\zeta_{\text{SRO}} = 52$ nm (thick black line). Note that for the infinite SL single mode is excited. (b) Dispersion relation of a SL from linear-chain model (thick black line) back-folded into the mini-Brillouin zone (thin blue line)

small ($\Delta\omega/\omega = 4.5 \cdot 10^{-5}$), indicating an excellent acoustic impedance matching, which is evident also from Fig. 5 where almost the entire soundwave is transmitted to the substrate with essentially zero reflection amplitude.

If we simulate a finite SL, i.e., we do not consider the periodic boundary condition, and add a substrate beneath the SL, the symmetry is broken by both the surface of the SL and the interface to the substrate. Under these conditions, several modes are excited with considerable amplitude (cf. green curve in Fig. 6(a)). The mode density in the simulation depends on the number of substrate unit cells taken into account, however, clearly the modes in the vicinity of the SL mode and its harmonics still have enhanced weight. Here we chose the substrate approximately three times thicker than the SL, in order to prevent reflections from the backside within the simulated timescale in Fig. 5(b). It is the breaking of the symmetry by the surface and the substrate that induces the high occupation of low-frequency modes near $\omega = 0$ indicating a propagating sound wave. If the excitation is changed to the exponentially decaying absorption of energy in the SL, only slight modifications of the phonon population spectrum $|A_j(\omega)|^2$ is observed.

There are several advantages of the normal-mode analysis as compared to a numerical propagation of the differential equation [21]: (i) It allows rapid calculation of strain pattern for any time t . (ii) Individual modes can be switched off to disentangle complex dynamics. (iii) The wavevector Q of each mode predicts where the corresponding time dependence will show up in the UXRD signal. (iv) Wavepacket

dynamics including the coupling of SL and substrate is interpreted as interference of waves.

3.2 Comparison to experimental data

We first discuss the coarse findings depicted in Fig. 5. For the SL coupled to the substrate, several eigenmodes in the vicinity of ω_{SL} with approximately equal spatial periodicity are excited, however, they extend into the substrate with similar amplitude as well. According to the mini-BZ scheme, at early times these modes give rise to a standing wave composed of waves with $-Q_{\text{SL}}$ propagating toward the surface and Q_{SL} propagating toward the substrate. This standing wave pattern which is localized in the SL disappears when all waves have propagated into the substrate and hence no time dependence with frequency ω_{SL} remains in the SL. The waves leave the multilayer as propagating sound waves having the central frequency of the SL mode and the wavevector $Q_{\text{SL}}^* = 2\pi/d_{\text{SL}}^*$, which is determined by the ratio of the substrate sound velocity v_{STO} and the average sound velocity in the SL, i.e., $d_{\text{SL}}^* = v_{\text{STO}}T_{\text{SL}} = d_{\text{SL}} \cdot v_{\text{STO}}/v_{\text{SL}}$ [16]. The higher harmonics of the SL mode with frequency $\omega_{\text{SL}} = 2\pi/T_{\text{SL}}$ also show considerable—albeit much smaller—amplitudes and support the spatiotemporal sharpness of the sound features observed in Fig. 5. In previous experiments, these folded acoustic phonons at ω_{SL} were observed as intensity modulations of the SL Bragg reflections [1–4]. In a SL these phonons are back-folded to $Q = 0$ (green dispersion relation in Fig. 6), and hence they show up in the UXRd measurements at the Bragg angle of stationary SL reflections. When the wavepacket has traveled into the substrate, these modes yield sidebands to the substrate at $G_{\text{STO}} \pm nQ_{\text{SL}}^*$, where n is an integer [16]. The origin of these modes can be seen by the small wavelets that are generated at each interface of the SL.

The surface and the contact layer (interface to the substrate) are the spatial origin of the low-frequency modes [cf. Fig. 5(b)]. The reflection of the compressive wavepackets at the surface results in an expansion wave traveling straight through the SL into the substrate with marginal reflection at the interface. The contact layer launches a compression wave into the substrate and another one toward the surface, where it is converted into an expansion wave. Inspection of the average strain per double layer in Fig. 5(b) at around 15–20 ps shows that one half of the SL is expanded while the other half has preserved the average lattice constant. This qualitatively explains the experimentally observed disappearance of the original SL peak and the appearance of a shifted peak (Fig. 2). There is no continuous shift of the UXRd curve because there is no region in the SL which has an intermediate strain. The initially larger width of the appearing peak is readily explained by the fact that only a small spatial fraction of the SL contributes at these times

($t < 20$ ps). The very same low-frequency acoustic modes give rise to the sidebands of the substrate peak shown in Fig. 3. In particular, at $t = 39$ ps only the right shoulder exists as the substrate is compressed [blue in Fig. 5(b)] and at 73 ps also the expansion wave has entirely entered the substrate [green in Fig. 5(b)] inducing the shoulder on the left.

The atomic motion calculated from the linear-chain model also allows to extract information on the energy transport by coherent phonons. We compute the kinetic energy of the atoms from their velocity dx_i/dt and the potential energy from the stress as a function of time for both individual types of SL layer and the substrate. Figure 7 shows the total energy stored in coherent phonons in a box with a cross section of 1 cm^2 .² At $t = 0$ all energy is quasi-instantaneously stored as potential energy in the SRO layers. As one would expect for a single excited oscillator (phonon mode), the energy is converted into kinetic energy and back to potential energy, with two maxima for each type of energy per period. The oscillation period of 3.2 ps is verified by the experimental data [1–4]. On the timescale of sound propagation ($T = D/v_{\text{SL}}$) the vibrational energy leaks into kinetic and potential energy of the substrate. Accordingly, the sum of potential and kinetic energy of the SL decays to half its initial value within 35 ps. The modulation amplitude of the potential energy is reduced by a factor of two faster, namely within 18 ps. This modulation is a direct measure of the energy stored in modes in the vicinity of the superlattice mode ω_{SL} . However, the damping of the signal oscillation amplitude observed in UXRd experiments [1, 4] is underestimated, indicating that additional factors such as anharmonic interaction and dephasing play a role. From the lattice positions $x_i(t)$ we can also calculate the average expansion of the entire SL which reaches a maximum after $T = P \cdot d_{\text{SL}}/v_{\text{SL}} = 35$ ps, in excellent agreement with previous measurements [4]. The maximum wave vector transfer q_{max} observed in Fig. 2 is used to calibrate the maximum average strain in the simulation [(1)].

After $t = 35$ ps already half of the total energy stored in longitudinal acoustic waves has moved from the SL into the contact layer and further into the substrate. It is important to note that this timescale for energy loss is not a coupling time constant, but a timescale describing the interference of the various excited normal modes, which give rise to a propagating sound wave with a particular wave vector. Unless strong differences in the acoustic impedance of the SL and the substrate lead to substantial reflection of waves at the interface, the expansion wave starting from the surface of the SL reaches the substrate after 35 ps.

²Here we plot the fraction of total energy in a fixed volume stored in the SL, the contact layer and the substrate. Plotting energy densities would not allow to see the energy conservation for the sum of energies.

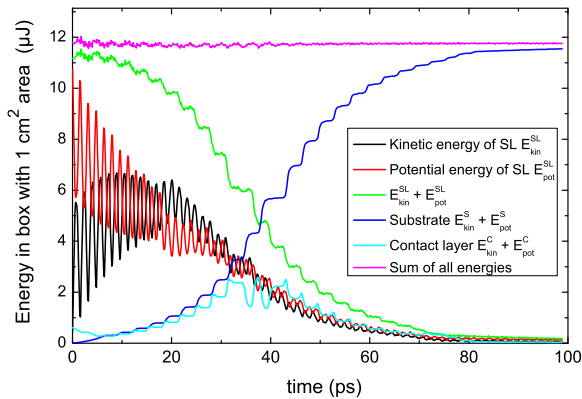


Fig. 7 Energy balance for the finite SL calculated from the linear-chain model. Both the kinetic and potential energy (stress) of the SL have two maxima per period. The energy of the propagating sound wave leaks out of the SL and travels through the contact layer (light blue) into the substrate (dark blue). We assume no considerable heat conduction on this timescale. For an infinite SL the kinetic energy would return to zero after each period (not shown), while in the present case the propagating sound wave always carries kinetic energy

In the discussion of UXR D experiments the diffraction of X-ray photons is described as resulting from the scattering by a reciprocal lattice vector and/or a phonon wavevector which describes a delocalized vibration mode. However, the X-ray-diffraction condition probes only particular spatial parts of the sample in which the Bragg condition is fulfilled, even though the vibrational mode is delocalized over the entire crystal.

The loss of modulation amplitude in UXR D signals [1–4] can be explained in our model as resulting from the coupling of the observed part of the sample (SL) to unobserved regions of the sample (substrate). The intensity modulations in the UXR D signal originate from eigenmodes with frequency ω_{SL} . Similarly, the low-frequency acoustic part of the spectrum consists of normal modes which have amplitude in the SL and the substrate. Figure 2 shows the rapid disappearance of a SL reflection and the appearance of a shifted peak which is completed after 70 ps. The dynamically interfering normal modes subsequently show no time dependence of the SL reflection which only probes the spatial region of the SL. Instead, the observation of the shoulders of the substrate peak in Fig. 3 demonstrates that at this time the coherent sound wave is in the substrate.

This implies that when calculating the coherent wave energy from the transient position of the appearing rocking curve we have to use the value for $t > 70$ ps, as this corresponds to the final state with a tensile and compressive sound wave traveling deeper into the substrate and a quasi-stationary expansion of the SL which is represented in our model by the red spacer sticks (heat expansion) in Fig. 4(c). The springs of the SL in this figure are at their equilibrium position, i.e., there is no coherent sound left in the SL. In

other words, the coherent wave energy is imposed on the sample by the initial condition which requires the compression of springs in the metallic layers of the SL (Fig. 4(b)) with respect to the final conditions at $t \rightarrow \infty$ (Fig. 4(c)). Hence, the expansive strain ϵ_{heat} for $t > 70$ ps, which is approx. 77% of the maximum expansion ϵ_{max} , measures the heat expansion of the SL and consequently the entire coherent sound energy which is encoded in the compressed springs of Fig. 4(b) at $t = 0$. For intermediate times the SL peak position is measuring a complex combination of heat expansion and additional expansion and compression due to the coherent sound waves.

Previous experiments have shown pronounced oscillations of the X-ray diffraction efficiency of SL peaks since the structure factor of the SL unit cell is modulated with the frequency ω_{SL} of the SL phonon [1–4, 7, 8]. From the linear-chain model we can deduce the energy contained in the excited modes in the vicinity of ω_{SL} (cf. Fig. 6(a)). These modes contribute approx. 30% to the total coherent mode energy because the energy per mode scales as $|A_j|^2 \omega_j^2$. The SL phonon modes itself, however, are neither responsible for the splitting of the appearing peak nor for the shoulders of the substrate. Instead, within the SL they cause the modulation of the peak intensity of SL peaks and within the substrate they give rise to sidebands to the substrate peak at $G_{\text{STO}} \pm n \cdot Q_{\text{SL}}$.

We stress that within our model, at $t = 0$ the delocalized eigenmodes are excited with their respective amplitudes A_j and merely the evolution of the relative phases of the modes leads to the complex pattern of standing and propagating sound waves in the SL and the substrate.

3.3 Quantitative calculation of rocking curves

In order to quantify the comparison of the model calculations and the measurement, the strain profile derived from the linear-chain model is used to calculate the XRD signal according to the Darwin formalism, taking into account the deformation of each unit cell [24]. The X-ray rocking curves $R(q, t)$ resulting from the strain pattern depicted in Fig. 5 are plotted in Fig. 2(a). For comparison with experiments (Fig. 2(c)) we plot the calculated difference spectra $R(q, t) - R_0(q)$ in Fig. 2(b).

For large time delay (orange curves in Fig. 2) the entire SL peak has changed its position, i.e. the difference signal is maximally negative around the initial position $q(t \leq 0)$ and reaches its positive maximum around the new position q_{max} . For intermediate times, a doublet shows up, indicating that half of the SL has already expanded whereas the remaining part still exhibits an unchanged SL period. Note that the difference of the central positions of the two peaks is larger at early times (green, blue and cyan). This corresponds to the fact that the early expansion of the layers near the surface is larger compared to the later-expanding near-substrate

layers which is due to the inhomogeneous excitation profile $\Delta(z)$. This particular feature is also visualized by the dark red color code for large expansion in the strain contour plot (Fig. 5).

While the essential features of the SL peak would be represented by a kinematic XRD theory as well, the calculation of the substrate peak (Fig. 3) and its shoulders definitely requires the used dynamical diffraction calculations. In particular, we have to add a virtually infinite STO substrate underneath the unit cells of the SL and the substrate used for the coherent phonon simulation, since the extinction length for X-rays is $1 \mu\text{m}$ at the Bragg peak and elsewhere limited by the absorption length of $10 \mu\text{m}$. Figure 3 again shows very good agreement of simulation and experiment. Not only the effect size and timing is well reproduced, but also details like the smoothly decaying right shoulder as opposed to the decreasing in two steps seen for the left shoulder.

4 Conclusion

A simple linear-chain model is used to calculate the ultrafast motion of atoms in a superlattice coupled to a substrate upon optical excitation of the opaque layers, which results in the generation of coherent acoustic phonon modes. The surface of the SL and the SL-substrate interface break the translational symmetry of the multilayer, leading to normal modes having approximately the spatial periodicity of the SL mode, d_{SL} , and nearly equal amplitude in both the SL and the substrate. The observed energy loss from the superlattice oscillation, which has been measured previously in UXR data experiments [1–4], is predicted in this model. The time-evolution of these modes and their interference subsequently develops propagating waves which transport a large fraction of 99% of the initial energy in the coherent acoustic modes discussed in this article into the substrate within 100 ps. This requires and therefore evidences the excellent acoustic impedance matching between the epitaxial SRO and STO layers considered here. The mixed behavior originates from the fact that two small sound wavepackets are launched at each interface within the SL, giving rise to acoustic pulse trains traveling toward the surface and the substrate, respectively. The former are reflected at the sample surface and eventually also leave the SL into the substrate.

In the example discussed in this article, we demonstrate that the SL reflection does not probe the occupation of phonon modes but rather the spatial strain pattern resulting from the interference of phonon modes in the region of the SL. The loss of modulation amplitude in UXR signals from the SL is due to the destructive interference of modes in the spatial region of the SL. The coherent sound energy initially deposited in the SL is not dissipated but coherently

transported into the STO substrate by the concomitant constructive mode interference therein which forms a propagating strain wave. This strain wave is probed by UXR in the vicinity of the substrate reflection (Fig. 3).

As presented, our model which solely describes sound propagation is able to correctly predict the observation of a peak splitting in UXR data. In a previous publication [25] the curve splitting instead of a shifting was interpreted as a feature indicative of a phase transition. The cited publication reports additional evidence (threshold behavior, an “isosbestic point”...) for the phase transition. In the present paper we show that a peak splitting in a transient rocking curve is not sufficient to conclude a phase transition. To the best of our knowledge this is the first report on the splitting of a Bragg peak of a thin film or SL due to sound propagation. As most thin film samples are grown on substrates, we expect the discussed features to appear in several future UXR studies.

Acknowledgements We thank Chris Milne, Renske van der Veen and Steve Johnson for their help with the experiments at the FEMTO-slicing beamline (XOSLA) of the Swiss Light Source at the PSI, Villigen, Switzerland and Ionela Vrejoiu from Max-Planck Institute for Microstructure Physics in Halle for fruitful discussions and for providing the sample experimentally investigated. M.B. would like to thank Dr. Michael Woerner (MBI Berlin) for very fruitful discussions on the model and simulations using “spacer sticks”. We gratefully acknowledge the financial support by the BMBF via grant No. 03WKPO3A and the Deutsche Forschungsgemeinschaft via grant No. BA2281/3-1.

Appendix

We divide (2) by m_i and define $\Delta_i(t) = F_i(t)/m_i$, $\kappa_{i,i} = -(k_i + k_{i+1})/m_i$ and $\kappa_{i,i+1} = \kappa_{i+1,i} = k_{i+1}/m_i$. Moreover, $\kappa_{i,j} = 0$ if $|i - j| > 1$, since only nearest neighbors are connected by springs. The values for $i = 1$ and $i = N$ must be set according to the correct boundary conditions, namely, $\kappa_{1,1} = -(k_2)/m_1$ and $\kappa_{N,N} = -(k_N)/m_N$. For the surface of the SL ($i = 1$) this yields a proper description for all times. The layer $i = N$ is chosen so deep in the substrate that it does not move within the simulated timescale. This gives the system of equations

$$\ddot{x}_i + \sum_{n=1}^N \kappa_{i,n} x_n = \Delta_i(t). \quad (4)$$

The homogeneous system ($\Delta = 0$) can be recast into the vector equation

$$\frac{d^2}{dt^2} \mathbf{X} = \mathbf{K} \mathbf{X} \quad (5)$$

where $\mathbf{X} = (x_1, \dots, x_N)^T$ is the vector containing all displacements and \mathbf{K} is the tri-diagonal matrix

19. F. Zamponi, Z. Ansari, C. v. Korff Schmising, P. Rothhardt, N. Zhavoronkov, M. Woerner, T. Elsaesser, M. Bargheer, T. Troitzsch-Ryll, M. Haschke, Femtosecond hard X-ray plasma sources with a kilohertz repetition rate. *Appl. Phys. A* **96**, 51 (2009)
20. P. Beaud, S.L. Johnson, A. Streun, R. Abela, D. Abramsohn, D. Grolimund, F. Krasniqi, T. Schmidt, V. Schlott, G. Ingold, Spatiotemporal stability of a femtosecond hard-X-ray undulator source studied by control of coherent optical phonons. *Phys. Rev. Lett.* **99**(17), 174801 (2007)
21. J. Li, R. Clinite, X. Wang, J. Cao, Simulation of ultrafast heating induced structural dynamics using a one-dimensional spring model. *Phys. Rev. B* **80**(1), 014304 (2009)
22. P. Kostic, Y. Okada, N.C. Collins, Z. Schlesinger, J.W. Reiner, L. Klein, A. Kapitulnik, T.H. Geballe, M.R. Beasley, Non-Fermi-liquid behavior of SrRuO_3 : Evidence from infrared conductivity. *Phys. Rev. Lett.* **81**(12), 2498 (1998)
23. M. Bargheer, N. Zhavoronkov, J.C. Woo, D.S. Kim, M. Woerner, T. Elsaesser, Excitation mechanisms of coherent phonons unravelled by femtosecond X-ray diffraction. *Phys. Status Solidi (b)* **243**(10), 2389 (2006)
24. S.A. Stepanov, E.A. Kondrashkina, R. Köhler, D.V. Novikov, G. Materlik, S.M. Durbin, Dynamical X-ray diffraction of multilayers and superlattices: Recursion matrix extension to grazing angles. *Phys. Rev. B* **57**(8), 4829–4841 (1998)
25. N. Gedik, Y. Ding-Shyue, G. Logvenov, I. Bozovic, A.H. Zewail, Nonequilibrium phase transitions in cuprates observed by ultrafast electron crystallography. *Science* **316**(5823), 425 (2007)

Tailoring interference and nonlinear manipulation of femtosecond x-rays

M. Herzog, D. Schick, W. Leitenberger, R. Shayduk, R. M. van der Veen, C. J. Milne, S. L. Johnson, I. Vrejoiu and M. Bargheer.

New J. Phys. **14**, 013004 (2012).

New Journal of Physics

The open-access journal for physics

Tailoring interference and nonlinear manipulation of femtosecond x-rays

Marc Herzog¹, Daniel Schick¹, Wolfram Leitenberger¹,
Roman Shayduk², Renske M van der Veen^{3,4},
Christopher J Milne^{3,4}, Steven L Johnson³, Ionela Vrejoiu⁵
and Matias Bargheer^{1,2,6}

¹ Institut für Physik und Astronomie, Universität Potsdam, Karl-Liebknecht-Str. 24-25, 14476 Potsdam, Germany

² Helmholtz-Zentrum Berlin für Materialien und Energie GmbH, Hahn-Meitner-Platz 1, 14109 Berlin, Germany

³ Swiss Light Source, Paul Scherrer Institut, 5232 Villigen PSI, Switzerland

⁴ Laboratoire de Spectroscopie Ultrarapide, Ecole Polytechnique Fédérale de Lausanne, 1015 Lausanne, Switzerland

⁵ Max-Planck-Institut für Mikrostrukturphysik, Weinberg 2, 06120 Halle, Germany

E-mail: bargheer@uni-potsdam.de

New Journal of Physics **14** (2012) 013004 (9pp)

Received 14 August 2011

Published 6 January 2012

Online at <http://www.njp.org/>

doi:10.1088/1367-2630/14/1/013004

Abstract. We present ultrafast x-ray diffraction (UXRD) experiments on different photoexcited oxide superlattices. All data are successfully simulated by dynamical x-ray diffraction calculations based on a microscopic model, that accounts for the linear response of phonons to the excitation laser pulse. Some Bragg reflections display a highly nonlinear strain dependence. The origin of linear and two distinct nonlinear response phenomena is discussed in a conceptually simpler model using the interference of envelope functions that describe the diffraction efficiency of the average constituent nanolayers. The combination of both models facilitates rapid and accurate simulations of UXRD experiments.

⁶ Author to whom any correspondence should be addressed.

A large variety of x-ray optics that can be used to monochromatize, focus and analyze the phase of hard x-rays have been invented and realized. Many of them have become standard tools in x-ray science [1] and some more recent developments include e.g. hard-x-ray interferometers with microelectronvolt resolution [2] and nanointerferometers based on refractive lenses [3]. Of particular interest is understanding the manifold physical processes in solids on atomic length and time scales for which hard x-rays providing a subpicosecond time resolution are mandatory [4–8]. Several methods to modify the time structure of x-ray pulses or pulse trains have been reported [9–11]. The concept of exploiting phonons in solid samples generated by femtosecond laser pulses as an ultrafast gateable x-ray mirror [12] has very recently been experimentally implemented using a layered nanostructure composed of the perovskite oxides SrTiO₃ (STO) and SrRuO₃ (SRO) [13]. The authors observed a giant response of a particular Bragg peak showing an intensity increase by a factor of 25 with a gating time of less than 1 ps. The general mechanism was explained as resulting from the expansion of the metallic SRO nanolayers and the concomitant compression of the STO nanolayers that consequently alters the structure factor of the observed Bragg reflection. The artificial spatial layering period was found to set the time scale of the transient gate and the measured diffraction curves could be simulated rather precisely, however, a detailed understanding of the ultrafast x-ray response required for purpose-oriented designing of nanostructures was lacking.

In this paper, we present a detailed analysis of the simulation of transient Θ – 2Θ x-ray diffractograms of periodically layered epitaxial nanostructures, also called superlattices (SL). We show numerical calculations obtained from combined results of (i) a linear-chain model computing the photoexcited lattice dynamics of a given sample [14] and (ii) fully dynamical x-ray diffraction (XRD) calculations. In the following, we refer to these combined linear-chain and dynamical XRD calculations as LCDX. The predicted features of the transient intensities of SL Bragg reflections—including linear and highly nonlinear responses to phonon amplitudes—are interpreted by a conceptually simpler envelope model (EM) that merely considers homogeneous deformations of the single layers. The EM already demonstrates key features that lead to the distinct nonlinear XRD dynamics of such SLs. A comparison to results of ultrafast x-ray diffraction (UXRD) experiments on two different SLs shows the very high degree of precision achieved by the LCDX. The presented analysis will be very valuable for the interpretation of UXRD data in general, and specifically for creating novel devices based on such nonlinear phenomena that utilize the tailorable x-ray interference in artificial nanostructures.

We test our numerical calculations by applying them to two different epitaxial SL samples both composed of metallic and dielectric perovskite oxides. In particular, we consider the previously investigated SL [SRO₂₀/STO₃₈]₁₁ [13] and a SL containing the ferromagnetic metal La_{0.7}Sr_{0.3}MnO₃ (LSMO), namely [LSMO₂₃/STO₃₅]₁₅. The index of each component represents the number of perovskite unit cells per layer, and the overall index gives the number of repeat units of the double layer (DL). This structural characterization of the samples was done by matching Θ – 2Θ diffractograms with simulations utilizing dynamical XRD theory according to the Darwin formalism [15]. Figures 1(a) and 2(a) show the XRD measurements (gray bullets) and the corresponding simulations (red solid line) for SRO/STO and LSMO/STO, respectively, without any laser excitation. In the following, we develop the EM that explains the particular

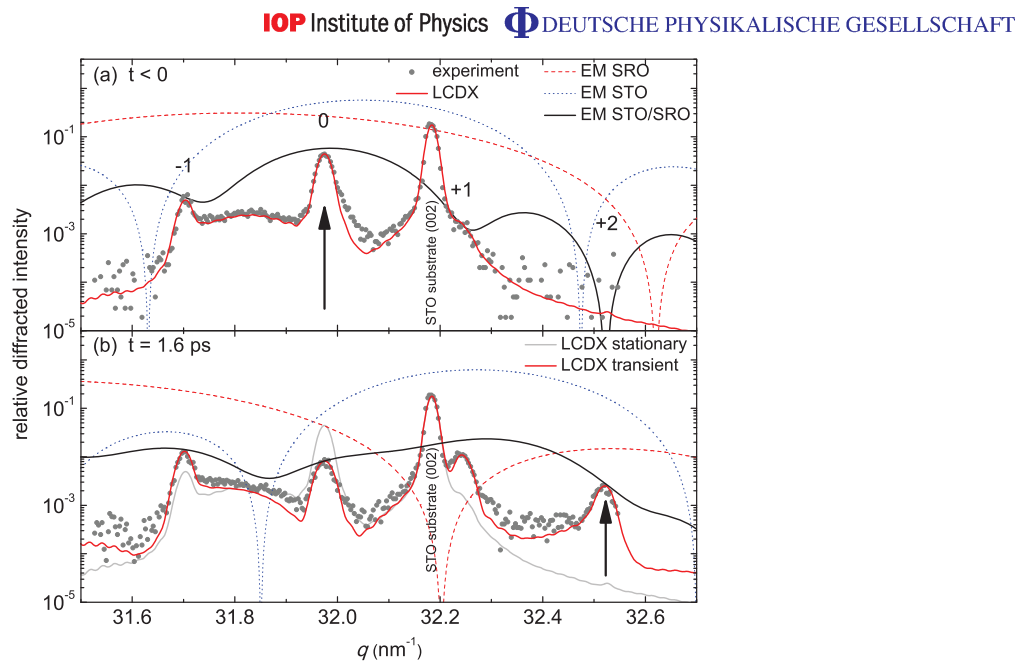


Figure 1. Experimental Θ – 2Θ scans (gray bullets) of the SRO/STO SL. The broken lines show the calculated single-layer envelope functions (scaled for clarity), the black solid line is the DL envelope function (scaled by the number of DL squared), and the red solid line is the resulting SL diffractogram of the LCDX at (a) $t < 0$ and (b) $t = 1.6$ ps after optical excitation with a fluence of 36.8 mJ cm^{-2} . The arrows mark the SL peaks considered in figure 3.

shape of these diffraction curves and provides a fundamental understanding of transient changes upon photoexcitation by femtosecond laser pulses.

As the thickness of the individual layers in both SLs is much smaller than the extinction depth ξ of the x-rays, the corresponding diffractograms are essentially the Fourier transform of their electron densities. Figures 1 and 2 show the square modulus of the diffracted x-ray amplitude $A_M(q)$ ($A_I(q)$) for a single metallic (insulating) layer of the respective sample as a red dashed (blue dotted) line. These curves match a sinc^2 function (the Fourier transform of a homogeneous slab), and we will refer to such curves as envelope functions. The width Δq of such envelope functions is inversely proportional to the real-space thickness d of the respective layer and their center position q_{env} encodes the average strain of that single layer. The envelope of one DL, $|A_{\text{DL}}|^2 = |A_M + A_I|^2$ (black line in figures 1 and 2) accounts for interference of the complex single-layer amplitudes⁷. The DL envelope is scaled by the respective number of DL squared. Clearly, it determines the intensity of the observed SL Bragg reflections since the SL Bragg peaks touch the DL envelope in figures 1(a) and 2(a). In other words, the observed intensity $I(q_{\text{SL}}, t)$ of a particular SL reflection at q_{SL} can be estimated from the relation $I \propto |A_{\text{DL}}|^2$. The SL Bragg peaks thus ‘sample’ the DL envelope at discrete wavevectors that are selected by the Laue condition $q_{\text{SL}} = n \cdot \frac{2\pi}{d_{\text{SL}}} = n \cdot g_{\text{SL}}$, where g_{SL} is the reciprocal lattice vector corresponding to the SL period $d_{\text{SL}} = d_M + d_I$ and $n \in \mathbb{N}$. The single-layer envelope functions themselves have significant intensity only in the q -range around the bulk Laue conditions

⁷ To be precise, one also has to account for the phase shifts due to transmission through the top layer before and after the reflection from the bottom layer. This effect is accounted for in the calculations.

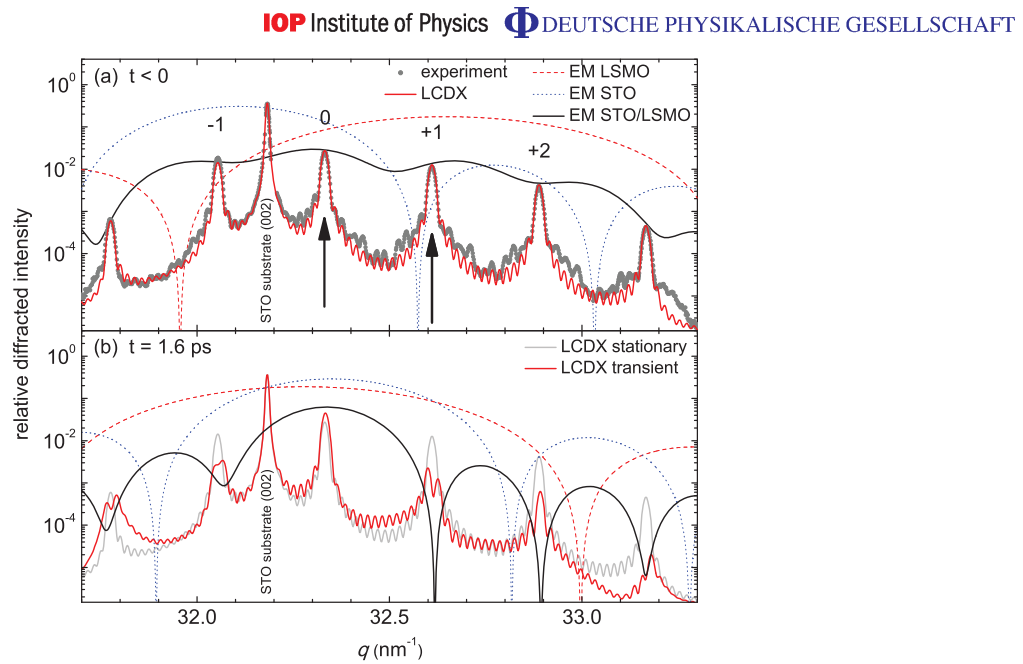


Figure 2. Experimental Θ – 2Θ scans (gray bullets) of the LSMO/STO SL recorded at the EDR-beamline of BESSY II (Helmholtz–Zentrum Berlin). The meaning of the lines and panels is analogous to figure 1, and the arrows mark the SL peaks considered in figure 4.

$q_{M/I} = m \cdot \frac{2\pi}{c_{M/I}}$, where $c_{M/I}$ are the out-of-plane lattice constants of the metal and the insulator, respectively, and $m \in \mathbb{N}$.⁸ For materials with similar c_M and c_I , we number the SL reflections as satellites to the Laue condition $q^{(0)} = \frac{2\pi}{c_{av}} = 2\pi(n_M + n_I)/(n_M c_M + n_I c_I)$ of the so-called zero-order SL peak (ZOP) corresponding to the average lattice constant c_{av} in one DL [16]. Here n_M and n_I correspond to the number of unit cells in the metallic and insulating layers, respectively.

We can now use the above introduced EM to predict the general features of transient changes of diffractograms after laser-pulse excitation such as presented in figure 1. The ultrafast deposition of the excitation energy in the metallic layers of the SL triggers their impulsive expansion [13] which shifts the red dashed envelope to smaller q values. The concomitant compression of STO shifts the blue dotted envelope to larger q values (compare the envelopes in panels (a) and (b) of figures 1 and 2). The magnitude of the envelope shifts is determined by the amplitude of this collective, spatially and temporally periodic lattice motion also referred to as SL phonon mode [14, 17]. As a consequence, the DL envelope function and thus the SL Bragg peak intensities are altered. Eventually, the entire SL will expand within the time $T_{exp} = D/v_{SL}$, where D and v_{SL} are the total SL thickness and the sound velocity in the SL, respectively. For small time delays $t \ll T_{exp}$, however, the SL period remains approximately constant and the SL Bragg peak positions q_{SL} do not change [18]. Here, we exclusively focus on these short-time dynamics.

The UXR experiments were performed at the FEMTO-slicing beamline of the Swiss Light Source (SLS), providing a time resolution of 140 ± 30 fs [19]. The samples were excited

⁸ In this paper, we exclusively consider the bulk (002) reflections.

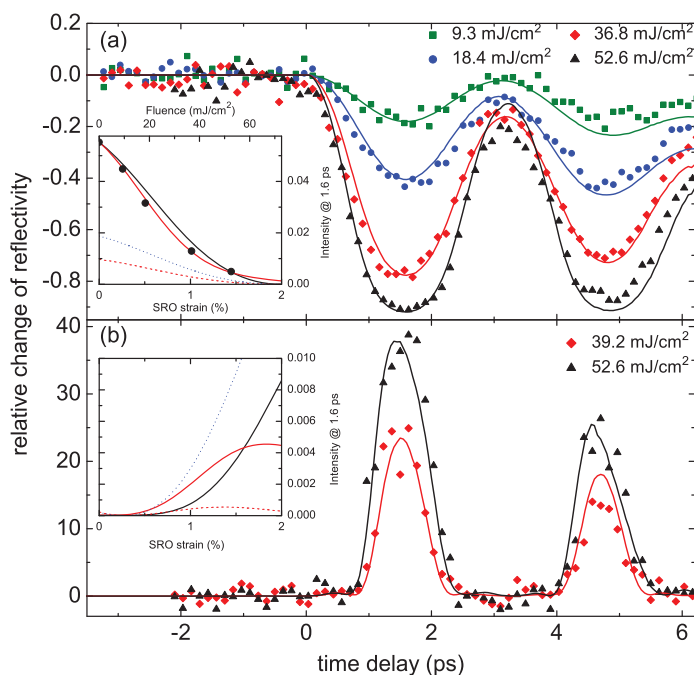


Figure 3. Relative change of Bragg intensity of (a) the ZOP and (b) the +2 SL peak for the SRO/STO SL after optical excitation with different pump fluences. The solid lines represent LCDX calculations. The insets show the calculated SL peak intensities at 1.6 ps according to the EM (black solid line) and LCDX (red solid line). Also, the contributions from individual layers are shown (broken lines). The inset in panel (a) also includes the corresponding experimental data obtained from the transients (bullets).

by ~ 120 fs pump pulses at 800 nm wavelength where the optical penetration depths $\xi_{\text{SRO}} \approx 52$ nm and $\xi_{\text{LSMO}} \approx 90$ nm generate an exponentially decaying stress pattern along the SL stack that is correctly accounted for in the LCDX [14, 20, 21]. As an example, the gray bullets in figures 1(a) and (b) show the measured Θ - 2Θ scans of the STO/SRO SL before and 1.6 ps after excitation, respectively, encompassing four SL reflections (-1 to $+2$). We also recorded the intensity of selected SL Bragg peaks as a function of time delay for different pump fluences. The symbols in figures 3 and 4 illustrate the strong modulations of the relative intensity change $[I(t) - I_0]/I_0$ where $I(t)$ is the measured x-ray intensity at time delay t and I_0 is the measured unpumped signal. Here, it is directly verified that the maximum expansion of the metallic layers of both the SRO/STO and the LSMO/STO SL is reached after 1.6 ps.

In the following, we discuss the simulation of UXRD data. We highlight the linear and nonlinear response of distinct Bragg reflections of the two SLs, starting with the ZOP of the SRO/STO SL. The DL envelope of the excited SRO/STO SL in figure 1(b) matches the experimental SL peak intensities very well, if we assume a homogeneous SRO expansion of 1.3% for a laser fluence of 36.8 mJ cm^{-2} . Only the +1 SL peak close to the substrate peak is overestimated by the EM⁹. If we use the LCDX, we are able to properly calculate the x-ray

⁹ The overestimation of the +1 peak remains even if the complete SL including the substrate is simulated according to the EM (see [13]). This discrepancy between the EM and the exact LCDX is thus due to the inhomogeneous excitation density along the SL stack.

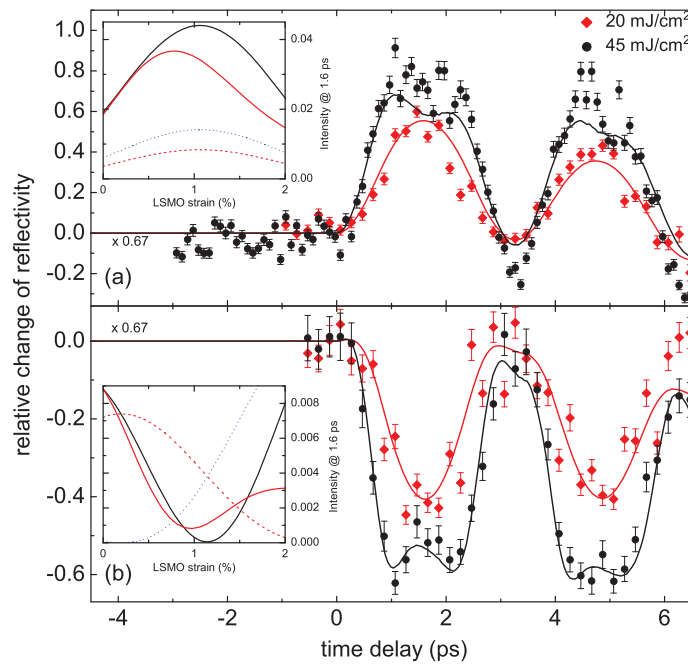


Figure 4. Relative change of the Bragg intensity of (a) the ZOP and (b) the +1 SL peak for the LSMO/STO SL. See figure 3 and the text for plot details.

curve of this particular sample at each point in time and for any strain amplitude. The resulting red line in figure 1(b) shows excellent agreement with the experimental data at 1.6 ps, assuming an average SRO strain of 1.1%.

The photoinduced structure dynamics discussed above lead to a strong decrease of the ZOP intensity with increasing SRO strain, as can be seen in figure 3(a) [13]. According to the EM, this is because the ZOP is governed by the steep flanks of the mutually departing single-layer envelopes. The inset of figure 3(a) compares the ZOP intensity at 1.6 ps as measured (black bullets) and as predicted by the EM (black line) and LCDX (red line). In addition, the contributions of the metallic (red dashed) and insulating (blue dotted) layers are indicated. The EM already yields very good qualitative agreement and illustrates the wide range of linearity up to $\sim 1\%$ average SRO strain. Notably, the LCDX precisely matches the measured ZOP intensity at 1.6 ps (inset). Furthermore, it even accurately reproduces the recorded time scans in figure 3(a). For the highest pump fluence, we deduce an average SRO strain of 1.45% at 1.6 ps.

In the case of SRO/STO ZOP, the linear regime is intrinsically limited because at a certain strain level the ZOP intensity has to vanish, which is indeed the case at about 2% SRO strain. At this point, the first-order minima of both single-layer envelopes approach $q^{(0)}$ (cf inset of figure 3(a)).

In addition to this trivial deviation from linearity, other nonlinear x-ray responses could be identified. As seen in figure 1(a), the +2 SL peak is nearly forbidden in the stationary SL because it is enclosed by the first minima of the SRO and STO layer envelopes [13]. Panel (b) shows that this peak exhibits a strongly enhanced intensity at 1.6 ps due to the structural dynamics. The inset of figure 3(b) indicates the highly nonlinear dependence of this reflection on the SRO

expansion as predicted by the EM (black line). A small strain initially suppresses the peak intensity as it completely shifts the minima of the single-layer envelopes to $q^{(+2)}$. Only above a threshold strain of $\sim 0.5\%$ does this peak attain considerable intensity, mainly due to the increase of the STO envelope function (blue dotted line).

A comparison of the experimental transient intensity of the +2 SL peak with the LCDX calculations presented in figure 3(b) again reveals very good agreement. As the SL phonon amplitude builds up, the intensity first remains unchanged within the signal-to-noise ratio of the experiment up to 800 fs, then rapidly increases to its maximum at about 1.6 ps and subsequently drops back to zero where it again remains for 800 fs. This behavior is repeated for the next periods with lower amplitude according to the energy loss of the SL phonon [14]. This ‘gating’ of x-ray Bragg reflectivity has an FWHM duration of $\lesssim 900$ fs around the maximum at 1.6 ps. Although the EM covers all essential features of the +2 SL peak response (nonlinearity, threshold behavior), the inset of figure 3(b) indicates that the EM predictions quantitatively deviate from the precise LCDX simulations.

As a further test of our models, we present experimental and numerical results for the LSMO/STO SL, including similar linear and nonlinear effects. In addition, however, a transient destructive interference of the diffracted components of the individual layers is identified. The $\Theta-2\Theta$ scan of the SL is shown in figure 2. Again, the ZOP of the LSMO/STO SL is located between the individual envelope functions, however this time with interchanged envelope positions of the metallic and insulating layers. According to the EM, this should lead to an increase of the ZOP intensity due to approaching envelope maxima. This is confirmed by the UXRD measurements reported in figure 4(a), which shows the response of the ZOP. The corresponding inset reveals that the EM predicts a linear increase of the ZOP intensity at 1.6 ps up to $\sim 0.5\%$ LSMO strain (black line); at $\sim 1\%$ it reaches a maximum and then even starts to drop again. This non-monotonic dependence can again be understood by the two approaching envelope functions which maximally overlap at an LSMO strain of $\sim 1\%$ where they provide the highest intensity for the ZOP. For higher strain, the ZOP intensity decreases as the envelope maxima separate again. The experimental data at higher pump fluence in figure 4(a) are indeed indicative of this behavior since we observe a clear plateau around 1.6 ps meaning that the turning point has been reached. Once more, the LCDX satisfactorily simulates the data, although the effects are overestimated and thus have to be scaled down to coincide with the experimental data. The reason for this will be discussed below. The inset in figure 4(a) shows that the EM (black line) qualitatively approximates the LCDX (red line).

In the case of other SL peaks, figure 2(b) reveals that the EM yields a crude underestimation of the peak intensities for a homogeneous LSMO strain of 1.15%. We exemplify the underlying mechanism by investigating the +1 SL peak of the LSMO/STO SL at $q^{(+1)} = q^{(0)} + g_{\text{SL}}$ in more detail. Figure 2(b) as well as the inset of figure 4(b) demonstrate that even though both single-layer envelope functions predict a considerable intensity at 1.15% LSMO strain, the DL envelope vanishes. This is caused by the destructive interference of the x-ray waves diffracted from one LSMO and the adjacent STO layer. The experimental data in figure 4(b) indeed show that for high excitation fluence the signal minimum of the transient around 1.6 ps splits up, verifying the destructive interference and the implied non-monotonic dependence on strain. The LCDX (solid lines in figure 4(b)) predicts the relative intensity decrease to be 50% larger compared to what we measured, most likely because the XRD simulations assume a perfect crystal lattice without any kind of disorder or interdiffusion. The simpler EM even predicts a perfect destructive interference of the x-rays which is much less pronounced in the LCDX

calculations since the true strain pattern is taken into account. Thus, it is not surprising that the LCDX still overestimates the effect of the interference. A similar reason holds for the ZOP.

In conclusion, we have presented predictions of combined model calculations simulating the transient strain field dynamics of photoexcited metal/insulator SLs and the induced transient XRD response. We compare these predictions to various UXRD data taken on SRO/STO and LSMO/STO SLs and find excellent agreement for both linear and nonlinear x-ray response to the induced strain. In particular, we have theoretically predicted and experimentally observed a peculiar destructive interference of x-ray waves in an LSMO/STO SL and a highly nonlinear response in an SRO/STO SL. The observations are interpreted by means of a simpler EM connecting the overall x-ray response to the structural dynamics of the individual layers. The EM correctly covers all transient features and often allows quantitative estimations. For precise simulations, the LCDX has to be evaluated. The presented findings emphasize that UXRD experiments can be accurately interpreted to reveal the transient structural dynamics of epitaxial crystals on subpicosecond time scales. They will open paths for simulation-based design of future ultrafast x-ray devices exploiting such nonlinear or interference phenomena that can be tailored into the nanostructures.

Acknowledgments

The time-resolved experiments were performed on the X05LA beamline at the Swiss Light Source, Paul Scherrer Institut, Villigen PSI, Switzerland. We thank the DFG for supporting the project via BA 2281/3-1 and SFB 762.

References

- [1] Authier A 2003 *Dynamical Theory of X-Ray Diffraction* (Oxford: Oxford University Press)
- [2] Shvyd'ko Yu V, Lerche M, Wille H C, Gerdau E, Lucht M, Rüter H D, Alp E E and Khachatryan R 2003 x-ray interferometry with microelectronvolt resolution *Phys. Rev. Lett.* **90** 013904
- [3] Snigirev A, Snigireva I, Kohn V, Yunkin V, Kuznetsov S, Grigoriev M B, Roth T, Vaughan G and Detlefs C 2009 x-ray nanointerferometer based on Si refractive bilenses *Phys. Rev. Lett.* **103** 064801
- [4] Bargheer M, Zhavoronkov N, Woerner M and Elsaesser T 2006 Recent progress in ultrafast x-ray diffraction *Chem. Phys. Chem.* **7** 783–92
- [5] Chergui M and Zewail A H 2009 Electron and x-ray methods of ultrafast structural dynamics: advances and applications *Chem. Phys. Chem.* **10** 28–43
- [6] Johnson S L, Vorobeva E, Beaud P, Milne C J and Ingold G 2009 Full reconstruction of a crystal unit cell structure during coherent femtosecond motion *Phys. Rev. Lett.* **103** 205501
- [7] Lindenberg A M *et al* 2005 Atomic-scale visualization of inertial dynamics *Science* **308** 392–5
- [8] Sokolowski-Tinten K *et al* 2003 Femtosecond x-ray measurement of coherent lattice vibrations near the Lindemann stability limit *Nature* **422** 287–9 (arXiv:10.1038/nature01490)
- [9] Grigoriev A, Dal-Hyun Do, Dong Min Kim, Chang-Beom Eom, Evans P G, Adams B and Dufresne E M 2006 Subnanosecond piezoelectric x-ray switch *Appl. Phys. Lett.* **89** 021109
- [10] Navirian H A, Herzog M, Goldshteyn J, Leitenberger W, Vrejoiu I, Khakhulin D, Wulff M, Shayduk R, Gaal P and Bargheer M 2011 Shortening x-ray pulses for pump-probe experiments at synchrotrons *J. Appl. Phys.* **109** 126104
- [11] Tanaka Y, Hara T, Yamazaki H, Kitamura H and Ishikawa T 2002 Optical switching of x-rays using laser-induced lattice expansion *J. Synchrotron Rad.* **9** 96–8

- [12] Bucksbaum P H and Merlin R 1999 The phonon Bragg switch: a proposal to generate sub-picosecond x-ray pulses *Solid State Commun.* **111** 535
- [13] Herzog M, Leitenberger W, Shayduk R, van der Veen R, Milne C J, Johnson S L, Vrejoiu I, Alexe M and Hesse D 2010 Ultrafast manipulation of hard x-rays by efficient Bragg switches *Appl. Phys. Lett.* **96** 161906
- [14] Herzog M, Schick D, Gaal P, Shayduk R, von Korff Schmising C and Bargheer M 2011 Analysis of ultrafast x-ray diffraction data in a linear-chain model of the lattice dynamics *Appl. Phys. A* **at press**
- [15] Als-Nielsen J and McMorrow D 2001 *Elements of Modern X-Ray Physics* (New York: Wiley)
- [16] Bauer G 1996 *Optical Characterization of Epitaxial Semiconductor Layers* (Berlin: Springer)
- [17] Bargheer M, Zhavoronkov N, Gritsai Y, Woo J C, Kim D S, Woerner M and Elsaesser T 2004 Coherent atomic motions in a nanostructure studied by femtosecond x-ray diffraction *Science* **306** 1771–3
- [18] von Korff Schmising C, Bargheer M, Kiel M, Zhavoronkov N, Woerner M, Elsaesser T, Vrejoiu I, Hesse D and Alexe M 2007 Coupled ultrafast lattice and polarization dynamics in ferroelectric nanolayers *Phys. Rev. Lett.* **98** 257601
- [19] Beaud P, Johnson S L, Streun A, Abela R, Abramsohn D, Grolimund D, Krasniqi F S, Schmidt T, Schlott V and Ingold G 2007 Spatiotemporal stability of a femtosecond hard-x-ray undulator source studied by control of coherent optical phonons *Phys. Rev. Lett.* **99** 174801
- [20] Kostic P, Okada Y, Collins N C, Schlesinger Z, Reiner J W, Klein L, Kapitulnik A, Geballe T H and Beasley M R 1998 Non-fermi-liquid behavior of SrRuO_3 : evidence from infrared conductivity *Phys. Rev. Lett.* **2009** 2498–501
- [21] Liu H L, Lu K S, Kuo M X, Uba L, Uba S, Wang L M and Jeng H T 2006 Magneto-optical properties of $\text{La}_{0.7}\text{Sr}_{0.3}\text{MnO}_3$ thin films with perpendicular magnetic anisotropy *J. Appl. Phys.* **99** 043908

Ultrafast manipulation of hard x-rays by efficient Bragg switches

M. Herzog, W. Leitenberger, R. Shayduk, R. M. van der Veen, C. J. Milne, S. L. Johnson, I. Vrejoiu, M. Alexe, D. Hesse and M. Bargheer.

Appl. Phys. Lett. **96**, 161906 (2010).

Ultrafast manipulation of hard x-rays by efficient Bragg switches

M. Herzog,¹ W. Leitenberger,¹ R. Shayduk,² R. M. van der Veen,^{3,4} C. J. Milne,^{3,4} S. L. Johnson,³ I. Vrejoiu,⁵ M. Alexe,⁵ D. Hesse,⁵ and M. Bargheer^{1,2,6,a)}

¹*Institut für Physik und Astronomie, Universität Potsdam, Karl-Liebknecht-Str. 24-25, 14476 Potsdam, Germany*

²*Helmholtz-Zentrum Berlin für Materialien und Energie GmbH, Hahn-Meitner-Platz 1, 14109 Berlin, Germany*

³*Swiss Light Source, Paul Scherrer Institut, 5232 Villigen PSI, Switzerland*

⁴*Laboratoire de Spectroscopie Ultrarapide, Ecole Polytechnique Fédérale de Lausanne, 1015 Lausanne, Switzerland*

⁵*Max-Planck-Institut für Mikrostrukturphysik, Weinberg 2, 06120 Halle, Germany*

⁶*Max-Planck-Institut für Kolloid- und Grenzflächenforschung, Am Mühlenberg 1, 14476 Potsdam-Golm, Germany*

(Received 24 February 2010; accepted 30 March 2010; published online 23 April 2010)

We experimentally demonstrate efficient switching of the hard x-ray Bragg reflectivity of a SrRuO₃/SrTiO₃ superlattice by optical excitation of large-amplitude coherent acoustic superlattice phonons. The rocking curve changes drastically on a 1 ps timescale. The (0 0 116) reflection is almost extinguished ($\Delta R/R_0 = -0.91$), while the (0 0 118) reflection increases by more than an order of magnitude ($\Delta R/R_0 = 24.1$). The change of the x-ray structure factor depends nonlinearly on the phonon amplitude, allowing manipulation of the x-ray response on a timescale considerably shorter than the phonon period. Numerical simulations for a superlattice with slightly changed geometry and realistic parameters predict a switching-contrast ratio $\Delta R/R_0$ of 700 with high reflectivity. © 2010 American Institute of Physics. [doi:10.1063/1.3402773]

Ultrafast x-ray techniques have become more and more prevalent in various scientific disciplines that are interested in directly observing atomic motion in real time. Very recently the first hard x-ray free electron laser has started operation,¹ and similar large-scale facilities are being constructed. In the meantime, widely available synchrotron radiation sources are usually limited to ~ 100 ps pulses. Faster time resolution at these sources has been realized in a few cases by ultrafast modulation of the electron beam in the storage ring (slicing or low-alpha mode),²⁻⁵ or by using ultrafast streak camera detectors to achieve time resolutions down to several hundred femtoseconds.⁶⁻⁸ In such cameras a photocathode converts the x-ray pulse into an electron pulse with similar time structure, and this electron pulse is subsequently manipulated with rapidly varying electric fields. So far, an efficient device to manipulate the time structure of a hard x-ray pulse itself is missing, although some concepts using coherent optical phonons in crystals have been discussed theoretically.^{9,10}

Here, we report on ultrafast x-ray diffraction measurements that demonstrate vast changes of the various Bragg peaks of a SrRuO₃/SrTiO₃ (SRO/STO) superlattice on a timescale of 1 ps. These modulations are triggered by the excitation of the structure with femtosecond laser pulses. As a consequence, the (0 0 116) superlattice reflection is strongly reduced, whereas the (0 0 118) reflection simultaneously exhibits a huge increase. The results are compared to numerical simulations evidencing that the change of the x-ray structure factor for the (0 0 118) superlattice peak depends nonlinearly on the phonon amplitude. This results in a nonsinusoidal modulation of the peak intensity in time. The

x-ray response can thus be manipulated on a timescale shorter than the phonon period, leading to ultrafast x-ray pulses with a full width at half maximum of $\Delta T = 1$ ps. Finally, we show numerical simulations of the rocking curve of a superlattice with realistic parameters predicting a switching-contrast ratio $\Delta R/R_0$ of 700 for such ultrafast gating of x-rays. This demonstrates the potential application of superlattices as an ultrafast Bragg switch.

The investigated superlattice consists of ten bilayers of the perovskite oxides SRO and STO terminated by a STO capping layer. The thin layers were epitaxially grown by pulsed laser deposition along the [001] direction on top of a STO substrate with a 42 nm thick SRO buffer layer.^{11,12} For sample characterization static x-ray diffraction measurements [Fig. 1(a)] with a high x-ray flux at 8818 eV have been performed at the EDR beamline of BESSY II.¹³ The ultrafast x-ray experiments were carried out at the FEMTO-slicing beamline of the Swiss Light Source (SLS) (Ref. 4) with x-ray pulses of 140 ± 30 fs pulse duration, a photon energy of 5200 eV and a mean photon number of ~ 20 photons per x-ray pulse.¹⁴ A femtosecond Ti:Sa laser system generating the 800 nm excitation pulses with 115 fs pulse duration was synchronized to the x-ray pulses at a repetition rate of 1 kHz. The relatively low x-ray flux consequently results in a smaller signal-to-noise ratio as seen in Fig. 1(b), which shows the measured diffracted x-ray intensity I_d normalized by the incident x-ray intensity I_i . We call $R = I_d/I_i$ the Bragg reflectivity, or short, reflectivity. In addition, the data sets were corrected for the so called *halo* background, which is generated by incompletely damped electrons from previously sliced bunches.⁴

The high structural perfection of the sample is evident from the very sharp peaks in the static rocking curve in Fig. 1(a). In order to deduce the structural parameters of the su-

^{a)}Author to whom correspondence should be addressed. Electronic mail: bargheer@uni-potsdam.de.

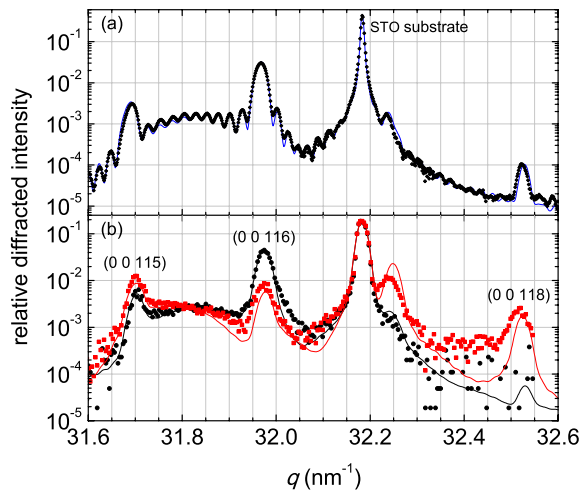


FIG. 1. (Color online) (a) Black diamonds: static rocking curve recorded at BESSY II with full x-ray flux. (b) Rocking curve of the unexcited SRO/STO superlattice (black bullets) and 1.6 ps after laser pulse excitation with a fluence of 37 mJ/cm^2 at 800 nm (red squares). These data sets were measured at the SLS in FEMTO-slicing mode. The solid lines are the corresponding numerical simulations.

perlattice, numerical simulations based on dynamical diffraction theory have been performed, which also account for the Debye–Waller effect and interface roughness. The simulation [solid line in Fig. 1(a)] yields the following parameters for the individual layers: Layer thickness $d_{\text{SRO}}=5.54 \text{ nm}$ and $d_{\text{STO}}=12.94 \text{ nm}$ and out-of-plane lattice constant of the perovskite unit cell $c_{\text{SRO}}=0.3957 \text{ nm}$ and $c_{\text{STO}}=0.3921 \text{ nm}$. Moreover, interface layers of intermixed SRO and STO unit cells with $d_{\text{mix}}=1.96 \text{ nm}$ and $c_{\text{mix}}=0.3923 \text{ nm}$ had to be assumed to simulate the data.¹⁵

When the sample is excited by an optical pulse, the rocking curve varies drastically on an ultrafast timescale. The largest intensity changes are observed when the x-ray pulse probes the transient structure at $t=1.6 \text{ ps}$ after the pump pulse. The corresponding rocking curve for a pump fluence of 37 mJ/cm^2 is shown in Fig. 1(b) (red squares). The diffracted x-ray intensity exhibits a relative increase of $\Delta R^{118}/R_0^{118}=13.7$ for the (0 0 118) superlattice reflection and a respective decrease of $\Delta R^{116}/R_0^{116}=-0.80$ for the (0 0 116) reflection.

In Fig. 2, the temporal evolution of these two Bragg peak intensities is plotted for a higher excitation fluence of 53 mJ/cm^2 . $R^{116}(t)$ shows an oscillatory response that resembles a damped cosine function with a period of 3.2 ps . The diffraction efficiency of the (0 0 116) reflection is maximally suppressed at $t=1.6 \text{ ps}$ down to $0.09 \times R_0^{116}$. The transient Bragg reflectivity $R^{118}(t)$ exhibits the same period but clearly shows peaks having a full width at half maximum of $\Delta T=1 \text{ ps}$ rather than a sinusoid. Thus, widely available $\sim 100 \text{ ps}$ x-ray pulses from synchrotron radiation sources reflected from the sample at (0 0 118) would be shaped into 1 ps bursts as opposed to a sine wave. The maximum relative change of the diffracted intensity of the (0 0 118) reflection is $\Delta R^{118}/R_0^{118}=24.1$.

The physical mechanism behind this transient x-ray response can be understood as follows. The optical pump light is absorbed in the metallic SRO layers exclusively, leading to

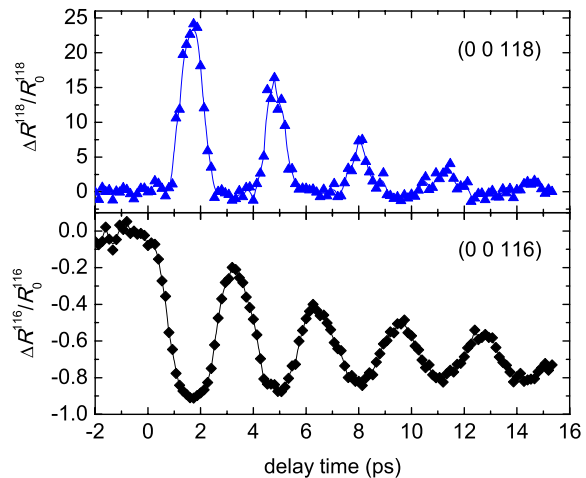


FIG. 2. (Color online) Relative change of the transient x-ray Bragg reflectivity of superlattice reflection (0 0 116) (black diamonds) and (0 0 118) (blue triangles) after excitation ($\lambda=800 \text{ nm}$ and fluence 53 mJ/cm^2). The solid lines are guidelines to the eye.

an expansion of these layers. At short timescales this expansion must be compensated by a compression of the optically transparent STO layers, as they are squeezed equally from both sides. Essentially, the induced atomic motion corresponds to a standing longitudinal acoustic wave with a wavelength determined by the spatial double-layer period d_{SL} of the superlattice. The temporal period of this coherent acoustic phonon mode corresponds to the time $T_{\text{ph}}=d_{\text{SL}}/v_{\text{av}}$ it takes a sound wave to propagate through one SRO/STO double layer with thickness $d_{\text{SL}}=d_{\text{SRO}}+d_{\text{STO}}+2d_{\text{mix}}=22.8 \text{ nm}$ at the average longitudinal sound velocity $v_{\text{av}}\approx 7.3 \text{ nm/ps}$ [$v_{\text{SRO}}=6.3 \text{ nm/ps}$ (Ref. 16) and $v_{\text{STO}}=7.8 \text{ nm/ps}$ (Ref. 17)]. This explains the measured phonon period of 3.2 ps .

For simplicity, we assume homogeneous strain in identical layers for the numerical simulations of the rocking curves of the optically excited structure. The solid lines in Fig. 1(b) correspond to zero strain (black solid line) and 1.6% strain (red solid line) in SRO, respectively. For the larger fluence (Fig. 2) we calculate a SRO peak strain of 1.8% . The very good agreement between the calculated curves and the experimental data already indicates that the simulations correctly account for the induced transient structural changes, i.e., an expansion of SRO and a compression of STO (the intermixed interface layers are kept constant). The model has been previously applied for different samples as well.¹⁸

In order to emphasize the potential of superlattices as a means for manipulating x-rays on ultrafast timescales, we have performed numerical simulations for structures with only slightly different geometries which, however, exhibit greatly improved switching contrasts. Essentially, the layer thicknesses have been varied in order to maximally suppress the (0 0 118) reflection in the unexcited state. In the experiments reported above the dynamics were completely reversible, that is, the samples were not damaged. We therefore applied the identical SRO strain level in the simulations for the theoretical structure. Figure 3 shows the simulated rocking curves for zero strain (dashed line) and 1.8% peak strain (solid line) in the SRO layers of a superlattice with the thick-

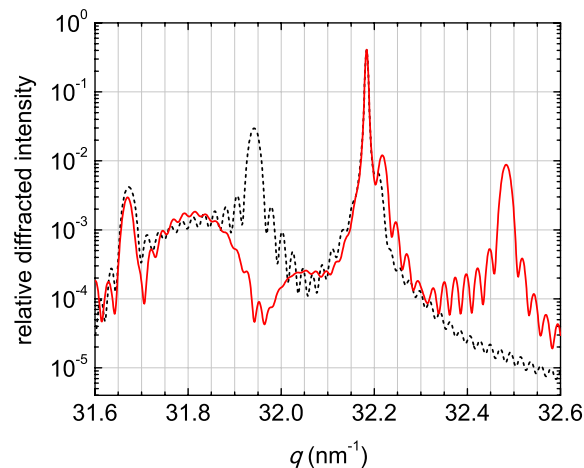


FIG. 3. (Color online) Simulation of tailored SRO/STO superlattice with a maximized contrast ratio of the (0 0 118) reflection. The black dashed (red solid) line shows the rocking curve of the stationary (excited) superlattice.

ness parameters $d_{\text{SRO}}=8.7$ nm and $d_{\text{STO}}=14.5$ nm, and the same out-of-plane lattice constants as stated above.¹⁹ The intensity of the (0 0 118) reflection changes by a factor of $\Delta R/R_0=700$ up to a reflectivity of 1% of the incident x-ray intensity. However, the nonlinear response to the strain still holds and therefore the corresponding time structure after laser excitation is basically identical to the behavior shown in Fig. 2. The switching contrast could be improved even further by changing the constituent materials in the layers.

In conclusion, we have demonstrated that the optical excitation of superlattice structures by femtosecond laser pulses can be exploited to manipulate hard x-rays on a 1 ps time-scale. In contrast to previous suggestions, the crucial idea of this concept is to modulate the diffraction efficiency of stationary forbidden superlattice Bragg peaks with very low background by laser excitation of large-amplitude high-wave vector acoustic phonons. We have experimentally shown both switching the x-ray reflectivity *on* and *off* by using different superlattice diffraction orders of the very same SRO/STO superlattice. Numerical simulations with realistic structural parameters suggest that the performance can be greatly improved by further tailoring the epitaxial structures. The presented experimental method may be used to generate 1 ps

x-ray pulses from conventional ~ 100 ps pulses in electron storage rings for ultrafast x-ray diffraction experiments.

The time-resolved experiments were performed on the X05LA beamline at the Swiss Light Source, Paul Scherrer Institut, Villigen PSI, Switzerland. We thank the DFG for supporting the project via Grant Nos. BA 2281/3-1 and SFB 762.

¹B. McNeil, *Nat. Photonics* **3**, 375 (2009).

²R. Schoenlein, S. Chattopadhyay, H. Chong, T. Glover, P. Heimann, C. Shank, A. Zholents, and M. Zolotarev, *Science* **287**, 2237 (2000).

³S. Khan, K. Hollmack, T. Kachel, R. Mitzner, and T. Quast, *Phys. Rev. Lett.* **97**, 074801 (2006).

⁴P. Beaud, S. Johnson, A. Streun, R. Abela, D. Abramsohn, D. Grolimund, F. Krasniqi, T. Schmidt, V. Schlott, and G. Ingold, *Phys. Rev. Lett.* **99**, 174801 (2007).

⁵M. Abo-Bakr, J. Feikes, K. Hollmack, P. Kuske, W. B. Peatman, U. Schade, G. Wüstefeld, and H.-W. Hübers, *Phys. Rev. Lett.* **90**, 094801 (2003).

⁶Z. Chang, A. Rundquist, J. Zhou, M. M. Murnane, H. C. Kapteyn, X. Liu, B. Shan, J. Liu, L. Niu, M. Gong, and X. Zhang, *Appl. Phys. Lett.* **69**, 133 (1996).

⁷J. Liu, J. Wanga, B. Shan, C. Wang, and Z. Chang, *Appl. Phys. Lett.* **82**, 3553 (2003).

⁸J. Feng, H. J. Shin, J. R. Nasiatka, W. Wan, A. T. Young, G. Huang, A. Comin, J. Byrd, and H. A. Padmore, *Appl. Phys. Lett.* **91**, 134102 (2007).

⁹P. Bucksbaum and R. Merlin, *Solid State Commun.* **111**, 535 (1999).

¹⁰J. Sheppard, P. Sondhaus, R. Merlin, P. Bucksbaum, R. Leed, and J. Wark, *Solid State Commun.* **136**, 181 (2005).

¹¹I. Vrejoiu, G. L. Rhun, L. Pintilie, D. Hesse, M. Alexe, and U. Gösele, *Adv. Mater. (Weinheim, Ger.)* **18**, 1657 (2006).

¹²C. v. Korff Schmising, A. Harpoeth, N. Zhavoronkov, Z. Ansari, C. Aku-Leh, M. Woerner, T. Elsaesser, M. Bargheer, M. Schmidbauer, I. Vrejoiu, D. Hesse, and M. Alexe, *Phys. Rev. B* **78**, 060404(R) (2008).

¹³Energy bandwidth 2×10^{-4} , divergence 270 μrad , *p*-polarization.

¹⁴Energy bandwidth 1.5×10^{-4} , vertical convergence of 840 μrad due to focussing, *s*-polarization.

¹⁵The parameters for the simulations of the SLS data had to be slightly adjusted within the structural inhomogeneities.

¹⁶S. Yamanaka, T. Maekawa, H. Muta, T. Matsuda, S. Kobayashi, and K. Kurosaki, *J. Solid State Chem.* **177**, 3484 (2004).

¹⁷Y. H. Ren, M. Trigo, R. Merlin, V. Adyam, and Q. Li, *Appl. Phys. Lett.* **90**, 251918 (2007).

¹⁸C. v. Korff Schmising, M. Bargheer, M. Kiel, N. Zhavoronkov, M. Woerner, T. Elsaesser, I. Vrejoiu, D. Hesse, and M. Alexe, *Phys. Rev. Lett.* **98**, 257601 (2007).

¹⁹The assumption of perfect interfaces in the simulation, i.e., no intermixing, is not crucial. The presence of three intermixed unit cells would diminish the switching ratio by less than a factor of 2 with almost unchanged maximum reflectivity.

PAPER IV

Transient x-ray reflectivity of epitaxial oxide superlattices investigated by femtosecond x-ray diffraction

M. Herzog, W. Leitenberger, R. Shayduk, R. M. van der Veen, C. J. Milne, S. L. Johnson, I. Vrejoiu, M. Alexe, D. Hesse and M. Bargheer.

Ultrafast Phenomena XVII - Proceedings of the 17th International Conference, 290 (2011).

Transient X-ray Reflectivity of Epitaxial Oxide Superlattices Investigated by Femtosecond X-ray Diffraction

Marc Herzog¹, Wolfram Leitenberger¹, Roman Shayduk², Renske M. van der Veen^{3,4}, Christopher J. Milne^{3,4}, Steven L. Johnson³, Ionela Vrejoiu⁵, Marin Alexe⁵, Dietrich Hesse⁵, Matias Bargheer^{1,2}

¹ Dep. of Physics and Astronomy, University of Potsdam, Potsdam, Germany

E-mail: bargheer@uni-potsdam.de

² Helmholtz-Zentrum Berlin, Berlin, Germany

³ Swiss Light Source, Paul Scherrer Institut, Villigen, Switzerland

⁴ Laboratory of Ultrafast Spectroscopy, Ecole Polytechnique Fédérale de Lausanne, Lausanne, Switzerland

⁵ Max Planck Institute of Microstructure Physics, Halle, Germany

INTRODUCTION. In order to understand the dynamics of matter on atomic length and time scales one relies on experimental methods that allow both spatial and temporal resolution of the physics in the system of interest. Although X-ray diffraction gives the opportunity to precisely map the position of atoms the desired sub-picosecond time resolution has been realized just during the last decade. While the most recent generation of brilliant and short x-ray sources, free electron lasers, has just started operation [1], capacities at these facilities will be very limited. Widely available synchrotron radiation sources are usually limited to approx. 100 ps pulses, but time resolution can be improved by ultrafast modulation of the electron bunches (slicing or low-alpha) or by means of ultrafast streak cameras. All these methods rely on manipulating electrons whereas methods for directly manipulating hard x-ray pulses are missing, although some theoretical concepts have been discussed [2,3].

We present results from ultrafast x-ray diffraction (XRD) experiments at the FEMTO-slicing beamline at the Swiss Light Source [4] on a periodic epitaxial multilayer with 10 repeat units of SrRuO₃/SrTiO₃ (SRO/STO) bilayers [5,6], also referred to as superlattice (SL). The sample is excited by illumination with strong laser pulses. The transient crystal structure of the sample after the excitation is probed with femtosecond x-ray pulses. The XRD pattern exhibits characteristic SL Bragg peaks (Fig. 1 (a)) which are drastically modulated on a 1-ps timescale after laser pulse excitation due to the generation of coherent SL phonons. In particular, we observed strong suppression and growth of different Bragg reflections by more than one order of magnitude after only 1.6 ps. Moreover, the reflected x-ray intensity partly depends nonlinearly on the laser-induced strain field which may be exploited to directly manipulate hard x-rays, e.g., to shape long x-ray pulses from synchrotrons into 1 ps pulses that may be used in time-resolved XRD experiments.

EXPERIMENTAL DETAILS. Both SRO and STO belong to the class of perovskite oxides and possess a pseudocubic crystal structure. The investigated SL was grown by pulsed laser deposition [7] on a (001) STO substrate with a 42 nm SRO buffer layer. Prior to the time-resolved experiments the precise struc-

4. Physics – Condensed Phase, Surfaces, and Low Dimensional Systems

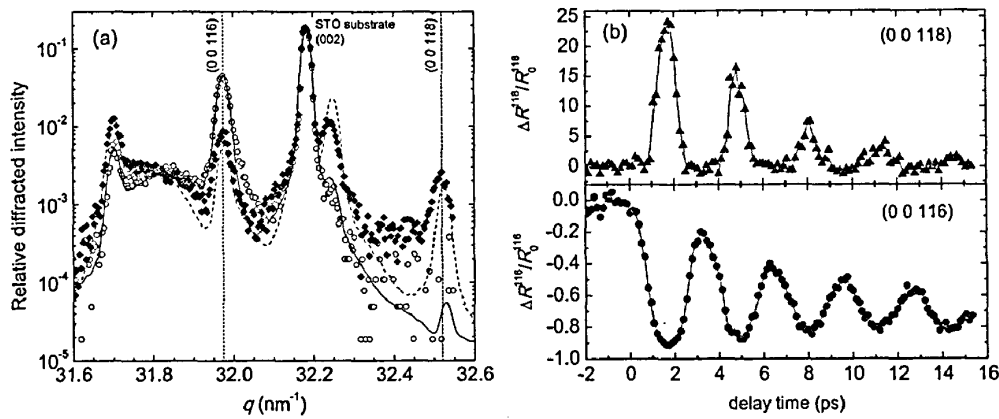


Figure 1: (a) Rocking curves of an SRO/STO SL. The Bragg peaks exhibit maximum intensity variations 1.6 ps after excitation (fluence 37 mJ/cm²) (solid diamonds) as compared to the unpumped rocking curve (open circles). The dashed (solid) lines are fits from dynamical XRD simulations to the pumped (unpumped) data and the vertical dashed lines indicate the positions in q-space for the transients shown in the right panel. (b) Relative change of the reflectivity of the (0 0 118) and (0 0 116) reflection after excitation (fluence 53 mJ/cm²).

ture of the SRO/STO SL was characterized by fitting dynamical XRD simulations to static XRD data obtained at the EDR beamline of the synchrotron radiation source BESSY II [5]. The sample has layer thicknesses of $d_{\text{SRO}}=5.54$ nm, $d_{\text{STO}}=12.94$ nm and $d_{\text{mix}}=1.96$ nm with pseudocubic out-of-plane lattice parameters $c_{\text{SRO}}=0.3957$ nm, $c_{\text{STO}}=0.3921$ nm and $c_{\text{mix}}=0.3923$ nm, respectively. The subscript "mix" refers to interdiffusion layers between the different materials SRO and STO. The high structural perfection and periodicity of the sample is evident from very sharp equidistant Bragg peaks.

The time-resolved experiments utilized an optical pump–x-ray probe technique. The 800 nm pump pulses of 115 fs pulse duration were generated by a Ti:Sa laser system and 140 ± 30 fs hard x-ray pulses were produced in an undulator employing the laser-electron slicing technique [4]. The time delay between the two pulses, τ , which is determined by a mechanical delay line, defines the time at which the transient structure of the SL is probed.

RESULTS AND DISCUSSION.

The measured rocking curve of the SRO/STO SL around the STO substrate peak is depicted in Fig. 1 (a). The equidistant Bragg peaks reflect the artificial periodicity of the SL. Compared to the unpumped state (open circles) the intensity of these SL peaks has considerably altered only 1.6 ps after the pump pulse (solid diamonds) which corresponds to the time of the maximum intensity variation.

In Fig. 1 (b) we present the transient relative change of the x-ray diffraction intensity of two SL peaks. The maximum changes which we observed at a pump fluence of 53 mJ/cm² are a suppression of the (0 0 116) reflection by 91% and an increase of an initially almost forbidden reflection (0 0 118) by more than 2400%. Interestingly, the intensity of the (0 0 118) reflection depends nonlinearly on the

4. Physics – Condensed Phase, Surfaces, and Low Dimensional Systems

phonon amplitude and thus shows a non-sinusoidal oscillation in contrast to (0 0 116). The temporal structure of the strong intensity increase is shaped into separated peaks with a FWHM of 1.0 ps. Fig. 1 (b) also demonstrates that the maximum intensity modulations are indeed reached after 1.6 ps.

Our interpretation of the observations is as follows. The 800 nm pump pulses are absorbed exclusively in the metallic SRO layers, resulting in an intraband excitation of the conduction band electrons. Subsequently, an ultrafast electron-phonon coupling transfers energy into the phonon system within a few 100 fs which triggers an expansion of SRO. This expansion is compensated by a compression of the STO layers on short times. The resulting strain field corresponds to a standing strain wave with the periodicity given by the SL. It is this so called SL phonon mode that modulates the x-ray structure factor and leads to the observed oscillations in the diffracted x-ray intensity. The temporal period of the excited phonon mode is determined by the individual layer thicknesses of the bilayer and the respective elastic constants and basically corresponds to the transit time of a longitudinal acoustic wave through the bilayer. Evaluation for the present sample exactly yields the measured 3.2 ps period.

The fits from dynamical XRD simulations where we assumed homogeneous strain in identical layers reveal a phonon amplitude that corresponds to a maximum SRO strain of 1.8% for the highest excitation fluence of 53 mJ/cm². The very good agreement between the simulations and the experimental data (Fig. 1 (a)) shows that our model correctly accounts for the transient dynamics of the sample. Simulations show that even small changes in the layer thicknesses of the bilayers can lead to much larger amplitudes of the x-ray modulations for identical phonon amplitudes. For instance, changing the number of unit cells per layer by only a few increases the rising factor of the (0 0 118) reflection to more than 700 with maximum diffraction efficiency of about 1%.

CONCLUSIONS. We observed large modulations of the diffracted x-ray intensity of a SRO/STO SL due to the selective laser-excitation of a coherent acoustic SL phonon mode. Simulations of the transient XRD data revealed the generation of enormous strain in the SRO layers up to 1.8% within 1.6 ps. A nonlinear dependence of the intensity of a particular Bragg reflection on the phonon amplitude was identified which results in a pulse-like transient x-ray reflectivity of 1 ps width. This behaviour may be exploited to curtail long pulses of hard x-rays from a conventional synchrotron into 1-ps pulses for ultrafast XRD experiments.

Acknowledgments. The time-resolved experiments were performed on the X05LA beamline at the Swiss Light Source, Paul Scherrer Institute, Villigen PSI, Switzerland. We thank the DFG for supporting the project via BA 2281/3-1 and SFB 762.

- 1 B. McNeil, Nat. Photonics 3, 375 (2009).
- 2 P. Bucksbaum et al., Solid State Commun. 111, 535 (1999).
- 3 J. Sheppard et al., Solid State Commun. 136, 181 (2005).
- 4 P. Beaud et al., Phys. Rev. Lett. 99, 174801 (2007).
- 5 M. Herzog et al., Appl. Phys. Lett. 96, 161906 (2010).
- 6 C. v. Korff Schmising et al., Phys. Rev. B 78, 060404(R) (2008).
- 7 I. Vrejoiu et al., Adv. Mater. 18, 1657 (2006).

Comparing the oscillation phase in optical pump-probe spectra to ultrafast x-ray diffraction in the metal-dielectric $\text{SrRuO}_3/\text{SrTiO}_3$ superlattice

A. Bojahr, D. Schick, L. Maerten, M. Herzog, I. Vrejoiu, C. von Korff Schmising, C. J. Milne, S. L. Johnson and M. Bargheer.

Phys. Rev. B **85**, 224302 (2012).

Comparing the oscillation phase in optical pump-probe spectra to ultrafast x-ray diffraction in the metal-dielectric SrRuO₃/SrTiO₃ superlattice

André Bojhr,¹ Daniel Schick,¹ Lena Maerten,¹ Marc Herzog,¹ Ionela Vrejoiu,² Clemens von Korff Schmising,³ Chris Milne,⁴ Steven L. Johnson,⁵ and Matias Bargheer^{1,6,*}

¹*Institute of Physics and Astronomy, University of Potsdam, Karl-Liebknecht-Strasse 24-25, 14476 Potsdam, Germany*

²*Max-Planck-Institut für Mikrostrukturphysik, Weinberg 2, 06120 Halle, Germany*

³*Institut für Optik und Atomare Physik, TU Berlin, Strasse des 17. Juni 135, 10623 Berlin*

⁴*Swiss Light Source, Paul Scherrer Institut, 5232 Villigen PSI, Switzerland and Laboratoire de Spectroscopie Ultrarapide, Ecole Polytechnique Federale de Lausanne, 1015 Lausanne, Switzerland*

⁵*Institute for Quantum Electronics, ETH Zurich, Wolfgang-Pauli-Strasse 16, 8093 Zurich, Switzerland*

⁶*Helmholtz Zentrum Berlin, Albert-Einstein-Strasse 15, 12489 Berlin, Germany*

(Received 6 April 2012; revised manuscript received 16 May 2012; published 19 June 2012)

We measured the ultrafast optical response of metal-dielectric superlattices by broadband all-optical pump-probe spectroscopy. The observed phase of the superlattice mode depends on the probe wavelength, making assignments of the excitation mechanism difficult. Ultrafast x-ray diffraction data reveal the true oscillation phase of the lattice which changes as a function of the excitation fluence. This result is confirmed by the fluence dependence of optical transients. We set up a linear chain model of the lattice dynamics and successfully simulated the broadband optical reflection by unit-cell resolved calculation of the strain-dependent dielectric functions of the constituting materials.

DOI: 10.1103/PhysRevB.85.224302

PACS number(s): 63.20.Ry, 42.65.Es

I. INTRODUCTION

Optical femtosecond spectroscopy is an established tool to infer ultrafast dynamics in molecules and solids. Time constants such as the exponential decay or the oscillation period can often be directly ascribed to microscopic processes such as relaxation or vibration. A detailed modeling of the ultrafast optical response requires the quantum-chemical modeling of molecular potentials in the case of molecular systems or calculation of the dielectric function of solids. With the broader accessibility of various experimental setups for ultrafast x-ray diffraction (UXRD), the findings from all-optical experiments can be cross-checked by directly looking at the lattice motion, including a real time measurement of the absolute atomic amplitudes. In the case of bulk semiconductors UXRD allowed conclusions to be drawn on modifications of the strain fronts induced by the fast diffusion of hot carriers.¹⁻³ For bulk bismuth UXRD in combination with *ab initio* simulations revealed how the lattice potential changes with the time-dependent carrier density.⁴ UXRD and ultrafast electron-diffraction studies show that, for increasing excitation fluence, electronic pressure gains importance versus phonon pressure in metallic systems.^{5,6} All these processes influence the oscillation phase of the excited phonons. In reverse, measuring the oscillation phase elucidates the excitation mechanisms.

The influence of Raman excitation has been discussed in bulk systems, superlattices, and multilayers.⁷ Under strictly nonresonant conditions this excitation causes a sine-like phase of the lattice motion. In contrast the so-called dispersive excitation of coherent phonons (DECP)⁸ results in a cosine-like lattice motion.⁹ DECP is exclusively observed in opaque materials and can be described by the imaginary part of the Raman tensor.¹⁰ Additional excitation mechanisms which show a displaced equilibrium of the lattice oscillation

are surface charge screening, the photo Dember effect, or heating of the lattice by rapid electron-phonon scattering.¹¹ In many cases the oscillation phase was measured by all-optical techniques and ascribed to the phase of the lattice motion. Raman scattering with real and imaginary tensor contributions is held responsible for the excitation of coherent phonons in metallic systems (Cd, Zn, Zr) as well.^{12,13} In the most intensively investigated material, the semimetal Bi, the microscopic interpretation of the excitation is developed in detail. Theory predicts the time-dependent change of the interatomic potential during the relaxation of photoexcited carriers.^{4,14} A similarly detailed interpretation of the excitation in terms of quasiparticle generation is exemplified for Si.¹⁵ UXRD would yield direct experimental information on the lattice motion in this case. However, there is only a single UXRD experiment that measures lattice dynamics (polaritons) induced by nonresonant Raman excitation.¹⁶

Several all-optical studies measured a fluence dependent phase of oscillations, which was ascribed to the simultaneous action of DECP and Raman mechanisms.¹⁷ Superlattices exhibit phonon modes which are very well suited for fundamental tests, as their periods can be tuned via the layer thickness. Especially for UXRD experiments they yield high signal-to-noise ratio of the experimental signal. The nanosized layers support zone folded acoustic phonons¹⁸ with few-picosecond oscillation periods, well suited for distinguishing tiny phase differences. Optical excitation of the opaque constituent of a superlattice yields a standing strain wave where the opaque material is periodically expanded while the transparent material is compressed. For GaAs/AlGaAs superlattices a UXRD study under high fluence conditions revealed a dominant DECP mechanism¹⁹ whereas all-optical measurements under low-fluence conditions suggest the Raman mechanism.⁷ Although it is well established to use such ultrafast structural techniques, the problem of determining the arrival time of the x-ray or

electron pulses with high precision relative to the pump pulse persists. A direct and detailed comparison of ultrafast optical response over a broad spectral range with the actual lattice motion determined by ultrafast diffraction techniques under identical excitation conditions is lacking.

In this contribution we revisit the metal-dielectric superlattice (SL) composed of SrRuO₃ (SRO) and SrTiO₃ (STO), for which it was shown by UXRd measurements that there are at least two contributing mechanisms for photoexcited lattice dynamics: thermal expansion by electron-phonon and phonon-phonon interaction and ultrafast magnetostriction.²¹ We present a fluence-dependent UXRd study which shows a relative phase shift of about 130 fs of the lattice motion, indicating that for high fluence the photon energy is coupled more rapidly to the expansion. At high fluences the measured phase of the lattice motion is consistent with an instantaneous DECP mechanism within the experimental error. In broadband optical reflectivity measurements we find that the oscillation phase of the all-optical signal strongly depends on the probe wavelength; however, we can confirm the relative shift of the oscillation phase with fluence. To determine the absolute phase of the lattice oscillation we perform a combined optical pump-probe and UXRd experiment without moving any components.

In order to better understand the broadband optical response, the lattice dynamics are calculated in a masses-and-springs model and calibrated in phase and amplitude using the UXRd data. The calculated spatiotemporal strain pattern is used to simulate the optical response by using the strain-dependent dielectric functions of SRO and STO, where the dependence $\partial N_{\text{SRO}}/\partial \eta$ of the complex refractive index N_{SRO} on the strain η is the only freely adjustable parameter. The agreement of these x-ray calibrated simulations with the optical response is very good. These data directly show that all-optical pump-probe data can exhibit nearly arbitrary oscillation phases, even if the lattice dynamics are fixed.

II. SETUP AND EXPERIMENTAL RESULTS

The sample consists of 10 double layers of STO/SRO (13 nm/7.5 nm) deposited by pulsed laser deposition on an STO substrate.²² In all experiments presented in this manuscript we use pump pulses with a wavelength of $\lambda_{\text{pump}} = 800$ nm. Figure 1(a) presents fluence-dependent UXRd data recorded at the MicroXAS-FEMTO beamline of the Swiss Light Source (SLS).²³ The amplitude of the oscillation has been analyzed²⁴ and discussed previously.²⁰ The according strain amplitude is reproduced in Fig. 1(b). Panel 1(c) shows the delay t_0^{osc} of the oscillation phase extracted from fitting the data in panel 1(a) to an analytical function [Eq. (1)] describing the sample response, which will be further discussed in Sec. IV. In short, the symmetric superlattice-phonon mode of the metallic/insulating superlattice is excited by expanding the metal layers. For the highest fluence the oscillation starts approximately 130 fs earlier. Figure 2(a) shows the transient optical reflectivity of the sample at $\lambda_{\text{probe}} = 670$ nm. The rapid rise of the reflectivity originates from quasi-instantaneous heating of the metal electrons. The rising edge determines the arrival time of the optical pump pulse. The slanted arrows indicate the delay of the oscillation for lower pump fluence. For

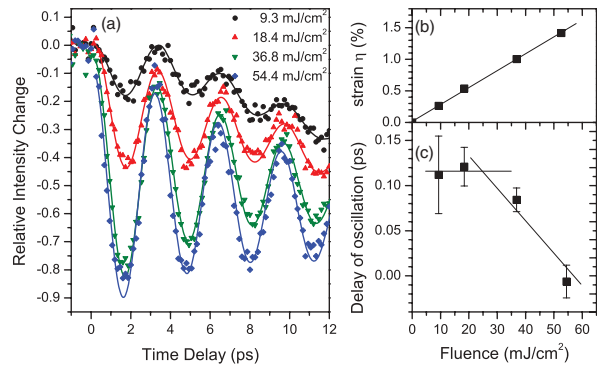


FIG. 1. (Color online) (a) UXRd measurements of the (0 0 116) reflection of the SRO/STO SL recorded at the SLS $\lambda_{\text{pump}} = 800$ nm for different fluences. (b) Strain amplitude derived from the data in panel (a) by comparison to a dynamical x-ray diffraction simulation (Ref. 20). (c) Oscillation phase extracted from the measured data using the fit function of eq. 1. The error bars correspond to a 68% confidence interval from fitting the relative phase. The absolute phase is obtained by comparison to the experiments at the laser-based plasma source discussed in Fig. 4.

an accurate evaluation we subtract the incoherent background (dotted line) and fit oscillations to the data. The resulting linear fluence dependence of the amplitude is shown in Fig. 2(b). The phase delay is plotted in Fig. 2(c) and compared to the UXRd result. The excellent agreement suggests that indeed for low fluence the oscillation is delayed by about 130 fs due to a finite electron-phonon coupling time as the expansion is dominated by phonon-phonon interaction. In contrast, for high fluence the

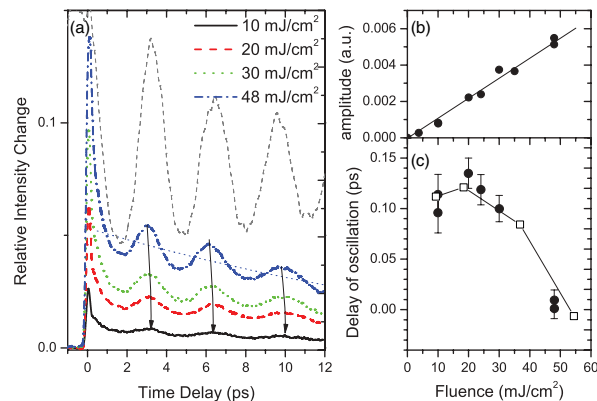


FIG. 2. (Color online) (a) Measured optical reflectivity $\lambda_{\text{probe}} = 670$ nm for different fluences. The dotted line indicates the incoherent background contribution which is subtracted from each transient to fit the oscillations and to plot Fig. 3(a). The thin dashed line shows the UXRd measurement for comparison. (b) Oscillation amplitude as a function of the fluence. (c) Comparison of the relative oscillation phase of the optical signal (solid circles) to the phase determined by UXRd [open squares reproduced from Fig. 1(c)]. The error bars of the relative phase are determined from the maximum deviation of phases in two measurement series. The absolute phase is shifted to agree with the UXRd data.

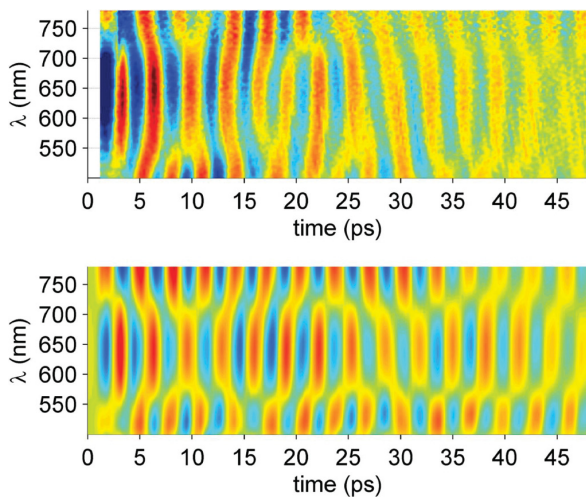


FIG. 3. (Color) (a) Experimentally measured change of the optical reflectivity from $\lambda_{\text{probe}} = 500$ to 780 nm at normal incidence after exciting the sample at $\lambda_{\text{pump}} = 800$ nm as a function of time delay. The electronic response and a slowly varying signal contribution have been subtracted as exemplified in Fig. 2(a). (b) Results from the simulation described in the text. The slowly varying background has been subtracted as well. The simulations show that the spectral position of the phase change at 560 and 720 nm is given by an interference of light reflected from the surface and the interface to the substrate.

time for coupling the energy into the expansion mode is so fast that we cannot distinguish it from an instantaneous response.

Our broadband optical pump-probe setup is similar to those reported in the literature,^{25,26} where a white-light continuum serves as the probe pulse. Hence, we not only measure the data at 670 nm (Fig. 2) but over the full visible range. The analysis teaches us to interpret all-optical data with great care. After subtraction of the slowly varying background for each wavelength as exemplified by the dotted line in Fig. 2(a), the broadband data exhibit complex dependence of the phase on the probe wavelength [Fig. 3(a)].

A general problem in UXR D experiments is the precise determination of the time zero. For all-optical pump-probe data we cross-checked that the rising edge of the signal corresponds to $t = 0$ by sum-frequency generation of pump and probe in a beta-Barium-Borate (BBO) crystal. To calibrate the time origin of the UXR D data, we repeated the UXR D experiment at the laser-based femtosecond diffractometer at the University of Potsdam.²⁷ We removed the x-ray optic which is used for the standard operation of the diffractometer.^{27,28} The Bragg condition selects a small angular range of the generated x-ray pulses which are diffracted from the sample (hatched beam in the schematic in Fig. 4). We introduce slits along this x-ray beam to ensure that, after removing the copper tape for x-ray generation, only laser photons propagating along this x-ray probe path impinge on the sample, now as optical probe pulses.

To switch between optical and x-ray probes, only the copper band and a $10 \mu\text{m}$ thick plastic film are removed from the beam path. The optical probe pulse and the x-ray probe-pulse have

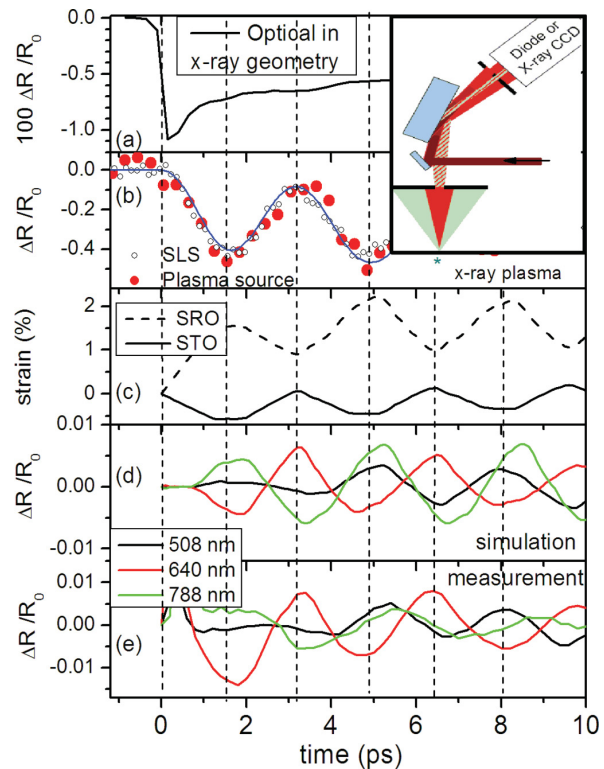


FIG. 4. (Color) (a) All-optical response measured in the same configuration for $\lambda_{\text{pump}} = 800$ nm and $\lambda_{\text{probe}} = 800$ nm. The schematic shows the combined optical/x-ray pump-probe geometry. Optical (red) and x-ray (green) probe pulses collinearly propagate through a slit towards the sample. Both emerge from the laser focus on the copper tape which generates the x-ray pulses and which is removed for optical probing. (b) UXR D data from the laser-based plasma source (red dots) with removed x-ray optics to precisely determine the zero time delay. The signal is shifted by 250 fs to earlier times with respect to the data as measured, according to the analysis described in the text. For comparison we show the UXR D data measured at the SLS [open circles, reproduced from Fig. 1(a)]. The blue line is the simulated UXR D signal based on the calculated lattice dynamics. (c) Simulated average strain in STO (solid) and SRO (dashed) pattern which is consistent with the observed x-ray diffraction signal. (d) Simulated optical reflectivity for three selected probe wavelengths. (e) Corresponding color-coded horizontal cuts through Fig. 3(a).

the same geometric path. The optical path is different due to the decreased group velocities c^* in air for x rays ($c_{\text{x-ray}}^* - c$)/ $c < 10^{-6}$ and 800 nm light pulses ($c_{\text{opt}}^* - c$)/ $c = 3 \times 10^{-4}$. The 300 mm path in air behind the laser focus makes the x rays arrive 300 fs earlier than the laser pulse traveling the same path in the all-optical experiment. In addition the laser passes through 5 cm of vacuum before the focus in the x-ray experiment, which is replaced by an air path in the optical experiment, adding another 50 fs to the time delay. A contribution in the opposite direction is the additional time delay of the x-ray pulses due to the propagation of electrons in the metal target before the x-ray production. This leads to a temporally extended x-ray

pulse with a duration in the 100–200 fs range²⁹ as compared to the 40 fs laser pulses. In essence this delays the x-ray pulse by about 100 fs, since the leading edge of the x-ray pulse must coincide with the optical excitation pulse as the first generated x rays travel at the speed of light, and the trailing edge is delayed by the x-ray pulse duration which is given by the hot electrons moving through the copper target.³⁰

In short, the time axis of the UXRD experiment must be shifted by 250 fs with respect to the all-optical experiment. Time zero is determined by the steepest slope due to the electronic heating in SRO detected in the all-optical experiment [Fig. 4(a)], which is consistent with the time overlap determined in a thin BBO crystal for second-harmonic generation. Now the UXRD signal is measured in exactly the same configuration and plotted in Fig. 4(b) already shifted as discussed above. For comparison the data from Fig. 1(a) measured at the SLS are shown as well. Panel 4(c) compares this to simulations discussed below, which also predict the optical response for three selected wavelengths [panel 4(d)], which are in excellent agreement with the measured data at these wavelengths [panel 4(e)]. The pump fluence in both the UXRD and the optical experiment was approximately 20 mJ/cm². In total, Fig. 4 summarizes how time zero is compared in all-optical and UXRD experiments and how both data sets are linked to the simulation of lattice dynamics discussed in the next section.

Earlier UXRD measurements on the very same STO/SRO SL reported an additional delay of approximately 500 fs for weak excitation.^{21,31,32} Very careful analysis of all experiments shows that this discrepancy can be partly ascribed to a modified oscillation phase for the higher pump fluence and partly to the group-velocity delay of the optical pulses and x-ray pulses in air which was neglected at that time.

III. SIMULATIONS

As a theoretical support of our interpretations, we have set up a linear chain model of the superlattice in which instantaneous stress is generated by optically induced heating of the lattice. The elastic constants are known and the spatio-temporal strain pattern has been previously calculated.³³ On the timescale $t < 10$ ps heat diffusion can be neglected and it is not relevant for the stress generation.³⁴ In the optical signal it gives rise to a slowly varying background that is subtracted before considering the oscillations. The average strain in the SRO and STO layers resulting from this calculation is given in Fig. 4(c). The simulated strain map with unit-cell resolution is the common starting point to predict both the UXRD signal [panel 4(b)] and the all-optical signal [panel 4(d)]. The simulated solid line in panel 4(b) is obtained from using the calculated spatio-temporal strain pattern³³ in a dynamical x-ray diffraction simulation.²⁰

To calculate the optical response we specify the complex index of refraction $N(z, t) = n + i\kappa$ for each unit cell along growth direction of the superlattice for each timestep and calculate the optical reflectivity in a standard optical matrix formalism. For STO both the wavelength-dependent index of refraction $n_{\text{STO}}(\lambda)$ and its derivative $dn_{\text{STO}}/d\eta = 0.5$ with respect to strain η are taken from the literature.^{35–37} The complex refractive index $N_{\text{SRO}}(\lambda) = n_{\text{SRO}}(\lambda) + i\kappa_{\text{SRO}}(\lambda)$ of SRO

is derived from the literature.³⁸ The derivatives for SRO are unknown and hence we use $dn_{\text{SRO}}/d\eta$ and $d\kappa_{\text{SRO}}/d\eta$ as fitting parameters to match the observed data simultaneously for all probe wavelengths. We already obtain a reasonable agreement [compare Figs. 3(a) and 3(b) and Figs. 4(d) and 4(e)] if we assume $dn_{\text{SRO}}/d\eta = dn_{\text{STO}}/d\eta = 0.5$ and $d\kappa_{\text{SRO}}/d\eta = 1.5$ independent of wavelength. Additional variations of the optical constants with the wavelength could yield even more accurate agreement. However, already at the current level of simulation the agreement of the optical broadband data with simulations presented in Fig. 3(b) gives us confidence in our interpretation. From an experimental point of view the validation via UXRD is a preferable cross-check.

IV. DISCUSSION

For $t > 0$ the UXRD signals can be well fitted by the following function:

$$S(t) = -A \sin\left(\pi \frac{t - t_0^{\text{osc}}}{T_{\text{osc}}}\right)^2 \exp\left(-\frac{t - t_0^{\text{osc}}}{T_{\text{dec}}}\right) - m(t - t_0^{\text{lin}}). \quad (1)$$

The shape of this fitting function is uniquely determined by the physics contained in the simulation. The oscillatory part originates from the excitation of a single zone-folded LA phonon mode which modulates the x-ray diffraction structure factor of the superlattice reflection, and the decay is essentially due to the propagation of the excitation into the substrate.²⁰ The linear slope on the signal is explained by the shift of the Bragg reflection due to the average heat expansion of the superlattice.

Such a simple fitting function does not exist for the all-optical counterpart. Figure 3 illustrates that the optical signals suffer from a beating due to the interference of probe pulses reflected from the interfaces, from the phonons in the SL, and from the propagating sound wave. Despite this complicated situation, the straightforward simulation yields excellent agreement.

Now we turn to the discussion of the phase shift observed in both experiments. From the carefully determined time zero of the UXRD signal with an accuracy of about ± 100 fs, we can directly conclude that the assumption of an instantaneous stress generation in our simulation is very good, since the phase of the signal at the highest fluence corresponds to a perfect cosine, i.e., to a displacive excitation without considerable additional delay due to electron-phonon coupling. The phase of the lattice motion in the simulation is in good agreement with by the UXRD measurement.

The fluence dependent study in Fig. 1 shows that for lower fluence the lattice stress starts about 130 fs later, yielding an estimate of the electron-phonon coupling time. Although the absolute determination of the time zero is only accurate within ± 100 fs, the relative phase delay of 130 ± 50 fs is determined with sufficient accuracy. The same clear trend is observed in the oscillation phase of the all-optical signal at 670 nm [Fig. 2(c)]. Below a fluence of about 20 mJ/cm² the electronic pressure is likely negligible compared to the lattice contribution to the expansion. Hence, below this fluence the phase is set by the electron-phonon coupling time in SRO. In the simplest models for metals, the electronic heat capacity rises linearly with the temperature and the lattice contribution

saturates to the Doulong-Petit limit. However, calculations based on the electronic density of states (DOS) show that for most metals this is not true under strong nonequilibrium conditions.³⁹ Since for the case of the bad metal SRO with strong electron correlations, simulations of the DOS strongly depend on the method used,⁴⁰ and we do not attempt to predict the electronic stress contributions.

In the semiconducting material InSb a phase shift of the oscillations towards earlier times was observed for higher fluence.² This was attributed to a decreasing lattice heating time for strong excitation, essentially because the reduced lifetime of LO phonons⁴¹ limits the carrier-lattice thermalization dynamics.⁴² Similar arguments could apply in the case of SRO. Specifically, the observation of an oscillation starting earlier for higher fluence is in contrast to the observation of electronic pressure in elementary metallic systems such as aluminum and gold.^{5,6} In these metals a larger electron-phonon coupling time leads to larger effect size in the opposite direction, namely because the electron-lattice heat transfer takes longer for high fluence. We cannot rule out that contributions from impulsive Raman scattering play a role in the phase shift; however, all processes in question—Raman, electronic pressure, lattice heat expansion—scale linearly with the pump fluence in the simplest models and would not explain a fluence dependence

of the phase. Therefore we think that time- and temperature-dependent modification of the electron-phonon interaction must be responsible for the observed phase delay.

In conclusion, we have presented ultrafast x-ray diffraction (UXRD) and all-optical pump-probe experiments on the metal-dielectric superlattice STO/SRO. Only the combination of both methods allows one to experimentally deduce the absolute phase of the optically induced lattice motion. From fluence-dependent UXRD we extract a relative shift of the oscillation phase of the lattice which is readily ascribed to electronic pressure. The same fluence dependence of the phase is observed in all-optical experiments. However, the complex wavelength dependence of the broadband data highlight that the oscillation phase of all-optical experiments must be interpreted with care. Our x-ray calibrated simulations of the all-optical data validates the detailed interpretation.

ACKNOWLEDGMENTS

We thank R. van der Veen for her valuable experimental support at the MicroXAS-FEMTO beamline. We gratefully acknowledge the financial support by the BMBF via Grant No. 03WKP03A and the Deutsche Forschungsgemeinschaft (DFG) (Grant No. BA2281/3-1).

^{*}bargheer@uni-potsdam.de

¹A. Morak, T. Kaempfer, I. Uschmann, A. Luebecke, E. Foerster, and R. Sauerbrey, *Phys. Status Solidi B* **243**, 2728 (2006).

²F. S. Krasniqi, S. L. Johnson, P. Beaud, M. Kaiser, D. Grolimund, and G. Ingold, *Phys. Rev. B* **78**, 174302 (2008).

³P. Sondhaus, O. Synnergren, T. N. Hansen, S. E. Canton, H. Enquist, A. Srivastava, and J. Larsson, *Phys. Rev. B* **78**, 115202 (2008).

⁴D. M. Fritz, D. A. Reis, B. Adams, R. A. Akre, J. Arthur, C. Blome, P. H. Bucksbaum, A. L. Cavalieri, S. Engemann, S. Fahy *et al.*, *Science* **315**, 633 (2007).

⁵J. Li, R. Clinite, X. Wang, and J. Cao, *Phys. Rev. B* **80**, 014304 (2009).

⁶M. Nicoul, U. Shymanovich, A. Tarasevitch, D. von der Linde, and K. Sokolowski-Tinten, *Appl. Phys. Lett.* **98**, 191902 (2011).

⁷A. Bartels, T. Dekorsy, H. Kurz, and K. Köhler, *Phys. Rev. Lett.* **82**, 1044 (1999).

⁸H. J. Zeiger, J. Vidal, T. K. Cheng, E. P. Ippen, G. Dresselhaus, and M. S. Dresselhaus, *Phys. Rev. B* **45**, 768 (1992).

⁹C.-K. Sun, J.-C. Liang, and X.-Y. Yu, *Phys. Rev. Lett.* **84**, 179 (2000).

¹⁰T. E. Stevens, J. Kuhl, and R. Merlin, *Phys. Rev. B* **65**, 144304 (2002).

¹¹T. Dekorsy, G. Cho, and H. Kurz, in *Light Scattering in Solids VIII*, Vol. 76 of *Topics in Applied Physics*, edited by M. Cardona and G. Güntherodt (Springer, Berlin, 2000), pp. 169–209.

¹²V. V. Kruglyak, R. J. Hicken, G. P. Srivastava, M. Ali, B. J. Hickey, A. T. G. Pym, and B. K. Tanner, *Phys. Rev. B* **76**, 012301 (2007).

¹³M. Hase, K. Ishioka, J. Demsar, K. Ushida, and M. Kitajima, *Phys. Rev. B* **71**, 184301 (2005).

¹⁴S. L. Johnson, P. Beaud, C. J. Milne, F. S. Krasniqi, E. S. Zijlstra, M. E. Garcia, M. Kaiser, D. Grolimund, R. Abela, and G. Ingold, *Phys. Rev. Lett.* **100**, 155501 (2008).

¹⁵M. Hase, M. Kitajima, A. Constantinescu, and H. Petek, *Nature (London)* **426**, 51 (2003).

¹⁶A. Cavalleri, S. Wall, C. Simpson, E. Statz, D. W. Ward, K. A. Nelson, M. Rini, and R. W. Schoenlein, *Nature (London)* **442**, 664 (2006).

¹⁷K. J. Yee, Y. S. Lim, T. Dekorsy, and D. S. Kim, *Phys. Rev. Lett.* **86**, 1630 (2001).

¹⁸C. Colvard, T. A. Gant, M. V. Klein, R. Merlin, R. Fischer, H. Morkoc, and A. C. Gossard, *Phys. Rev. B* **31**, 2080 (1985).

¹⁹M. Bargheer, N. Zhavoronkov, Y. Gritsai, J. C. Woo, D. S. Kim, M. Woerner, and T. Elsaesser, *Science* **306**, 1771 (2004).

²⁰M. Herzog, D. Schick, W. Leitenberger, R. Shayduk, R. M. van der Veen, C. J. Milne, S. L. Johnson, I. Vrejoiu, and M. Bargheer, *New J. Phys.* **14**, 013004 (2012).

²¹C. von Korff Schmising, A. Harpoeth, N. Zhavoronkov, Z. Ansari, C. Aku-Leh, M. Woerner, T. Elsaesser, M. Bargheer, M. Schmidbauer, I. Vrejoiu *et al.*, *Phys. Rev. B* **78**, 060404 (2008).

²²M. Herzog, W. Leitenberger, R. Shayduk, R. van der Veen, C. J. Milne, S. L. Johnson, I. Vrejoiu, M. Alexe, D. Hesse, and M. Bargheer, *Appl. Phys. Lett.* **96**, 161906 (2010).

²³P. Beaud, S. L. Johnson, A. Streun, R. Abela, D. Abramsohn, D. Grolimund, F. S. Krasniqi, T. Schmidt, V. Schlott, and G. Ingold, *Phys. Rev. Lett.* **99**, 174801 (2007).

²⁴The strain amplitude is derived by comparing the model and experimental data in the inset of Fig. 3(a) in Ref. 20. Since the agreement is nearly perfect, the mapping of fluence on strain yields

the linear function presented in Fig. 1(b). We do not attempt to discuss the tiny deviations, as we focus here on the phase of the oscillations.

- ²⁵I. Bozovic, M. Schneider, Y. Xu, R. Sobolewski, Y. H. Ren, G. Lüpke, J. Demsar, A. J. Taylor, and M. Onellion, *Phys. Rev. B* **69**, 132503 (2004).
- ²⁶S. Brivio, D. Polli, A. Crespi, R. Osellame, G. Cerullo, and R. Bertacco, *Appl. Phys. Lett.* **98**, 211907 (2011).
- ²⁷D. Schick, A. Bojahr, M. Herzog, C. von Korff Schmising, R. Shayduk, W. Leitenberger, P. Gaal, and M. Bargheer, *Rev. Sci. Instrum.* **83**, 025104 (2012).
- ²⁸F. Zamponi, Z. Ansari, C. von Korff Schmising, P. Rothhardt, N. Zhavoronkov, M. Woerner, T. Elsaesser, M. Bargheer, T. Trobitzsch-Ryll, and M. Haschke, *Appl. Phys. A* **96**, 51 (2009).
- ²⁹F. Zamponi, Z. Ansari, M. Woerner, and T. Elsaesser, *Opt. Express* **18**, 947 (2010).
- ³⁰C. Reich, P. Gibbon, I. Uschmann, and E. Förster, *Phys. Rev. Lett.* **84**, 4846 (2000).
- ³¹C. von Korff Schmising, M. Bargheer, M. Kiel, N. Zhavoronkov, M. Woerner, T. Elsaesser, I. Vrejoiu, D. Hesse, and M. Alexe, *Appl. Phys. B* **88**, 1 (2007).
- ³²M. Woerner, C. von Korff Schmising, M. Bargheer, N. Zhavoronkov, I. Vrejoiu, D. Hesse, M. Alexe, and T. Elsaesser, *Appl. Phys. A* **96**, 83 (2009).
- ³³M. Herzog, D. Schick, P. Gaal, R. Shayduk, C. von Korff Schmising, and M. Bargheer, *Appl. Phys. A* **106**, 489 (2012).
- ³⁴R. Shayduk, H. A. Navirian, W. Leitenberger, J. Goldshteyn, I. Vrejoiu, M. Weinelt, P. Gaal, M. Herzog, C. von Korff Schmising, and M. Bargheer, *New J. Phys.* **13**, 093032 (2011).
- ³⁵M. Cardona, *Phys. Rev.* **140**, A651 (1965).
- ³⁶A. Giardini, *J. Opt. Soc. Am.* **47**, 726 (1957).
- ³⁷M. L. Hassel Ledbetter and S. Kim, *Phase Transitions* **23**, 61 (1990).
- ³⁸P. Kostic, Y. Okada, N. C. Collins, Z. Schlesinger, J. W. Reiner, L. Klein, A. Kapitulnik, T. H. Geballe, and M. R. Beasley, *Phys. Rev. Lett.* **81**, 2498 (1998).
- ³⁹Z. Lin, L. V. Zhigilei, and V. Celli, *Phys. Rev. B* **77**, 075133 (2008).
- ⁴⁰H.-T. Jeng, S.-H. Lin, and C.-S. Hsue, *Phys. Rev. Lett.* **97**, 067002 (2006).
- ⁴¹K. T. Tsen, J. G. Kiang, D. K. Ferry, and H. Morkoc, *Appl. Phys. Lett.* **89** (2006).
- ⁴²A. H. Chin, R. W. Schoenlein, T. E. Glover, P. Balling, W. P. Leemans, and C. V. Shank, *Phys. Rev. Lett.* **83**, 336 (1999).

PAPER VI

Nanoscale heat transport studied by high-resolution time-resolved x-ray diffraction

R. Shayduk, H. Navirian, W. Leitenberger, J. Goldshteyn,
I. Vrejoiu, M. Weinelt, P. Gaal, M. Herzog,
C. von Korff Schmising and M. Bargheer.

New J. Phys. **13**, 093032 (2011).

Nanoscale heat transport studied by high-resolution time-resolved x-ray diffraction

Roman Shayduk¹, Hengameh Navirian¹, Wolfram Leitenberger², Jevgenij Goldshteyn¹, Ionela Vrejoiu³, Martin Weinelt⁴, Peter Gaal², Marc Herzog², Clemens von Korff Schmising⁵ and Matias Bargheer^{1,6}

¹ Helmholtz Zentrum Berlin, Albert-Einstein-Strasse 15, 12489 Berlin, Germany

² Institute of Physics and Astronomy, University of Potsdam, Karl-Liebkecht-Strasse 24-25, 14476 Potsdam, Germany

³ Max-Planck-Institut für Mikrostrukturphysik, Weinberg 2, 06120 Halle, Germany

⁴ Freie Universitaet Berlin, Fachbereich Physik, Institut für Experimentalphysik, Arnimallee, 14 14195 Berlin, Germany

⁵ Atomic Physics Division, Department of Physics, Lund University, PO Box 118, 22100 Lund, Sweden

E-mail: bargheer@uni-potsdam.de

New Journal of Physics **13** (2011) 093032 (11pp)

Received 21 June 2011

Published 20 September 2011

Online at <http://www.njp.org/>

doi:10.1088/1367-2630/13/9/093032

Abstract. We report on synchrotron-based high-repetition rate ultrafast x-ray diffraction (UXRD) experiments monitoring the transport of heat from an epitaxial $\text{La}_{0.7}\text{Sr}_{0.3}\text{MnO}_3/\text{SrTiO}_3$ superlattice (SL) into the substrate on timescales from 100 ps to 4 μs . Transient thermal lattice expansion was determined with an accuracy of 10^{-7} , corresponding to a sensitivity to temperature changes down to 0.01 K. We follow the heat flow within the SL and into the substrate after the impulsive laser heating leads to a small temperature rise of $\Delta T = 6$ K. The transient lattice temperature can be simulated very well using the bulk heat conductivities. This contradicts the interpretation of previous UXRD measurements, which predicted a long-lasting expansion of SrRuO_3 for more than 200 ps. The disagreement could be resolved by assuming that the heat conductivity changes in the first hundred picoseconds.

⁶ Author to whom any correspondence should be addressed.

Contents

1. Introduction	2
2. Instrumental setup	3
3. Experimental results	5
4. Discussion and simulation of the heat flow in $\text{La}_{0.7}\text{Sr}_{0.3}\text{MnO}_3/\text{SrTiO}_3$ superlattices	7
Acknowledgments	10
References	11

1. Introduction

The development of tailored materials on the nanometer scale demands a detailed understanding of thermal transport properties, especially for multi-gigahertz nanoelectronics and superlattices (SLs) for thermoelectrics [1–4]. Ultrafast x-ray diffraction (UXRD) at synchrotrons offers a direct material-specific probe of local heat expansion on the timescale down to 100 ps, relevant for heat transport on this small length scale [5]. The material is excited (pumped) periodically by short laser pulses which are electronically synchronized with the periodic synchrotron x-ray pulses. This technique has been successfully applied to the detailed analysis of lattice expansion due to coherent acoustic phonons (sound waves) in bulk semiconductor materials [6], to the measurement of ultrafast dynamics in semiconductor SLs [7] and to the unfolding of these SL phonons when they propagate into the substrate [8]. A recent report extends these investigations to the expansion of oxide SLs [9], which have been explored with a time resolution of 150 fs using femto-slicing at a synchrotron [10]. The driving mechanism of coherent acoustic phonons is classified as thermal expansion, in which both electrons and phonons may contribute to the expansion [11]. The coherent acoustic phonons propagating at the speed of sound leave the SL within 80 ps after excitation.

In this paper, we study thermal lattice expansion in a pseudomorphic $\text{La}_{0.7}\text{Sr}_{0.3}\text{MnO}_3$ (LSMO)/ SrTiO_3 (STO) SL on timescales from 100 ps to 4 μs after laser heating of the metallic LSMO layers. X-rays penetrate into the materials, which can be identified in UXRD by their distinct Bragg angles. The individual lattice expansions are deduced from the transient shift of the x-ray diffraction (XRD) curves with an unprecedented accuracy of 10^{-7} , owing to the high repetition rate (208 kHz) of the laser system. The experimental observations are in excellent agreement with heat diffusion simulations on timescales from 4 ns to 4 μs , yielding typical bulk values for heat conductivity in the SL. The SL thickness is 338 nm and consists of 15 periods of LSMO/STO double layers epitaxially grown on STO (001) substrate. The LSMO layers are opaque to the 800 nm laser radiation and absorb energy, while the STO layers are transparent.

It has been reported that for a similar SrRuO_3 (SRO)/STO SL, the absorbing SRO layers remain considerably expanded even after 200 ps, while at the same time the insulating STO layers are expanded only slightly [12, 13]. On this timescale no modulation due to coherent acoustic phonons remains in the SL and only the hot phonons or electrons contribute to the ‘thermal’ expansion.

We will show that in order to agree with the above observations, the heat diffusion equation would require extremely low values for the heat conductivity of the SL, compared with that of the bulk. Although there are many reports on additional heat resistance in SLs due to nanometer layer thickness and the presence of interfaces, we estimate that the accepted formulae do not

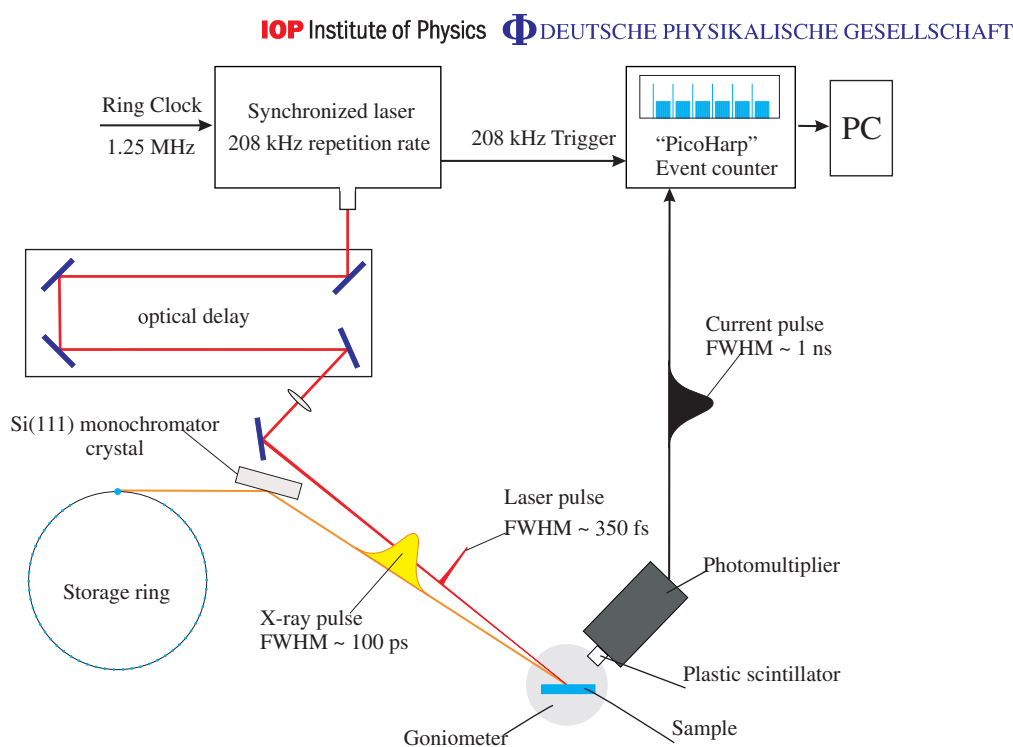


Figure 1. Simplified scheme of the experimental setup. For the explanation, see the main text.

predict considerable deviation from bulk [1, 14]. This may indicate that *transient* processes reduce the heat conductivity on timescales of ~ 100 ps after excitation.

2. Instrumental setup

The pump–probe setup is assembled at the storage ring BESSY II (Berlin, Germany). The EDR bending magnet beam line provides x-ray radiation in the broad energy range of 4–15 keV, which is monochromatized by a single Si(111) crystal. The total monochromatic photon flux was 2×10^5 photons $(\text{s mA mm}^2)^{-1}$ at the energy of 8.9 keV.

The pump–probe repetition rate is a compromise between the pulse energy required to induce large structural changes and the laser power. In typical UXRD setups, the repetition rate is of the order of a few kilohertz, allowing for high pump fluences [5, 10, 15]. Such excitation conditions often result in nonlinear sample response. In some cases, a low pulse intensity is preferable where the effects induced in the sample are linear. In this case, the laser repetition rate can be increased, resulting in an advantageous increase of the useable x-ray photon flux. The repetition rate of the x-ray probe photons of 1.25 MHz is determined by the round-trip time of the electron bunches in the storage ring. This high repetition rate facilitates shot-noise-limited single x-ray photon counting and therefore allows detection of weak changes in the sample.

Figure 1 shows a schematic diagram of the experimental setup for the UXRD experiments. A Ti:sapphire laser system (Coherent RegA) with the pulse duration set to 350 fs was synchronized with the master clock of the storage ring in order to operate at one-sixth of the 1.25 MHz ‘bunch marker’ signal (~ 208 kHz). The laser has a synchronization loop in which the actual laser output is detected and compared with the master clock. To keep the output pulses

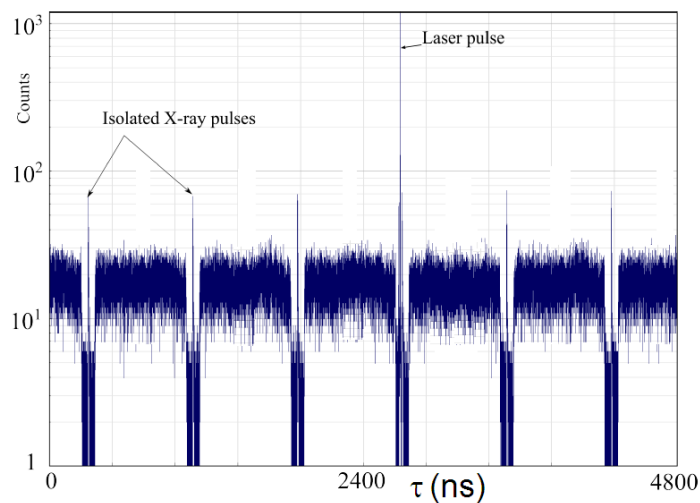


Figure 2. Typical synchrotron bunch pattern including the optical laser pulse as a function of the single-photon arrival time τ . The full time interval corresponds to the laser repetition rate of ~ 208 kHz and is equal to the duration of six electron revolutions in the ring.

synchronized with the ring clock, the length of the laser oscillator cavity is actively controlled and continuously adjusted. The ultrashort laser pulses are used to impulsively heat the SL with an absorbed fluence of 0.7 mJ cm^{-2} . The change in temperature is followed by UXRD.

For the detection of the x-rays, we used a plastic scintillator ($< 0.5 \text{ ns}$ rise time). The scintillator converts the x-ray radiation into optical photons with a typical yield of $10\,000 \text{ photons MeV}^{-1}$. For a single 8.9 keV photon about 100 optical photons are generated, detected by a photomultiplier (Hamamatsu) and sent via a current amplifier (FEMTO) to a single-photon counting module (PicoQuant ‘PicoHarp’) for counting the current pulses. The x-ray photon flux per bunch was small enough to prevent counting multiple x-ray photons as a single event. As the plastic scintillator is transparent for the laser light, the same detector is used to detect attenuated laser pulses. This allows us to coarsely adjust the temporal overlap between the laser pump and x-ray probe pulses.

During the diffraction experiment with full laser power, the detector is shielded by an Al-coated Be window that fully blocks the optical laser reflected from the sample. Figure 2 shows the histogram of the x-ray pulse sequence as a function of the single photon arrival time τ together with the pump–laser pulse. The time structure of the electrons in the ring becomes visible after summing up the x-ray photon events repeatedly using the $\sim 208 \text{ kHz}$ trigger of the synchronized laser. The histogram shows six periods of the ring bunch pattern, a sequence of 350 bunches with a period of 2 ns is followed by a 100 ns gap filled by a single x-ray pulse (hybrid mode of BESSY II). The strong single spike at 2694 ns in the histogram corresponds to the optical laser pulses with $\sim 208 \text{ kHz}$ repetition rate. Thus, for every sixth isolated x-ray pulse the sample is excited by the pump pulse. The accuracy in determining the preliminary time overlap using this method is limited by the scintillator response time jitter, which is of the order of half a nanosecond. For more accurate x-ray and laser timing (within 100 ps) we use ultrafast processes, which occur in the sample after laser excitation described in the next

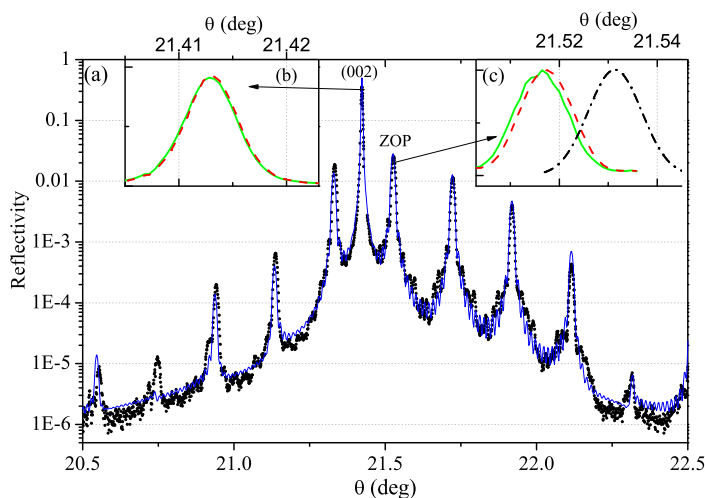


Figure 3. (a) Experimental diffraction curve (black dots) of the LSMO/STO SL near the (0 0 2) substrate peak and simulation (blue line) according to dynamical diffraction. (b) Barely visible transient shift of the substrate peak (red line: at 4 μ s; green line: at 100 ns). (c) Diffraction curves of the zero-order peak (ZOP) of the SL (dash dotted black line: no laser on the sample; dashed red line: at 4 μ s; solid green line: at 100 ps). Note the substantial permanent heating (26 K) induced by the laser pulse. The time dependence of the transient heating (positions of green curves in (b) and (c)) is plotted in figure 4.

section. The pump–probe delay can be set by varying the optical path length of the laser with sub-picosecond precision; however, the timing-jitter of the electronic synchronization is of the order of 1 ps and the actual time resolution is given by the x-ray pulse duration of ~ 100 ps.

3. Experimental results

We typically scan θ – 2θ diffraction curves, keeping the electronically and optically controlled time delays fixed. This allows for the observation of all shape modifications of the rocking curve, including peak shifts and intensity changes. By varying the optical delay for each scan we are able to monitor the XRD changes on sub-nanosecond timescales.

An extended θ – 2θ diffraction curve of the LSMO/STO multilayer is shown in figure 3. It consists of the (002) Bragg reflection of the STO substrate and a number of SL Bragg reflections. The spacing of the SL reflections is defined by the SL period, while the width of the SL reflections is inversely proportional to the total SL thickness.

The position $q^{(0)} = \frac{2\pi}{c_{\text{av}}}$ of the so-called zero-order SL peak (ZOP) corresponds to the average lattice constant of a single double layer (DL) which is given by

$$c_{\text{av}} = \frac{n_{\text{M}}c_{\text{M}} + n_{\text{I}}c_{\text{I}}}{n_{\text{M}} + n_{\text{I}}}, \quad (1)$$

where n_{M} and n_{I} correspond to the number of unit cells in the metallic LSMO and insulating STO layers with lattice constants c_{M} and c_{I} , respectively. The ZOP is the brightest SL reflection since it profits from the diffraction efficiencies of both bulk constituents, which are significant

(large envelope) only around their bulk Laue conditions in a q -range given by the inverse thickness (n_{MCM} and n_{IC1}) of a single metallic or insulating layer.

The energy deposited in the SL induces its thermal expansion. The time it takes a sound wave—a wavepacket of acoustic phonons—to propagate through the SL is 40 ps [16]. Therefore, at delay times of about 100 ps after excitation, the strain in the SL is governed only by the transient temperature profile.

Figure 3(c) shows the ZOP at 100 ps after laser excitation (solid green), 4 μs later (red dashed) and without laser illumination of the sample (black dotted). The shift of the diffraction peak at 4 μs delay describes the static, average temperature rise of the SL, which depends on the average power of the laser. The large shift with respect to the black dotted curve shows that the high average power of the laser leads to a rather large average temperature rise. Clearly the solid green line recorded at a delay of 100 ps shows an additional shift toward lower angles. This demonstrates that laser excitation leads to an ultrafast expansion of the SL, which relaxes toward the static, average thermal expansion on the nano- to microsecond timescale.

Figure 3(b) shows the tiny shift of the substrate reflection after 100 ns (solid green) compared with 4 μs (red dashed) after excitation.

We note that the diffraction curve at 4 μs is obtained by counting the corresponding x-ray photons (see figure 2) without the need for scanning the delay. Therefore, for each individual optical delay position the reference peak for 4 μs delay is measured simultaneously, allowing for a very precise determination of *transient* peak shifts (for a delay of 4 μs the actual picosecond delay can be neglected). In addition, the single-photon counting eliminates photomultiplier noise or gain fluctuations, leading to an unprecedented level of accuracy.

Figure 4(a) shows transient peak shifts of the ZOP (blue bullets) and the substrate (002) reflection (black squares) on the picosecond timescale. The transient shift of the ZOP is fitted by an error function, the derivative of which is a Gaussian with full-width at half-maximum (FWHM) of 100 ps. This is approximately the width of the x-ray pulse. The delay time zero, where x-ray and laser pulses coincide, is therefore given by the time when the peak is half-way shifted. We see no shift of the substrate peak on this timescale, since there is not enough time for the heat to propagate from the SL deep into the substrate. Notably, the SL peak is already shifted for negative time delays by approximately one-tenth of the maximum shift. This is probably due to pre-pulses of the laser system which pump the sample before the main pulse.

The shift of the Bragg peaks can be used to determine the temperature change of the SL and substrate from the relation

$$\cot \theta \Delta \theta = -\alpha \Delta T, \quad (2)$$

where α is the linear thermal expansion coefficient of the corresponding material, $\Delta \theta$ is the change of the Bragg angle from its stationary value θ and T is the temperature. We take the thermal expansion coefficient measured in thin films, since epitaxial strain may modify the expansion in an anisotropic way. Figure 4(c) shows the transient peak shifts and temperature rise of both the substrate and the SL on an extended timescale. The substrate peak is sensitive to the averaged temperature of the first few microns of the substrate; therefore the shift appears much later than that for the SL. As soon as the heat has diffused deeper than the x-rays penetrate, the shift starts to vanish again. It is worth noting that statistical error bars for the peak positions are significantly smaller for longer times, since more x-ray pulses separated by only 2 ns can be used for counting at fixed resolving power $\Delta t/t$ (cf figure 2), resulting in an increased count rate. The standard deviation for the relative change of the substrate peak position

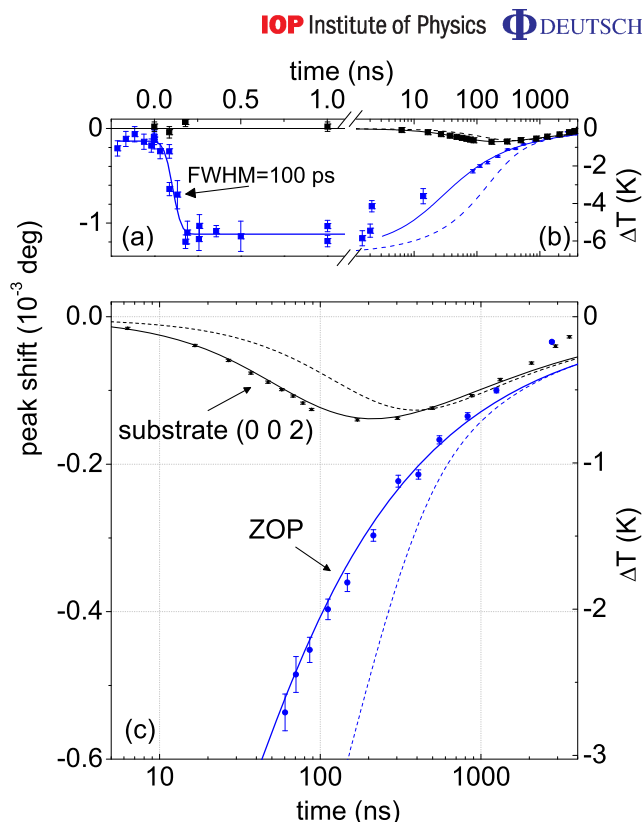


Figure 4. (a) Transient peak shift of the substrate peak (small black dots) and ZOP of the SL (large blue dots). The error-function fit (blue line) corresponds to the Gaussian FWHM of the synchrotron pulse with a duration of ~ 100 ps. (b) The same peak shifts on longer timescales, together with fitting curves according to the diffusion equation with the heat conductivity of 6.9 W (m K)^{-1} (solid lines). The dashed lines indicate the crude misfit of a simulation with ten times smaller heat conductivity than predicted by previous experiments [12] (see text). (c) The same as (b), but with a clearer visibility of the very small error bars down to 10^{-7} .

is less than 10^{-7} degrees, which corresponds to an accuracy in the temperature measurement of 0.01 K.

4. Discussion and simulation of the heat flow in $\text{La}_{0.7}\text{Sr}_{0.3}\text{MnO}_3/\text{SrTiO}_3$ superlattices

The experimental measurement of the transient shift of the SL and substrate Bragg peaks (figure 4) can be readily translated into a transient temperature change indicated on the right abscissa using equation (2) with the thermal expansion coefficient α_{SL} of the SL. Thus, the experiments quantify the heat flow from the SL into the substrate that occurs on the 10–100 ns timescale. The temperature rise in the substrate is smaller because the detection volume is given by the extinction depth of the x-rays ($\approx 1.5 \mu\text{m}$), which is five times larger than the SL thickness. In addition, the temperature rise profile of the excited SL decays as the heat flows into the substrate.

Table 1. Properties of the LSMO/STO SL used in the calculations. The results obtained from simultaneously fitting the SL and substrate data in figure 4 (blue and black solid lines) are in boldface.

Physical property	Units	Material		
		LSMO	STO	SL
Thickness	nm	8.85	13.7	338
Density	kg m ⁻³	5600	5120	5308
Thermal conductivity κ	W (m K) ⁻¹	2.8 [18]–4 [19]	11.1 [20]	6.9
Heat capacity C	J (kg K) ⁻¹	545.4 [21]	530 [22]	536
Thermal expansion coefficient α	1 K ⁻¹	1.16×10^{-5} [23]	1.1×10^{-5} [23]	1.1×10^{-5}
Speed of sound	m s ⁻¹	6500 [24]	7800 [24]	7232

For a quantitative comparison, we simulated the heat transport in a first approximation by treating the SL as a medium with an effective thermal conductivity κ_{SL} and heat capacity C_{SL} . Although C_{SL} can be calculated as a weighted average of the constituent layers (table 1), the situation for the conductivity is more complex and we choose to determine this value from a fit to the experimental data. For macroscopic systems the heat resistance of a layered material is the direct sum of the heat resistances of its components. Deviations from the simple sum rule were observed on small length scales in SLs, in which the high densities of interfaces result in additional phonon scattering mechanisms and the wave properties of the heat-carrying phonons are modified by zone folding [1, 2]. In the present SL, we can disregard interference since the mean free path of phonons [17] at room temperature is $L = 3\kappa/C \cdot v \approx 1$ nm, where C is the average heat capacity and v the average group velocity of acoustic phonons. In any case, all these additional phonon scattering mechanisms result in a *permanent* change of heat transport properties, which should be visible on all timescales.

In the following, we show that the static change of heat transport in our SL is negligible, but there must be mechanisms that result in *transient* effects on heat transport. We use a one-dimensional (1D) model, since the lateral size of the excited region is much larger than the probed depth of the sample. In this model, heat is initially distributed within the 15 LSMO layers of the SL according to the exponentially decaying absorption profile for the 800 nm light pulses. STO is transparent at this wavelength. The heat then equilibrates among the LSMO and STO layers and finally diffuses into the substrate. The thermal properties of the materials are taken from the literature (see table 1). The heat conduction coefficient of the SL and of the substrate, as well as the total absorbed energy density, were free parameters that were determined by solving the diffusion equation, computing the expected Bragg peak position and varying the parameters until the deviations of both experimental transients (SL and substrate) and simulations were minimized globally for all delays⁷.

The results of the heat conduction simulations are shown in figure 5. To check the numerical computation accuracy, the total heat in the sample was calculated for each time. It remains constant within 0.8% throughout the simulated time axis. A specific variation of the

⁷ To speed up the fitting procedure, we calculated the peak position of the substrate by a Gaussian weight of the substrate strain around the extinction depth. Then we used dynamical XRD theory to verify that the correct substrate peak position was obtained using this approximate method. The best fit is shown in figure 4 by solid lines and the resulting heat conduction parameters are collected in table 1 in boldface.

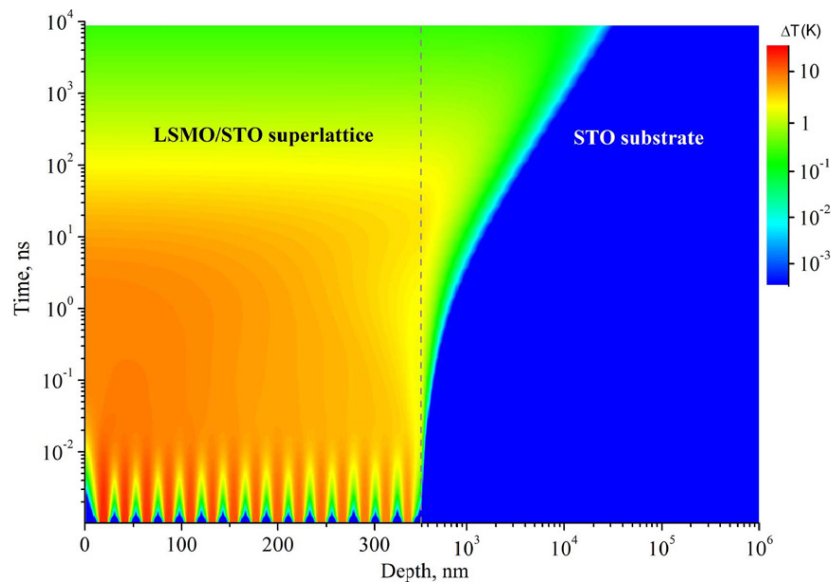


Figure 5. Contour plot of the calculated temperature rise of the sample as a function of depth and time according to the diffusion equation with the heat conductivity of 6.9 W (m K)^{-1} , which leads to the best fit in figure 4. Note that this simulation predicts complete equilibration of heat between the STO and LSMO layers of the SL within 10–20 ps.

heat conduction coefficients of either the LSMO or the STO layer or the interface does not affect the fit as long as their weighted averages coincide. Figure 4(c) shows that the 1D heat conduction model reproduces the experimental data up to 1000 ns excellently. At later times, the measured cooling rate is higher than predicted in the 1D simulations because the in-plane heat conduction can no longer be neglected and the problem becomes 3D.

The fitted heat conduction coefficient for the SL $\kappa_{\text{SL}} = 6.9 \text{ W (m K)}^{-1}$ agrees well with the value obtained from the sum of heat resistances, with an expected range of $\kappa_{\text{SL}}^{\text{sum}} = 5.2\text{--}6.5 \text{ W (m K)}^{-1}$ given by the spread in the literature data for κ_{LSMO} (see table 1). Thus no deviation from the bulk heat conduction due to the nanoscale size of the SL is observed in our experiment.

The effects due to the interference of phonon waves in the SL are negligible according to the small phonon mean free path $L = 1 \text{ nm}$. Assuming fully diffuse and inelastic scattering (in the high temperature limit) and neglecting scattering within the layers, the interface conductivity in the SL can be estimated as [1, 14]

$$\kappa_{\text{SL}} = \frac{C_1 v_1 C_2 v_2}{C_1 v_1 + C_2 v_2} \frac{d_1 + d_2}{2}, \quad (3)$$

where C_i is the specific heat, v_i is the sound velocity and d_i is the layer thickness of layer i . This formula yields $\kappa_{\text{SL}} = 122 \text{ W (m K)}^{-1} \gg \kappa_{\text{SL}}^{\text{sum}}$, so neglecting the interface scattering is also a valid approximation.

Remarkably, the simulation of heat transport reported in figure 5 predicts that the temperature completely equilibrates within 10–20 ps between the STO and the LSMO layers

of the SL. This is in stark contrast to previous UXRd measurements on a comparable⁸ SL of the SRO/STO layer, where it has been argued that the heat remains within the metallic SRO layers for at least 200 ps after excitation [12, 13]. In order to increase the LSMO/STO temperature equilibration time in our simulations by one order of magnitude to match *this* equilibration time of at least 200 ps reported in the literature [12, 13], the effective heat conduction within the SL would have to be reduced by one order of magnitude. For such parameters the heat conduction equation predicts the temperature change shown in figure 4(c) by the dashed lines, which show a strong deviation from the experimental curves in the 1–200 ns time range.

The observation of poor heat conduction shortly after the laser pulse excitation and bulk heat conduction for nanosecond timescales suggests that the thermal conductivity is time dependent. This may be a manifestation of the fact that the concept of thermal equilibrium is not applicable within the first hundred picoseconds. While electron–phonon scattering is much faster (~ 1 ps), optical phonons are predominantly excited in ionic crystal lattices. The equilibration of optical and acoustic phonon temperatures may require much longer in oxide SLs. The energy and wavevector of these optical modes cannot be conserved in the dominant optical phonon decay channel into two acoustic phonons of opposite k -vector known from semiconductors such as GaAs, since the energy of the optical phonons is larger than that for the acoustic phonons with the highest energy. Since optical phonons have a group velocity close to zero, they propagate heat less efficiently. Only after an equilibration time of about 100 ps does the population of the heat-carrying acoustic modes become considerable, supporting efficient heat transport comparable to the bulk heat conduction in thermal equilibrium. This would imply that deposition of heat by optical excitation, used in many heat pulse experiments, could only be described by an effective heat conduction coefficient that is time dependent on the sub-nanosecond timescale. In this scenario, the heat would be confined to the SRO layers after 200 ps, as demanded in [12, 13], although the heat conduction on the nanosecond timescale is described by the bulk values observed here. Rather challenging future experiments that measure several Bragg reflections simultaneously can in principle clarify whether the rapid heat diffusion within the SL implied by figure 5 really takes place.

In conclusion, we have demonstrated how UXRd at a high repetition rate (208 kHz) can be used to accurately measure the heat diffusion in multilayered samples on the nanoscale and on the timescale from 100 ps to a few μ s. The heat conduction simulations using bulk constants describe very well the thermal diffusion from an SL into the substrate on the nanosecond timescale. However, the same simulations predict that heat transport in SLs with layer periods in the nanometer range proceeds in a few picoseconds. This is in clear disagreement with the interpretation of previous UXRd work, which has measured strong differences in the heat expansion of the constituting layers even after 200 ps. The combination of these results suggests that on very short timescales the parameter describing thermal conductivity becomes time dependent.

Acknowledgments

We gratefully acknowledge R Schumann (Max-Born-Institute, Berlin, Germany) for assistance with the alignment and synchronization of the laser system. We thank the DFG for supporting

⁸ SRO is a ferromagnetic metal with the same crystal structure and a heat conductivity [25] of 5.7 W (m K)^{-1} , which is somewhat larger than the value for LSMO. The layering sequence is very similar as well: $d_{\text{SRO}} = 7.5 \text{ nm}$ and $d_{\text{STO}} = 12.9 \text{ nm}$.

this work via BA 2281/3-1 and SFB 762. CvKS thanks the Swedish Research Council (VR) for financial support.

References

- [1] Goodson K E and Ju Y S 1999 *Annu. Rev. Mater. Sci.* **29** 261–93
- [2] Cahill D G *et al* 2003 *J. Appl. Phys.* **93** 793
- [3] Sootsman J R, Chung D Y and Kanatzidis M G 2009 *Angew. Chem., Int. Ed. Engl.* **48** 8616–39
- [4] Chowdhury I *et al* 2009 *Nat. Nanotechnol.* **4** 235
- [5] Sheu Y M *et al* 2008 *Phys. Rev. B* **78** 045317
- [6] Rose-Petruck C, Jimenez R, Guo T, Cavalleri A, Siders C W, Rksi F, Squier J A, Walker B C, Wilson K R and Barty C P J 1999 *Nature* **398** 310
- [7] Bargheer M, Zhavoronkov N, Gritsai Y, Woo J C, Kim D S, Woerner M and Elsaesser T 2004 *Science* **306** 1771
- [8] Trigo M *et al* 2008 *Phys. Rev. Lett.* **101** 025505
- [9] Navirian H A, Herzog M, Goldshteyn J, Leitenberger W, Vrejoiu I, Khakhulin D, Wulff M, Shayduk R, Gaal P and Bargheer M 2011 *J. Appl. Phys.* **109** 126104
- [10] Herzog M, Leitenberger W, Shayduk R, van der Veen R, Milne C J, Johnson S L, Vrejoiu I, Alexe M and Hesse D 2010 *Appl. Phys. Lett.* **96** 161906
- [11] Li J, Clinite R, Wang X and Cao J 2009 *Phys. Rev. B* **80** 014304
- [12] von Korff C, Schmising A, Zhavoronkov N, Woerner M, Elsaesser T, Bargheer M, Schmidbauer M, Vrejoiu I, Hesse D and Alexe M 2009 *Phys. Procedia* **3** 333
- [13] Woerner M, von Korff Schmising C, Bargheer M, Zhavoronkov N, Vrejoiu I, Hesse D, Alexe M and Elsaesser T 2009 *Appl. Phys. A* **96** 83
- [14] Chen G 1998 *Phys. Rev. B* **57** 14958
- [15] Neutze R, Wouts R, Techert S, Davidsson J, Kocsis M, Kirrander A, Schotte F and Wulff M 2001 *Phys. Rev. Lett.* **87** 195508
- [16] von Korff Schmising C, Bargheer M, Kiel M, Zhavoronkov N, Woerner M, Elsaesser T, Vrejoiu I, Hesse D and Alexe M 2007 *Appl. Phys. B* **88** 1
- [17] Ashcroft N W and Mermin D N 1976 *Solid State Physics* (Philadelphia, PA: Saunders)
- [18] Huang Q, Cheng Y, Liu X, Xu X and Zhang S 2006 *Ultrasonics* **44** e1223
- [19] Fujishiro H, Kanoh S and Ikebe M 2002 *J. Phys. Soc. Japan* **71** 142
- [20] Suemune Y 1965 *J. Phys. Soc. Japan* **20** 174
- [21] Niu D, Liu X, Huang Q and Zhang S 2005 *J. Physique IV* **125** 249
- [22] de Ligny D and Richet P 1996 *Phys. Rev. B* **53** 3013
- [23] Farag N, Bobeth M, Pompe W, Romanov A E and Speck J S 2005 *Phys. Status Solidi a* **202** R44
- [24] Ren Y H, Trigo M, Merlin R, Adyam V and Li Q 2007 *Appl. Phys. Lett.* **90** 251918
- [25] Yamanaka S, Maekawa T, Muta H, Matsuda T, Kobayashi S and Kurosaki K 2004 *J. Solid State Chem.* **177** 3484

PAPER VII

Calibrated real time detection of nonlinearly propagating giant strain waves

A. Bojahr, M. Herzog, D. Schick, I. Vrejoiu and
M. Bargheer.

submitted.

Calibrated real time detection of nonlinearly propagating strain waves

André Bojahr, Marc Herzog, Daniel Schick, Ionela Vrejoiu¹ and Matias Bargheer^{1,*}

^{1a} *Helmholtz Zentrum Berlin, Albert-Einstein-Str. 15, 12489 Berlin, Germany,* ^b *Institute of Physics and Astronomy, University of Potsdam, Karl-Liebknecht-Strasse 24-25, 14476 Potsdam, Germany,*

^c *Max-Planck-Institut für Mikrostrukturphysik, Weinberg 2, 06120 Halle, Germany*

(Dated: June 29, 2012)

Epitaxially grown metallic oxide transducers support the generation of ultrashort strain pulses in SrTiO₃ (STO) with high amplitudes up to 0.5%. The strain amplitudes are calibrated by real time measurements of the lattice deformation using ultrafast x-ray diffraction (UXRD). We determine the speed at which the strain fronts propagate by broadband picosecond ultrasonics and conclude that above a strain level of approx. 0.2% the compressive and tensile strain components travel at considerably different sound velocities, indicating nonlinear wave behavior. Simulations based on an anharmonic linear-chain model are in excellent accord with the experimental findings and show how the spectrum of coherent phonon modes changes with time.

Acoustic wave propagation and the deformation of solids are usually analyzed within the approximation of harmonic interatomic potentials leading to the concept of decoupled acoustic phonons including their dispersion relation which is nearly linear for small wavevectors k_p . An anharmonicity must be introduced into the interaction potential in order to describe deformation under very high stress. But also small phonon amplitude phenomena are connected to phonon-phonon interaction processes, such as heat expansion and heat conduction.¹ For the material investigated in this letter, SrTiO₃ (STO), all these properties have been studied in detail, since STO is the generic dielectric (quantum paraelectric) perovskite oxide with a variety of interesting properties near its structural phase transition at 105 K. The elastic constants were determined by ultrasound measurements², the damping of acoustic phonons was investigated by the linewidth of Brillouin scattering³ and apparent deviations of the acoustic dispersion were discussed in the context of picosecond ultrasonics measurements.⁴ Recently ultrafast x-ray diffraction (UXRD) was used to accurately measure the propagation and decay of quasi-monochromatic strain pulses in STO.⁵

In theory, the changes in the occupation of phonon modes are described as phonon damping due to scattering from defects or anharmonic interaction with thermally activated phonons.⁶⁻⁹ For high strain amplitudes also interactions among coherent phonons are possible, which leads to a shape change of coherent phonon pulses. In particular the self-steepening of strain pulses giving rise to N-waves, shock waves and the soliton pulse trains in sapphire were measured after a long propagation length of more than one-hundred microns¹⁰⁻¹³. These solitons were observed at low temperatures where phonon damping is weak and were discussed by nonlinear wave equations.¹³⁻¹⁵

In this letter we investigate the nonlinear propagation of giant longitudinal acoustic (LA) bipolar strain waves in SrTiO₃. We calibrate the strain amplitude by UXRD and show how the mode spectrum constituting the wave changes as a function of time. Simulations based on an anharmonic linear-chain model yield excellent agreement with ultrashort broadband optical reflectivity measurements and show that compressive strain

components propagate faster than tensile strain components. The dependence of the sound velocity on the strain gives rise to a self-steepening of the strain front.

We use an epitaxially grown La_{0.7}Sr_{0.3}MnO₃ (LSMO) transducer film on a SrTiO₃(100) substrate, fabricated by pulsed-laser deposition. The red curve in Fig. 1a shows a θ - 2θ scan of the sample recorded at the EDR beamline of the synchrotron BESSYII of the Helmholtz-Zentrum-Berlin. The bright substrate peak at 23.25° is cut off to show the less intense layer peak (LSMO) at 23.58° more clearly. The excellent agreement to the simulation confirms the crystalline perfection of the epitaxial film with a thickness of $d_{LSMO} = 36$ nm, which is very robust against high excitation densities and supports high strain amplitudes. To calibrate the amplitude of the strain wave we measure the expansion of the metallic layer via the shift of the x-ray diffraction signal (Fig. 1 b+c) after optical excitation by 50 fs laser pulses around 800 nm wavelength with a fluence of 20 mJ/cm². To probe the structural dynamics we use an x-ray plasma source which provides jitter free x-ray pulses with a duration of approx. 200 fs.¹⁶ The transient angular shift $\Delta\theta$ of the LSMO Bragg peak can be read from Fig. 1b for time delays up to 15 ps. The shift is connected to the layer strain ε by Bragg's law. Fig. 1c shows the diffraction curve for a time delay of 12 ps yielding an induced LSMO strain of $\varepsilon = 0.2\%$.

The observed time dependence of the LSMO Bragg peak can be understood as follows:^{17,18} The absorbed pump pulse induces a quasi-instantaneous thermal stress which is unbalanced at the layer boundaries. This leads to two strain fronts which propagate away from the air-LSMO and LSMO-STO interfaces eventually building up a bipolar strain pulse in the STO substrate.¹⁹ The maximum expansion occurs at $T = d_{LSMO}/v_{LSMO} = 6$ ps after the excitation, when the expansion waves starting from the surface and the interface have traveled through the film at the velocity of sound in LSMO, v_{LSMO} .²⁰ After 12 ps the coherent strain wave has completely left the LSMO layer and entered the STO substrate. Reflections of the sound wave at the interface with good acoustic impedance-matching can be neglected.^{17,20-22}

In previous experiments we have confirmed that the layer

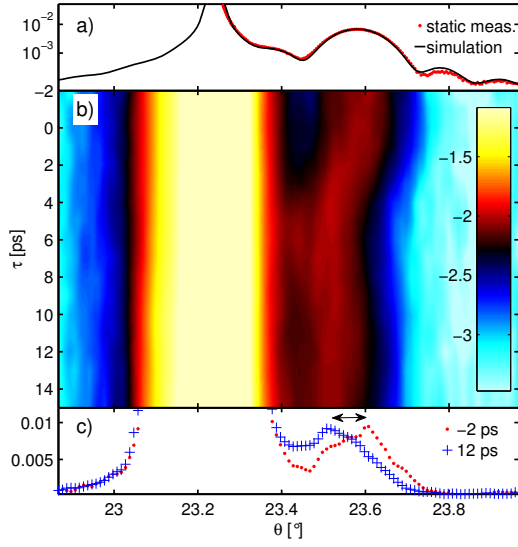


FIG. 1. (color online) **a)** Static θ - 2θ scan of the [002] peaks of the LSMO-STO sample showing a weak and broad layer (LSMO) peak and a much narrower and larger STO substrate peak. **b)** Transient of the UXRD signal after pumping with a laser pulse. The layer peak shifts to smaller angles indicating the expansion of LSMO within 6 ps. **c)** Two cuts of panel **b)** with pump-probe delays -2 ps (before pumping) and 12 ps (when the strain pulse has left the layer).

strain depends linearly on the excitation fluence²³ and that the corresponding bipolar strain wave is propagating into the STO substrate.¹⁷ Hence we conclude a calibration factor of 0.01% LSMO strain per 1 mJ/cm² fluence. The strain amplitude of the bipolar pulse in the STO is half of LSMO strain after 12 ps weighted with the ratio of the layer and substrate sound velocities which considers the bipolar pulse stretching in the STO.^{17,20-22}

Having calibrated the amplitude of the lattice response, we follow the propagation of the bipolar strain pulse by optical pump probe measurements. The setup is very similar to the broadband picosecond ultrasonics setup reported by Pontecorvo *et al.*²⁴. We split the 800 nm laser light into two parts. The intense part is used to pump the sample with fluences ranging from 14 to 47 mJ/cm² and the smaller part is focused into a sapphire plate to generate a white light supercontinuum pulse. This spectrally broad light pulse ranging from 470 to 700 nm is reflected from the sample under an angle of 45° with respect the surface normal. We measured the relative transient reflectivity change $\Delta R/R_0$ of the sample for four different fluences at pump-probe delays up to 1 ns with a resolution of 1 ps. Fig. 2 shows the response of the sample after correction for the chirp of the white light probe pulse and after subtraction of the slowly varying background which is associated with the transient heat in the LSMO film. Fig. 2a shows the relative change of reflectivity for the lowest (14 mJ/cm²)

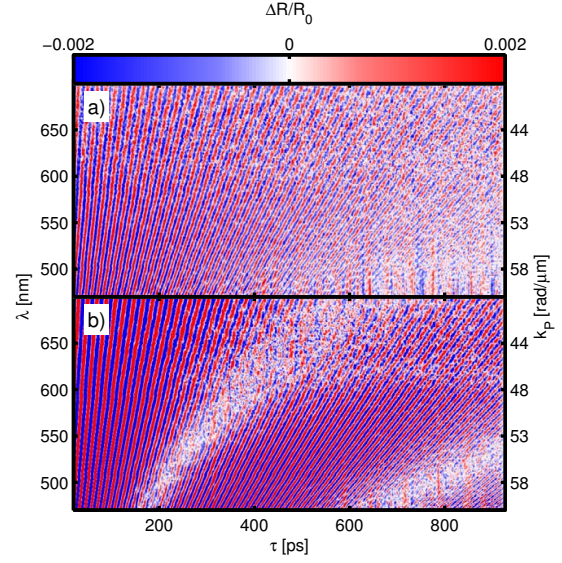


FIG. 2. (color online) Relative optical reflectivity change of the LSMO-STO sample for a pump fluence of **a)** 14 mJ/cm² and **b)** 47 mJ/cm². The low frequency background was subtracted by high pass filtering. The probe pulse wavelength is given by λ (left axis). Both measurements show Brillouin oscillations which are attributed to the photon backscattering on a phonon with k -vector k_p (right axis). For strong excitation conditions **b)** we observe a beating in these oscillations.

and 2b for the highest (47 mJ/cm²) fluence.

All measurements show pronounced oscillations which exhibit a period increasing with the probe wavelength. In addition to these so called "Brillouin oscillations" we observe at high fluences a beating on these oscillations with decreasing period for increasing fluence. The oscillations can be understood as an interference of the light wave reflected by the sample surface with the light wave reflected due to the refractive index change induced by the propagating strain wave.¹⁹ Alternatively, if one describes the propagating wave front as a superposition of longitudinal acoustic phonons with wavevector k_p , the "reflection" of the probe light from the strain pulse can be understood as Brillouin backscattering of optical light with wavevector k_L .

Due to momentum conservation this process is subject to the Brillouin backscattering condition

$$k_p = 2k_L = \frac{4\pi}{\lambda} n(\lambda) \cos(\beta), \quad (1)$$

where $n(\lambda)$, λ and β are the refractive index of STO, the wavelength of the probing laser light and the internal propagation angle with respect to the surface normal, respectively. The angle β is known by Snell's law and the refractive index of STO is taken from the literature.²⁵

The linear dispersion relation of acoustic phonons near the Brillouin zone center $\omega(\lambda)/k_p = v_s$, thus relates the observed

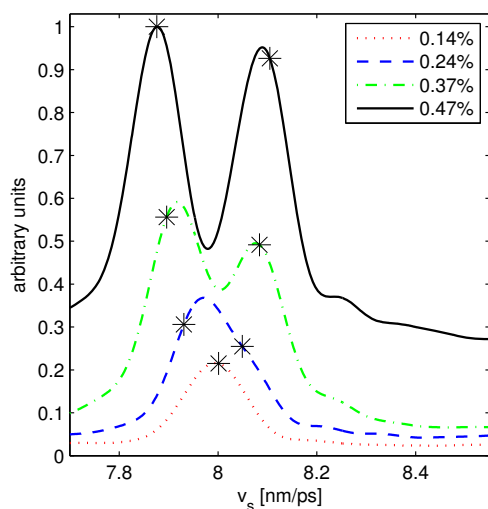


FIG. 3. (color online) Measured sound velocity distribution of the induced strain pulse in STO. The different pump fluences were calibrated with the UXRd measurements to the resulting induced strains of the LSMO layer which is directly linked to the strain amplitude of the bipolar strain pulse in the STO. The narrow distribution for 0.14% strain implies that the entire strain pulse essentially propagates with a speed around 8 nm/ps. With increasing strain amplitude the sound velocity distribution gets broader and eventually a double peaked distribution is established. At high excitation levels different parts of the strain pulse propagate with different velocities. The stars indicate the sound velocities of the self-steepened sound pulses simulated in Fig. 4(a).

oscillation frequency $\omega(\lambda)$ to the speed of sound for the LA phonons in STO, v_s :

$$v_s = \frac{\omega(\lambda)\lambda}{4\pi n(\lambda) \cos(\beta)}. \quad (2)$$

In order to derive the sound velocity from our measured data (Fig. 2a+b) we calculate the Fast Fourier Transform $I(\omega, \lambda)$ along the time-axis for each probe wavelength λ . This yields a relation between λ and the related oscillation frequencies $\omega(\lambda)$, which implies a dependence of the sound velocity v_s on the phonon wavevector k_p according to the Brillouin backscattering condition. We use Eqn. 2 as a coordinate transformation $v_s(\omega(\lambda), \lambda)$ which transforms our Fourier transformed data into a wavelength dependent sound velocity distribution $I(v_s, \lambda)$. By integration of the calculated result over all wavelengths we obtain Fig. 3 which shows the measured sound velocity distributions for different photoinduced LSMO strains calibrated by the results of the UXRd measurement. At low strain (0.14%) we observe a single peak around 8 nm/ps which is in a good agreement with the known sound velocity of the LA phonons in STO.²¹ This peak validates the linear dispersion at low fluence. A nonlinear dispersion (k_p dependent sound velocity) would lead to a broadened distribution.

However, with increasing strain amplitude we find a splitting in the sound velocity distribution. This implies that for large strains the speed of sound depends on the strain amplitude. The strain amplitude itself modulates the sound velocity of the medium.

To verify these assignments and to understand the underlying excited phonon spectrum, we simulate the lattice dynamics in a linear-chain model which was successfully tested against UXRd data in several cases.^{17,26} In addition to the model proposed in Ref. 17, we introduce an anharmonic potential between adjacent oscillators in order to describe the nonlinear wave propagation. Moreover, we add an empirical phonon damping term proportional to the velocity difference of adjacent oscillators. Mathematically the system is described by N coupled oscillators where each oscillator describes one lattice plane (half unit cell) of the LSMO thin film or the STO substrate. The set of N coupled second order ordinary differential equations is:

$$m_i \ddot{x}_i = k_i(\Delta_i - \Delta_{i-1}) + a_i(\Delta_i^2 - \Delta_{i-1}^2) + m_i \gamma_i (\dot{\Delta}_i - \dot{\Delta}_{i-1}) + F_i(t) \quad (3)$$

where $\Delta_i = x_{i+1} - x_i$ and $i = 2..N - 1$. The potential is nearly harmonic with a small cubic term. This leads to a linear and parabolic force term in the coupling force of Eqn. 3, where m_i is the mass of the oscillator, k_i is the spring constant, a_i is the anharmonicity parameter and γ_i is a material specific damping constant.^{27,28}

The elastic properties of LSMO and STO were taken from literature^{20,21}. For the anharmonicity of STO we make a first approximation from the hydrostatic pressure dependence of the elastic constants.² The anharmonicity in the LSMO transducer film has only little influence on the dynamics because of the short propagation length. In the end it is used as a fitting parameter which turns out to be twice as large as the STO anharmonicity. For the damping parameter γ_i we use a value which yields good agreement for phonon damping in STO observed by UXRd.⁵

$F_i(t)$ describes the driving force of the oscillators due to the optical excitation process. We assume an instantaneous force step $F_i(t)$ at time zero according to the strong electron-phonon coupling in the metallic oxides.²⁹ The spatial excitation profile $F_i(t)$ follows an exponential decay determined by the penetration depth of the optical pump light. Accordingly, deeper lying unit cells exhibit less expansion.¹⁷

Figure 4a shows the simulated strain profile for different times after excitation of the sample with the smallest (black line) and largest (blue line) strain amplitude in the co-propagating frame of reference. The center of the bipolar pulse which has a strain level close to zero propagates with the normal speed of sound, which is only valid in harmonic approximation. In the regions with high amplitude the strain modulates the elastic constants. This nonlinear interaction between the masses changes the shape of the bipolar pulse, in particular leading to a self-steepening pulse front and tail. The tensile part is slower and the compressive part is faster than the sound velocity v_s of the harmonic linear chain. The speed

of the pulse front propagation is read from the simulation and indicated in Fig. 3 as stars. The good agreement verifies the interpretation of the measured splitting of the sound velocity distribution.

For further comparison to the measurement and to interpret the impact of the anharmonic interaction on the classical decoupled oscillators called phonons, we analyze the simulated strain profiles in Fig. 4a by calculating the Fourier amplitudes $A(k_p, t)$ of sinusoidal waves composing the wavepacket for each time delay t . This is essentially an amplitude of phonons (decoupled modes) which describe the wavepacket. For better comparison to the experimental observable we plot A/λ in Fig. 4c, because for a transparent medium the reflectivity modulations scale inversely with λ according to equations (35 - 38) in the seminal paper of Thomsen et al.¹⁹. The distribution of coherently excited phonons rapidly shifts to smaller k_p vectors.

Figure 4b shows the amplitude of the measured Brillouin oscillations (Fig. 2b), which are proportional to the phonon amplitude of the phonon with k -vector k_p .¹⁹ During the time sequence 240, 320 and 410 ps the first minimum of the phonon amplitude is moving through the experimental window of observation given by the Brillouin condition (Eqn. 2). These minima represent the fact, that at a certain point in time these phonons are not occupied. This is the fundamental interpretation of the beating of the measured oscillations. The simulation reproduces also the second measured amplitude minimum (Fig. 2b), which moves into the observed wavelength range about 800 ps after excitation (not shown).

We now discuss the physics behind the anharmonic linear chain model leading to the excellent agreement of theory and experiment. Deformations are only reversible if they are infinitely slow and if the thermodynamic system is in equilibrium at any time. This is not the case for phonons which have a finite oscillation period. The phonon has to damp out because of the intrinsic irreversibility of the oscillation. In other words, the coherent phonon amplitude goes down by dissipating energy to the heat bath⁵⁻⁹. In our model we consider this fact by the hydrodynamic damping term γ in the second line of Eqn. 3.

The force term to second order in strain is given by the in principle anharmonic interactions of atoms which contributes only at high strain conditions. The set of differential equations (Eqn. 3) can be approximated by a Korteweg-de Vries-Burgers Equation (KdVB) if the phonon wavelength is much bigger than the lattice constant.³⁰ This is advantageous to find asymptotic solutions such as solitons. Our approach is useful for the calculation of solutions with certain excitation conditions and for considering acoustic mismatches of different materials. We can account for dispersion higher than third order and compute solutions with phonon wavelengths close to the lattice constant.

In conclusion we determined the transient phonon spectra of nonlinearly propagating strain pulses in strontium titanate by transient reflectivity measurements for different fluences,

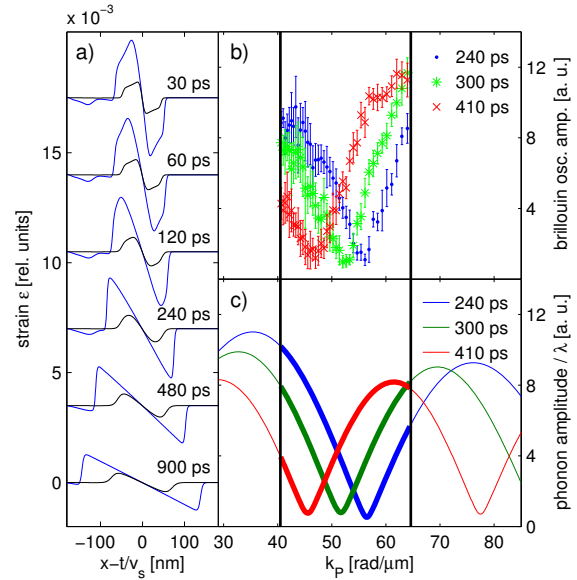


FIG. 4. (color online) **a)** Spatial profile of the bipolar strain pulse in the STO for different propagation times in a frame of reference propagating with the speed of sound v_s for a high amplitude (blue line, 0.47) and low amplitude (black line, 0.14). For large amplitude the tensile part of the pulse propagates with subsonic and the compressive part with supersonic speed indicated by the stars in Fig. 3. **b)** Measured amplitude of oscillations for each wavelength connected to the k -vectors by the Brillouin backscattering condition. The region between the vertical black lines indicates the k -vectors that can be accessed by the optical white light. **c)** Phonon amplitude divided by the wavelength λ (see text) as a function of k -vector calculated from Fourier-Transforms of the simulated strain profile, showing good agreement with the measurement in panel (b)

which are experimentally calibrated by time-resolved x-ray diffraction. An anharmonic linear-chain model with phonon damping reproduces the measured spectra in a quantitative way and verifies the interpretation of the transient reflectivity measurements. The anharmonicity thus changes the phonon occupation in time and leads to compressive and tensile strain fronts traveling at 1% higher and slower speed, respectively.

We thank the DFG for supporting the project via BA 2281/3-1 and SFB 762.

* bargheer@uni-potsdam.de

- [1] N. D. Ashcroft, Neil W. ; Mermin. *Solid state physics*, (Saunders College, Fort Worth 1976), 1st edn..
- [2] A. G. Beattie and G. A. Samara. Pressure Dependence of the Elastic Constants of SrTiO[sub 3]. *Journal of Applied Physics* 42, 2376 (1971).
- [3] A. Koreeda, T. Nagano, S. Ohno and S. Saikan. Quasielastic light scattering in rutile, ZnSe, silicon, and SrTiO3. *Phys. Rev. B* 73, 024303 (2006).

- [4] S. Brivio, D. Polli, A. Crespi, R. Osellame, G. Cerullo and R. Bertacco. Observation of anomalous acoustic phonon dispersion in SrTiO₃ by broadband stimulated Brillouin scattering. *Appl. Phys. Lett.* 98, 211907 (2011).
- [5] M. Herzog, A. Bojahr, J. Goldshteyn, W. Leitenberger, I. Vrejoiu, D. Khakulin, M. Wulff, R. Shayduk, P. Gaal and M. Bargheer. Detecting optically synthesized quasi-monochromatic sub-terahertz phonon wavepackets by ultrafast x-ray diffraction. *Appl. Phys. Lett.* 100, 094101 (2012).
- [6] A. Akhiezer. On the absorption of sound in solids. *J. Phys. (USSR)* 1, 277 (1939).
- [7] H. J. Maris. The absorption of sound waves in perfect dielectric crystals. *Phil. Mag.* (1965).
- [8] W. Chen, H. J. Maris, Z. R. Wasilewski and S.-i. Tamura. Attenuation and velocity of 56 GHz longitudinal phonons in gallium arsenide from 50 to 300 K. *Phil. Mag. Part B* 70, 687 (1994).
- [9] B. C. Daly, K. Kang, Y. Wang and D. G. Cahill. Picosecond ultrasonic measurements of attenuation of longitudinal acoustic phonons in silicon. *Phys. Rev. B* 80, 174112 (2009).
- [10] P. J. S. van Capel and J. I. Dijkhuis. Optical generation and detection of shock waves in sapphire at room temperature. *APPLIED PHYSICS LETTERS* 88, 151910 (2006).
- [11] P. J. S. van Capel, H. P. Porte, G. van der Star and J. I. Dijkhuis. Interferometric detection of acoustic shock waves. *Journal of Physics: Conference Series* 92, 012092 (2007).
- [12] O. L. Muskens and J. I. Dijkhuis. High Amplitude, Ultrashort, Longitudinal Strain Solitons in Sapphire. *Phys. Rev. Lett.* 89, 285504 (2002).
- [13] P. J. S. van Capel and J. I. Dijkhuis. Time-resolved interferometric detection of ultrashort strain solitons in sapphire. *Phys. Rev. B* 81, 144106 (2010).
- [14] H. Y. Hao and H. J. Maris. Experiments with acoustic solitons in crystalline solids. *Phys. Rev. B* 64, 064302 (2001).
- [15] H. J. Maris and S. Tamura. Propagation of acoustic phonon solitons in nonmetallic crystals. *Phys. Rev. B* 84, 024301 (2011).
- [16] D. Schick, A. Bojahr, M. Herzog, C. von Korff Schmising, R. Shayduk, W. Leitenberger, P. Gaal and M. Bargheer. Normalization Schemes for Ultrafast X-Ray Diffraction Using a Table-Top Laser-Driven Plasma Source. *submitted* (2011).
- [17] M. Herzog, D. Schick, P. Gaal, R. Shayduk, C. von Korff Schmising and M. Bargheer. Analysis of ultrafast X-ray diffraction data in a linear-chain model of the lattice dynamics. *Appl. Phys. A* 106, 489 (2012).
- [18] K. Sokolowski-Tinten, C. Blome, C. Dietrich, A. Tarasevitch, M. Horn von Hoegen, D. von der Linde, A. Cavalleri, J. Squier and M. Kammler. Femtosecond X-Ray Measurement of Ultrafast Melting and Large Acoustic Transients. *Phys. Rev. Lett.* 87, 225701 (2001).
- [19] C. Thomsen, H. T. Grahn, H. J. Maris and J. Tauc. Surface generation and detection of phonons by picosecond light pulses. *Phys. Rev. B* 34, 4129 (1986).
- [20] Y. H. Ren, M. Trigo, R. Merlin, V. Adyam and Q. Li. Generation and detection of coherent longitudinal acoustic phonons in the La_{0.67}Sr_{0.33}MnO₃ thin films by femtosecond light pulses. *Appl. Phys. Lett.* 90, 251918 (2007).
- [21] R. O. Bell and G. Rupprecht. Elastic Constants of Strontium Titanate. *Phys. Rev.* 129, 90 (1963).
- [22] P. Gaal, D. Schick, A. Bojahr, M. Herzog and M. Bargheer. Ultrafast Switching of hard X-rays. *not published yet* (2012).
- [23] M. Woerner, C. von Korff Schmising, M. Bargheer, N. Zhavoronkov, I. Vrejoiu, D. Hesse, M. Alexe and T. Elsaesser. Ultrafast structural dynamics of perovskite superlattices. *Applied Physics A: Materials Science & Processing* 96, 83 (2009).
- [24] E. Pontecorvo, M. Ortolani, D. Polli, M. Ferretti, G. Ruocco, G. Cerullo and T. Scopigno. Visualizing coherent phonon propagation in the 100 GHz range: A broadband picosecond acoustics approach. *APPLAB* 98, 011901 (2011).
- [25] M. Cardona. Optical Properties and Band Structure of SrTiO₃ and BaTiO₃. *Phys. Rev.* 140, A651 (1965).
- [26] M. Herzog, D. Schick, W. Leitenberger, R. Shayduk, R. M. van der Veen, C. J. Milne, S. L. Johnson, I. Vrejoiu and M. Bargheer. Tailoring interference and nonlinear manipulation of femtosecond x-rays. *New J. Phys.* 14, 013004 (2012).
- [27] E. M. Landau, Lew D. ; Lific. *Lehrbuch der theoretischen Physik*, vol. 7: Elastizittstheorie, (Akad.-Verl., Berlin1991), 7., unvernd. aufl. edn.. Aus dem Russ. bers.
- [28] E. Arévalo, Y. Gaididei and F. G. Mertens. Soliton dynamics in damped and forced Boussinesq equations. *The European Physical Journal B - Condensed Matter and Complex Systems* 27, 63. 10.1140/epjb/e20020130 (2002).
- [29] A. Bojahr, D. Schick, L. Maerten, M. Herzog, I. Vrejoiu, C. von Korff Schmising, C. J. Milne, S. L. Johnson and M. Bargheer. Comparing the oscillation phase in optical pump-probe spectra to ultrafast x-ray diffraction in the metal-dielectric SrRuO₃/SrTiO₃ superlattice. *Phys. Rev. B* 85, 224302 (2012).
- [30] E. Arévalo, F. G. Mertens, Y. Gaididei and A. R. Bishop. Thermal diffusion of supersonic solitons in an anharmonic chain of atoms. *Phys. Rev. E* 67, 016610 (2003).

PAPER VIII

Detecting optically synthesized quasi-monochromatic sub-terahertz phonon wavepackets by ultrafast x-ray diffraction

M. Herzog, A. Bojahr, J. Goldshteyn, W. Leitenberger,
I. Vrejoiu, D. Khakhulin, M. Wulff, R. Shayduk, P. Gaal
and M. Bargheer.

Appl. Phys. Lett. **100**, 094101 (2012).

Detecting optically synthesized quasi-monochromatic sub-terahertz phonon wavepackets by ultrafast x-ray diffraction

M. Herzog,¹ A. Bojahr,¹ J. Goldshteyn,² W. Leitenberger,¹ I. Vrejoiu,³ D. Khakhulin,⁴ M. Wulff,⁴ R. Shayduk,² P. Gaal,¹ and M. Bargheer^{1,2,a)}

¹Institut für Physik und Astronomie, Universität Potsdam, Karl-Liebknecht-Str. 24-25, 14476 Potsdam, Germany

²Helmholtz-Zentrum Berlin für Materialien und Energie GmbH, Wilhelm-Conrad-Röntgen Campus, BESSY II, Albert-Einstein-Str. 15, 12489 Berlin, Germany

³Max-Planck-Institut für Mikrostrukturphysik, Weinberg 2, 06120 Halle, Germany

⁴European Synchrotron Radiation Facility (ESRF), 6 rue Jules Horowitz, 38000 Grenoble, France

(Received 10 January 2012; accepted 7 February 2012; published online 27 February 2012)

We excite an epitaxial SrRuO₃ thin film transducer by a pulse train of ultrashort laser pulses, launching coherent sound waves into the underlying SrTiO₃ substrate. Synchrotron-based x-ray diffraction (XRD) data exhibiting separated sidebands to the substrate peak evidence the excitation of a quasi-monochromatic phonon wavepacket with sub-THz central frequency. The frequency and bandwidth of this sound pulse can be controlled by the optical pulse train. We compare the experimental data to combined lattice dynamics and dynamical XRD simulations to verify the coherent phonon dynamics. In addition, we observe a lifetime of 130 ps of such sub-THz phonons in accordance with the theory. © 2012 American Institute of Physics. [<http://dx.doi.org/10.1063/1.3688492>]

Ultrafast x-ray diffraction (UXRD) is a powerful tool for monitoring atomic motion in solids on the related length and timescales. In principle, each displacement field within a crystal can be decomposed into discrete phonon modes of respective frequency ω and wavevector Q which are related by the phonon dispersion relation $\omega = \omega(Q)$. One key aspect of UXRD is the direct correspondence of a phonon-induced real-space periodicity $\lambda = 2\pi/Q$ within a host crystal of lattice spacing c and the finite diffraction intensity at wavevector transfer $q = |\mathbf{k}_{\text{in}} - \mathbf{k}_{\text{out}}| = G \pm Q$, where \mathbf{k}_{in} and \mathbf{k}_{out} are the incident and diffracted x-ray photon wavevectors, respectively, and $G = 2\pi/c$ is the reciprocal lattice vector of the host crystal.^{1,2} This relation is depicted in Fig. 1(a) for $G + Q$. Each phonon mode Q is, thus, responsible for x-rays diffracted into sharp sidebands of the main crystal Bragg reflection at $G \pm Q$ which oscillate at their respective eigenfrequency $\omega(Q)$. These features have been theoretically discussed by Larsson *et al.*²

Early UXRD experiments verified these relations by observing UXRD signals of longitudinal acoustic (LA) phonons in bulk crystals.¹⁻³ In these experiments, the intense and ultrashort laser pulses excite bipolar strain waves into the bulk crystal⁴ which have a broad phonon spectrum that accordingly generates contributions in a broad vicinity of the bulk Bragg reflection. The linear dispersion relation of LA phonons, $\omega = v_{\text{LA}}Q$, was verified by tuning q , where v_{LA} is the LA sound velocity.

For various physical and technical issues (such as phonon spectroscopy, phonon-phonon scattering, etc.), it is favorable to selectively generate high-frequency monochromatic phonon beams instead of spectrally broad pulses as in the first UXRD experiments. Several techniques have been developed, e.g., via thermomodulation⁵ or piezoelectric trans-

ducers.⁶ Roshchupkin and co-workers observed XRD sidebands due to continuous surface acoustic waves in langatate crystals.⁷ Acoustoelectrically amplified phonons below 10 GHz forming a continuous monochromatic bulk sound wave have also been detected by XRD.⁶ Solely optical techniques provide tunability of the phonon frequencies into the THz region. Optical multi-pulse excitation has been used to coherently control LA phonons in bulk InSb.⁸ Recently, high-frequency narrow-bandwidth tunable LA phonon pulses were coherently excited by optical pulse trains and subsequently verified by optical means.^{9,10} Alternatively, the single-pulse photoexcitation of semiconductor superlattices generates folded LA phonons.^{11,12} Due to coupling to the substrate, these folded phonons unfold into the substrate which results in similar phonon pulses as discussed here.¹³ Such unfolding could be monitored by UXRD; however, the corresponding weak signatures in the diffraction curves were mainly dominated by the strong superlattice Bragg peaks.¹⁴ Moreover,

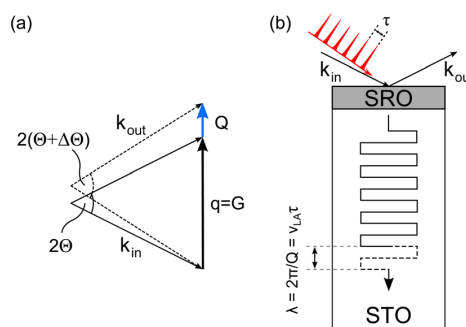


FIG. 1. (Color online) (a) Schematic representation of coherent XRD from a reciprocal lattice vector G (solid lines) and from an additional phonon of wavevector Q (dashed lines). The same process is possible for G and Q being antiparallel. (b) Schematic of the experiment. Each laser pulse launches a bipolar strain wave into the substrate (dashed line) resulting in a phonon wavepacket with central wavevector Q (dashed and solid line).

^{a)}Electronic mail: bargheer@uni-potsdam.de.

these unfolded phonon wavepackets have a fixed central frequency defined by the spatial superlattice period.^{13,14}

In this letter, we synthesized a quasi-monochromatic phonon pulse by excitation of a SrRuO₃ (SRO) thin film transducer epitaxially grown by pulsed laser deposition³² on a SrTiO₃ substrate¹⁵ with a train of ultrashort optical laser pulses (schematically shown in Fig. 1(b)). Relevant material properties of SRO and STO can be found in, e.g., Refs. 27, 28, 33, and 34. Each laser pulse impulsively launches a single spectrally broad bipolar strain pulse with high amplitude into the substrate (schematically depicted by the dashed line in Fig. 1(b)).¹⁶ The optical pulse train with pulse frequency $\nu = \tau^{-1}$ and N pulses thus synthesizes a coherent phonon wavepacket¹⁰ with wavevector $Q_p = 2\pi\nu/v_{LA}$, where v_{LA} is the LA sound velocity of the STO substrate. Using UXRD, we observe clear sidebands to the STO Bragg peak as the x-ray photons scatter from the monochromatic phonons according to $q = G + Q_p$. The selective excitation of coherent phonons with a specific Q_p allows us to directly monitor the 130 ps lifetime of these sub-THz phonons which undergo strong damping attributed to thermoelastic damping and Akhiezer's mechanism of relaxation damping.^{17–19} The central wavevector of the observed wavepacket can be controlled by the pulse repetition rate ν and the bandwidth is inversely proportional to N . By tuning ν , one can thus map out the LA phonon dispersion relation $\omega(Q)$.

The time-resolved XRD experiments were performed at the undulator beamline ID09B at the synchrotron source ESRF.²⁰ The general experimental setup working at 1 kHz repetition rate was described in Ref. 21. The storage ring was running in 16-bunch mode generating ≈ 100 ps x-ray pulses. We chose a photon energy of 12 keV for the experiments and utilized only one sample (cf. Ref. 21). The optical pulse train was produced by a mirror composed of four alternately stacked glass plates and spacer rings giving eight reflections from the air-glass interfaces. The plates and rings had a thickness of 710 μm and 1100 μm , respectively, corresponding to pulse spacing of $\tau \approx 7.2$ ps ($\nu \approx 140$ GHz) at normal incidence, which was verified by optical cross-correlation measurements. Due to the rather low reflectivity of the air-glass interfaces, the energy distribution within the pulse train was almost homogeneous. The integrated fluence at the sample was set to ≈ 44 mJ/cm², i.e., each pulse contributed a mean fluence of ≈ 5.5 mJ/cm².

The inset of Fig. 2(a) shows the static rocking curve around the (002) STO substrate Bragg peak from which we deduced a SRO layer thickness of ≈ 15.4 nm. The high-angle side of the STO substrate Bragg peak has very little contribution from the SRO layer which allows to observe the sidebands of the phonon wavepackets without any congestion from the top layer(s). This situation is even improved by the shift of the SRO peak towards lower angles due to the photoinduced thermal expansion. The robust perovskite oxide SRO has a fast electron-phonon coupling and is, thus, perfectly suited as a thin film transducer which can be triggered by strong laser-pulse excitation in order to generate phonon spectra with a high frequency cutoff.^{22–25}

Figure 2(a) shows the measured rocking curves in the vicinity of the (002) STO substrate Bragg peak before (open black diamonds) and 130 ps after (solid red bullets) the ar-

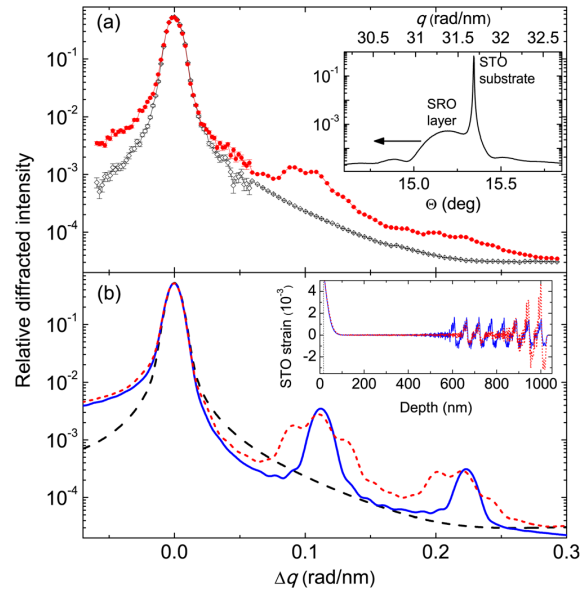


FIG. 2. (Color online) (a) Experimental rocking curves (measured piecewise) of the high-angle side of the STO substrate peak before (open black diamonds) and 130 ps after (solid red bullets) excitation by a pulse train with 7.2 ps pulse separation. Inset: static rocking curve measured with a high-resolution x-ray photodiode. The arrow indicates the shift of the SRO peak due to the photoinduced thermal expansion. (b) Simulations of the measured rocking curves without excitation (long-dashed black) and with excitation by a pulse train having a uniform (solid blue) and non-uniform (short-dashed red) pulse energy distribution. Inset: calculated strain pattern 130 ps after excitation with uniform (solid blue) and non-uniform (dashed red) pulse energy distribution.

rival of the first pump pulse of the pulse train. The rocking curve at positive time delay shows a distinct sideband evidencing the excitation of a coherent narrow-bandwidth phonon wavepacket with a central wavevector around $\Delta q = Q_p^{(1)} = 0.11$ nm⁻¹. Moreover, the excitation of the second harmonic around $\Delta q = Q_p^{(2)} = 0.22$ nm⁻¹ with much weaker amplitude can be inferred from Fig. 2. Although we observe clearly separated harmonics, the sidebands are rather broad and exhibit additional modulations. The comparatively large penetration depth of the 800 nm pump light in SRO ($\xi_{SRO} \approx 52$ nm) results in nearly homogeneous excitation of the thin film transducer.^{13,26} The individual bipolar strain pulses thus roughly have a rectangular and steplike shape and consequently higher harmonics of Q_p are generated. Since we have an independent measure of ν , the linear LA phonon dispersion relation readily yields $v_{LA} \approx 7.9$ nm/ps which perfectly agrees with the literature values.^{27,28}

In order to understand the experimental data in more detail, we utilized numerical model calculations to simulate the experiment. First, we use a linear-chain model of masses and springs to calculate the coherent lattice dynamics.¹³ The multiple pump pulse excitation necessitates the inclusion of heat diffusion into the simulation. The resulting spatio-temporal strain maps then serve as an input for dynamical XRD simulations to calculate the transient rocking curves.^{26,29} The simulated transient rocking curves are plotted in Fig. 2(b). We first assume a pulse train of 8 identical pulses with 7.2 ps pulse separation. The calculated strain field at 130 ps is shown in the inset of Fig. 2(b). The corresponding rocking

curve (solid blue) exhibits sharp Bragg peaks at the experimentally observed wavevector $\Delta q = 0.11 \text{ nm}^{-1}$ and its higher harmonics.

The experimental peak width is much broader than for the idealized simulation. This may originate from varying pulse energies at the probe area. For instance, a different pointing of the individual optical pump beams due to non-parallel glass plates of the mirror stack would generate different excitation densities at the fairly distant probe spot for each pulse. To account for such effects, we further assumed a non-uniform pump pulse energy distribution within the pulse train which results in the dashed red curve in Fig. 2. This rocking curve satisfactorily approximates the shape of the experimental data. The individual pulse energies are proportional to the corresponding amplitudes of the bipolar strain pulses plotted in the inset of Fig. 2(b). Thus, a controlled variation of the pulse energy distribution in principle allows to generate arbitrary phonon spectra in addition to the tunability of the central wavevector by the pulse frequency ν .

Finally, we analyze the time-dependence of the first-order sideband of the phonon wavepacket. For this, we evaluate the integrated intensity of the main part between $\Delta q = 0.08 \text{ rad/nm}$ and $\Delta q = 0.14 \text{ rad/nm}$ for each measured time delay. The result is given by the symbols in Fig. 3. We fit this transient by an exponential function which is set to zero before $t = 0$ and convoluted by a Gaussian representing the limited time-resolution. The solid black line in Fig. 3 shows the best fit from which we extract a decay time $\tau_{\text{data}} = 130 \pm 8 \text{ ps}$. If we perform an analogous evaluation on the simulated data, we obtain the dashed red line. Here, the decay time is $\tau_{\text{sim}} \approx 600 \text{ ps}$ which is essentially determined by (1) the x-ray absorption as the strain pulse propagates deeper into the substrate (absorption length at 12 keV in STO is $\approx 54 \mu\text{m}$) and (2) normal dispersion of the phonon wavepacket. Since our lattice dynamics model does not include anharmonic phonon interactions, τ_{sim} marks an upper limit. The fact that $\tau_{\text{data}} \ll \tau_{\text{sim}}$ thus implies a rather efficient attenuation of the phonon wavepacket. Combining τ_{sim} and theoretical estimations including Akhiezer's mechanism of relaxation damping^{17,18} and thermoelastic damping¹⁹ yields a decay time of $\approx 200 \text{ ps}$ which is close to our measured phonon lifetime. We also obtain very similar values ($\approx 130 \text{ ps}$)

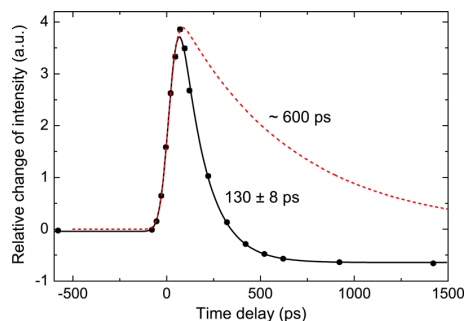


FIG. 3. (Color online) Time evolution of the integrated intensity of the 1st order sideband in Fig. 2(a) (black bullets) and the corresponding fit (solid black line). For comparison, we also show the corresponding transient obtained from the simulation which disregards anharmonic interactions in Fig. 2(b) (dashed red line).

by extrapolation of previously measured sub-GHz sound attenuation in STO (Refs. 30 and 31) according to $\tau_{\text{decay}} \sim \omega^{-2}$ given by Akhiezer's damping.^{17–19} More insight in the exact phonon attenuation dynamics could be gained by using shorter x-ray probe pulses since the observed phonon lifetime is close to the time-resolution of the experiment.

In conclusion, we presented UXRD data that evidence the efficient generation of quasi-monochromatic coherent LA phonon wavepackets at 140 GHz . We could explain and successfully simulate the corresponding sidebands of the STO substrate Bragg peak using a microscopic lattice dynamics model and dynamical XRD simulations. As the sidebands originate from a scattering of x-ray photons from selectively synthesized phonons with specific Q vector, the transient intensity of the sidebands directly measures the lifetime of these sub-THz LA phonons which is in accordance with theory and earlier acoustic experiments in the sub-GHz range. We believe that the combination of continuously tunable selective excitation of monochromatic phonon-pulses and UXRD will prove to be a versatile tool for investigation of sound attenuation and anharmonic phonon-phonon interactions in various materials with physically interesting coupling mechanisms at hypersonic frequencies.

We thank the BMBF for funding the project via Grant No. 05K10IP1 and the DFG via Grant No. BA2281/3-1.

- ¹D. A. Reis, M. F. DeCamp, P. H. Bucksbaum, R. Clarke, E. Dufresne, M. Hertlein, R. Merlin, R. Falcone, H. Kapteyn, M. M. Murnane *et al.*, *Phys. Rev. Lett.* **86**, 3072 (2001).
- ²J. Larsson, A. Allen, P. H. Bucksbaum, R. W. Falcone, A. Lindenberg, G. Naylor, T. Missalla, D. A. Reis, K. Scheidt, A. Sjögren *et al.*, *Appl. Phys. A* **75**, 467 (2002).
- ³C. Rose-Petrucci, R. Jimenez, T. Guo, A. Cavalieri, C. W. Siders, F. Rksi, J. A. Squier, B. C. Walker, K. R. Wilson, and C. P. J. Barty, *Nature* **398**, 310 (1999).
- ⁴C. Thomsen, H. T. Grahn, H. J. Maris, and J. Tauc, *Phys. Rev. B* **34**, 4129 (1986).
- ⁵E. P. N. Damen, A. F. M. Arts, and H. W. de Wijn, *Phys. Rev. Lett.* **74**, 4249 (1995).
- ⁶S. D. LeRoux, R. Colella, and R. Bray, *Phys. Rev. Lett.* **35**, 230 (1975).
- ⁷D. Roshchupkin, A. Erko, L. Ortega, and D. Irzhak, *Appl. Phys. A* **94**, 477 (2009).
- ⁸O. Synnergren, T. N. Hansen, S. Canton, H. Enquist, P. Sondhaus, A. Srivastava, and J. Larsson, *Appl. Phys. Lett.* **90**, 171929 (2007).
- ⁹J. D. Choi, T. Feurer, M. Yamaguchi, B. Paxton, and K. A. Nelson, *Appl. Phys. Lett.* **87**, 081907 (2005).
- ¹⁰C. Klieber, E. Peronne, K. Katayama, J. Choi, M. Yamaguchi, T. Pezeril, and K. A. Nelson, *Appl. Phys. Lett.* **98**, 211908 (2011).
- ¹¹M. Bargheer, N. Zhavoronkov, Y. Gritsai, J. C. Woo, D. S. Kim, M. Woerner, and T. Elsaesser, *Science* **306**, 1771 (2004).
- ¹²P. Sondhaus, J. Larsson, M. Harbst, G. A. Naylor, A. Plech, K. Scheidt, O. Synnergren, M. Wulff, and J. S. Wark, *Phys. Rev. Lett.* **94**, 125509 (2005).
- ¹³M. Herzog, D. Schick, P. Gaal, R. Shayduk, C. v. Korff Schmising, and M. Bargheer, *Appl. Phys. A* **106**, 489 (2012).
- ¹⁴M. Trigo, Y. M. Sheu, D. A. Arms, J. Chen, S. Ghimire, R. S. Goldman, E. Landahl, R. Merlin, E. Peterson, M. Reason *et al.*, *Phys. Rev. Lett.* **101**, 025505 (2008).
- ¹⁵The sample was grown by pulsed laser deposition (Ref. 32) and included a protective coating in the form of a 1–2 nm STO capping layer.
- ¹⁶The epitaxial growth of the thin film transducer is not mandatory for generating the plane wave strain pulses. The almost perfectly matched acoustic impedances of SRO and STO ensure that there are no acoustic post-pulses and the amplitude of the strain pulses in the substrate is maximized (mass densities $\rho_{\text{SRO}} = 6.26 \text{ g/cm}^3$ and $\rho_{\text{STO}} = 5.12 \text{ g/cm}^3$, LA sound velocities $v_{\text{LA}}^{\text{SRO}} = 6312 \text{ m/s}$ and $v_{\text{LA}}^{\text{STO}} = 7876 \text{ m/s}$ from Refs. 27, 33, and 34). The impedance matching is required for the tunability of the central wavevector of the phonon wavepacket.

- ¹⁷T. O. Woodruff and H. Ehrenreich, *Phys. Rev.* **123**, 1553 (1961).
- ¹⁸A. Koreeda, T. Nagano, S. Ohno, and S. Saikan, *Phys. Rev. B* **73**, 024303 (2006).
- ¹⁹J. Y. Duquesne and B. Perrin, *Phys. Rev. B* **68**, 134205 (2003).
- ²⁰M. Wulff, A. Plech, L. Eybert, R. Randler, F. Schotte, and P. Anfinrud, *Faraday Discuss.* **122**, 13 (2003).
- ²¹H. A. Navirian, M. Herzog, J. Goldshteyn, W. Leitenberger, I. Vrejoiu, D. Khakhulin, M. Wulff, R. Shayduk, P. Gaal, and M. Bargheer, *J. Appl. Phys.* **109**, 126104 (2011).
- ²²C. von Korff Schmising, M. Bargheer, M. Kiel, N. Zhavoronkov, M. Woerner, T. Elsaesser, I. Vrejoiu, D. Hesse, and M. Alexe, *Appl. Phys. B* **88**, 1 (2007).
- ²³C. von Korff Schmising, A. Harpoeth, N. Zhavoronkov, Z. Ansari, C. Aku-Leh, M. Woerner, T. Elsaesser, M. Bargheer, M. Schmidbauer, I. Vrejoiu *et al.*, *Phys. Rev. B* **78**, 060404 (2008).
- ²⁴M. Herzog, W. Leitenberger, R. Shayduk, R. van der Veen, C. J. Milne, S. L. Johnson, I. Vrejoiu, M. Alexe, and D. Hesse, *Appl. Phys. Lett.* **96**, 161906 (2010).
- ²⁵C. von Korff Schmising, M. Bargheer, M. Kiel, N. Zhavoronkov, M. Woerner, T. Elsaesser, I. Vrejoiu, D. Hesse, and M. Alexe, *Phys. Rev. Lett.* **98**, 257601 (2007).
- ²⁶M. Herzog, D. Schick, W. Leitenberger, R. Shayduk, R. M. van der Veen, C. J. Milne, S. L. Johnson, I. Vrejoiu, and M. Bargheer, *New J. Phys.* **14**, 013004 (2012).
- ²⁷R. O. Bell and G. Rupprecht, *Phys. Rev.* **129**, 90 (1963).
- ²⁸Y. H. Ren, M. Trigo, R. Merlin, V. Adyam, and Q. Li, *Appl. Phys. Lett.* **90**, 251918 (2007).
- ²⁹S. A. Stepanov, E. A. Kondrashkina, R. Köhler, D. V. Novikov, G. Materlik, and S. M. Durbin, *Phys. Rev. B* **57**, 4829 (1998).
- ³⁰R. Nava, R. Callarotti, H. Ceva, and A. Martinet, *Phys. Lett. A* **28**, 456 (1968).
- ³¹R. Nava, R. Callarotti, H. Ceva, and A. Martinet, *Phys. Rev.* **188**, 1456 (1969).
- ³²I. Vrejoiu, G. Le Rhun, L. Pintilie, D. Hesse, M. Alexe, and U. Gösele, *Adv. Mater.* **18**, 1657 (2006).
- ³³S. Yamanaka, T. Maekawa, H. Muta, T. Matsuda, S. Kobayashi, and K. Kurosaki, *J. Solid State Chem.* **177**, 3484 (2004).
- ³⁴G. J. Fischer, Z. Wang, and S.-i. Karato, *Phys. Chem. Miner.* **20**, 97 (1993).

PAPER IX

Shortening x-ray pulses for pump-probe experiments at synchrotrons

H. A. Navirian, M. Herzog, J. Goldshteyn,
W. Leitenberger, I. Vrejoiu, D. Khakhulin, M. Wulff,
R. Shayduk, P. Gaal and M. Bargheer.

J. Appl. Phys. **109**, 126104 (2011).

Shortening x-ray pulses for pump-probe experiments at synchrotrons

H. A. Navirian,¹ M. Herzog,^{1,a)} J. Goldshteyn,¹ W. Leitenberger,² I. Vrejoiu,³ D. Khakhulin,⁴ M. Wulff,⁴ R. Shayduk,¹ P. Gaal,² and M. Bargheer^{1,2}

¹Helmholtz-Zentrum Berlin für Materialien und Energie GmbH, Wilhelm-Conrad-Röntgen Campus, BESSY II, Albert-Einstein-Str. 15, 12489 Berlin, Germany

²Institut für Physik und Astronomie, Universität Potsdam, Karl-Liebknecht-Str. 24-25, 14476 Potsdam, Germany

³Max-Planck-Institut für Mikrostrukturphysik, Weinberg 2, 06120 Halle, Germany

⁴European Synchrotron Radiation Facility (ESRF), 6 rue Jules Horowitz, BP220, 38043 Grenoble, France

(Received 7 April 2011; accepted 5 May 2011; published online 23 June 2011)

We implemented an experimental scheme for ultrafast x-ray diffraction at storage rings based on a laser-driven Bragg-switch that shortens the x-ray pulses emitted from an undulator. The increased time-resolution is demonstrated by observing changes of intensity, position and width of the diffraction peaks of a $\text{La}_{0.7}\text{Sr}_{0.3}\text{MnO}_3/\text{SrTiO}_3$ superlattice sample after optical excitation, i.e., by quantitatively measuring the propagation of an expansion wave through the sample. These experimental transients with timescales of 35 to 60 ps evidence a reduction of the x-ray pulse duration by a factor of two. © 2011 American Institute of Physics. [doi:10.1063/1.3601057]

Hard x-rays derived from modern synchrotron light sources have ideal properties for structure analysis by x-ray diffraction (XRD). The x-rays are generated by short electron bunches traveling in storage rings, yielding x-ray pulses with a duration on the order of 150 ps. Ultrafast x-ray diffraction (UXRD) uses this time structure in order to access the transient dynamics by pump-probe experiments. An optical pump pulse excites atomic motion in a sample and a time-delayed hard x-ray probe pulse measures the lattice changes for different delay times τ , creating a series of snapshots of the atomic positions. In this stroboscopic scheme the time-resolution is limited by the x-ray pulse duration. One option to obtain ~ 100 fs x-ray pulses—albeit with relatively low photon flux—is slicing of the electron bunches in an undulator using intense femtosecond laser pulses.^{1–3} Because this well-established method is operational at only few beamlines worldwide, and the x-ray free electron lasers (XFELs) will add only few experimental stations,⁴ alternative methods are explored. The “low alpha mode” shortens synchrotron pulses considerably, but simultaneously reduces the x-ray flux at all beamlines around the same storage ring.^{5,6} Finally, laser-driven x-ray plasma sources have the advantage of being a table-top setup, but lack the tunability of wavelength.⁷ The nearly instantaneous drop of the Debye-Waller factor in laser excited InSb was exploited to shorten x-ray pulses, however, this method has not been implemented into a long term stable setup.⁸ Recently, we have demonstrated the potential of using coherent phonons in superlattices (SL) to realize switchable Bragg mirrors, which can reduce the pulse duration down to 1 ps (Ref. 9).

In this Communication, we report on the implementation of this scheme at a synchrotron beamline, however, we exploit the somewhat slower change of the Bragg-peak position to truncate the x-ray pulse, instead of the structure-factor change discussed previously which leads to a series of ultrashort x-

ray bursts.⁹ The modified x-rays diffracted from this Bragg switch (BS), a $\text{SrRuO}_3/\text{SrTiO}_3$ (SRO/STO) SL, are subsequently used as a probe for the transient x-ray response of a $\text{La}_{0.7}\text{Sr}_{0.3}\text{MnO}_3/\text{SrTiO}_3$ (LSMO/STO) SL sample. We demonstrate the shortening of x-ray pulses at the European Synchrotron Radiation Facility (ESRF) by approximately a factor of two down to ~ 60 ps and we were able to record transients with time scales of 35 ps.

The measurements were performed with 12 keV x-rays from the undulator beamline ID09B at the ESRF, Grenoble, France.¹⁰ The storage ring was operating in the 4-bunch mode with a current of 10 mA per bunch and 708 ns time separation between them. Figure 1 shows a schematic of the setup. A Ti:Sapphire laser providing 600 fs pulses with

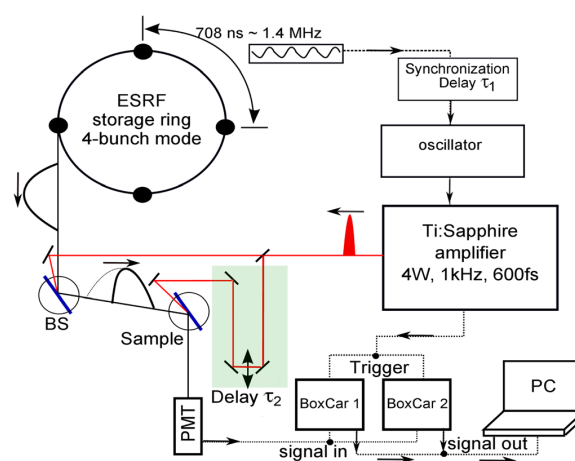


FIG. 1. (Color online) Schematic of the experimental setup. The electronic delay τ_1 gives the relative timing of the first laser pulse and the x-ray pulse at the Bragg switch (BS). The mechanical delay τ_2 sets the timing of the excitation of the sample relative to the x-ray pulse emitted by the BS. Note the schematically illustrated temporal profile of the x-ray pulse before and after diffraction and truncation by the BS.

^{a)}Electronic mail: marc.herzog@uni-potsdam.de.

800 nm wavelength at a repetition rate of ~ 1 kHz was electronically synchronized with the electron-bunch pattern, allowing for a tunable delay τ_1 between laser and x-ray pulses. The timing jitter was on the order of 5 ps, much shorter than the x-ray pulse duration. The laser output was split into two parts, one of which excited the Bragg switch (BS) being the SRO/STO SL described previously with a fluence of 45 mJ/cm^2 (Ref. 9). The second part was guided onto a LSMO/STO SL acting as the sample of interest (fluence of 2.4 mJ/cm^2). This epitaxial heterostructure consists of 15 periods of 13.7 nm thick STO layers and 8.8 nm thick layers of the ferromagnetic metal LSMO grown on a 1 mm STO substrate by pulsed laser deposition¹¹ as determined from high-resolution XRD. Both the BS and the sample were mounted on independent goniometers enabling individual *xyz*-positioning and adjustment of the Bragg angles (Fig. 1). A mechanical delay line was used to control the relative timing of the pump pulses for the BS and the sample. Since τ_1 was set such that the first laser pulse and the ESRF x-ray pulse were coincident at the BS, the delay line effectively varied the time delay τ_2 between the second laser pulse and the diffracted x-ray pulse at the sample.

The x-ray pulses from the storage ring impinge on the BS at a repetition rate of 1.41 MHz and at a fixed angle Θ_1 defined by the maximum of the (002) zero-order SL peak (ZOP) and are then diffracted toward the sample.^{9,12} These pulses are subsequently diffracted from the sample and detected by a plastic scintillator with a rise-time of 1 ns and a Hamamatsu photomultiplier tube (PMT). The analog output of the PMT is electronically gated by two Boxcar integrators which are set to detect x-ray pulses before and after the optical pump pulse, respectively. This way, we are able to evaluate the difference in x-ray intensity diffracted from of the pumped and unpumped sample, respectively, which significantly enhances the signal-to-noise ratio.

In the first part of the experiment, the x-rays diffracted from the BS are directly detected without secondary reflection from the sample. Delay τ_1 was varied to record the transient response of the ZOP peak of the BS [red squares in Fig. 2(a)]. The decreasing signal was fitted using the formula

$$\frac{\Delta R(\tau)}{R_0} = \frac{A}{2} \left\{ 1 - \operatorname{erf} \left[\frac{4 \ln 2 (\tau - \tau_0)}{\sigma} \right] \right\} \quad (1)$$

where A , τ_0 and σ are the fitting parameters. Here, σ represents the full width at half-maximum (FWHM) of the Gaussian corresponding to the derivative of Eq. (1) which is also indicated in Figs. 2(b) and (c). The best fit to the data [blue line in Fig. 2(a)] yields $\sigma = 108.5$ ps which is comparable to but slightly smaller than direct streak camera measurements of the ESRF x-ray pulse [$\sigma_{\text{SC}} \approx 125$ ps FWHM, dashed line in Fig. 2(a)]. The measured intensity decreases because the Bragg peak position changes to lower angles due to the expansion of the BS triggered by the absorption of the laser pulse.^{9,13} The time scale $T_{\text{shift}}^{\text{BS}} = D_{\text{BS}}/v_{\text{eff}} \approx 35$ ps for the expansion of the BS is determined by its total thickness ($D_{\text{BS}} \approx 250$ nm) and its effective sound velocity, $v_{\text{eff}} \approx 7.2$ nm/ps ($v_{\text{SRO}} = 6.3$ nm/ps¹⁴ and $v_{\text{STO}} = 7.8$ nm/ps¹⁵) (Refs. 9 and 13). The 108.5 ps time scale measured here is obviously

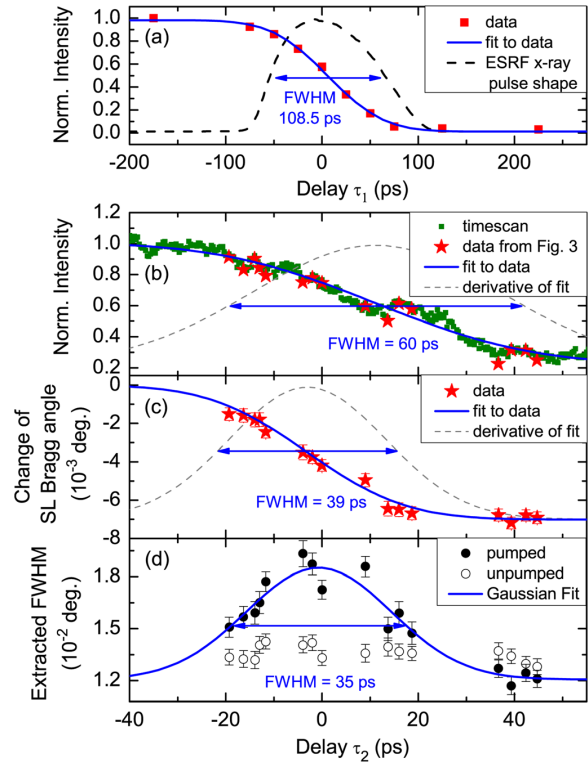


FIG. 2. (Color online) (a) Normalized diffracted intensity of BS vs delay τ_1 (red squares), fit to the data (solid line) and streak-camera characterization of x-ray pulse shape (dashed line). (b) Normalized diffracted intensity of the LSMO/STO ZOP vs delay τ_2 from direct measurement (green squares) and derived from rocking curves in Fig. 3 (red stars), fit to the data (solid line) and scaled derivative of the fit (dashed line). The same delay τ_2 was varied for the next panels: (c) Angular change of the ZOP extracted from Fig. 3 (red stars), fit to the data (solid line) and scaled derivative of the fit (dashed line). (d) Peak width (FWHM) of rocking curves for pumped (bullets) and unpumped sample (circles), and Gaussian fit (solid line).

limited by the x-ray pulse duration as it is much longer than the intrinsic dynamics of the Bragg peak. If τ_1 is set to negative values the entire x-ray pulse is reflected from the BS. For large positive τ_1 the Bragg peak position has changed and the diffraction efficiency of the BS at Θ_1 reaches a minimum. At intermediate delays the x-ray pulse is only partly reflected and we expect a truncated x-ray pulse as schematically indicated in Fig. 1.

For the second part of the experiment, we set τ_1 to the value where 60% of the x-ray intensity is reflected and define this as $\tau_1 = 0$ [cf. Figure 2(a)]. At this time delay the laser pulse and the maximum of the x-ray pulse nearly coincide. We aligned the LSMO/STO SL sample to be hit by the diffracted x-ray pulse and scanned the Bragg angle Θ_2 of the sample to obtain the extended rocking curve around the (002) STO substrate reflection shown in the inset of Fig. 3. Fixing Θ_2 at the maximum of the ZOP and scanning τ_2 , we recorded the transient presented in Fig. 2(b) which again exhibits a decreasing signal due to the expansion of the LSMO/STO SL. The best fit according to Eq. (1) yields $\sigma = 60$ ps. The sample thickness $D_S \approx 340$ nm and the

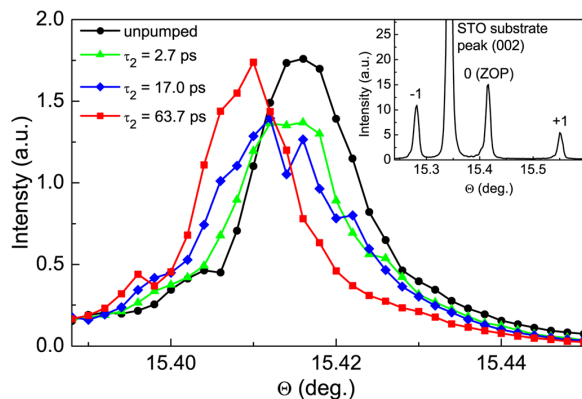


FIG. 3. (Color online) Selected transient rocking curves of the LSMO/STO ZOP used to obtain the data in Figs. 2(b)–(d). Shown are the scaled unpumped (black bullets) and pumped curves at delays $\tau_2 = 2.7$ ps (green triangles), 17.0 ps (blue diamonds) and 63.7 ps (red squares). Inset: Extended static rocking curve around STO substrate peak and ZOP.

sound velocity of LSMO ($v_{\text{LSMO}} = 6.5$ nm/ps¹⁵) determine the time scale of expansion to be $T_{\text{shift}}^S \approx 47$ ps. Both Figs. 2(a) and (b) measure the intensity decrease caused by the shifting Bragg peaks of the BS and the sample, respectively. The ratios of measured and calculated timescales [108/35 = 3.1 for (a) and 60/47 = 1.3 for (b)] readily suggest that the x-ray pulse probing the sample must have been approximately a factor of two shorter than the 125 ps x-ray pulse of the ESRF, confirming that it was successfully truncated by the BS. We stress that tuning τ_1 to positive (negative) values would truncate the x-ray pulse earlier (later) and would thus diffract shorter (longer) x-ray pulses with an accordingly smaller (larger) total intensity given by Fig. 2(a).

In order to analyze the transient response of the LSMO/STO sample in more detail, several ZOP rocking curves at different pump-probe delays τ_2 were recorded. A selection of these is depicted in Fig. 3. The black curve shows the rocking curve of the unpumped LSMO/STO SL which has to be scaled down to 60% [cf. Figure 2(a)] to give the same integrated intensity as the curves of the pumped sample. The reason is that the x-ray pulses probing the unpumped sample stem from an also unpumped BS so that the full non-truncated x-ray pulse hits the sample. The red curve shows the ZOP at its new position at $\tau_2 = 63.7$ ps, evidencing a relative expansion of $\varepsilon = 0.04\%$. The integrated intensity of the ZOP is constant for all time delays, however, for intermediate times we observe a significant peak broadening as can be directly seen in Fig. 3. In order to quantify the angular change and peak broadening we fitted Gaussian functions to the rocking curves. The extracted peak positions and widths are plotted in Figs. 2(c) and (d), respectively. The data show that the change in peak position (FWHM of ≈ 39 ps) is accompanied by a transient broadening of the rocking curve (FWHM of ≈ 35 ps) which is maximal when the peak position is half-way shifted. This behavior is consistent with an expansion wave triggered by the impulsive heating of the LSMO/STO SL. It is launched at the surface of the SL and

propagates toward the substrate.¹³ When the expansion front has propagated halfway through the SL, one expects a double-peak structure: one peak at the angular position of the unperturbed lattice (black bullets in Fig. 3) and a second peak at the shifted angular position corresponding to the expanded half of the SL (red squares in Fig. 3). Due to the relatively small expansion of 0.04% the separation of these two peaks is rather small and we thus, measure a broadened rocking curve at intermediate times which in principle also includes interference effects.

In conclusion, we have demonstrated a reliable setup for UXRD at synchrotrons where a laser-driven x-ray Bragg switch is used to significantly decrease and control the pulse duration of hard x-rays by truncation of the synchrotron pulses. With these pulses shortened by approximately a factor of two we have performed UXRD experiments on a LSMO/STO SL. Not only an expansion by 0.04% could be detected but, moreover, we could confirm that the laser excitation in such SLs transiently broadens the Bragg reflection because at early times the strain propagation yields different lattice constants at the surface and near the substrate. The same setup is capable of gating the x-ray pulses down to 1 ps using the principle proposed by Herzog *et al.*,⁹ however, the excitation laser is required to have a pulse duration ≤ 200 fs in order to efficiently launch the fast SL oscillations.

We thank the BMBF for funding the project via Grant No. 05K10IP1 and the DFG via SFB 762.

- ¹R. Schoenlein, S. Chattopadhyay, H. Chong, T. Glover, P. Heimann, C. Shank, A. Zholents, and M. Zolotarev, *Science* **287**, 2237 (2000).
- ²S. Khan, K. Holldack, T. Kachel, R. Mitzner, and T. Quast, *Phys. Rev. Lett.* **97**, 074801 (2006).
- ³P. Beaud, S. Johnson, A. Streun, R. Abela, D. Abramsohn, D. Grolimund, F. Krasniqi, T. Schmidt, V. Schlott, and G. Ingold, *Phys. Rev. Lett.* **99**, 174801 (2007).
- ⁴B. McNeil, *Nat. Photonics* **3**, 375 (2009).
- ⁵M. Abo-Bakr, J. Feikes, K. Holldack, P. Kuske, W. B. Peatman, U. Schade, G. Wüstefeld, and H.-W. Hübers, *Phys. Rev. Lett.* **90**, 094801 (2003).
- ⁶I. Radu, C. Stamm, N. Pontius, T. Kachel, P. Ramm, J.-U. Thiele, H. A. Dürr, and C. H. Back, *Phys. Rev. B* **81**, 104415 (2010).
- ⁷F. Zamponi, Z. Ansari, C. von Korff Schmising, P. Rothhardt, N. Zhavoronkov, M. Woerner, T. Elsaesser, M. Bargheer, T. Trobitzsch-Ryll, and M. Haschke, *Appl. Phys. A* **96**, 51 (2009).
- ⁸J. Larsson, P. Heimann, A. Lindenberg, P. Schuck, P. Bucksbaum, R. Lee, H. Padmore, J. Wark, and R. Falcone, *App. Phys. A* **66**, 587 (1998).
- ⁹M. Herzog, W. Leitenberger, R. Shayduk, R. M. van der Veen, C. J. Milne, S. L. Johnson, I. Vrejoiu, M. Alexe, D. Hesse, and M. Bargheer, *Appl. Phys. Lett.* **96**, 161906 (2010).
- ¹⁰M. Wulff, A. Plech, L. Eybert, R. Randler, F. Schotte, and P. Anfinrud, *Faraday Discuss.* **122**, 13 (2003).
- ¹¹I. Vrejoiu, G. Le Rhun, L. Pintilie, D. Hesse, M. Alexe, and U. Gösele, *Adv. Mater.* **18**, 1657 (2006).
- ¹²Here we adopt the notation of SL peak orders described in, e.g., G. Bauer and W. Richter, *Optical Characterization of Epitaxial Semiconductor Layers* (Springer, Berlin, 1996). The SRO/STO (002) ZOP corresponds to the (0 0 116) SL reflection of previous publications.
- ¹³C. v. Korff Schmising, M. Bargheer, M. Kiel, N. Zhavoronkov, M. Woerner, T. Elsaesser, I. Vrejoiu, D. Hesse, and M. Alexe, *Phys. Rev. Lett.* **98**, 257601 (2007).
- ¹⁴S. Yamanaka, T. Maekawa, H. Muta, T. Matsuda, S. Kobayashi, and K. Kurosaki, *J. Solid State Chem.* **177**, 3484 (2004).
- ¹⁵Y. H. Ren, M. Trigo, R. Merlin, V. Adyam, and Q. Li, *Appl. Phys. Lett.* **90**, 251918 (2007).

PAPER X

Ultrafast switching of hard x-rays

P. Gaal, D. Schick, M. Herzog, A. Bojahr, R. Shayduk,
J. Goldshteyn, H. A. Navirian, W. Leitenberger, I. Vrejoiu,
D. Khakhulin, M. Wulff and M. Bargheer.

submitted.

Ultrafast Switching of hard X-rays

June 27, 2012

Ultrafast structural dynamics can be monitored by time-resolved x-ray techniques, provided that the probing x-ray pulse is sufficiently short [1, 2]. Unfortunately, large-scale facilities like synchrotrons, which offer the best experimental conditions in terms of stability and brilliance, do not deliver short pulses. The solution was to shorten the pulse length in existing synchrotrons using electron slicing schemes [3, 4] and finally to build new facilities like free-electron-laser (FEL) sources [5, 6, 7]. However, the large demand for beamtime at ultrashort, brilliant and stable x-ray pulses from the ultrafast community is not yet satisfied. Here we present a new approach on shortening hard x-ray pulses from synchrotrons down to several picoseconds (ps), by employing an x-ray switch as an ultrafast gating device. This device, which we call the PicoSwitch, is easy to use and allows long term operation over several weeks without any observable degradation.

To date, various schemes exist, that can manipulate or resolve the time structure of a synchrotron x-ray pulse. All of them are indirect in the sense that they do not act on the x-ray pulse itself. Either the electron bunch in the storage ring is manipulated (e.g., femtoslicing or cranked RF cavities), or electrons generated in photocathodes are used to spatially map the temporal structure of the synchrotron pulse on a screen. [8, 9] Here we demonstrate a new approach allowing to directly manipulate the time structure of a ≈ 100 ps x-ray pulse by modulating the x-ray diffraction efficiency on ultrafast timescales. Several early experiments reported switching of hard x-rays resulting in pulses of 100 ps and more [10, 11, 12, 13, 14]. A promising concept is based on optical phonons [15], however, it could not yet be realized experimentally [16]. A modified approach based on superlattices has been presented by Herzog et al. [17]. They demonstrated a modulation of the diffraction efficiency of $\Delta R/R = 24.1$ during 1 ps. However, the first modulation is followed by several post pulses, which significantly protracts

the switching time. Our new concept builds on the experience with previous approaches. Here we excite coherent strain waves in a thin metallic oxide film in order to modify the diffraction efficiency of the structure at a fixed Bragg angle on picosecond time scales. An exemplary gate is shown in Figure 1 b). A good switch provides short rise- and fall times t_r and t_f and a short *on*-time ΔT . Also the diffraction efficiency before (η_0) and after (η_∞) the switching should be low, whereas it should be high in the *on*-state (η_{max}). This automatically increases the switching contrast C_0 and C_∞ . Figure 1 a) shows the measured and simulated time-dependent diffraction efficiency of the particular PicoSwitch structure discussed below in this article. In the first part of this contribution, we present a full characterization of the PicoSwitch both experimentally and theoretically. In the second part we apply our approach in a real synchrotron based ultrafast pump-probe experiment.

The PicoSwitch consists of a d_{SRO} 15.4 nm thin layer of SrRuO₃ (SRO) which was epitaxially grown on a SrTiO₃ (STO) substrate.[18] A static rocking curve recorded at the ID09B beamline at the ESRF (see methods section) is shown by the green line in Figure 2 a). The black line is a simulation of the structure using dynamic diffraction theory.[19] To record the ultrafast response of the PicoSwitch to hard x-rays, we resort to the ultrafast x-ray diffraction (UXRD) setup at the Plasma X-ray Source (PXS, see methods section) at the University of Potsdam.[20] Figure 2 b) shows the shift of the SRO layer peak as a function of delay time after excitation of the PicoSwitch with an ultrashort 800 nm pump pulse. The interpretation of coherent phonon dynamics of an excited layer is straightforward [21] and the red solid line shows a simulation using a linear-chain model. [22] Excitation of the PicoSwitch with an ultrashort optical pulse launches coherent expansion waves starting at the air/SRO and SRO/STO interfaces through the SRO-layer, shifting the layer Bragg peak to lower angles. The expansion waves propagate at the sound velocity in SRO of $v_{SRO} = 6.3$ ps/nm. Reflection of the strain wave at the surface converts the expansion that was launched at the SRO/STO interface into a compression wave, which propagates back through the layer and into the substrate, thus shifting the Bragg peak back to about 2/3 compared to the maximum expansion. The coherent dynamics last for $2 \cdot d_{SRO} / v_{SRO} \leq 5$ ps = τ_{switch} , i.e., the time it takes for the strain waves to propagate through the layer twice. For later times, the peak position is given by the remaining heat expansion, and the heat conduction cools the layer on a ns timescale. [23] Hence, there is an angular range, which extends from 23.0° to 22.75° in Figure 2 b), where the ultrafast coherent phonon propagation is responsible for the rise and fall of the diffraction efficiency. This range can be exploited for ultrafast x-ray switching. For a quantitative comparison of the experimental signal with theory we feed the spatio-temporal strain

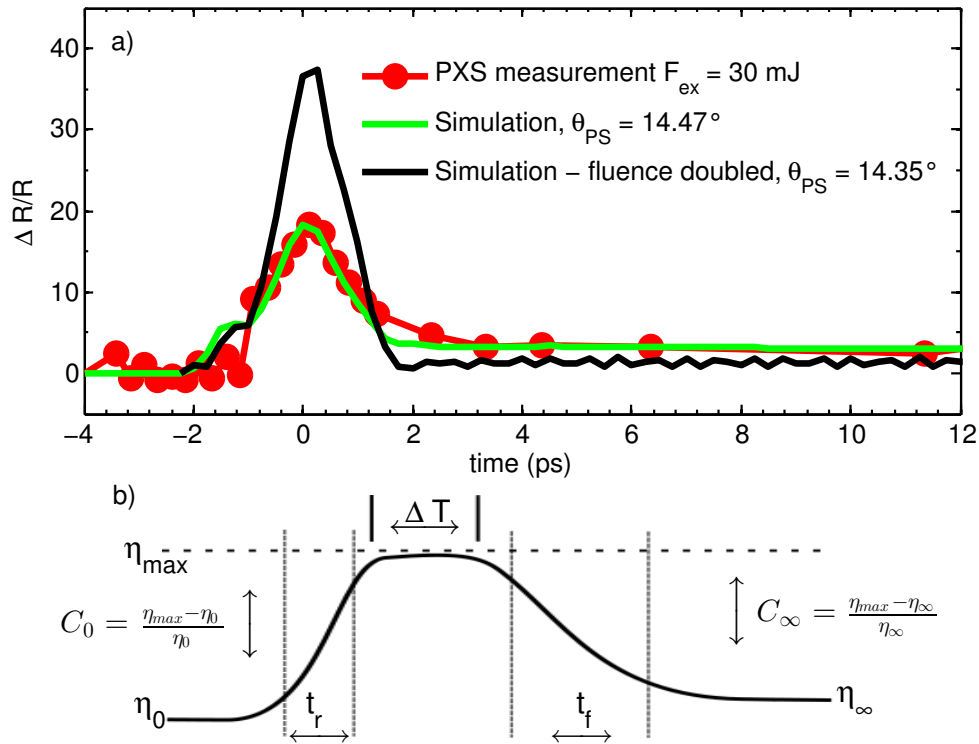


Figure 1: a) Measurement (red bullets) and simulations (green and black solid lines) of the PicoSwitch. The measurement was performed at the PXS at the University of Potsdam. The simulations show excellent agreement with the measured data (green line) and predict a larger contrast and switching efficiency for higher pump fluences (black line). b) Gate parameters defining the performance of an x-ray switch: turn-on time ΔT , rises- and fall-time t_r and t_f , respectively, diffraction efficiency before (η_0), during (η_{max}) and after (η_∞) switching and contrast before (C_0) and after (C_∞) switching.

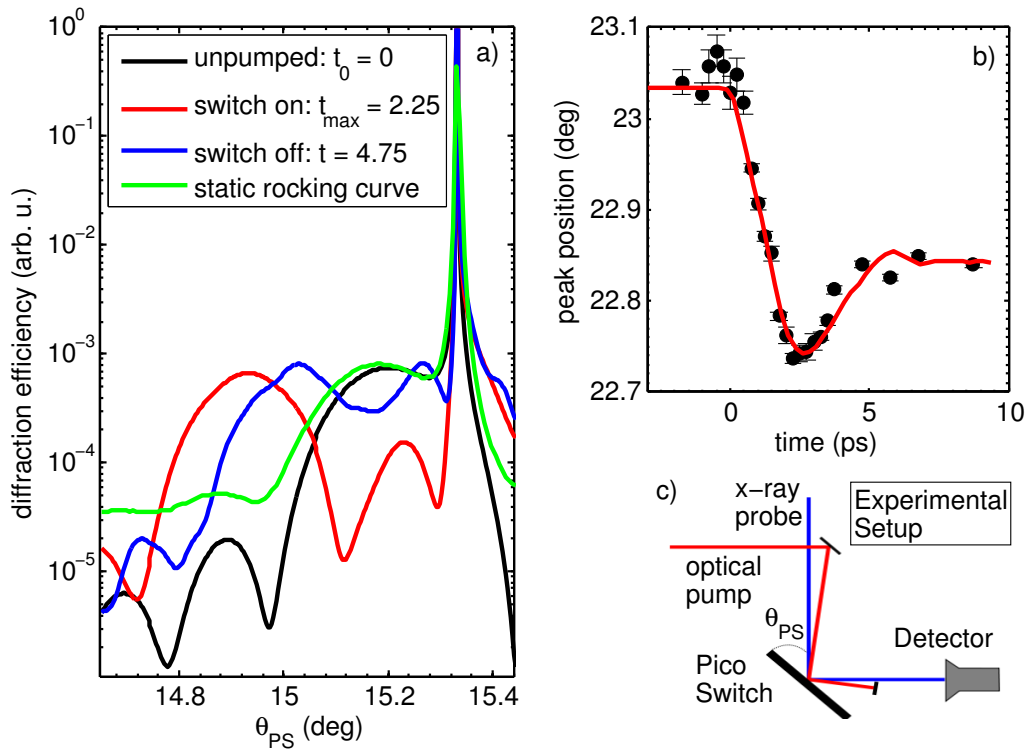


Figure 2: Characterization of the PicoSwitch: a) green: measured diffraction curve of the PicoSwitch. The data were recorded at the ID09B beamline at ESRF at an x-ray energy of 12 keV. Black: simulation of the unexcited structure; red: simulation for maximum layer expansion 2.25 ps after optical excitation; blue: simulation at $\tau = 4.75$ ps after optical excitation. At this delay all coherent sound waves have propagated into the substrate. b) Ultrafast shift of the layer peak measured at the Plasma X-ray-Source (PXS) at University of Potsdam with an x-ray energy of 8.047 keV. c) Sketch of the experimental setup.

map calculated in a linear chain model into a simulation of the dynamical x-ray diffraction, yielding the x-ray response of the PicoSwitch $R(t, \theta)$. [22] The result yields the perfect agreement with the measured dynamics of the peak shift demonstrated in Figure 2 b) and the corresponding intensity change plotted in Figure 1 a) when keeping the angle of the Bragg switch fixed. Figure 2 a) shows the simulations for a broader angular range. The red curve represents a simulated rocking curve at a time delay of 2.25 ps after excitation. At this moment the thin layer is maximally expanded. The blue curve, which is simulated for a delay of 4.74 ps depicts the situation where the coherent compression wave has propagated into the substrate and thus terminates the coherent dynamics in the PicoSwitch.

Now we apply the PicoSwitch in a real synchrotron based pump-probe experiment to measure coherent phonon dynamics in a nanolayer-sample. Experiments were performed at ID09B beamline at ESRF. The output of a Ti:sapphire laser amplifier is split into two beams in order to pump the PicoSwitch and the sample separately with delays t and τ , respectively. The time axis are referenced to the maximum of the x-ray pulse from the synchrotron. The pump fluence was set to 15 mJ/cm^2 on both the PicoSwitch and the sample. The experimental setup is discussed in more detail in the methods section and a schematic is shown in Figure 5. The electronic delay t is set so that the diffraction efficiency of the switch is turned on and off approximately when the maximum of the 100 ps x-ray pulse from the synchrotron impinges on the PicoSwitch, as shown in Figure 3 a). During the experiment, the first time axis t is held constant. The pump-probe delay τ shifts the optical pump pulse for the sample against the shortened x-ray pulse. The sample under investigation was a 70 nm SRO single layer grown on an STO substrate. [18] The diffraction angle of the sample θ_S is set to the maximum of the SRO layer peak. Figure 3 b) shows the measured relative change of the diffracted x-ray intensity measured at the detector (black bullets) as a function of the pump-probe delay τ . The green dash-dotted, black solid, red dotted and blue dashed line represent simulations of the x-ray response assuming the simulated shortened probe pulses depicted in Figure 3 c) with the same color code. The shape of the switched pulse is determined by the Bragg angle θ_{PS} chosen on the PicoSwitch and by the pump fluence. The simulated signals plotted as lines in Figure 3 b) depict the normalized correlation of the the samples x-ray response $R(t)$ at the fixed angle θ_S with the shortened probe pulse $P(t, \theta_{PS})$ for various diffraction angles θ_{PS} of the PicoSwitch .

$$X_c(\tau, \theta_{PS}) = \int_{-\infty}^{\infty} P(t, \theta_{PS}) \cdot R(t - \tau) dt \quad (1)$$

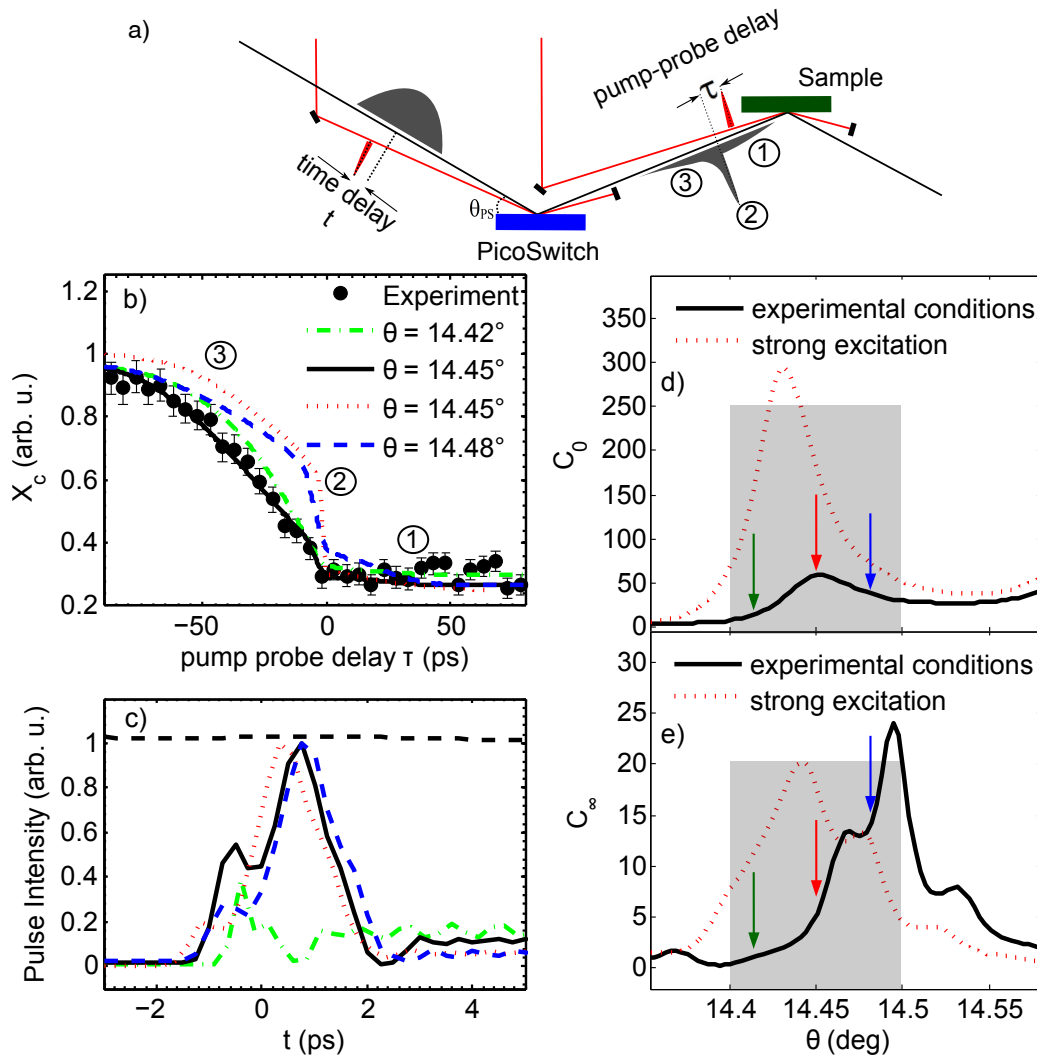


Figure 3: Synchrotron based time-resolved experiment: a) sketch of the experimental setup showing the real time axis t and the pump probe delay τ . Since the optical excitation pulse arrives earlier at the sample than the gated section of the x-ray probe pulse, the pump-probe delay τ is positive. The probe pulse is divided into three sections: leading edge (1), ultrafast gate (2) and trailing edge (3). b) Measured (black dots) and simulated (green dotted, black solid and blue dashed lines) pump-probe correlation signal X_c . The simulations were obtained with Equation 1 for $\theta_{PS} = 14.42^\circ$ (green dash-dotted line), $\theta_{PS} = 14.45^\circ$ (black solid line) and $\theta_{PS} = 14.48^\circ$ (blue dashed line). The red dotted lines shows a simulation for $\theta_{PS} = 14.45^\circ$ where the pump fluence on the PicoSwitch was increased by 25%. c) Shortened x-ray probe pulses for different incident angles on the PicoSwitch. The color code is similar to b). d) Simulated initial (C_0) and e) final (C_∞) contrast as defined in Figure 1 for different Bragg angles on the PicoSwitch. The black solid lines shows a simulation which reproduces the experimental results. The red dotted lines show a contrast for 25% stronger excitation for comparison. The colored vertical bars mark the angles at which the probe pulses in b) and c) were calculated. The gray shaded area marks the angular resolution of the PXS measurement (see methods section).

In the following we explain the impact of different probe pulse shapes on the measured signal. For a better understanding, we divide the gated probe pulse shown in Figure 3 a) in three sections: (1) and (3) are determined by the initial and final contrast C_0 and C_∞ , respectively, while (2) represents the ultrafast gate from the PicoSwitch. The contrast depends on the Bragg angle on the PicoSwitch, as shown in Figure 3 d) and e). The colored arrows mark the Bragg angle on the PicoSwitch at which the corresponding signals shown in Figure 3 a) and b) were obtained. Note that features appearing in X_c at positive pump-probe delays stem from badly suppressed background photons in the leading edge of the probe pulse marked (1) in Figure 3 a). Features at negative τ originate from the trailing edge of the probe pulse, which is marked (3) and is determined by the thermal relaxation of the PicoSwitch after optical pumping. [23] The sharp drop in X_c , which is observed in the red, blue and black simulation in Figure 3 a) is caused by the short and intense section of the probe pulse and is marked (2).

Our experimental data are best reproduced by the simulation shown in the black solid line. It shows a rather slow initial decay (3) and it is flat after the gated probe pulse (1), i.e., for positive τ . This indicates a large initial contrast C_0 , which is marked by the red arrow in Figure 3 d). The small contribution of X_c at $\tau = 0$ ps indicates the response to the ultrafast switching.

The simulation for larger θ_{PS} (blue dashed line) shows a lower initial and higher final contrast, leading to deviations from the observed correlation (black bullets). The dash-dotted green line (smaller θ_{PS}) shows a case where both the initial and final contrast C_0 and C_∞ are lower. Hence, the ultrafast feature at $\tau = 0$ ps disappears and in addition there are deviations from the measured signal at negative τ . In essence Figure 3 shows that we have performed an ultrafast x-ray diffraction experiment with a synchrotron probe pulse which was shortened to approximately 2 ps as indicated in Figure 3 b) by the black line.

For an optimized performance in future applications the PicoSwitch must be pumped with about 25% higher optical pump fluence. The simulation shown in the red dotted line in Figure 3 d) and e) demonstrates an increased initial and final contrast at the θ_{PS} chosen in the experiment. This parameter setting on the PicoSwitch would result in a correlation signal X_c shown in the black solid line in Figure 3 b). The corresponding probe pulse is shown in Figure 3 c). The essential difference to the pulse used in the experiment is the higher contrast. The switching time is identical. Thus, the PicoSwitch is suitable for generating probe pulses that are capable of resolving ultrafast dynamics on a picosecond time scale. We would like to point out that the PicoSwitch can sustain such high fluences up to 40 mJ/cm² without degra-

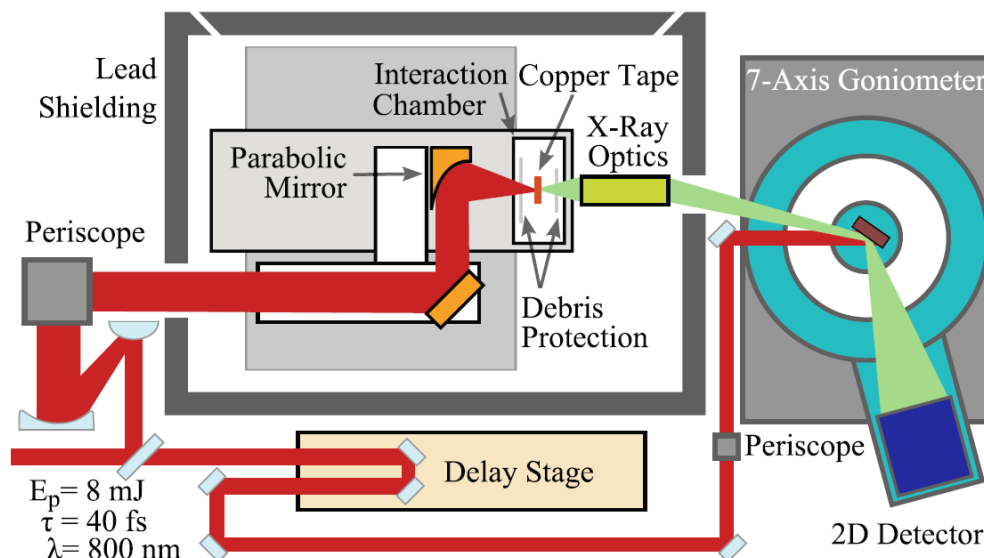


Figure 4: Ultrafast x-ray diffraction setup at the University of Potsdam.

dation.

In conclusion, we have characterized and applied an ultrafast x-ray switch for gating synchrotron x-ray pulses on picosecond timescales. The shape of the shortened pulse can be adjusted by selecting the Bragg angle on the switch and by tuning the pump fluence. The switching relies on coherent phonon dynamics which modulate the diffraction efficiency. The rise and fall times t_r and t_f are determined by the layer thickness and the speed of sound in the material. We demonstrated a high switching contrast with a maximum diffraction efficiency of $\eta_{max} \approx 10^{-3}$. The structure allows for repetitive switching and no long term degradation effects have yet been observed. Hence, the device is suited for permanent installation in time-resolved beamline setups. The applicability of the PicoSwitch was demonstrated in a synchrotron based pump-probe experiment where we measured coherent lattice dynamics in a nanostructured sample with picosecond resolution.

1 Methods

Time-resolved experiments have been carried out at the Plasma X-ray Source (PXS) [20] at the University of Potsdam (UP) and at the ID09B beamline at ESRF Grenoble, France. The PXS setup at UP is shown in Figure 4. We employ a Coherent Legend Duo laser system as a source for sub 40 fs

800 nm pulses which are focused on a copper target in a vacuum chamber. The target is wrapped on a system of spools together with debris protection tapes. Interaction of the copper target with the highly intense laser pulses leads to the emission of characteristic Cu K_α x-ray ($E = 8.047$ keV) bursts of 150 fs duration [20, 24]. X-ray photons, which are emitted in a solid angle of 4π , are collected with a Montel x-ray focusing mirror having an image ratio of 1:7. The mirror is mounted 875 mm from the sample. The 4π emission angle and the focal distance reduce the angular resolution to approximately 0.1° in a diffraction experiment, as indicated by the gray shaded area in Figure 3 d) and e). Reflected x-ray photons from the sample are detected with a two-dimensional silicon diode array detector (Dectris Pilatus 100K).

At the ID09B beamline, another Coherent Legend laser system is employed to pump both the PicoSwitch and the sample. The setup is shown in Figure 5. The laser pulse duration was limited to 600 fs. The laser oscillator was electronically phase-locked to the synchrotron repetition rate, which allows to determine the time delay t between the amplified optical and x-ray pulses with an accuracy better than 5 ps, which is significantly shorter than the x-ray pulse length. The gated probe pulse is inherently synchronized to the pump laser after the switching. For the second optical path, a mechanical delay stage has been introduced to realize the pump-probe delay τ . X-ray photons have been detected with a plastic scintillator (BC400-series) attached to a Hamamatsu photomultiplier tube (H7422). The detector signal was fed to a time-correlated single-photon counting unit (PicoHarp300) controlled by a computer.

References

- [1] M. Bargheer, N. Zhavoronkov, M. Woerner and T. Elsaesser, *Recent Progress in Ultrafast X-ray Diffraction*, ChemPhysChem **7**, 783-792 (2006)
- [2] A. Rousse, C. Rischel and J.-C. Gauthier, *Femtosecond x-ray crystallography*, Rev.Mod.Phys. **73**, 17-31 (2001)
- [3] R. W. Schoenlein, S. Chattopadhyay, H. H. W. Chong, T. E. Glover, P. A. Heimann, C. V. Shank, A. A. Zholents and M. S. Zolotarev, *Generation of Femtosecond Pulses of Synchrotron Radiation*, Science **287**, 2237-2240 (2000)
- [4] P. Beaud, S.L. Johnson, A. Streun, R. Abela, D. Abramsohn, D. Grolimund, F.S. Krasniqi, T. Schmidt, V. Schlott and G. Ingold,

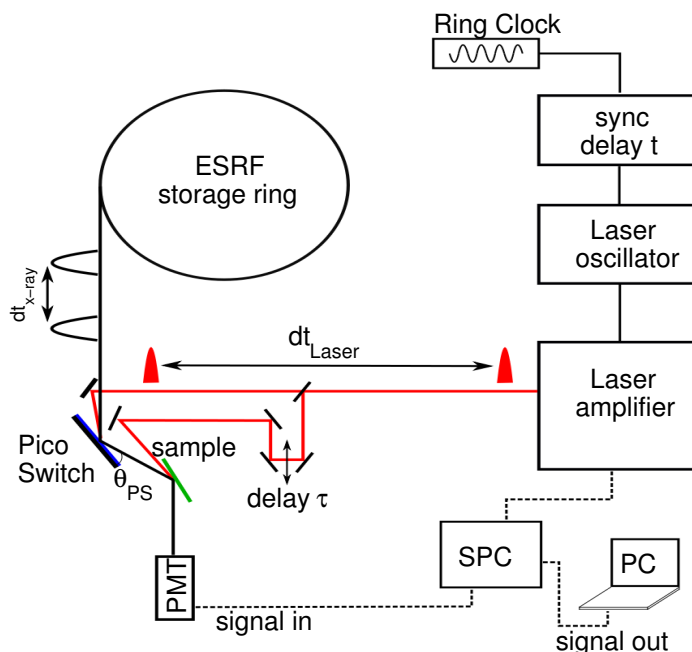


Figure 5: Experimental setup at ID09B at ESRF. The laser oscillator is synchronized to the ring clock, i.e., to the repetition rate of the synchrotron $1/dt_{x\text{-ray}} = 1/177$ ns. The time delay t determines when the the PicoSwitch is excited. The laser amplifier operates at a repetition rate of $1/dt_{laser} = 1$ kHz. X-ray photons diffracted from the sample are captured with a plastic scintillator and subsequent optical photons are amplified in a photo-multiplier tube (PMT). The electronic signal is fed into a single photon counting module (SPC) triggered by the laser amplifier clock. Experimental data is recorded on a PC. The pump-probe delay τ is realized with a mechanical translation stage.

- Spatiotemporal Stability of a Femtosecond HardX-Ray Undulator Source Studied by Control of Coherent Optical Phonons*, Phys. Rev. Lett. **99**, 174801 (2007)
- [5] P. Emma, R. Akre, J. Arthur, R. Bionta, C. Bostedt, J. Bozek, A. Brachmann, P. Bucksbaum, R. Coffee, F.-J. Decker, Y. Ding, D. Dowell, S. Edstrom, A. Fisher, J. Frisch, S. Gilevich, J. Hastings, G. Hays, Ph. Hering, Z. Huang, R. Iverson, H. Loos, M. Messerschmidt, A. Miahnahri, S. Moeller, H.-D. Nuhn, G. Pile, D. Ratner, J. Rzepiela, D. Schultz, T. Smith, P. Stefan, H. Tompkins, J. Turner, J. Welch, W. White, J. Wu, G. Yocky and J. Galayda, *First lasing and operation of an ångstrom-wavelength free-electron laser*, Nature Photonics **4**, 641-647 (2010)
- [6] D. Pile, *X-rays: First light from SACLA*, Nature Photonics **5**, 456-457 (2011)
- [7] G. Geloni, E. Saldin, L. Samoylova, E. Schneidmiller, H. Sinn, T. Tschentscher and M. Yurkov, *Coherence properties of the European XFEL*, New. J. Phys. **12**, 035021 (2010)
- [8] H. Enquist, H. Navirian, R. Nueske, C. von Korff Schmising, A. Jurgilaitis, M. Herzog, M. Bargheer, P. Sondauss and J. Larsson, *Subpicosecond hard x-ray streak camera using single-photon counting*, Opt. Lett. **35**, 3219-3221, (2012)
- [9] Z. Chang, A. Rundquist, J. Zhou, M. M. Murnane, H. C. Kapteyn, X. Liu, B. Shan, J. Liu, L. Niu, M. Gong and X. Zhang, *Demonstration of a sub-picosecond x-ray streak camera*, Appl. Phys. Lett. **69** 133 (1996)
- [10] J. S. Wark, R. R. Whitlock, A. A. Hauer, J. E. Swain and P. J. Solone, *Subnanosecond x-ray diffraction from laser-shocked crystals*, Phys. Rev. B **40** 5705 (1989)
- [11] E. Zolotoyabko and J. P. Quintana², *Control of synchrotron x-ray diffraction by means of standing acoustic waves*, Rev. Sci. Instrum. **75**, 699 (2004)
- [12] D. S. Allam, *A piezoelectric beam chopper*, J. Phys. E, **3**, 1022 (1970)
- [13] A. Grigoriev, D.-H. Do, D. M. Kim, C.-B. Eom, P. G. Evans, B Adams and E. M. Dufresne, *Subnanosecond piezoelectric x-ray switch*, Appl. Phys. Lett. **89**, 021109 (2006)

- [14] H. Navirian, M. Herzog, J. Goldshteyn, W. Leitenberger, I. Vrejoiu, D. Khakhulin, M. Wulff, R. Shayduk, P. Gaal and M. Bargheer, *Shortening x-ray pulses for pump-probe experiments at synchrotrons*, J. Appl. Phys., **109**, 126104 (2011)
- [15] P. H. Bucksbaum and R. Merlin, *The phonon Bragg switch: a proposal to generate sub-picosecond X-ray pulses*, Sol. Stat. Com. **111**, 535-539 (1999)
- [16] J. M. H. Sheppard, P. Sondhauss, R. Merlin, P. Bucksbaum, R. W. Lee and J. S. Wark, *The phonon Bragg switch: a proposal to generate sub-picosecond X-ray pulses*, Sol. Stat. Com. **136**, 181-185 (2005)
- [17] M. Herzog, W. Leitenberger, R. Shayduk, R. van der Veen, C. J. Milne, S. L. Johnson, I. Vrejoiu, M. Alexe and D. Hesse, *Ultrafast manipulation of hard x-rays by efficient Bragg switches*, Appl. Phys. Lett. **96**, 161906 (2011)
- [18] I. Vrejoiu, M. Ziese, A. Setzer, P. D. Esquinazi, B. I. Birajdar, A. Lotnyk, M. Alexe and D. Hesse, *Interfacial strain effects in epitaxial multiferroic heterostructures of $PbZr_xTi_{1-x}O_3/La_{0.7}Sr_{0.3}MnO_3$ grown by pulsed-laser deposition*, Appl. Phys. Lett. **92**, 152506 (2008)
- [19] J. Als-Nielsen and D. J. McMorrow, *Elements of Modern X-Ray Physics*, John Wiley & Sons, Ltd. (2001)
- [20] D. Schick, A. Bojahr, M. Herzog, C. von Korff Schmising, R. Shayduk, W. Leitenberger, P. Gaal and M. Bargheer, *Normalization schemes for ultrafast x-ray diffraction using a table-top laser-driven plasma source*, Rev. Sci. Instrum. **83**, 025104 (2012)
- [21] K. Sokolowski-Tinten, M. Horn von Hoegen, D. von der Linde, A. Cavalleri, C. W. Siders, F. L. H. Brown, D. M. Leitner, Cs. Toth, C. P. G. Barty, J. A. Squier, K. R. Wilson and M. Kammler. *Transient lattice dynamics in fs-laser-excited semiconductors probed by ultrafast x-ray diffraction*, J. de Physique IV **11**, Pr2-473 (2001).
- [22] M. Herzog, D. Schick, P. Gaal, R. Shayduk, C. v. Korff Schmising and M. Bargheer, *Analysis of ultrafast X-ray diffraction data in a linear-chain model of the lattice dynamics*, Appl. Phys. A (1-11) (2011)

- [23] R. Shayduk, H. Navirian, W. Leitenberger, J. Goldshteyn, I. Vrejoiu, M. Weinelt, P. Gaal, M. Herzog, C. von Korff Schmising and M. Bargheer, *Nanoscale heat transport studied by high-resolution time-resolved x-ray diffraction*, New J. Phys. **13**, 093032 (2011)
- [24] F. Zamponi, Z. Ansari, C. von Korff Schmising, P. Rothhardt, N. Zhavoronkov, M. Woerner, T. Elsaesser, M. Bargheer, T. Trobitsch-Ryll and M. Haschke, *Femtosecond hard X-ray plasma sources with a kilohertz repetition rate*, Appl. Phys. A **96**, 51-58 (2009)

PAPER XI

Normalization schemes for ultrafast x-ray diffraction using a table-top laser-driven plasma source

D. Schick, A. Bojahr, M. Herzog, C. von Korff Schmising,
R. Shayduk, W. Leitenberger, P. Gaal and M. Bargheer.
Rev. Sci. Instrum. **83**, 025104 (2012).

Normalization schemes for ultrafast x-ray diffraction using a table-top laser-driven plasma source

D. Schick,¹ A. Bojahr,¹ M. Herzog,¹ C. von Korff Schmising,² R. Shayduk,³ W. Leitenberger,³ P. Gaal,³ and M. Bargheer^{3,a)}

¹*Institut für Physik & Astronomie, Universität Potsdam, Karl-Liebknecht-Str. 24-25, 14476 Potsdam, Germany*

²*Institut für Optik und Atomare Physik, Technische Universität Berlin, Straße des 17. Juni 135, 10623 Berlin, Germany*

³*Helmholtz Zentrum Berlin, Albert-Einstein-Strasse 15, 12489 Berlin, Germany*

(Received 1 November 2011; accepted 10 January 2012; published online 7 February 2012)

We present an experimental setup of a laser-driven x-ray plasma source for femtosecond x-ray diffraction. Different normalization schemes accounting for x-ray source intensity fluctuations are discussed in detail. We apply these schemes to measure the temporal evolution of Bragg peak intensities of perovskite superlattices after ultrafast laser excitation. © 2012 American Institute of Physics. [doi:10.1063/1.3681254]

I. INTRODUCTION

Ultrafast x-ray diffraction (UXRD) allows for tracking atomic motion on its specific time scale in various physical, chemical, and biological processes.^{1–3} In most UXRD experiments the pump-probe scheme is employed, in which the sample is excited repetitively by an ultrafast stimulus, e.g., a fs laser pulse, and is probed subsequently at different time delays between pump and probe pulses.

Besides accelerator-based x-ray sources with fs time resolution,^{4–7} laser-driven plasma x-ray sources (PXS) proved to be a practical alternative for UXRD experiments with no beamtime limitation, relatively low costs for build-up and maintenance as well as an intrinsic synchronisation between the optical pump and x-ray probe pulses.⁸ In conventional x-ray tubes electrons are accelerated onto a metal target to generate characteristic line emission (K-shell ionization and recombination) and a broad bremsstrahlung background. This process can also be driven efficiently by focusing an intense laser pulse of more than 10^{16} W cm⁻² onto a metal target. Under proper conditions free electrons are generated and instantaneously accelerated back into the metal by the next half-cycle of the laser's electric field.^{9–15} The released x-ray pulses typically have a duration of a few hundred fs which is generally determined by the interaction time of the electrons with the metallic target.

Even though sources working at kilohertz repetition rate offer a relatively high flux of up to 3×10^6 ph/s on the sample using x-ray optics^{16,17} long integration times are necessary to acquire a sufficient signal-to-noise ratio (SNR) in most UXRD experiments. Moreover, large intensity fluctuations of PXS sources, compared to conventional x-ray tubes, call for advanced normalization schemes.

In this review we present a brief description of the new UXRD setup at the University of Potsdam. On the example of ultrafast Bragg peak intensity oscillations of two perovskite superlattices we discuss different normalization approaches and their experimental applicability. In particular, we intro-

duce a rapid scanning technique adapted from all-optical experiments as well as a scheme which utilizes the single reflection of a Montel x-ray optic to measure the incoming x-ray flux directly.

II. SYSTEM CHARACTERISTICS

In recent years, different designs of laser-driven plasma x-ray sources have been successfully applied to numerous UXRD experiments.^{18–21} The PXS setup at the University of Potsdam is a further development of the system introduced in Ref. 22. In addition to its excellent degree of automation and stability as well as its high standard of radiation safety, the setup can be employed in various x-ray diffraction and reflection geometries.^{23–25}

The PXS is driven by a two-stage Ti:sapphire amplifier (Legend Duo, COHERENT) working at 1 kHz repetition rate with a center wavelength of 800 nm and a pulse energy of 8 mJ compressed into a pulse duration of 40 fs. The laser beam is split into a main part of 80% for the x-ray generation and the remaining pulse energy is guided via a motorized mechanical delay line to excite the sample at a defined time before the probing x-ray pulse. The laser plasma is generated on a copper tape running in an evacuated interaction chamber, which can be moved within the fixed focal plane of the laser, perpendicular to the spooling direction of the tape. Thereby one can write multiple tracks onto one tape prolonging the measurement time up to 10 h. Both the entrance and exit window of the vacuum chamber are protected by plastic tapes which catch most of the copper debris that is ejected by the laser plasma. The generated x-ray pulses (dominantly characteristic Cu K_α and K_β lines) are collected, focused, and monochromatized to only Cu K_α energies by a Montel multilayer optic (INCOATEC) with a convergence of 0.3° and a focal spot size of only 200–300 μm FWHM at a distance $d = 1000$ mm from the source. The selected x-ray optic is adapted to the experimental needs which specify the energy bandwidth, angular distribution, and spot size of the x-rays at the sample. In most of our experiments

^{a)}Electronic mail: bargheer@uni-potsdam.de.

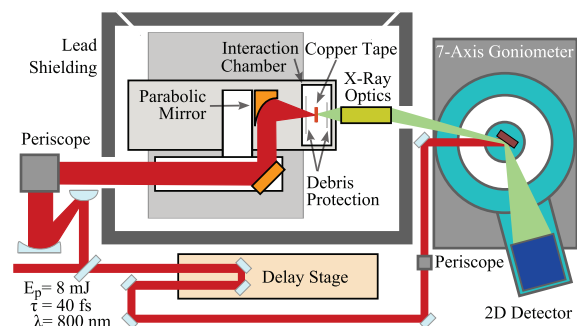


FIG. 1. (Color online) The laser is focused onto a copper tape inside a vacuum chamber to generate fs x-ray pulses. Both copper tape and plastic debris-protection tapes run perpendicular to the plane of drawing. To write new tracks on the copper band, the entire vacuum chamber is translated. The x-rays are collected, monochromatized, and focused onto the sample by a multilayer Montel optic. The diffracted x-rays are detected by a fast read-out CMOS 2D camera.

on epitaxial thin films and multilayers a symmetric θ - 2θ geometry is applied. Here, the sample is placed in the x-ray focal plane to reduce time smearing effects due to a generally inevitable non-collinearity between laser pump and x-ray probe beam and to probe a homogeneously excited part of the sample. The x-ray detector can be easily exchanged, but we commonly use a fast read-out CMOS 2D camera (Pilatus 100 k, DECTRIS) to record diffracted x-ray photons. The complete setup is sketched in Fig. 1.

The performance of the PXS can be characterized by three main parameters: pulse length, photon flux, and intensity stability. Since there is no detector that is fast enough to measure the duration of ultrashort x-ray pulses directly we rely on several successful experiments in our and other groups^{21,25} which evidence the sub-ps temporal resolution of PXS machines.

The x-ray flux can be improved by an increase of the laser intensity on the metal target, but only up to a certain saturation limit.^{10,12} From there on a further increase of the x-ray flux can be achieved by a larger interaction volume of the laser-produced electrons with the target, e.g., by larger foci, which will increase the x-ray source size in return. At very high laser intensities in the relativistic limit the efficiency rises again, however, at the expense of a high background of high energetic radiation. For our setup we achieved nearly 10^{11} ph/s with Cu K_α energy in the full solid angle of 4π under optimal conditions. Only 5×10^5 ph/s of the total flux are focused onto the sample using the Montel x-ray optic at a normal performance. Thus, the number of diffracted photons per pulse for a typical Bragg peak with 1% peak reflectivity is well below ten for our system. Consequently, we are within the single photon counting regime for each detector pixel, because the divergence of the diffracted x-rays yields 10–100 illuminated pixels on the detector area depending on the exact sample-detector-position.

Of course, the optimal performance of the PXS requires extensive tuning of all mechanical and optical components. Although we benefit heavily from the engineering knowledge and skills which are included in the commercial and semi-commercial components of our setup, we cannot avoid all me-

chanical and optical instabilities which cause x-ray intensity fluctuations on several time scales. In general, we distinguish short-term fluctuations and long term drifts. The latter ones occur within minutes up to hours and can be explained by contamination of the PXS interaction chamber by copper debris, side shifts of the copper tape, and also by the increasing roughness of the copper tape after writing multiple tracks with the laser onto it. These long-term drifts can result in intensity changes and jumps of up to 50% and are not periodic in time.

Short-term fluctuations include all intensity instabilities typically within a few seconds down to pulse-to-pulse fluctuations. They are caused by the driving laser, unstable optical components but mainly by the position instabilities of the spooled copper tape with respect to the laser focus as well as target material inhomogeneities. Under certain conditions (which we usually avoid) very large intensity bursts can be observed in the integrated energy range from 1–100 keV, which may be assigned to electron beam generation²⁶ and the subsequent bremsstrahlung creation in the surrounding aluminium and lead walls of the vacuum chamber. These fluctuations can be easily suppressed by any type of monochromator in the setup, such as a Montel optic.

III. NORMALIZATION SCHEMES

As already described above only a few photons per pulse are diffracted in a typical UXR experiment. In order to measure temporal intensity changes of only a few percent with a sufficient SNR it is necessary to accumulate thousands up to millions of diffracted x-ray pulses over minutes and hours of measurement time. In general, the short-term fluctuations of the incoming x-ray flux increase the statistical error of the recorded signal. A reliable normalization technique can help to cancel the contribution of the intensity fluctuations to the signal and to minimize the necessary averaging time. Normalization is definitely mandatory in case of long-term drifts, which describe the changing mean value of the fluctuating x-ray intensity over absolute measurement time t . Because of the non-periodic behaviour in time of these drifts it is not easy to average them out. Hence, the measured signal would mainly represent the intensity drift of the source rather than the response of the sample under investigation if no normalization is applied.

We choose two superlattice (SL) samples in order to evaluate different normalization approaches. These artificial heterostructures consist of N_{SL} epitaxially grown double layers made of a metallic and insulating perovskite material. The spatial period $d_{SL} = d_{metal} + d_{insulator}$ of a double layer leads to SL Bragg peaks at multiple integers of the reciprocal SL vector $g_{SL} = 2\pi/d_{SL}$ where we adapt the enumeration of the SL peaks from Ref. 27. In the UXR experiments an 800 nm fs-pulse excites the sample, but is only absorbed in the metallic layers of the SL and thus induces a periodic stress profile.^{28,29} As a result, a coherent longitudinal phonon mode is excited which corresponds to an anti-phase oscillation of the individual layer thicknesses in each double layer. These structural dynamics lead to a periodic intensity change of most SL Bragg peaks. For many superlattice peaks the intensity of the x-ray Bragg reflection is proportional to the

amplitude of the superlattice phonon (i.e., expansion of the metallic layers and compression of the dielectric layers in between), since the contribution of the two layer materials to the structure factor of the reflections is varied linearly. In some cases this x-ray interference leads to additional modulation as for the peak SL+1 in Figs. 5 and 7 making the response even faster.³⁰ For both samples studied in this paper, the signal can be well approximated by a cosine-like oscillation due to the quasi-instantaneous stress. The oscillations are exponentially damped as the energy stored in the superlattice phonons propagates into the substrate.²⁹ Since in the current paper we only use the fast response for a demonstration of the setup, we refrain from further discussion of the physics and settle for observing the good applicability of the fit function. The according oscillation period of the coherent phonon mode is given by the double layer period d_{SL} and the material-specific sound velocities and is only a few ps for the considered samples. Thus, we can prove the sub-ps temporal resolution of the PXS. In order to observe the coherent phonon oscillation of the SL the integrated intensity of the diffracted x-rays $R(\tau)$ from a single SL Bragg peak has to be measured for different time delays τ . In analogy to all-optical pump-probe experiments we refer to $R(\tau)$ as transient x-ray reflectivity.

In the experiment the measured signal $S(\tau, t)$ also depends on the absolute time t because of the fluctuations and drifts of the incoming intensity $I(t)$:

$$S(\tau, t) = R(\tau) I(t).$$

In order to extract the reflectivity $R(\tau)$ from the real signal a normalization scheme must provide a measure which is proportional to $I(t)$ and at the same time independent of the delay τ . Obviously, this can be achieved by an additional detector that monitors only $I(t)$. For the observation of structure factor changes of a Bragg reflection we are only interested in the relative reflectivity change

$$\frac{S(\tau, t) - S_0(t)}{S_0(t)} = \frac{[R(\tau) - R_0] I(t)}{R_0 I(t)} = \frac{\Delta R(\tau)}{R_0},$$

where $R_0 = R(\tau < 0)$ denotes the unpumped reflectivity and $S_0(t) = S(\tau < 0, t)$ the measured unpumped signal. Here the incoming intensity $I(t)$ cancels out if $S(\tau, t)$ and $S_0(t)$ can be measured simultaneously or within a sufficiently small time interval Δt in which $I(t)$ can be assumed to be constant, e.g., for Δt smaller than long-term drifts of the x-ray source, and hence a direct measure of $I(t)$ is not necessary.

However, the applicability of a certain normalization method can be limited by various factors such as the x-ray diffraction geometry or the investigated sample itself. In the upcoming paragraphs we describe general approaches for normalization and give examples of their implementation from our and other groups.

A. Low-repetition rate normalization

The first SL sample consists of 11 double layers made of 7.9 nm metallic SrRuO₃ (SRO) and 14.9 nm dielectric SrTiO₃ (STO) epitaxially grown on a SRO buffer layer and a STO substrate by pulsed laser deposition.³¹ This sample was already studied intensively^{29,32,33} and has a SL phonon

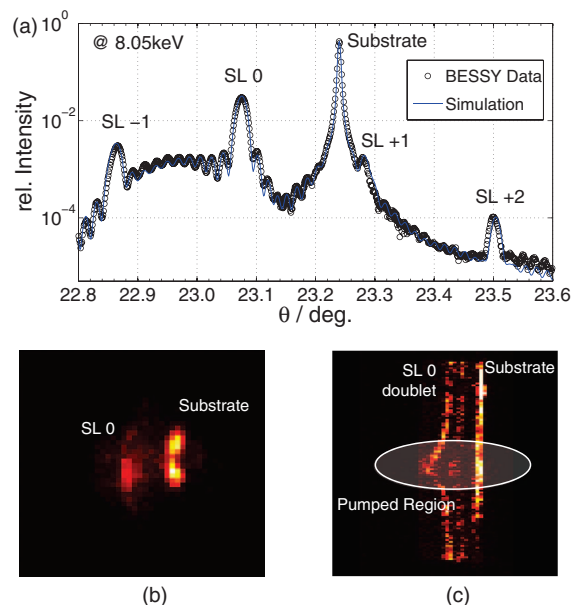


FIG. 2. (Color online) (a) The θ - 2θ diffraction scan of the STO/SRO SL features the sharp and intense STO substrate Bragg peak as well as several SL Bragg peaks. The experimental 2D diffraction patterns of the 0th SL Bragg peak are shown in two configurations. (b) The sample is placed in the focus of the Montel x-ray optic. (c) The sample is illuminated by the direct PXS emission without x-ray optics. The 0th SL Bragg peak appears as a $K_{\alpha 1, \alpha 2}$ doublet. The $K_{\alpha 2}$ Bragg reflection of the substrate is not within the divergence of the x-rays on the sample.

oscillation period of 3.2 ps, which can be derived most easily from the transient reflectivity change of the 0th SL Bragg peak. The θ - 2θ diffraction curve of the STO/SRO SL is shown in Fig. 2(a). It was measured at the energy-dispersive reflectometry (EDR) beamline of the storage ring BESSY II of the Helmholtz-Zentrum Berlin at a photon energy of 8.82 keV. For better comparison with the PXS data the θ -axis of the diffraction curve was rescaled for the Cu K_{α} energy of 8.05 keV.

PXS driven UXRD experiments generally feature a rather large angular distribution of the incoming x-ray beam because of the used focussing x-ray optics or, in case of no optics, because of the divergence of the nearly point-like x-ray emission from the laser plasma. Thus, it is favourable to use 2D x-ray cameras, or at least 1D arrays, in order to record the available angular information of the diffracted photons. In case of a diode-like point detector angular information or even the total information of the diffracted intensity, which misses the angular acceptance of the detector, is lost. Unfortunately, typical CCD x-ray cameras have a very low frame rate because of their long dead-time up to several seconds, which is mainly due to their long read-out time. Accordingly, the integration time for a single diffraction image should be well above 1 min in order to have a sufficiently high duty cycle of the detector. Otherwise a large fraction of the precious diffracted x-ray photons cannot be detected. The drawback of slow frame rates can be balanced by taking advantage of the large number of CCD pixels in order to record simultaneously the signal and normalization with the same CCD camera.²¹

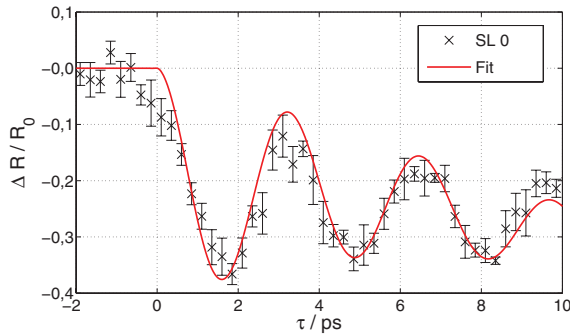


FIG. 3. (Color online) The relative reflectivity $\Delta R/R_0$ of the 0th SL Bragg peak of the SRO/STO SL was measured with the substrate normalization scheme. The error bars are determined by averaging 10 independent delay scan.

As it can be seen from Fig. 2(a) the angular separation between the 0th SL peak and the STO substrate peak is smaller than 0.3° . Thus, it is possible to record both peaks simultaneously within the convergence of our Montel optic, see Fig. 2(b). The same situation can be achieved without the use of an x-ray optics, where the divergence on the sample depends on its distance to the x-ray source. In the latter case, see Fig. 2(c), the sample is completely illuminated by the direct PXS emission. Within the collected angular range the 0th SL peak is visible as a $K_{\alpha 1, \alpha 2}$ doublet, whereas the $K_{\alpha 2}$ contribution of the strong substrate is cut off by the finite size of the sample.

The dielectric STO substrate is not optically excited by the 800 nm pump pulse. For delays larger than the time for sound propagation through the thin SL layers (in our case $\tau > 35$ ps) propagating sound waves originating from within the SL influence the structure of the STO substrate.^{29,34} Within this defined delay window the substrate peak reflectivity R_{sub} is constant. Consequently, the recorded signal of the substrate peak $S_{\text{sub}}(t)$ only depends on the absolute time t and can thus be utilized as a measure of the incoming intensity $I(t)$. Here we directly benefit from the large detector area, since no additional hardware is required to employ this normalization scheme. The data shown in Fig. 3 were obtained with this substrate normalization scheme while the sample was placed in the direct emission of the PXS without x-ray optics. Due to the repetition of the complete delay scan for several times we are able to plot also statistical error bars. The substrate normalization scheme strongly depends on the sample and the available angular distribution of the incoming x-rays. Furthermore, this method cannot be applied for large delays because of the transient change of the substrate reflectivity.

A more generally applicable normalization scheme is already indicated in Fig. 2(c) where the sample is placed in the direct PXS emission without x-ray optics. For a sufficiently large x-ray spot size on the sample also each point in the diffraction pattern originates from a different position on the sample. If the pumped region is smaller than the probe area on the sample also the diffraction pattern will contain a pumped and unpumped region. This situation can also be achieved with x-ray optics, but here the sample should be placed out of the x-ray focal plane in order to superimpose both areas more

easily. In this pumped-unpumped normalization scheme the transient signal $S(\tau, t)$ and the unpumped signal $S_0(t)$ can be measured simultaneously with the same CCD camera. We can apply this scheme as a normalization to determine the transient reflectivity change $\Delta R(\tau)/R_0$ for any crystalline sample.

However, a large fraction of the photons diffracted by the 0th SL Bragg peak does not contribute to the transient reflectivity $R(\tau)$. Moreover, the excitation on the sample is very inhomogeneous, as it is indicated by the curvature of the SL peak in Fig. 2(c). Another drawback of this scheme is the rather large x-ray footprint on the sample, which gives rise to an undesired time smearing and also maps different positions of the sample at once, which may be problematic for low-quality samples that lack lateral homogeneity.

For this specific STO/SRO SL sample the substrate normalization scheme is preferable compared to the pumped-unpumped method, because the SNR mainly depends on the total number of recorded photons, meaning the sum of photons contributing to the signal and to the normalization. This number is much higher for the intense substrate reflection. However, both normalization schemes can be applied in the so-called low-repetition rate regime for slow detectors without the need of additional hardware. It is even possible to apply both methods with or without x-ray optics, although one should prefer the use of the Montel x-ray optic because of the higher flux on the sample and the smaller x-ray energy bandwidth.

B. High-repetition rate normalization

The following normalization schemes are applied to a similar SL sample. This SL is made of 15 double layers of which each consist of 7.3 nm metallic $(\text{La}_{0.7}\text{Sr}_{0.3})\text{MnO}_3$ (LSMO) and 13.7 nm ferroelectric $(\text{Ba}_{0.7}\text{Sr}_{0.3})\text{TiO}_3$ (BST). Again the SL is grown epitaxially on a STO substrate. The θ - 2θ diffraction curve is shown in Fig. 4 and was again measured at the EDR beamline of the storage ring BESSY II of the Helmholtz-Zentrum Berlin.³⁵ The ultrafast response of this SL to an 800 nm fs pump pulse is very similar to the STO/SRO SL discussed above but with a slightly different period of the coherent SL phonon oscillation of 3.8 ps.

A common procedure to reduce statistical errors in a pump-probe experiment is increasing the repetition rate of the measurement. A well-known high-repetition rate

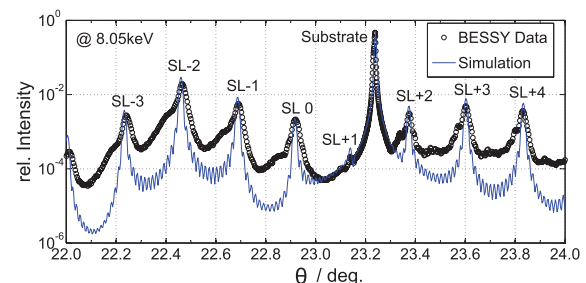


FIG. 4. (Color online) Several orders of SL Bragg peaks as well as an intense substrate Bragg peak are observable in the θ - 2θ scan of the LSMO/BST SL sample.

normalization scheme from all-optical experiments is chopping. Here the pump beam is periodically blocked in order to record the signal $S(\tau, t)$ and the unpumped signal $S_0(t)$ subsequently within a short time interval $\Delta t = 1/f_{\text{chop}}$ where f_{chop} is the chopping frequency. In this case half of the diffracted photons contribute to the signal and the other half to the normalization. If Δt is shorter than the time scale of long term drifts we can assume $I(t) = I(t + \Delta t)$ to be constant within this interval neglecting short-term fluctuations. Hence, we can apply this scheme to measure the relative reflectivity change $\Delta R(\tau)/R_0$. If Δt is even shorter than most of the characteristic short-term fluctuations of the PXS, chopping can also drastically reduce these sources of noise. Ideally, this requires a shot-to-shot temporal resolution of the x-ray camera. Because area detectors with kHz readout frequencies are just becoming available we have not implemented the chopping scheme, yet.

A very elegant way of normalization is again adapted from all-optical experiments and referred to as the rapid scanning method.³⁶ As the name suggests the complete delay range of interest of a pump-probe experiment is scanned very rapidly within a time interval Δt in which the incoming intensity $I(t)$ can again assumed to be constant. Thus, a single scan has to be faster than the time scale on which long-term drifts occur. It is not possible to scan the complete delay in a time shorter than all short-term fluctuations ($\Delta t < 5$ ms). Several of these fast delay scans are averaged to decrease the statistical errors caused by the fluctuations of the incoming intensity. With the rapid scanning method all diffracted photons contribute directly to the signal and no intensity is lost for normalization.

Similar to the chopping technique, the performance of rapid scanning is mainly limited by the frame rate of the x-ray detector and additionally by the speed of the delay stage. A complete delay scan has to be faster than the long-term drifts of the PXS which occur typically on the time scale of minutes. Hence, we do not have to utilize the Pilatus' full frame rate of up to 200 Hz but can work within a more easily controllable regime of ~ 1 Hz frame rate in order to scan a typical number of 50 delays well within 1 min of scan time.

A measurement of reflectivity oscillation for different SL Bragg peaks of the LSMO/BST SL is depicted in Fig. 5. The data were recorded with a frame rate of 2 Hz of the Pilatus camera and the complete scan was repeated up to 40 times.

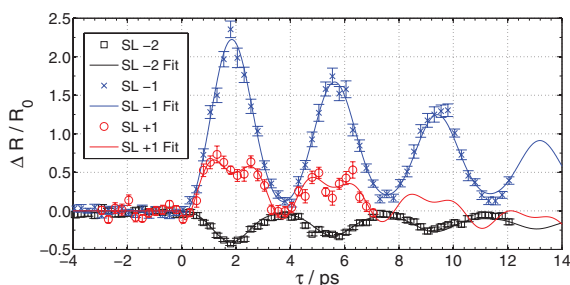


FIG. 5. (Color online) The rapid scanning technique was applied to measure the relative reflectivity $\Delta R/R_0$ of the SL-2, SL-1, and SL+1 Bragg peaks of the LSMO/BST SL. The data for each SL peak was accumulated within ~ 20 min per curve averaging over 40 complete delay scans with a frame rate of 2 Hz.

The total integration time per curve was ~ 20 min and we achieved an average relative error for all data points of 5.3%.

Rapid scanning provides a normalization without measuring the incoming intensity $I(t)$ directly. It is not capable of reducing short-term fluctuations in our implementation but can only average them out. This normalization technique is universally applicable. However, fast read-out x-ray detectors are the key part of this high-repetition normalization scheme, since one complete delay scan must be finished faster than the time scale of long-term fluctuations.

C. Direct normalization

In order to provide a sample-independent and direct measure of the incoming intensity $I(t)$ an additional detector is required. This detector then has to measure the PXS flux between source and sample ideally with the same frame rate as the x-ray camera records the diffraction signal. X-ray sensitive diodes are generally fast enough for this purpose and have a sufficiently high quantum efficiency to record also low x-ray intensities. Since the integrated intensity over the whole PXS spectrum is not proportional to the intensity of the characteristic x-ray emission lines used in the diffraction experiments, it is necessary to monitor the x-ray flux behind a monochromator or with an according energy-dispersive detector.³⁷ One usually has to bypass some fraction of the incoming x-ray beam onto the normalization detector which will reduce the flux on the sample accordingly. Such direct normalization schemes were already implemented, e.g., by placing an ionization chamber³⁸ or a thin diamond beam splitter²⁴ into the incoming x-ray beam.

In our setup the Montel x-ray optic acts as a monochromator since it transmits only the Cu K_α energies which are then diffracted from the sample. A detailed description of Montel optics can be found in the literature.^{16,39} The divergent emission of the source is focused in two dimensions by two sequential reflections from elliptically bent multilayer mirrors. The transmission profile of the optic shown in the inset of Fig. 6 reveals that in addition to this monochromatic focal region F there are two regions S which are produced by x-rays undergoing only a single reflection from one multilayer mirror. This radiation is monochromatic as well, and we can assume a linear relation between the intensity in the S regions and in the focus F. In a typical diffraction experiment the two S-beams do not hit the sample and are therefore useless. In our case we use an x-ray diode (CRYSTAL PHOTONICS) to monitor the x-ray flux in one of the S regions to have a direct and proportional measure of the monochromatic incoming intensity $I(t)$.

In order to verify the applicability of this normalization scheme we measured the direct intensity of the Montel focus F with the Pilatus camera in single-photon-counting mode and the intensity of a single reflection S with the x-ray diode simultaneously. The ratio of the diode and the Pilatus signal shown as red line in Fig. 6 proves the linear relation between the two signals. Accordingly, the normalized signal contains much less short-term fluctuations as compared to the original intensity which improves the SNR for UXRD experiments drastically. For very large fluctuations and drifts of about 50%

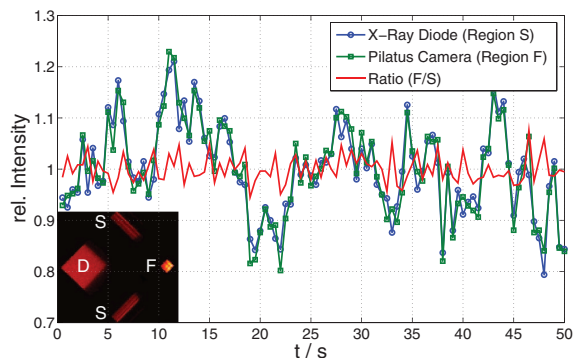


FIG. 6. (Color online) The focus F of the Montel optic was measured with the Pilatus camera (green square) simultaneously with the intensity of a single reflection S of the Montel optic by an x-ray diode (blue circle). The ratio of the Pilatus and diode signal (red line) features much less fluctuations than the original data. The transmission profile of the Montel optic is shown in the inset, where the direct transmission of the Montel optic is labelled as D.

of the PXS intensity a slight nonlinearity of the x-ray diode signal causes deviations of the normalized signal. This nonlinearity is most likely caused by an electronic offset of the diode itself and may be reduced by a suitable calibration routine. The direct normalization scheme reduces short-term fluctuations but cannot completely cancel large long-term drifts because of the diode's nonlinearity. Therefore, we combine this method with the rapid scanning technique to improve the SNR even further.

We apply this combination of diode-normalization and rapid scanning again for the measurement of SL Bragg peak oscillations of the LSMO/BST SL (Fig. 7). In comparison with the data shown in Fig. 5 the average relative error for each data point is further reduced to 4.6% although the total integration time per curve is reduced to only 10 min. This normalization scheme requires extensive technical efforts such as high-repetition x-ray cameras and an additional x-ray diode as well as an x-ray optic. On the other hand, this combined normalization technique is independent of the investigated sample and does not decrease the number of photons which account for the diffraction signal.

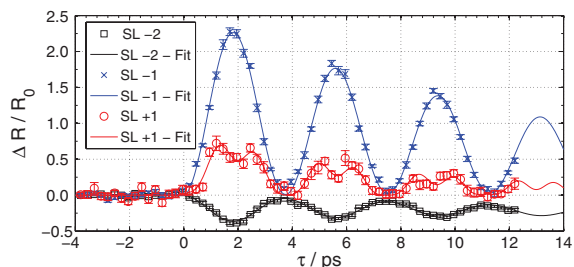


FIG. 7. (Color online) The reflectivity oscillations of three different SL Bragg peaks of a LSMO/BST SL were measured with a combination of the x-ray diode normalization and rapid scanning. The frame rate of the Pilatus was 1 Hz and each curve was obtained within a total integration time of ~ 10 min.

IV. CONCLUSIONS AND OUTLOOK

Even though PXS sources operated at kHz repetition rate are easy to use and feature high stability, advanced normalization schemes are necessary to achieve a sufficient SNR in UXRD experiments. Here we presented a detailed overview of low- and high-repetition rate normalization techniques as well as a diode-based direct normalization scheme utilizing the specific transmission profile of a Montel x-ray optic. With the combination of the direct intensity normalization and the rapid scanning we could drastically reduce short-term fluctuations and cancel long term drifts of the PXS, respectively. With the diode normalization scheme it is also possible to record time-resolved θ - 2θ scans over an angular range much larger than the divergence of the x-ray optics. Thereby not only peak intensity but also the position, width and shape of a Bragg peak can be precisely observed on an ultrafast time scale.

ACKNOWLEDGMENTS

We gratefully acknowledge the financial support by the BMBF via Grant No. 03WK03A and the Deutsche Forschungsgemeinschaft (DFG) (Grant No. BA2281/3-1). We thank Dr. Ionela Vrejoiu for fruitful discussions and for providing the samples experimentally investigated.

- ¹A. Rousse, C. Rischel, and J.-C. Gauthier, *Rev. Mod. Phys.* **73**, 17 (2001).
- ²M. Bargheer, N. Zhavoronkov, M. Woerner, and T. Elsaesser, *ChemPhysChem* **7**, 783 (2006).
- ³M. Chergui and A. H. Zewail, *ChemPhysChem* **10**, 28 (2009).
- ⁴R. W. Schoenlein, S. Chattopadhyay, H. H. W. Chong, T. E. Glover, P. A. Heimann, C. V. Shank, A. A. Zholents, and M. S. Zolotarev, *Science* **287**, 2237 (2000).
- ⁵K. Hollack, S. Khan, R. Mitzner, and T. Quast, *Phys. Rev. Lett.* **96**, 054801 (2006).
- ⁶P. Beaud, S. L. Johnson, A. Streun, R. Abela, D. Abramsohn, D. Grolimund, F. S. Krasniqi, T. Schmidt, V. Schlott, and G. Ingold, *Phys. Rev. Lett.* **99**, 174801 (2007).
- ⁷B. McNeil, *Nat. Photonics* **3**, 375 (2009).
- ⁸A. L. Cavalieri, D. M. Fritz, S. H. Lee, P. H. Bucksbaum, D. A. Reis, J. Rudati, D. M. Mills, P. H. Fuoss, G. B. Stephenson, C. C. Kao, D. P. Siddons, D. P. Lowney, A. G. MacPhee, D. Weinstein, R. W. Falcone, R. Pahl, J. Als-Nielsen, C. Blome, S. Düsterer, R. Ischebeck, H. Schlarb, H. Schulte-Schrepping, T. Tschentscher, J. Schneider, O. Hignette, F. Sette, and K. Sokolowski-Tinten, *Phys. Rev. Lett.* **94**, 114801 (2005).
- ⁹F. Brunel, *Phys. Rev. Lett.* **59**, 52 (1987).
- ¹⁰C. Reich, P. Gibbon, I. Uschmann, and E. Förster, *Phys. Rev. Lett.* **84**, 4846 (2000).
- ¹¹A. Cavalleri, C. W. Siders, F. L.H. Brown, D. M. Leitner, C. Tóth, J. A. Squier, C. P. J. Barty, K. R. Wilson, K. Sokolowski-Tinten, M. Horn von Hoegen, D. von der Linde, and M. Kammler, *Phys. Rev. Lett.* **85**, 586 (2000).
- ¹²F. Ewald, H. Schwoerer, and R. Sauerbrey, *Europhys. Lett.* **60**, 710 (2002).
- ¹³W. Krueer, *The Physics of Laserplasma Interactions* (Westview, New York, 2003).
- ¹⁴W. Lu, M. Nicoul, U. Shymanovich, A. Tarasevitch, P. Zhou, K. Sokolowski-Tinten, D. von der Linde, M. Mašek, P. Gibbon, and U. Teubner, *Phys. Rev. E* **80**, 026404 (2009).
- ¹⁵M. Nicoul, U. Shymanovich, A. Tarasevitch, D. von der Linde, and K. Sokolowski-Tinten, *Appl. Phys. Lett.* **98**, 191902 (2011).
- ¹⁶M. Bargheer, N. Zhavoronkov, R. Bruch, H. Legall, H. Stiel, M. Woerner, and T. Elsaesser, *App. Phys. B: Lasers Opt.* **80**, 715 (2005).
- ¹⁷N. Zhavoronkov, Y. Gritsai, M. Bargheer, M. Woerner, T. Elsaesser, F. Zamponi, I. Uschmann, and E. Förster, *Opt. Lett.* **30**, 1737 (2005).
- ¹⁸C. Rose-Petrucci, R. Jimenez, T. Guo, A. Cavalleri, C. W. Siders, F. Rksi, J. A. Squier, B. C. Walker, K. R. Wilson, and C. P. J. Barty, *Nature (London)* **398**, 310 (1999).

- ¹⁹K. Sokolowski-Tinten, C. Blome, J. Blums, A. Cavalleri, C. Dietrich, A. Tarasevitch, I. Uschmann, E. Forster, M. Kammler, M. Horn-von Hoegen, and D. von der Linde, *Nature (London)* **422**, 287 (2003).
- ²⁰C. von Korff Schmising, M. Bargheer, M. Kiel, N. Zhavoronkov, M. Woerner, T. Elsaesser, I. Vrejoiu, D. Hesse, and M. Alexe, *Phys. Rev. Lett.* **98**, 257601 (2007).
- ²¹M. Bargheer, N. Zhavoronkov, Y. Gritsai, J. C. Woo, D. S. Kim, M. Woerner, and T. Elsaesser, *Science* **306**, 1771 (2004).
- ²²F. Zamponi, Z. Ansari, C. von Korff Schmising, P. Rothhardt, N. Zhavoronkov, M. Woerner, T. Elsaesser, M. Bargheer, T. Trobitsch-Ryll, and M. Haschke, *Appl. Phys. A: Mater. Sci. Process.* **96**, 51 (2009).
- ²³*Time-Resolved X-Ray Scattering*, edited by K.-T. Tsen, J.-J. Song, M. Betz, and A. Y. Elezzabi (SPIE, Bellingham, Washington, 2011), Vol. 7937.
- ²⁴B. Freyer, J. Stingl, F. Zamponi, M. Woerner, and T. Elsaesser, *Opt. Express* **19**, 15506 (2011).
- ²⁵F. Zamponi, Z. Ansari, M. Woerner, and T. Elsaesser, *Opt. Express* **18**, 947 (2010).
- ²⁶J. Uhlig, C. G. Wahlström, M. Walczak, V. Sundström, and W. Fullagar, *Laser Part. Beams* **29**, 415 (2011).
- ²⁷G. Bauer, *Optical Characterization of Epitaxial Semiconductor Layers* (Springer-Verlag, Berlin, 1996).
- ²⁸M. Woerner, C. von Korff Schmising, M. Bargheer, N. Zhavoronkov, I. Vrejoiu, D. Hesse, M. Alexe, and T. Elsaesser, *Appl. Phys. A: Mater. Sci. Process.* **96**, 83 (2009).
- ²⁹M. Herzog, D. Schick, P. Gaal, R. Shayduk, C. von Korff Schmising, and M. Bargheer, *Appl. Phys. A* **1** (2011).
- ³⁰M. Herzog, D. Schick, W. Leitenberger, R. Shayduk, R. M. van der Veen, C. J. Milne, S. L. Johnson, I. Vrejoiu, and M. Bargheer, *New J. Phys.* **14**, 013004 (2012).
- ³¹I. Vrejoiu, G. Le Rhun, L. Pintilie, D. Hesse, M. Alexe, and U. Gösele, *Adv. Mater.* **18**, 1657 (2006).
- ³²C. von Korff Schmising, M. Bargheer, M. Kiel, N. Zhavoronkov, M. Woerner, T. Elsaesser, I. Vrejoiu, D. Hesse, and M. Alexe, *App. Phys. B* **88**, 1 (2007).
- ³³M. Herzog, W. Leitenberger, R. Shayduk, R. van der Veen, C. J. Milne, S. L. Johnson, I. Vrejoiu, M. Alexe, and D. Hesse, *Appl. Phys. Lett.* **96**, 161906 (2010).
- ³⁴C. von Korff Schmising, M. Bargheer, M. Kiel, N. Zhavoronkov, M. Woerner, T. Elsaesser, I. Vrejoiu, D. Hesse, and M. Alexe, *Phys. Rev. B* **73**, 212202 (2006).
- ³⁵In the simulation we assume a perfect sample structure. Accordingly, only the positions and amplitudes of the SL Bragg peaks are predicted correctly.
- ³⁶G. C. Cho, W. Kütt, and H. Kurz, *Phys. Rev. Lett.* **65**, 764 (1990).
- ³⁷M. Silies, H. Witte, S. Linden, J. Kutzner, I. Uschmann, E. Förster, and H. Zacharias, *Appl. Phys. A: Mater. Sci. Process.* **96**, 59 (2009).
- ³⁸K. Sokolowski-Tinten, private communication (2011).
- ³⁹U. Shymanovich, M. Nicoul, K. Sokolowski-Tinten, A. Tarasevitch, C. Michaelsen, and D. von der Linde, *Appl. Phys. B: Lasers Opt.* **92**, 493 (2008).

PAPER XII

Subpicosecond hard x-ray streak camera using single-photon counting

H. Enquist, H. Navirian, R. Nüske, C. von Korff Schmising,
A. Jurgilaitis, M. Herzog, M. Bargheer, P. Sondhaus and
J. Larsson.

Opt. Lett. **35**, 3219 (2010).

Subpicosecond hard x-ray streak camera using single-photon counting

Henrik Enquist,^{1,2} Hengameh Navirian,¹ Ralf Nüske,¹ Clemens von Korff Schmising,¹ Andrius Jurgilaitis,¹ Marc Herzog,³ Matias Bargheer,³ Peter Sondhaus,² and Jörgen Larsson^{1,*}

¹Atomic Physics Division, Department of Physics, Lund University, P.O. Box 118, SE-221 00 Lund, Sweden

²MAX-lab, Lund University, Lund, Sweden

³Institut für Physik und Astronomie, Universität Potsdam, Potsdam, Germany

*Corresponding author: jorgen.larsson@fysik.lth.se

Received June 7, 2010; revised August 19, 2010; accepted August 24, 2010; posted September 7, 2010 (Doc. ID 129590); published September 22, 2010

We have developed and characterized a hard x-ray accumulating streak camera that achieves subpicosecond time resolution by using single-photon counting. A high repetition rate of 2 kHz was achieved by use of a readout camera with built-in image processing capabilities. The effects of sweep jitter were removed by using a UV timing reference. The use of single-photon counting allows the camera to reach a high quantum efficiency by not limiting the divergence of the photoelectrons. © 2010 Optical Society of America

OCIS codes: 040.1490, 040.7480, 100.0118, 150.6044, 340.6720.

Time-resolved x-ray diffraction has become a standard tool for studies of the dynamics of laser excited solids [1]. Synchrotron radiation sources operating in standard mode produce high brilliance x-ray beams, but the time duration of the pulses is in the 50–500 ps range. Any experiment requiring better time resolution will need to rely on a fast detector. Streak cameras have been reported to give a time resolution down to 233 fs [2] for UV radiation in the accumulating mode and 350 fs using 1.5 keV x rays [3] in the single-shot mode. This time resolution is, however, not yet reached for hard x rays. The fastest streak cameras rely on limiting the divergence of the photoelectrons [4]. This implies a severe reduction in quantum efficiency.

In time-resolved x-ray diffraction experiments carried out at third-generation electron storage rings, the number of photons per pulse is relatively small and operation in the accumulating mode is necessary. The mechanisms limiting the time resolution of a streak camera are described in detail elsewhere [3–5]. The main factors are the sweep speed, the size of the input slit, the aberrations of the electron optics, and the energy spread of the photoelectrons. The field generated by the sweep plates also introduces additional dispersion [4,6].

In this Letter we describe an x-ray streak camera that uses single-photon counting to reduce the effects of dispersion and imperfect imaging. Images are analyzed in real time, and a UV timing reference is used to track and compensate the sweep jitter. The use of a readout camera with built-in image processing capabilities reduces the bandwidth required to transfer data to the host computer. Thus a frame rate of 2 kHz can be reached. The concept of a single-photon counting camera was first proposed by Mumane *et al.* [7], and a proof-of-principle demonstration was published by Larsson [8], who improved the time resolution of a commercial streak camera from 5 to 1.5 ps.

A set of experiments to demonstrate the performance of the streak camera was conducted at beamline D611 at the MAX-lab synchrotron radiation facility. This bending magnet beamline is designed for laser pump–x-ray probe experiments and produces about 5000 photons per pulse and

0.02% bandwidth. The pulse duration is 500 ps. A Ti:Al₂O₃ femtosecond laser system, operating at a repetition rate of 4.25 kHz, with a 790 nm center wavelength and 45 fs pulse duration was used for the measurements. The laser beam was split into three arms. Laser pulses with an energy of 100 μJ were used to trigger a photoconducting switch that generates the high voltage sweep ramp for the streak camera. Part of the pulse (200 μJ) was used to generate the third harmonic, which was sent onto the photocathode as a timing reference. Up to 700 μJ was available to pump the sample. The streak camera was mounted with a 100-μm-wide CsI photocathode in a 6° grazing incidence configuration [9]. Electrons were accelerated, using a mesh with a >90% open area ratio, to 8 kV over a gap of 2 mm. Subsequently, electrons were imaged from the cathode to a microchannel plate (MCP) with gain larger than 10⁸, enabling a single photoelectron emitted from the cathode to be detected by the readout camera. Thus, the overall quantum efficiency of the streak camera equals that of the photocathode. The quantum efficiency was deduced by measuring the photon flux using a calibrated x-ray diode and comparing it with the single-photon count rate and was found to be larger than 10%. The readout camera (Mikrotron MC1364) uses a complementary metal-oxide semiconductor sensor and has an embedded FPGA image processor that can perform a large part of the image analysis. This enables images to be analyzed in real time at frame rates of several kilohertz.

We will now discuss how single-photon counting in the accumulating mode can increase the temporal resolution compared to the single-shot mode [7,8]. The x rays are sent onto the photocathode together with a UV pulse derived from the same laser that is used to pump the sample. Each incident x-ray photon generates up to 20 photoelectrons [10]. If the aperture of the streak camera is not constrained, many of the photoelectrons can propagate to the MCP. Because of dispersion and imaging errors, electrons will travel individual trajectories and be imaged as a spot that can be irregular in shape. The idea behind single-photon counting is that the center of each spot can be determined with an accuracy smaller than the spot size. The uncertainty of the center position depends on the number

of detected photoelectrons per photon, and, hence, it is important to keep as many as possible to minimize statistical variations. Typically four photoelectrons per x-ray photon are detected. Each sweep generates an image in which all spots corresponding to photon events are found, and their center of gravity is determined. The UV pulse consists of several hundred photoelectrons, and its position can be determined with high precision and is used as a timing fiducial. As this pulse has a known fixed delay relative to the pump pulse, the position of this pulse can be used to remove the shot-to-shot jitter in the processed data.

To test the system, a second UV pulse was generated by splitting off part of the power in the reference beam. This second beam was then used as a simulated x-ray signal at a fixed delay of 8 ps. Figure 1(a) shows a gray scale image averaged for 1 s at a repetition rate of 4.25 kHz. The time resolution in this particular image is 2.5 ps. When the pulses are accumulated using the single-photon counting mode, the time resolution measured as the FWHM is 280 fs. The vast improvement can be seen in Fig. 1(b).

In the following we demonstrate the effective time resolution of our streak camera for hard x-ray pulses by repeating three previously performed ultrafast diffraction experiments.

The structural rearrangements associated to ultrafast melting of semiconductors, such as InSb, has previously been studied [11,12]. The disordering can be detected as a fast drop of x-ray diffraction efficiency [12]. An asymmetrically cut InSb sample was illuminated with laser pulses with a fluence of 38 mJ/cm². The incidence angle between laser and sample surface was 15°. The disordering was probed by x rays with a photon energy of 3.15 keV at an incidence angle of 0.9° and a bandwidth of 2%. The intensity of the (111) reflection was recorded. The sample was continuously translated to exchange the surface in order to avoid effects from ripple formation [13]. At the translation speed of 1 mm/s, the ripples did not reach a high enough amplitude to influence the measurement. This limited the data acquisition time to 30 s. Figure 2 shows the drop in x-ray diffraction as recorded by the streak camera in the single-photon counting mode. The curve was fitted to an error function, yielding an upper bound of 640 fs for the 90% to 10% fall time. The fall time of the (111) reflection has been measured at 430 fs [12]. A

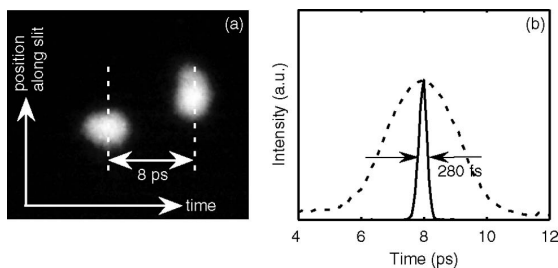


Fig. 1. Images showing two UV pulses separated by 8 ps. (a) Gray scale image of averaging mode and (b) lineout in averaging mode (dashed curve) and photon counting mode (solid curve). In the photon counting mode, the smearing effects of jitter and imaging are removed, yielding a time resolution of 280 fs.

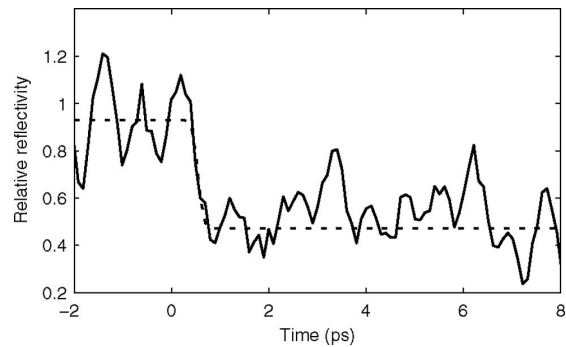


Fig. 2. Time-resolved drop in x-ray diffraction induced by nonthermal melting of InSb. The dashed line shows the fitted error function.

quadratic deconvolution yielded the time resolution of the streak camera to be 480 fs.

Laser excitation of bismuth (Bi) leads to the excitation of optical phonons [14]. The (111) reflection in Bi is very close to being forbidden. Excitation of the A_{1g} phonon mode induces a drop in the x-ray reflectivity followed by an oscillation. The period of the oscillation depends on temperature and excitation strength and is 340 fs for weak excitation [15] and 467 fs for stronger excitation [14]. A symmetric thin-film Bi sample was illuminated by laser pulses with a fluence of 4 mJ/cm² at an incidence angle of 45°. The phonons were probed by x rays with a photon energy of 3.2 keV. Figure 3 shows the drop in x-ray reflectivity associated with the excitation of the optical phonons. The accumulation time was 40 min. Fitting an error function yields an upper bound for the time resolution of 660 fs, which is large compared to the expected 170 fs fall time.

When a superlattice of SrTiO₃ (STO) and SrRuO₃ (SRO) is excited by a short laser pulse, large-amplitude coherent acoustic superlattice phonons can be generated. For an excited superlattice consisting of ten bilayers of 17.9 nm of STO and 6.3 nm of SRO, the (0 0 116) reflection shows a strong oscillating reduction of the reflectivity, with a period of 3 ps [16]. The sample was excited at a fluence of 30 mJ/cm², and the phonons were probed by x rays with a photon energy of 5.8 keV, and a bandwidth of 2×10^{-4} . Directly after excitation the reflectivity drops, followed by a damped oscillation, as shown in Fig. 4. This oscillation was compared to measurements done using a laser

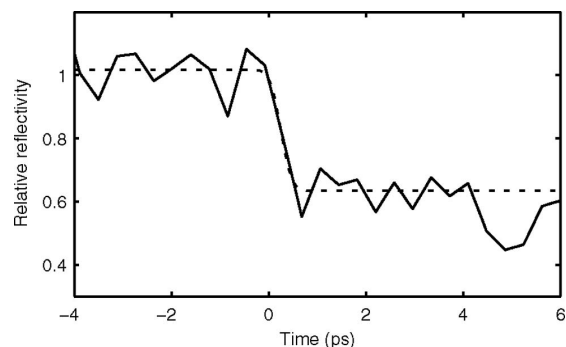


Fig. 3. Time-resolved diffraction of bismuth following laser excitation. The fitted error function is shown as a dashed line.

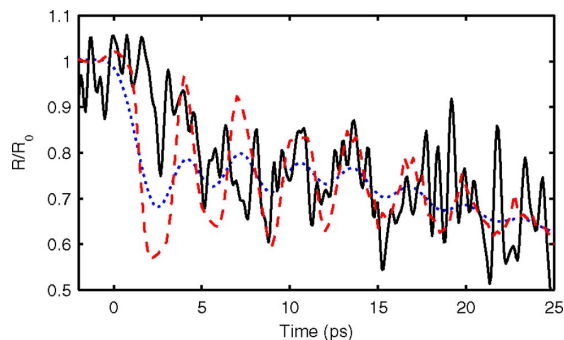


Fig. 4. (Color online) Oscillations in the x-ray reflectivity of the SrTiO₃/SrRuO₃ superlattice as recorded by the streak camera (solid curve) and from [16] (dashed curve). The dotted curve shows data from [16] filtered to simulate a time resolution of 2 ps.

plasma x-ray source at a time resolution of ~ 200 fs [17]. The comparison shows that the amplitude of the oscillation is unaffected by the temporal resolution of the streak camera. This is consistent with a resolution in the 400–600 fs range, as found in the studies of nonthermal melting and optical phonons in Bi. For a temporal resolution lower than 2 ps, the oscillation amplitude of the convoluted data is reduced, as illustrated in Fig. 4.

In conclusion, we have developed a hard x-ray streak camera capable of achieving subpicosecond resolution using single-photon counting. The performance has been demonstrated by reproducing three well-characterized experiments. The temporal spread due to jitter is removed by using a UV reference, and the single-photon counting compensates for smearing due to imperfect imaging and energy spread of the photoelectrons.

Streak cameras with subpicosecond time resolution will have a significant impact on the field of time-resolved science at synchrotron radiation facilities. They will also play a role at x-ray free-electron lasers. When lasers are synchronized to the accelerator it is essential to have a user-controlled diagnostic to track the delay between laser and x rays. By using a streak camera this can be measured directly at the position of the sample.

The authors thank the Swedish Research Council (VR), the Knut and Alice Wallenberg Foundation, the Crafoord Foundation, and the Carl Trygger Foundation for financial support. We also acknowledge the support of the European Commission via the Marie-Curie Program and the IRUVX-PP project.

References

1. D. Reis, K. Gaffney, G. Gilmer, and B. Torralva, *Mat. Res. Bull.* **31**, 601 (2006).
2. J. Feng, H. J. Shin, J. R. Nasiatka, W. Wan, A. T. Young, G. Huang, A. Comin, J. Byrd, and H. A. Padmore, *Appl. Phys. Lett.* **91**, 134102 (2007).
3. P. Gallant, P. Forget, F. Dorchie, Z. Jiang, J. C. Kieffer, P. A. Jaanimagi, J. C. Rebuffie, C. Goulmy, J. F. Pelletier, and M. Sutton, *Rev. Sci. Instrum.* **71**, 3627 (2000).
4. M. M. Shakya and Z. Chang, *Appl. Phys. Lett.* **87**, 041103 (2005).
5. D. Bradley, A. Roddie, W. Sibbett, M. Key, M. Lamb, C. Lewis, and P. Sachsenmaier, *Opt. Commun.* **15**, 231 (1975).
6. G. Huang, J. Byrd, J. Feng, H. A. Padmore, J. Qiang, and W. Wan, in *Proceedings of EPAC 2006, Edinburgh, Scotland* (2006), pp. 1250–1252.
7. M. Murnane, H. Kapteyn, and R. Falcone, *Appl. Phys. Lett.* **56**, 1948 (1990).
8. J. Larsson, *Opt. Lett.* **26**, 295 (2001).
9. D. Lowney, P. Heimann, H. Padmore, E. Gullikson, A. MacPhee, and R. Falcone, *Rev. Sci. Instrum.* **75**, 3131 (2004).
10. C. Ortiz and C. Caleman, *J. Phys. Chem. C* **111**, 17442 (2007).
11. A. Rousse, C. Rischel, and J. Gauthier, *Rev. Modern Phys.* **73**, 17 (2001).
12. A. Lindenberg, J. Larsson, K. Sokolowski-Tinten, K. Gaffney, C. Blome, O. Synnergren, J. Sheppard, C. Caleman, A. MacPhee, D. Weinstein, D. Lowney, T. Allison, T. Matthews, R. Falcone, A. Cavalleri, F. Fritz, S. Lee, P. Bucksbaum, D. Reis, J. Rudati, P. Fuoss, C. Kao, D. Siddons, R. Pahl, J. Als-Nielsen, S. Duesterer, R. Ischebeck, H. Schlarb, H. Schulte-Schrepping, T. Tschentscher, J. Schneider, D. von der Linde, O. Hignette, F. Sette, H. Chapman, R. Lee, T. Hansen, S. Techert, J. Wark, M. Bergh, G. Huldt, D. van der Spoel, N. Timneanu, J. Hajdu, R. Akre, E. Bong, P. Krejcik, J. Arthur, S. Brennan, K. Luening, and J. Hastings, *Science* **308**, 392 (2005).
13. A. Jurgilaitis, R. Nüske, H. Enquist, H. Navirian, P. Sondhaus, and J. Larsson, *Appl. Phys. A* **100**, 105 (2010).
14. K. Sokolowski-Tinten, C. Blome, J. Blurns, A. Cavalleri, C. Dietrich, A. Tarasevitch, I. Uschmann, E. Forster, M. Kammler, M. Horn-von Hoegen, and D. von der Linde, *Nature* **422**, 287 (2003).
15. M. Hase, K. Mizoguchi, H. Harima, S. Nakashima, M. Tani, K. Sakai, and M. Hangyo, *Appl. Phys. Lett.* **69**, 2474 (1996).
16. C. von Korff Schmising, M. Bargheer, M. Kiel, N. Zhavoronkov, M. Woerner, T. Elsaesser, I. Vrejoiu, D. Hesse, and M. Alexe, *Appl. Phys. B* **88**, 1 (2007).
17. C. von Korff Schmising, A. Harpoeth, N. Zhavoronkov, Z. Ansari, C. Aku-Leh, M. Woerner, T. Elsaesser, M. Bargheer, M. Schmidbauer, I. Vrejoiu, D. Hesse, and M. Alexe, *Phys. Rev. B* **78**, 060404 (2008).